



**UNIVERSITÀ  
DEGLI STUDI  
DI TRIESTE**

**UNIVERSITÀ DEGLI STUDI DI TRIESTE**  
**XXXIV CICLO DEL DOTTORATO DI RICERCA IN**  
**NANOTECNOLOGIE**

**Harnessing the plasmonic properties of gold  
nanoparticles: functionalization strategies coupled  
with novel spectroscopic tools**

Settore scientifico-disciplinare: FIS/03

**DOTTORANDO / A**  
**Ahmed Alsadig Ahmed Mohammed**

**COORDINATORE**  
**Prof. Alberto Morgante**

**SUPERVISORE DI TESI**  
**Dr. Loredana Casalis**

**TUTORE DI TESI**  
**Dr. Pietro Parrisè**

**ANNO ACCADEMICO 2021/2022**

*“Everything happens for a reason  
and that reason is usually physics”*

# Table of Contents

<b>Table of Contents</b> .....	<b>iii</b>
<b>List of Tables</b> .....	<b>viii</b>
<b>List of Figures</b> .....	<b>ix</b>
<b>List of Appendices</b> .....	<b>xviii</b>
<b>Acknowledgements</b> .....	<b>xix</b>
<b>Abstract</b> .....	<b>xx</b>
<b>Thesis overview and objectives</b> .....	<b>21</b>
1.1 Overview .....	21
1.2 Research motivation, objective, and outlines.....	22
<b>Background</b> .....	<b>24</b>
2.1 Nanotechnology .....	24
2.2 Nanoparticles and their properties.....	25
2.3 Gold Nanoparticles (AuNPs) .....	29
2.3.1 Chemical Synthesis of AuNPs.....	30
2.3.2 Colloidal Stability.....	32
2.4 The ligand shell: Self-Assembled Monolayer (SAM).....	33
2.5 Optical Properties of Metal Nanoparticles .....	36
2.5.1 Optical properties of metals.....	36
2.5.2 Surface Plasmons Resonance .....	38
2.5.3 Localized Surface Plasmons .....	39
2.5.4 Plasmonic coupling.....	41
2.6 Sensors and Biosensors .....	43
2.6.1 Surface plasmon resonance-based biosensors .....	44

2.6.2	Localized surface plasmon-based biosensors .....	46
2.6.3	Refractive index sensitivity .....	48
2.7	Thermal lens spectroscopy: beyond a technique on the horizon.....	49
2.7.1	Historical background.....	49
2.7.2	Sensitivity of TLS technique .....	51
2.7.3	TLS Configurations .....	52
2.7.4	Applications of TLS: chemical and biomedical analysis.....	54
2.8	Biomarkers, diseases, and therapeutic agents .....	55
2.8.1	Cancer biomarkers .....	55
2.8.2	Breast cancer and its subtypes .....	56
2.8.3	HER receptors: structure and function.....	57
2.8.4	HER2-ECD: a predictive protein breast cancer biomarker.....	59
2.8.5	Treatment of HER2-positive breast cancer patients .....	61
2.8.6	Anti-HER2 therapeutic agent: Trastuzumab.....	61
2.8.7	Novel antibody formats: Nanobodies .....	<b>Error! Bookmark not defined.</b>
<b>Materials and methods .....</b>		<b>65</b>
3.1	Chemicals .....	65
3.2	Synthesis of gold nanoparticles (AuNPs).....	66
3.3	Functionalization of AuNPs: NTA-based strategy.....	67
3.3.1	NTA and TOEG3 mixed-SAM.....	67
3.3.2	Co <sup>2+</sup> chelation and attachment of Histidine-Tagged HER2 Protein .....	67
3.3.3	Assessment of HER2-Trastuzumab recognition via indirect ELISA .....	67
3.3.4	LSPR-Based Detection of Trastuzumab using HER2 Decorated AuNPs .....	68
3.3.5	Filtering a human serum with Ni-NTA agarose matrix .....	69
3.4	Functionalization of AuNPs: DNA-based strategy .....	69



3.4.1	Single-stranded DNA sequences.....	69
3.4.2	Nanobodies optimization and production.....	69
3.4.3	C8-DNA Conjugate production.....	70
3.4.4	Preparation of ssDNA and ssDNA/TOEG6 customized SAM on AuNPs.....	70
3.4.5	Assessing the conformation of DNA strands on AuNP surface .....	71
3.4.6	Stability of ssDNA/TOEG6@AuNPs in a biological environment .....	72
3.4.7	Avidin interaction with Biotinylated AuNPs.....	72
3.4.8	Biofunctionalization of AuNPs with C8 nanobodies.....	73
3.4.9	Dot blot immunological assay for detection of HER2 antigen .....	73
3.4.10	Detection of HER2 using Online TLS coupled with MGEC .....	74
3.4.11	Investigating the interaction between ssDNA/TOEG6 coated AuNPs and lipid membranes.....	75
3.5	Functionalization of AuNPs: Click chemistry-based strategy .....	76
3.5.1	Preparation of water-soluble alkyne-functionalized AuNPs.....	76
3.5.2	Linking of azide modified molecules to the prepared particles.....	76
3.5.3	TLS analysis of the clicked dye-AuNPs.....	77
3.6	Characterization techniques .....	77
3.6.1	Ultraviolet/Visible (UV/Vis) spectrophotometry .....	78
3.6.2	Dynamic light scattering (DLS) .....	78
3.6.3	Transmission Electron Microscopy (TEM) .....	79
3.6.4	Scanning Electron Microscopy (SEM).....	80
3.6.5	Atomic Force Microscopy (AFM) .....	82
3.6.7	Thermal Lens Microscopy (TLS) .....	83
3.6.8	Gel electrophoresis .....	86
3.6.9	Fluorescence intensity measurements .....	87

<b>Results and Discussion.....</b>	<b>89</b>
<b>Development of plasmonic based-assay for trastuzumab Quantification .....</b>	<b>89</b>
4.1 Motivation .....	89
4.2 Introduction .....	90
4.3 Results and discussion.....	92
4.3.1 Characterization of Synthesized AuNPs.....	92
4.3.2 Passivation of AuNPs with NTA/TOEG3 SAM.....	93
4.3.3 Incorporation of Co <sup>2+</sup> and Immobilization of the His-Tagged HER2 .....	95
4.3.4 Detection of trastuzumab by LSPR in Buffer .....	95
4.3.5 Evaluating the Specificity of the Platform.....	101
4.3.6 Elucidating the Impact of Free His-Tagged HER2 on LSPR Response.....	101
4.3.7 LSPR Response upon Tuning the Density of the Surface Grafted SAM .....	102
4.3.8 Evaluating Trastuzumab detection by LSPR in Human serum .....	104
4.4 Conclusions .....	107
<b>Results and Discussion.....</b>	<b>108</b>
<b>DNA-coated gold nanoparticle: a versatile platform for biosensing applications ..</b>	<b>108</b>
<b>5.1 Motivation.....</b>	<b>108</b>
5.2 Introduction .....	109
5.3 Results and discussion.....	111
5.3.1 Characterization of synthesized AuNPs.....	111
5.3.2 Detection of AuNPs functionalized with different DNA density .....	111
5.3.5 ssDNA/TOEG6 customized SAM formation on AuNP surface.....	116
5.3.6 Conformational and electrophoretic analysis of the mixed-SAM .....	117
5.3.7 The stability of ssDNA/TOEG6@AuNPs in a physiological environment.....	119
5.3.8 The interaction between mixed-SAM coated AuNPs and the liposomes .....	120
5.3.9 Elucidating the functionality of the mixed-SAM coated AuNPs.....	121

5.3.10	Evaluating the binding capability of C8-terminated AuNPs .....	124
5.4	Conclusions .....	126
<b>Results and Discussion.....</b>		<b>129</b>
<b>Application of click chemistry in nanoparticle surface modification .....</b>		<b>129</b>
6.1	Motivation .....	129
6.2	Introduction .....	130
6.3	Results and discussion.....	132
6.3.1	Characterization of optimization of mixed-SAM AuNPs.....	132
6.3.2	Conjugating the NPs with red-fluorescent azide-activated probe.....	133
6.3.3	Confirmation of the conjugation through fluorescence amplified thermal lens spectroscopy. ....	135
6.3.4	Attempting the formation of click chemistry mediated assembly of AuNPs .....	136
6.4	Conclusions .....	138
<b>Summary and outlooks for future research .....</b>		<b>141</b>
7.1	Summary .....	141
7.2	Future research .....	144
7.2.1	NTA-based strategy .....	144
7.2.2	DNA-based strategy.....	145
7.2.3	Click chemistry-based strategy .....	145
Appendix .....		147
References .....		151

## List of Tables

<b>Table 1.2:</b>	A Summary of commonly used nanoparticles	6
<b>Table 2.2:</b>	Summary of physical properties for some of Au and Ag nanostructures	31

## List of Figures

<b>Figure 1.1:</b>	A schematic diagram illustrating the outline of this thesis based on the chapter's contents.	3
<b>Figure 2.2:</b>	Schematics displaying different forms of nanoparticles. Their size scale is presented in the context of various biological components.	23
<b>Figure 3.2:</b>	<b>A</b> – the size-dependent emission wavelength of quantum dots. <b>B</b> – Change in the magnetic behavior of iron oxide nanoparticles with the decrease of the core size, from superparamagnetic (top) to paramagnetic (bottom). <b>C</b> – Carbon nanostructures come in all shapes and sizes, from the famous football-shaped C60 to monster fullerenes and nanotubes containing thousands of carbon atoms. <b>D</b> – Plasmonic nanoparticles get polarized when subjected to incident light. This causes very strong absorbance at size-dependent wavelength.	25
<b>Figure 4.2:</b>	( <b>A</b> ) Turkevich method for the synthesis of AuNPs. ( <b>B</b> ) Series of steps involved in the Burst-shifirin method for the synthesis of AuNPs.	28
<b>Figure 5.2:</b>	Stabilization of nanoparticle dispersions by force balancing of ( <b>A</b> ) attractive Van der Waals (VdW) interactions. ( <b>B</b> ) with repulsive electrostatic and, ( <b>C</b> ) repulsive steric interactions to achieve colloidal stability.	29
<b>Figure 6.2:</b>	Schematic illustrates the process for the preparation of a self-assembled monolayer on a flat substrate. First, a clean surface is incubated in a solution containing the ligands with Sulfur head group for a certain time. Second, the substrate is withdrawn and thoroughly rinsed to remove the physisorbed material (the molecules that are not specifically bound)	31
<b>Figure 7.2:</b>	Surface functionalities of SAM coated AuNPs for various biomedical applications. Such flexibility in surface chemistry enables tailoring optical and chemical properties of the metallic nanostructures.	34
<b>Figure 8.2:</b>	( <b>A</b> ) Schematic depiction of a surface plasmon propagating along the x-axis at the metal dielectric interface with electric field lines ( <b>B</b> ) Dispersion relation for a surface plasmon and for photons in vacuum.	36

<b>Figure 9.2:</b>	(A) A schematic illustration of localized surface plasmons, resulting from collective oscillations of relocated electrons as a response to an external electrical field. Notice how electronic clouds are oscillating opposite from the direction of electric field. (B) The theoretical map depicts the electric field distribution surrounding a gold nanoparticle, demonstrating the highly localized enhancement in the close vicinity of the particle surface.	38
<b>Figure 10.2:</b>	(A) monodispersed ( <b>green</b> ) and plasmonic-coupled ( <b>red</b> ) AuNPs absorbance spectra. (B) Bringing two metallic nanoparticles close together causes the surface plasmon resonances to pair and alter their resonance frequencies, resulting in a change in the field's properties.	39
<b>Figure 11.2:</b>	Schematic illustration of typical components in biosensors	41
<b>Figure 12.2:</b>	(A) The SPR working principle, (B) a typical SPR sensorgram depicting the steps of an analytical cycle.	43
<b>Figure 13.2:</b>	A schematic illustrates the basic principle of the nanoplasmonic detection based on RIS. (A) The typical surface plasmon band obtained for plasmonic AuNPs. (B) A spectral shift of the plasmon band is observed when an analyte interacts directly or indirectly with the surface of a metal nanoparticle (e.g., AuNPs).	44
<b>Figure 14.2:</b>	Schematics illustrate the thermal lens configurations in single beam and dual beam systems in <b>A</b> , and <b>B</b> , respectively.	47
<b>Figure 15.2:</b>	Schematics illustrate the thermal lens configurations in single beam and dual beam systems	50
<b>Figure 16.2:</b>	Breast cancer is classified into three subtypes based on the histological expression of four markers (ER, PR, HER2, and Ki-67): hormone receptor (HR)-positive, HER2-positive, and triple-negative.	55
<b>Figure 17.2:</b>	HER receptors consist of four members: HER1, HER2, HER3, and HER4. HER1, HER3, and HER4 interact with a variety of growth factor ligands. Both homodimerization and heterodimerization of the tyrosine kinase domain enhance cell growth and survival signaling. Phosphorylated tyrosine residues on the intracellular domain of HER2 activate PI3-K/Akt, resulting in cell survival. Furthermore, HER2 activation leads to activation of the RAS/RAF/mitogen-activated protein kinase (MAPK) pathway.	57

<b>Figure 18.2:</b>	(A) Trastuzumab is composed of the antigen-binding fragment (Fab) of the murine monoclonal antibody 4D5, directed against the ECD of HER2. (B) Trastuzumab inhibits the release of HER2-ECD, hence inhibiting the development of P95, a membrane-bound fragment with constitutive tyrosine kinase activity. (C) Trastuzumab suppresses HER2 signaling; via recruits Fc-competent immune effector cells, which promotes tumor cell killing. (D) Trastuzumab promotes receptor downregulation by stimulating HER2 endocytosis.	59
<b>Figure 19.3:</b>	Experimental set-up used in the synthesis of citrate capped of AuNPs.	63
<b>Figure 20.3:</b>	Representation illustrates the attachment strategy of the His-tagged protein onto the surface of the Co(II)NTA/TOEG3 AuNPs.	65
<b>Figure 21.3:</b>	Indirect ELISA performed for trastuzumab antibody and His-HER2 antigen	66
<b>Figure 22.3:</b>	Reaction of an SH-modified VHH with a maleimide-modified oligo leads to the formation of a stable nanobody-oligonucleotide conjugate.	68
<b>Figure 23.3:</b>	A cartoon illustrates of the ssDNA@AuNPs sample preparation steps using low pH assisted method.	69
<b>Figure 24.3:</b>	A schematic briefly illustrates the dot blot immunological assay used to qualitatively confirm the binding between C8 nanobodies and HER2-ECD antigen.	71
<b>Figure 25.3:</b>	(A) digital Photograph of the MGEC, (B) scheme of handling procedure for loading the sample	72
<b>Figure26 .3:</b>	Schematic of AuNPs–Liposome preparation using reverse phase evaporation method.	73
<b>Figure 27.3:</b>	Coating of AuNPs with Alkyne/TOEG6 mixed-SAM, and linking of dye-modified azide to these nanoparticles using click chemistry.	74
<b>Figure 28.3:</b>	Zetasizer Nano ZS used for DLS readouts	76
<b>Figure 29.3:</b>	The schematic outline of a TEM	77
<b>Figure 30.3:</b>	SEM electron-sample interactions	78
<b>Figure 31.3:</b>	(A) and schematic diagram of an AFM, (B) Sample preparation used for Nanoparticle-AFM imaging	80

<b>Figure 32.3:</b>	(A) A schematic illustration of the mechanism of TL effect, (B) Typical TL signal thermal lens signal generation.	82
<b>Figure 33.3:</b>	Schematic illustration of the pump–probe photothermal lens setup.	82
<b>Figure 34.3:</b>	Diagram of an agarose gel electrophoresis apparatus	84
<b>Figure 35.3:</b>	A schematic depicts the fluorescence phenomena in a simplified Jablonski diagram. (B) The Infinite F200 PRO multimode microplate reader	85
<b>Figure 36.4:</b>	UV/Vis spectrum of AuNPs synthesized using citrate reduction method and the corresponding TEM micrograph. Red color of the solution confirmed the production of AuNPs.	90
<b>Figure 37.4:</b>	UV/Vis absorption UV/Vis absorption spectra of AuNPs coupled with different concentrations of TOEG3. The blue color indicated that the TOEG3 was insufficient to cover the surface of particles. Once a sufficient amount is used, the colloidal solution does not form agglomerates and the red color is maintained.	92
<b>Figure 38.4:</b>	UV/Vis spectra of citrate- and protected AuNPs to monitor surface modification. Inset: Gel electrophoresis bands for (1) citrate capped AuNPs, (2) NTA@AuNPs, (3) NTA/TOEG3@AuNPs	92
<b>Figure 39.4:</b>	Volume-weighted distributions of hydrodynamic diameters of nanoparticles as determined by dynamic light scattering after different functionalization steps. The measurements were triplicated, and the error bars in the plot represent the measurement standard deviation	94
<b>Figure 40.4:</b>	Indirect ELISA analysis performed for Trastuzumab antibody with various concentrations of His-HER2 antigen. Each measurement was conducted in duplicate.	96
<b>Figure 41.4:</b>	UV/Vis absorption spectra for His-HER2 decorated AuNPs before and after the incubation with trastuzumab. LSPR peaks redshifted upon varying the concentration of the antibody	96
<b>Figure 42.4:</b>	Quantification of the LSPR shift ( <b>blue dots</b> ) and normalized aggregation ratio ( <b>red dots</b> ) of immunoconjugates with various concentrations of trastuzumab. Dose-response presented in each plot was fitted with the four-parameter logistic sigmoidal curve. The coefficient values $\pm$ one standard deviation used in the fitting equation as follows: Base = $-0.42318 \pm 0.987$ , Max = $2.4566 \pm 1.01$ , Xhalf = $-3.9633 \pm 7.3$ , and Rate = $10.289 \pm 1.96$ . The analysis was performed with Igor Pro 6.02A software.	97



<b>Figure 43.4:</b>	SEM micrographs of (a) NTA/TOEG3 coated AuNPs, (b) HER2-decorated AuNPs treated with 10 $\mu\text{g/mL}$ of trastuzumab. Note the crosslinking of the nanoparticles caused by the presence of the target antibody.	97
<b>Figure 44.4:</b>	(a–d) Representative TEM images of (a) HER2-decorated AuNPs (b–d) incubated with 2, 10, and 20 $\mu\text{g/mL}$ of trastuzumab, respectively. The formation of a 3D network indicates the successful coupling of AuNPs through trastuzumab linking. (e) DLS readouts for AuNPs probes treated with various concentrations of trastuzumab (up to 10 $\mu\text{g/mL}$ ). Upon mixing the HER2-decorated AuNP probes with trastuzumab, the particles are clustered together, leading to an average particle size increase of the assay solution. The DLS measurements were conducted in triplicate.	98
<b>Figure 45.4:</b>	UV/Vis absorption spectra for His-HER2 incubated with various concentrations of non-HER2 recognizing antibody. The spectroscopic signal was similar to HER2 capped AuNPs.	100
<b>Figure 46.4:</b>	Spectrophotometric titration ranging from 6-32 nM free His-tagged HER2 concentrations.	100
<b>Figure 47.4:</b>	Comparison of the LSPR response for various concentrations of trastuzumab upon adjusting the SAM density on the surfaces of AuNPs. Note that, with a 20:80 ratio, no plasmonic response was observed across all doses of the antibody.	101
<b>Figure 48.4:</b>	DLS volume-weighted size distributions comparing AuNPs coated with NTA and TOEG3 SAM with molar ratios of 20:80, 50:50, and 80:20, respectively. The 50:50 molar ratio was chosen to reach to a compromise the number of His-HER2 proteins and the instability issue due to the electrostatic attractive forces which lead to nanoparticle plasmonic coupling prior the assay.	101
<b>Figure 49.4:</b>	Plasmonic response for His-tagged HER2-decorated particles incubated with various dilutions of human serum-containing trastuzumab. It is clearly seen the challenge in obtaining a plasmonic response when the assay was conducted in a diluted serum (> 5%).	103
<b>Figure 50.4:</b>	The presence of competing Histidine rich proteins that may have interfered and disrupted the bioconjugate leading to the less sensitive complex formation toward the target antibody.	103
<b>Figure 51.4:</b>	SDS-PAGE image of (1) empty lane, (2) 5% diluted serum, (3) flow through of the serum after incubation with the matrix, (4,5) first and second wash of the matrix, (6) after eluting the Ni-NTA	104

matrix with imidazole, (7) the Ni-NTA matrix. Note that proteins containing Histidine-repeats were released after the elution step.

- Figure 52.4:** LSPR shifts for the particles treated with various concentration of the target antibody dispersed in 1% and 5% filtered serum. Inset: the gel electrophoresis photograph revealed a slower mobility for the immunocomplex in the filtered diluted serum. 104
- Figure 53.5:** (A-B) TEM micrograph of synthesized AuNPs with a scale bar of 100 nm, and the statistical analysis indicating nanoparticles size distribution evaluated for over 250 nanoparticles. (C-D)  $2 \times 2 \mu\text{m}^2$  AFM non-contact mode AuNPs image deposited on poly-L-ornithine coated mica, and its corresponding statistical analysis. 111
- Figure 54.5:** UV/Vis spectra of ssDNA-AuNPs with different DNA: AuNPs density. The onset of aggregation reflected on the broadening in the spectrum of 100DNA indicates insufficient covering of the AuNPs surface. Notice the indiscernible differences in the surface plasmon resonance bands between all coated AuNPs. 112
- Figure 55.5:** TLS signal as a function DNA/AuNPs ratios. The calibration curve was obtained to determine the LOD of the system based on the equation:  $\text{LOD} = 3(\text{SD}/m)$ . Inset: Notice the significant difference in the sensitivity in comparison with the conventional UV/Vis spectroscopy for low DNA densities used in the study to coat the AuNPs. 114
- Figure 56.5:** The slab gel electrophoresis image of ssDNA-AuNPs with different loaded DNA densities. The image was converted to gray scale format. 114
- Figure 57.5:** (A) Electropherogram of ssDNA-AuNPs with different loaded DNA densities, the inset shows migration times (B) area under the peak versus various DNA densities coated AuNPs, (C) the inset shows a photograph of 300 DNA separation in the channel. (A) UV/Vis absorption spectra of functionalized AuNPs at each step of mixed SAM formation, (B) TEM image of ssDNA/TOEG6@AuNPs, (C) Gel electrophoresis digital photograph of AuNPs passivated with ssDNA and the mixed SAM. 115
- Figure 58.5:** (A) UV/Vis absorption spectra of functionalized AuNPs at each step of mixed SAM formation, (B) TEM image of ssDNA/TOEG6@AuNPs, (C) Gel electrophoresis digital photograph of AuNPs passivated with ssDNA and the mixed SAM. 116
- Figure 59.5:** (A) Electropherogram of loaded samples; citrate capped AuNPs (red) and the conjugates with DNA only (blue) or with DNA and TOEG6 (green). (B) Summary of volume weighted DLS measurements After each step of functionalization and the cartoon 121

illustrates possible configurations of adsorbed oligos on AuNP surface

- Figure 60.5:** Normalized optical spectra for AuNPs incubated with 1:1 diluted human serum at various incubation time. The aggregation seen in the optical profile (**green**) displays the aggregation behavior of the bare particles in the serum. Once coated with the mixed-SAM, a remarkable stability in the other optical spectra up to 24 hours was observed. 118
- Figure 61.5:** TEM micrographs of mixed-SAM coated AuNPs interacting with lipid model membranes. Scale bars: 150 nm (**white**), and 200 nm (**red**). Note the difference in the decoration density of the particles on the surface of the liposomes. 120
- Figure 62.5:** (**A and B**) TEM micrographs for the AuNPs-Liposomes mixture prepared in PBS. The presence of salt in PBS modulated the electrostatic interactions between the hybrid components rendering perturbation in the whole nano-Liposomes. Scale bar: 100 nm. 121
- Figure 63.5:** (**A**) Cartoon depicts the plasmonic coupling induced by the presence of the avidin in the assay solution. (**B**) DLS readouts on the functionalization steps. (**C**) UV/Vis spectra for Biotinylated AuNPs incubated with various concentrations of Avidin. The redshift in the LSPR indicates the interparticle crosslinking. (**D**) TEM micrograph displayed the NPs Avidin-induced aggregation ( $C_{\text{avidin}} = 35 \mu\text{g/mL}$ ). Scale bar: 200 nm. 122
- Figure 64.5:** (**A**) UV/Vis absorption spectra of Nanobody-terminated DNA/TOEG6@AuNPs. (**B**) Gel electrophoresis of AuNPs functionalized with: (1) ssDNA, (2) dsDNA (3) (dsDNA + C8 Nbs), (4) ssDNA/TOEG6, (5) dsDNA/TOEG6, (6) (dsDNA/TOEG6 + C8 Nbs). The arrow indicates the direction of the applied electric field, and the direction of migration. 123
- Figure 65.5:** (**A**) Volume-weighted DLS analysis showed that the resultant HER2 bioconjugation was achieved by the increment of  $D_H$  size from 38 to 41 nm for C8-terminated AuNPs and HER2@AuNPs respectively can be attributed to the antigen recognition, (**B**) dot blot immunological assay optical readouts. 124
- Figure 66.5:** (**A**) A schematic illustrates of the MGEC-TLS design employed for investigating HER2-ECD binding to C8 decorated AuNPs. The resulted immunoconjugates migrate toward the positive anode crossing the measurement point. Note that the design does not need to use bulky cost devices and long running time as well as scanning of the gel post electrophoresis. (**B**) MGEC-TLS signal acquisition time as a function of different steps of surface coating of AuNPs. The concentration of the 125

antigen was varied from 5-50 nM. (C) Calibration curve of HER2-ECD measured with MGEC-TLS. The signal acquisition time is plotted versus HER2-ECD concentration; experimental data was fitted with polynomial of third degree. (D) An example of a typical signal acquired during the measurements.

- Figure 67.6:** (A) digital photograph of AuNPs mixed with various concentrations of TOEG6. (B) optical profile of AuNPs capped with TOEG6 in a CuSO<sub>4</sub> containing solutions with their corresponding references. (C) UV/Vis spectra of AuNPs functionalized with different ratios of TOEG6 and alkyne-terminated ligands. (D) Gel electrophoresis bands for the alkyne/TOEG6 ( $\mu\text{M}$ ) ratios of: (1) 1:1, (2) 5:1, (3) 5: 1.5, (4) 5: 2, and (5) 5: 2.5 132
- Figure 68.6:** (A) Structural formula of AF594-Azide. (B) UV/Vis spectroscopy analysis and agarose gel electrophoresis (1%). The loaded samples in the gel analysis represented particles treated to varied conditions in which one of the reaction components was removed: without AF594 (**lane 1**), or without CuSO<sub>4</sub> (**lane 2**). (C) Fluorescence intensity measurements of free AF594 and clicked to NPs. (D) the absence of the Cu(I) indicated in the reaction solution confirms that AF594 was not clicked to the gold surface and remained “freer” in the assay solution, therefore, more fluorescence signals were recorded. 133
- Figure 69.6:** Schematic illustrates the amplified thermal lens effect induced by fluorescence energy transfer. 135
- Figure 70.6:** TL signals obtained: (A) for AuNPs and AF594 at various experimental conditions. (B) as a function of the dye concentration. 136
- Figure 71.6:** (A) Intended click-chemistry-mediated colorimetric assay design with two types of AuNPs, each modified with thiols terminated with an azide or alkyne functional group, (B) Digital photographs of AuNPs treated with various concentrations of azide-tagged ligand, (C) DLS measurements showed the slight change in the hydrodynamic size of AuNPs upon functionalization with Azide/TOEG6 ligands, (D) Optical profile of Azide/TOEG6 functionalized AuNPs 137
- Figure 72.7:** Schematic diagram of histidine-rich separation using MPNPs 144
- Figure 73.7:** An illustration of a colorimetric sandwich assay based on DNA-mediated AuNPs assembly 145

**Figure 74.7:** Cartoon illustrates the induced aggregation on a click-chemistry mediated mixed-SAM functionalized AuNPs. 145

## List of Appendices

Appendix 1	: The ligand-chain length presents a crucial parameter in forming stable yet functional nanoparticles. Although TOEG6 as a spacing ligand offers highly stable conjugates, the desired plasmonic effect upon the introduction of trastuzumab was challenging to be observed. The plausible explanation could be attributed to the steric hindrance induced by the slightly longer OEG chain.	146
Appendix 2	: UV/Vis spectrum and intensity-weighted size distribution (inset) of synthesized AuNPs	146
Appendix 3	: Calibration curve for the quantification of ssDNA attached per NP.	147
Appendix 4	: DLS readout of as prepared AuNPs with the corresponding TEM micrograph	148
Appendix 5	: Calibration curve for the azide-bearing dye (AF594)	148
Appendix 6	: Intended click-chemistry-mediated colorimetric assay design with two types of AuNPs, each modified with thiols terminated with an azide or alkyne functional group	149
Appendix 7	: digital photographs of the TOEG3 treated AuNPs, and Azide/OEG3 modified AuNPs prepared at different ligand ratios	149

## Acknowledgements

I would like to express my gratitude to several people who have made significant contributions to the completion of this work, whether academically or socially. Firstly, I would like to thank my supervisors, Dr. Loredana Casalis and Dr. Pietro Parisse, for providing me the opportunity to work in such a well-respected research group. Your thoughts, suggestions, guidance, and support have been instrumental in developing this work and my personal growth as a research scientist and will continue to be invaluable in the future. Your enthusiasm, knowledge, and time spent discussing findings, reading my reports, and listening to my presentations have all been extremely beneficial to me. I would also like to express my gratitude to Dr. Paola Posocco, Dr. Paolo Pengo, and Dr. Humberto Cabrera for their support, fruitful collaboration, guidance over the years, as well as the stimulating discussions. Finally, I want to deeply thank Università degli Studi di Trieste and Elettra Sincrotrone Trieste for providing me with a generous stipend over the last four years.

I sincerely would like to express my heartfelt gratitude to current and past fellow lab mates in the NanoInnovation lab (Carolina Paba, Hendrik Vondracek, Beatrice Senigagliesi, Behnaz Asbaghi, Luciana Gneo, Gesmi Milcovich, Fabio Perissinotto, Caterina Medeot, Elena Ferraguzzi, Alessandro Stumpo, and Alessia Norbedo, Martina Lotteri, Luca Davanzo, and Nicolò Tormena) for the stimulating discussions, countless coffees, and a pleasant group environment. Special thanks go to group members of Structural Biology Laboratory; especially Dr. Silvia Onesti's group (Luisa Napolitano, Giuseppe Cortone, Antonio Longo, Gianluca Centrone, Elisa De Piante, and Manil Kanade) for making the nanoparticle analysis in their lab so entertaining, and sharing the highs and lows of gel electrophoresis and western blotting outcomes.

My deepest gratitude and love go to my family. I want to thank my parents and my siblings, whose unconditional love and guidance are always there with me wherever I go and whatever I do. I must also thank Prof. Khalid Ibnaouf and Dr. Osamah Aldaghri, Adams Zambrotta, and Mohammed Sharif Hashim for providing constant motivation. Your unwavering support, encouragement, and patience have been influential, especially in the last two years.

Finally, my special thanks to all the people I enjoyed playing football with, for the beautiful memories, and for making my time in Trieste a fantastic experience.

## Abstract

### **Harnessing the plasmonic properties of gold nanoparticles: functionalization strategies coupled with novel spectroscopic tools**

Metallic plasmonic substrates such as gold nanoparticles (AuNPs) have fascinated researchers due to their usefulness in various interdisciplinary studies at the interface between applied physics, biochemistry, engineering, and medicine. A good understanding of the physics of these noble nanostructures, particularly the plasmonic and optical properties, can be employed to improve a wide range of sensors and electronic devices. The relevance of molecular recognition and the binding of biological and chemical entities to diagnostics, biosensors, and drug delivery has attracted significant research interest. By addressing material functionalization design and advanced characterization methods, this doctoral work aims to highlight efforts to exploit the surface modification strategies to enhance the responsiveness of nanoparticle substrates for improved detection of health-relevant biomolecules. The self-assembly of small ligands, such as alkanethiols, and oligonucleotides on the surface of AuNPs provided a possible starting route for the preparation of bio-nanomaterials with precise physicochemical properties. The versatile AuNPs were optimized and thoroughly characterized by employing electron microscopy techniques such as transmission electron microscope (TEM), atomic force microscopy (AFM), and scanning electron microscopy (SEM), spectroscopic techniques, including ultraviolet/visible (UV/Vis), dynamic light scattering (DLS), and thermal lens spectrometry (TLS), and biochemical assays (gel electrophoresis, Dot plot, Western plot, and the Enzyme Linked Immunosorbent Assay (ELISA)). Subsequently, the molecular recognition capabilities of functionalized AuNPs were investigated using multiple techniques, including novel detection routes such as the electrophoresis approach coupled with online TLS. This work establishes a versatile platform for AuNP engineering with controlled size and surface functionality. The strategies presented in this thesis aim to improve medical diagnostics to make them affordable for point-of-care scenarios to enhance the quality of human health.

**Keywords:** gold nanoparticle, self-assembled monolayer, localized surface plasmon resonance, biosensors, thermal lens spectrometry, DNA-directed immobilization, click chemistr



## Thesis overview and objectives

### 1.1 Overview

The 21<sup>st</sup> century has witnessed a boom in nanoscience and nanotechnology thanks to the groundbreaking advancements in nanoscale engineering and characterization techniques. Increased understanding of the interplays between the structure, properties, and functions of nanomaterials has fostered their relevance, particularly in life sciences. In contrast to top-down synthetic routes often used in inorganic nanomaterials, the self-assembly of synthetic ligands enables the preparation of novel class of nanosystems with well-defined structural and bio-physicochemical properties. This may be harvested for nanostructures that interact selectively with chemical and biological entities, the intriguing potentials of which have been remarkably shown especially for biomedical research.

To that goal, plasmonic materials such as gold nanoparticles are, an interesting model substrate, as they offer, via the rational assembly of their organic ligand shell, pathways to achieve the structural and functional fidelity required for specific bio-applications. By addressing the material functionalization design as well as advanced characterization methods, this doctoral work aims to shed light on fundamental aspects of these plasmonic nanostructures, i.e., the synthesis, functionalization and implications for relevant applications.

Versatile coating strategies that exploit self-assembled monolayers (SAM) of alkanethiols, all being based on the same responsive hybrid nanomaterial, are established in this thesis aiming at sensitive detection of drugs or biomarkers outside of specialized laboratories, by the use of localized surface plasmons. Due to the activation of localized surface plasmons, the optical characteristics of metal nanoparticles are particularly sensitive to changes in their surrounding environment, such as the binding of a biomolecule to their surface. This optical phenomenon is the basic principle behind nano-plasmonic sensing based on refractive index detection, a sensing scheme that offers real-time and label-free detection of molecular interactions. An increased

knowledge about how the surface modification affects the sensitivity is essential when developing plasmonic sensing nanotools with high throughput based on metal nanoparticles.

## **1.2 Research motivation, objective, and outlines**

Early detection of biomolecules for disease diagnosis is not a trivial task. The major challenge lies in the ability of identifying and quantifying molecules of interest, often at low concentrations, using rapid, non-invasive, cost-effective, and simpler to use than current available methods, while still preserving the high standard of selectivity and sensitivity required for accurate testing. Low volumes and low quantities of biological materials call for miniaturization of the developed assays. Nanodiagnosics is therefore centered on the development of innovative tools for early detection of disease-related entities, which requires the recognition and quantification of low amounts of disease biomarkers.

In this context, the aim of this doctoral study lies in the exploration of the spectroscopic properties of gold-based nanostructures (AuNPs) with defined size, shape, and surface coatings through tunable self-assembled mixed monolayers (mixed-SAMs) made of molecular binders specific for the biomarker of interest and short-chain bio-repellent molecules. By controlling the surface chemistry of the assembled structure, the key target of this research is to optimize design approaches that can be tailored to develop a non-invasive nanodiagnostic platform for breast cancer related biomarkers, focusing in particular on the extracellular domain (ECD) of Human Epidermal Growth Factor Receptor (HER2), and its targeting agent, trastuzumab, the monoclonal antibody used for therapy. Coupled with this, further consideration has been undertaken to investigate the potentiality of a novel approach based on a miniaturized gel electrophoresis chip (MGEC) integrated with online thermal lens (TL) detection for monitoring the surface functionalization of the nanoparticles with an attempt to combine the robustness of the plasmonic agent and the ultra-sensitivity of TL spectroscopy.

The following chapters are intended to put the work into a broader context and to provide an introduction to the various strategies and tools implemented in this study. **Figure 1.1** depicts a schematic description of the work given in this thesis. Briefly: *Chapter 2* introduces some theoretical background related to the work in the thesis. *Chapter 3* outlines the methodology of the material synthesis and characterization techniques used in this research. Discussion of the experimental outcomes are presented in *chapters 4-6*. A simple, label-free, and rapid approach to

quantify clinically relevant concentrations of trastuzumab using AuNPs as plasmonic scaffolds, decorated with HER2 binders mixed with oligoethylene glycol (OEG) molecules is described in *chapter 4*. The possibility to exploit DNA immobilization and subsequent recognition of DNA-attached binders through DNA-directed immobilization technique is demonstrated in *chapter 5*. By employing robust, easily engineered camelid nanobodies as binders, the possibility to quantify HER2-ECD biomarker is also presented. In *chapter 6*, the Cu(I)-catalyzed click reaction as a rapid and efficient attachment strategy for molecules that carry an azide/alkyne group is described. In the *Summary & outlooks for future research*, the summary of the important findings is reported along with the prospective works.

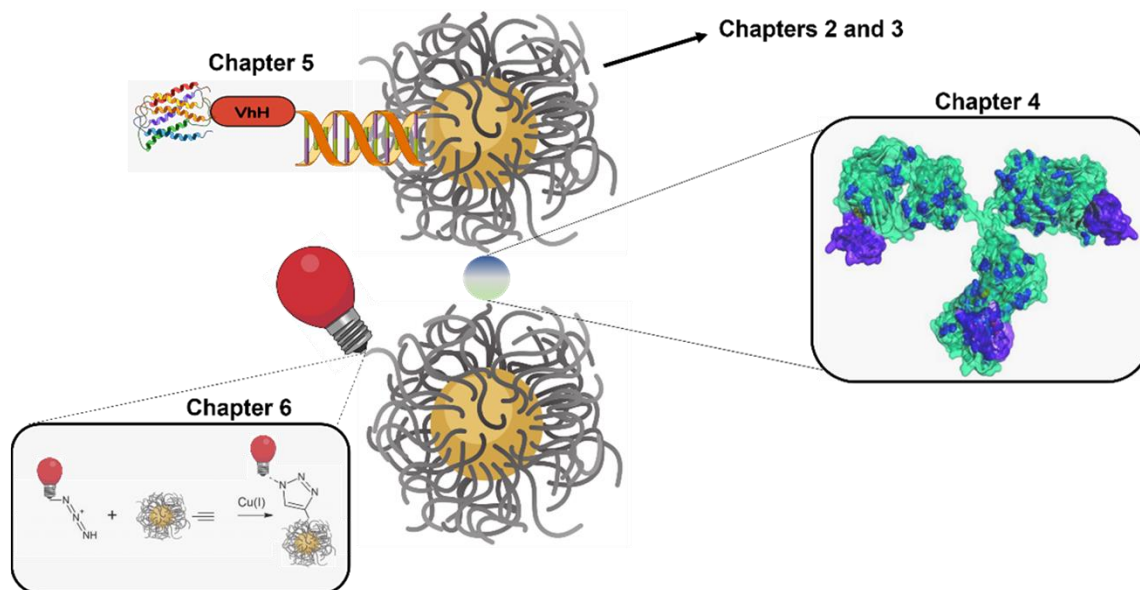


**Figure 1.1.** A schematic diagram illustrating the outline of this thesis based on the chapter's contents.

## Background

### 2.1 Nanotechnology

Nanotechnology operates at the first level of organization of atoms and molecules for both living and anthropogenic systems. This is where all systems' characteristics and functions are defined. Nanotechnology promises the ability to construct accurate machine and components of molecular size. In its original sense, 'nanotechnology' refers to the projected ability to construct items from the bottom up, employing processes and tools which are being developed to make high performance products. This theoretical capability was envisioned as early as 1959 by physicist Richard Feynman. According to national science foundation (NSF) and National Nanotechnology Initiative (NNI), Nanotechnology is the ability to understand, control and manipulate matter at the level of individual atoms and molecules. Nanotechnology is sometimes referred to as a general-purpose technology because in its advanced version it will have significant impact on almost all industries and all areas of society. While the term "nanotechnology" was only coined in 1974 by Norio Taniguchi (Taniguchi, 1974), humans have been using the benefits of nanoscale structures for thousands of years. It is unclear when exactly humans started making use of nanomaterials. Early examples include the use of colloidal gold and silver nanoparticles for glass staining by Romans in the 4th century BC, coloration in mosaic glass windows in the Middle Ages in Europe, pottery ornamentation, and carbon nanotubes and cementite nanowires to improve the edge sharpness of Damascus steel swords (Schaming & Remita, 2015). However, it was not until the 20th century that the ability to properly define and modify structures at the nanoscale scale became possible (Reineke, 2012). In 1909, Richard Zsigmondy used the term "nanometer" to describe particles with a diameter of  $10^{-9}$  m and to study colloids with a microscope (Zsigmondy, 1909). By 1959 a significant number of examples of such nanomaterials has been accumulated to prompt the leading physicist of the time Richard Feynman to give a seminal lecture entitled "There's plenty of room at the bottom" (Feynman, 2013). In this talk, Feynman laid out a challenge to chemists and physicists to figure out how to control matter at an atomic scale for controlled

functionality. He presented a vision of a large unexplored space at small size scale that could be used for information storage and in which billions of tiny machines that could be constructed to launch a cascade of building smaller and smaller machines until atoms and molecules themselves could be manipulated. He identified the need for further advancements in microscopy and manufacturing that would be required to make this concept a reality. However, true progress did not commence until Eric Drexler in 1980s popularized the field and formed Foresight Institute aimed towards advancement of nanotechnology (Drexler, 1986). The field was also tremendously benefited by developments in microscopy technologies, with the scanning tunnelling microscope and atomic force microscope being developed in 1981, and 1986, respectively (Binnig et al., 1986; Binnig & Rohrer, 1983). These and other technological breakthroughs led to discovery of fullerenes by Richard Smalley in 1985, and parallel discovery of semiconducting quantum dots by Alexey Ekimov in 1981, and Louis Brus in 1983 as the first identified and created nanoparticles (Kroto et al., 1985; Rossetti et al., 1983; ЕКИМОВ & ОНУЩЕНКО, 1981). In the last 30 years, the field has evolved at an exponential rate, resulting in a wide variety of nanoparticles with various physicochemical features. Nanotechnology has benefited several fields, including electronics, energy generation, medicine, biotechnology, optics, textiles, agriculture and construction (Sanchez & Sobolev, 2010; Schaming & Remita, 2015). In particular, the advancements in nanotechnology are increasingly driving biomedical innovations. Nanoparticles offer novel solutions that help improve diagnostics and therapeutic agents and their delivery, tissue repair, immune system modulation, and detection of infectious pathogens.

## **2.2 Nanoparticles and their properties**

Nanoparticles are constructs that possess unique physical and chemical characteristics associated with their being of 1–100 nm in size (Lidén, 2011). Biological molecules including antibodies, receptors on membranes, nucleic acids, and proteins are all in the same size range as nanometer-sized particles (**Figure 2**). Nanoparticles have distinct size-dependent physical and chemical properties, such as optical, catalytic, magnetic, thermodynamic, and electrochemical. A nanoparticle's chemical composition and shape also have an impact on its specific properties. The accurate targeting and quantification of molecules indicative of cellular disorders at the single-molecule level presents a demanding task for current high-throughput analysis systems. The use of nanoparticles in combination with other nanotechnology-based materials has the potential to

address this emerging challenge and offer technologies that enable diagnoses at the level of single cells and single molecule (B. Kim et al., 2010). To date, there have been numerous types of nanoparticles described in the literature. In contrast to bulk materials, nanoparticles have the majority of their atoms located on their surface. For example, for a  $1 \text{ cm}^3$  of iron, only 0.00001% of the atoms are located on the surface. In contrast, for  $10 \text{ nm}^3$  and  $1 \text{ nm}^3$ , these values become 10% and 100%, respectively (Link & El-Sayed, 2000). This atomic arrangement leads to a number of nanoparticle-specific properties (**Figure 2**). For example, quantum effects introduced by such atomic confinement, features such as narrow-wavelength fluorescence, ultra-high absorbance, or superparamagnetism are not observable in bigger particles or bulk materials. Furthermore, it yields a high surface-to-volume ratio, which maximizes the surface area available for chemical functionalization and bio-interactions for a given amount of material. It is worth mentioning that the surface-to-volume ratio changes rapidly as the nanoparticle's size increases, leading to very pronounced size-dependent effects, such as shifting the emission wavelength of quantum dots (QDs) (Chan & Nie, 1998). In addition, Surface area causes changes in the reaction time of a substance. The greater the surface-to-volume ration is as it relates to a reacting substance the faster the reaction time. The most commonly used nanoparticles are listed in **Table 1.2**.

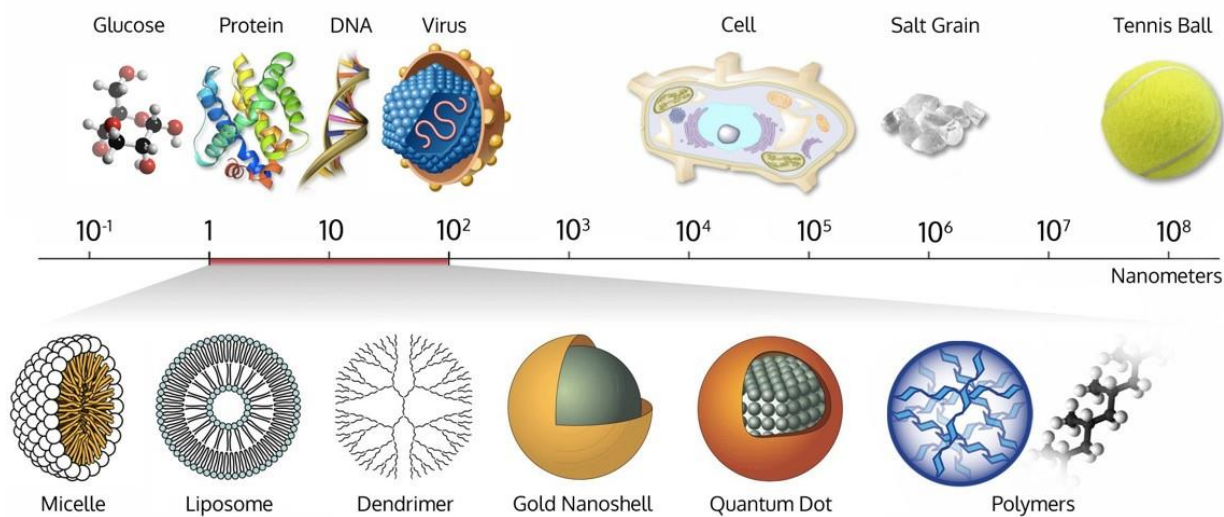


**Figure 2.2.** Schematics displaying different forms of nanoparticles. Their size scale is presented in the context of various biological components (Wich, 2015).

**Table 1.2.** A Summary of commonly used nanoparticles.

Nanoparticle	Size (nm)	Composition and Properties	Applications
Liposome	90-10 <sup>4</sup>	<ul style="list-style-type: none"> <li>Spherical vesicles, one or more layers of self-assembled lipid bilayer, hydrophilic core</li> <li>Encapsulate hydrophobic and hydrophilic drugs</li> </ul>	Transfection, drug and nucleic acid delivery (FDA approved)
Micelles	5-100	<ul style="list-style-type: none"> <li>Self-assembled spheroids of amphiphilic block co-polymer with hydrophobic core.</li> <li>Can encapsulate hydrophobic drug.</li> </ul>	Drug delivery (FDA approved)
Nanoparticle albumin-bound (NAB)	100-200	<ul style="list-style-type: none"> <li>Complexes of albumin proteins.</li> <li>Utilize native ability of albumin to deliver hydrophobic molecules, targets tumors.</li> </ul>	Drug delivery (FDA approved), fluorescence imaging
Polymeric nanoparticles	50-300	<ul style="list-style-type: none"> <li>Block co-polymers assembled into core-shell architecture, hydrophobic or hydrophilic core</li> <li>Can encapsulate hydrophobic and hydrophilic drugs or contrast agents</li> </ul>	Drug and nucleic acid delivery (FDA approved), fluorescence imaging
Dendrimers	2-10	<ul style="list-style-type: none"> <li>Radially branched polymers with repeat units</li> <li>High ligand density and payload capacity</li> <li>Controlled biodegradation</li> </ul>	Drug and gene delivery, dye-conjugated imaging agents for biosensors
Graphene	20-10 <sup>4</sup>	<ul style="list-style-type: none"> <li>2D sheet of <math>\pi</math>-stacked sp<sup>2</sup> carbon atoms</li> <li>High electricity and heat conduction</li> </ul>	MRI and X-ray contrast agents, drug and gene delivery, FRET, biosensor, electronics
Fullerenes	0.5-3	<ul style="list-style-type: none"> <li>Hollow spheres of graphene-like material</li> </ul>	
Carbon nanotubes	D: 0.5-3 L: 10-10 <sup>5</sup>	<ul style="list-style-type: none"> <li>Cylinders of graphene-like sheets</li> <li>Can consist of a single or multiple nested carbon sheets with 0.34 nm interlayer spacing</li> </ul>	
Plasmonic Au, Ag, Cu	3-200	<ul style="list-style-type: none"> <li>Very high extinction cross section due to surface plasmon resonance (SPR) field</li> <li>Quench fluorescence, enhance Raman absorption</li> <li>Simple and high-density surface functionalization (particularly for Au)</li> </ul>	Colorimetric sensors, FRET, SERS, microscopy, drug and nucleic acid delivery (Phase I), wound healing (FDA approved)
Magnetic SPION, CLIO	5-200	<ul style="list-style-type: none"> <li>Iron oxide or iron core with iron oxide shell</li> <li>Superparamagnetic or ferromagnetic</li> <li>Can increase magnetism by doping with Mn, Co</li> <li>Crosslinked dextran coat for biocompatibility</li> </ul>	MRI diagnostic (FDA approved), magnetic separation, guided drug delivery
Quantum dots CdSe, CdTe, etc.	3-30	<ul style="list-style-type: none"> <li>Made out of semiconductor nanomaterials</li> <li>Strong fluorescence, narrow size dependent emission, wide absorption spectrum</li> <li>Can quench dyes</li> <li>Potentially toxic (core contains Cd, Pb)</li> </ul>	Fluorescence imaging and spectroscopy, FRET, single molecule studies, barcodes for biosensing
Silica	3-100	<ul style="list-style-type: none"> <li>Biodegradable</li> <li>Available also in micro- or mesoporous form</li> <li>Can encapsulate dyes and drugs</li> <li>Easy surface functionalization</li> </ul>	Drug, gene and contrast agent (FDA approved) delivery, biosensors

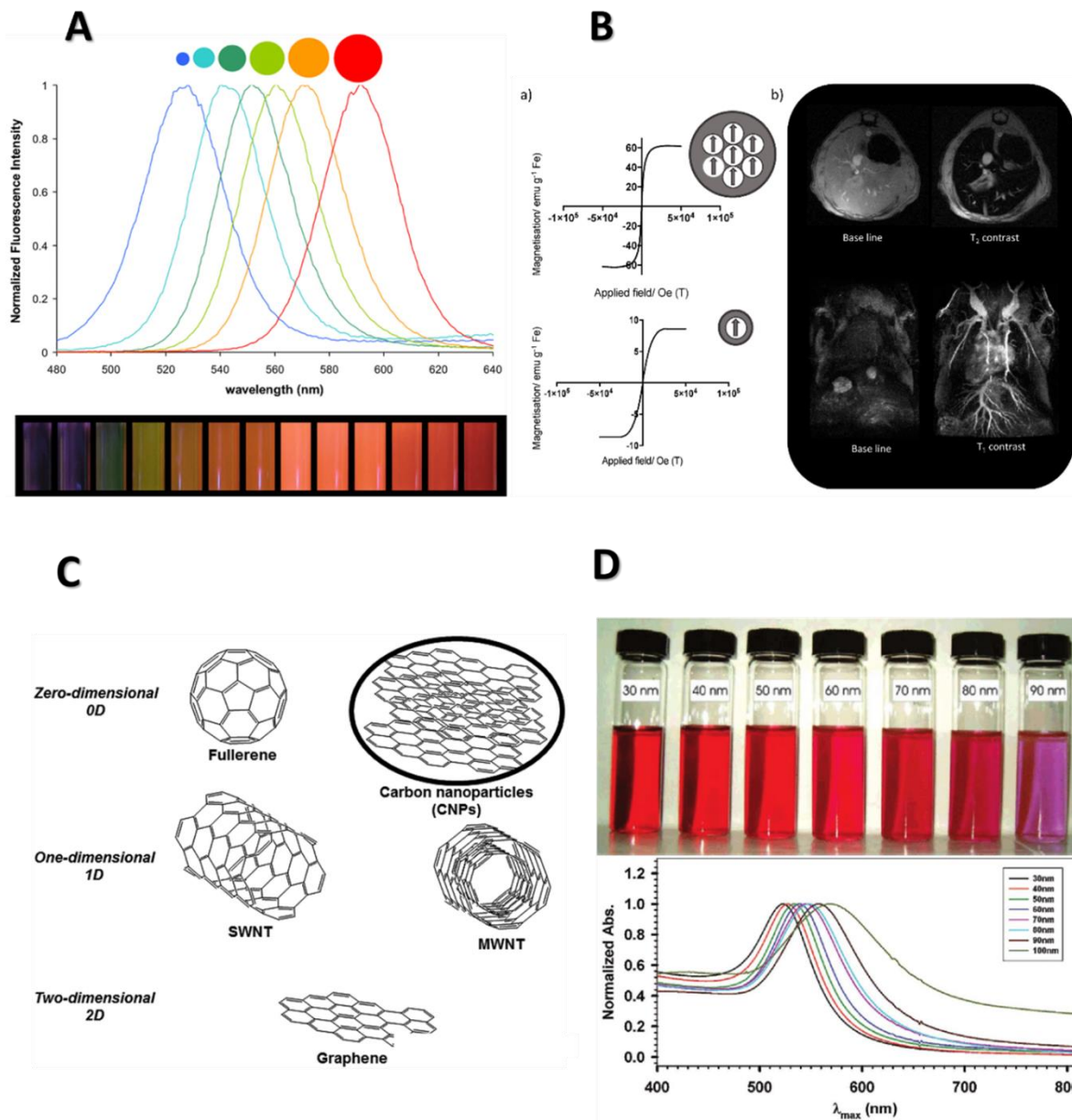


**Figure 3.2.** **A** – the size-dependent emission wavelength of quantum dots (Díaz-González et al., 2020). **B** – Change in the magnetic behavior of iron oxide nanoparticles with the decrease of the core size, from superparamagnetic (top) to paramagnetic (bottom), (Fernández-Barahona et al., 2020). **C** – Carbon nanostructures come in all shapes and sizes, from the famous football-shaped C60 to monster fullerenes and nanotubes containing thousands of carbon atoms (Testa et al., 2019). **D** – Plasmonic nanoparticles get polarized when subjected to incident light. This causes very strong absorbance at size-dependent wavelength (Subara & Jaswir, 2018).



### 2.3 Gold Nanoparticles (AuNPs)

Gold nanoparticles (AuNPs), used in this thesis, are members of the plasmonic nanoparticle family, which also includes silver and copper nano-colloids. However, due to their higher stability, ease of synthesis, and facile surface functionalization with a wide range of biomolecules, such as proteins, oligonucleotides allow for the development of smart platforms with enhanced capabilities that can be used in the wide range of bio-applications (Jain et al., 2007; Willets & Van Duyne, 2007). AuNPs with exact diameters ranging from 3 to 200 nm can be engineered. The structure of the AuNP can be viewed as an ionic lattice with confined conduction band electrons that are free to flow throughout the NP (García, 2011). An electromagnetic field of the particles exerts the force on these electrons bringing them to the surface on one side of the particle. A dipole is formed as a result of the charge difference created within the particle. The dipole can resonate with the incident photon oscillations, causing huge amplification of the electromagnetic field. This phenomenon is known as localized surface plasmon resonance (LSPR). LSPR occurs at a resonance wavelength determined by the distance between the positive and negative charges in the dipole and the area of the surface. Therefore, LSPR spectral maximum is a function of nanoparticle shape and size (as seen in **Figure 3.2D**). It can also be directly influenced by the surface chemistry. The main impact of LSPR is that it significantly enhances the effective extinction cross-section of the nanoparticles (effective area over which the nanoparticle absorbs or scatters light at the resonance maximum), up to tenfold that of their physical cross-section. This renders plasmonic nanoparticles optimal contrast agents for colorimetric assays. The interaction of nanoparticles with incident light is a result of both absorption and scattering mechanisms. The absorbed portion gets dissipated through vibrational processes thus generating heat, making plasmonic nanoparticles particularly suited for photothermal therapy (Li et al., 2022). Moreover, LSPR field not only increases the cross-section but also boosts or quenches the electromagnetic fields of other molecules near its surface. This includes an order of magnitude increase in molecule Raman scattering, or quenching of fluorescent dyes or QDs (Fabris, 2015; Ghosh & Chattopadhyay, 2015; Pons et al., 2007). Aside from their plasmonic capabilities, AuNPs are biocompatible and have a straightforward chemistry for surface coating with the appropriate ligands. This is accomplished by simply mixing AuNPs with a thiol-modified ligand of interest (such as DNA). When the sulfur atom interacts with the gold surface, a strong coordinate or covalent bond is formed (Hurst et al., 2006; Xue et al., 2014; Zhang et al., 2012). This process is remarkably rapid, resulting in the formation of a stable monolayer on a

nanoparticle surface at ambient temperature. Because of the small footprint of the bond, a high density of surface molecules can be accommodated. However, one drawback of the thiol bond is that biological systems often have multiple thiol-containing molecules (e.g., keratin, collagen, insulin) competing for the gold surface, leading in non-specific desorption. Thiol bonds can also impair interactions between gold atoms in the outer layer, causing the nanoparticle surface to break down (Xue et al., 2014). Generally speaking, the precise control over AuNP dimensions, size distribution, scalability of the synthesis, and the large accessible surface area that can be easily functionalized with a highly dense layer of thiolated ligands make AuNPs intriguing scaffolds for applications in the fields of drug delivery, and diagnostics (Giljohann et al., 2020).

### **2.3.1 Chemical Synthesis of AuNPs**

It was 1850 when Faraday pioneered the synthesis of colloidal gold solutions by reducing gold chloride with phosphorous. Since then, many efforts have been undertaken to synthesize AuNPs, controlling their shape, size, and surface chemistry, for their fascinating properties and promising applications. Among different methodologies, various chemical methods of syntheses of AuNPs were introduced. In general, there are two primary parts to the chemical reduction procedure of producing AuNPs: (i) reduction by agents, for instance formaldehyde, borohydrides, hydroxylamine, polyols, aminoboranes, citric and oxalic acids, hydrogen peroxide, sugars, sulfites, and ono electronic reducing agents including electron-rich transition-metal sandwich complexes; (ii) stabilization using agents, such as trisodium citrate dihydrate, phosphorus ligands, sulfur ligands (thiolates), oxygen and nitrogen-based ligands (including heterocyclic compounds), dendrimers, polymers and surfactants (particularly, cetyltrimethylammonium bromide (CTAB)). In 1951 *Turkevich and al.* proposed the reduction of tetrachloroauric acid ( $\text{HAuCl}_4$ ) with trisodium citrate ( $\text{Na}_3\text{C}_6\text{H}_5\text{O}_7$ ) in boiling water (100 °C) where the citrate serves as both a reducing and stabilizing agent (Turkevich et al., 1951). The "Turkevich approach" enables the stable preparation of colloidal nanoparticles with a diameter of 10-20 nm. This approach is still used and improved today due to its simplicity and reproducibility. *G. Frens*, in 1973, described in the same procedure the changing ratio between the gold precursor salt and the citrate, to obtain control of the size of AuNPs in the range of 16–147 nm (Frens, 1973). In 1994, *Brust* described a two-phase approach for synthesizing 1.5 nm - 5.2 nm AuNPs, using thiol ligands as a capping and reducing agent, as well as sodium borohydride ( $\text{NaBH}_4$ ) as a second reducing agent. In this approach, there are two

phases: a water phase and an oil phase, with a phase transfer agent like tetraoctylammonium bromide (TOAB) transferring the gold salt from the aqueous to the oil phase (toluene). The ratio of  $\text{HAuCl}_4$  to  $\text{NaBH}_4$  and the reaction temperature can be used to adjust particle size (Shah et al., 2014). *David J. Schiffrin* presented a simple purification technique for AuNPs from TOAB impurities in 2003, which can have a significant impact on their properties (Waters et al., 2003). The Turkevich and Brust-Schiffrin procedures allows the production of monodisperse spherical AuNPs (**Figure 4.2**), while seeded-growth method is the best way for producing other AuNP nanostructures. Herein, a strong reducing agent is utilized to make the seeds of nanoparticles, which are then used in a solution containing metal salt, a weak reducing agent, and a structure-directing agent. It is feasible to control the geometry of nanoparticles by adjusting the concentrations of the used agents (Ziegler & Eychmuller, 2011). Besides these methods, the scientific community has come up with new synthetic strategies that do not have toxic byproducts, called "green" methods. Several works demonstrate how it is possible to reduce and cap AuNPs using plants or plant extract with gold salt. Of course, size and shape are tunable by changing the pH, temperature, and concentrations of reagents. In the green methods, also several bacteria, yeasts, and biomolecules are used to synthesize AuNPs of various sizes (Castillo-Henrriquez et al., 2020; Lee et al., 2020).

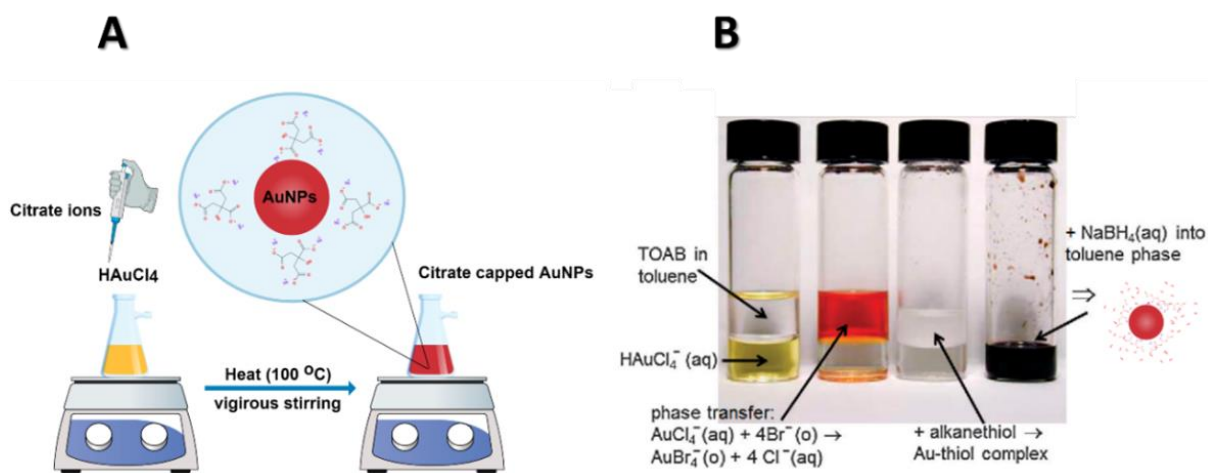


**Figure 4.2.** (A) Turkevich method for the synthesis of AuNPs. (B) Series of steps involved in the Brust-Schiffrin method for the synthesis of AuNPs (Liz-Marzán, 2013).

### 2.3.2 Colloidal Stability

Colloidal stability plays a critical role as it dictates the behavior and the fate of the NPs in various applications. The capping molecules utilized in the synthesis of the NPs are not only used to control the growth of the NPs during the synthesis but also to prevent aggregation by repulsion forces between the particles. These ligands are chosen based on the NPs core materials and dispersion medium. As their stability decreases (due to changes in the dispersion media, pH, ionic strength, etc.), they start to agglomerate and form large aggregates. Agglomeration occurs as a result of an attractive interaction between the surfaces of individual NPs and can be avoided by alter by surface modifications. These modifications can be implemented using different kinds of ligands that are capable of binding to the NPs surface preventing the aggregation by inducing repulsion forces among the individual NPs. These repulsion forces are either electrostatic repulsion which are originated due to the double layer of electric charges surrounding each NP (equally “charged” particles repel each other); or steric repulsion, which accounted between the molecules adsorbed on the surface of neighboring NPs (**Figure 5.2**). The size and the chemical nature of these molecules determine the stability degree. It is worth mentioning that the surfactants can passivate the particle surface by means of electrostatic attraction, hydrophobic interaction, or covalent binding depending on their functional groups. in many cases, thiolated ligands are added during/post the NPs synthesis to attach to the core and enhance colloidal stability (Brust et al., 1994; Sakura et al., 2005). Some of these ligands, such as DDT, are exclusively soluble in non-polar solvents (i.e., chloroform or hexane), but others, such as PEG and Mercaptohexanoic acid (MHA) are soluble in both of polar and non-polar solvents (Sperling & Parak, 2010).

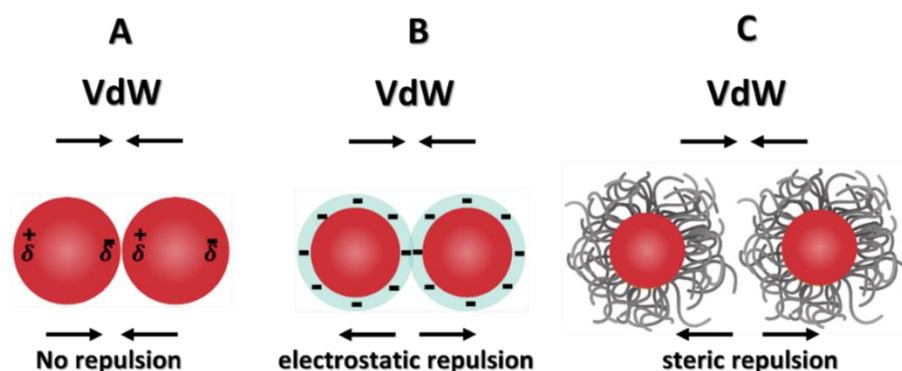


**Figure 5.2.** Stabilization of nanoparticle dispersions by force balancing of (A) attractive Van der Waals (VdW) interactions. (B) with repulsive electrostatic and, (C) repulsive steric interactions to achieve colloidal stability.

## 2.4 The ligand shell: Self-Assembled Monolayer (SAM)

Self-assembled monolayers (SAMs) are well-defined and organized single-layer assemblies of organic ligands formed spontaneously by the adsorption of organic species from solution or the gas phase onto solid (flat or curved) substrates (Schwartz, 2001). This absorption occurs spontaneously due to the balancing of forces acting at multiple energy scales, involving multiple degrees of freedom and often proceeding through several consecutive stages where 1D and 2D ordered structures can also exist. Thermodynamically, molecular self-assembly proceeds toward the state of lower entropy, and must therefore be compensated by the establishment of short-range intermolecular interactions and molecule-surface chemical interactions. The final close-packed two-dimensional crystalline monolayer lowers the free energy (Buschow, 2001). Organic adsorbates that are suitable for SAM formation typically composed of a headgroup, which binds the molecule to the surface; a spacer, which determines the specific intermolecular interactions, such as van der Waals, dipole or  $\pi$ - $\pi$  interactions; an endgroup, which confers specific chemical properties to the surface (hydrophobicity, charge, dipole, etc.). Thiolate, dithiolate, disulfide, carboxylate, amine, and phosphine moieties are the most common headgroups used for anchoring molecules onto metal surfaces (especially gold) (Love et al., 2005). The spacer acts as a barrier between the terminal-groups of the ligand and the metal surface, improving the stability and inert character of the system (Cao et al., 2006). The spacer generally composed of alkyl chains, polyethylene glycol (PEG)-containing chains, or aromatic oligomers. The stability of the layer is generally connected to the length of the spacer. Widely used terminal groups include carboxylate, methyl, quaternary ammonium, maleimide, azide, and biomarkers, which provide specific interfacial interactions with their surrounding media (Bain et al., 1989; Bain & Whitesides, 1988; Huang et al., 2015; Ilyas et al., 2013; Khantamat et al., 2015; Nuzzo & Allara, 1983; Shakiba et al., 2015). The evolution of the self-assembly process is strongly influenced by the headgroup's affinity for the substrate and by the lateral van der Waals interactions between spacer components, which are largely responsible for the SAM's molecular reordering and structural stabilization following initial chemisorption to the surfaces (Ferretti et al., 2000). By carefully selecting the head, spacer, and terminal groups, precise control of the SAM's structural and chemical properties can be achieved. Owing to their customizability and ease of use, SAMs provide a facile, versatile, and convenient system for creating highly ordered organic interfaces that allow specific tailoring and fine-tuning of surface properties (**Figure 6.2**). As a result, SAMs have been exploited

intensively in research for a wide range of applications in materials chemistry, biology, and nanotechnology. SAMs have been employed as a means to control surface properties such as wettability, friction, adhesion, corrosion protection, and lubrication (Huo et al., 2019; Paul et al., 2016). They have also been implemented in devices designed for biosensing, molecular sensing, attachments of biomolecules, and in nanofabrication techniques including microcontact printing and constructive lithography (Hoeppener et al., 2003; Zeira et al., 2011).

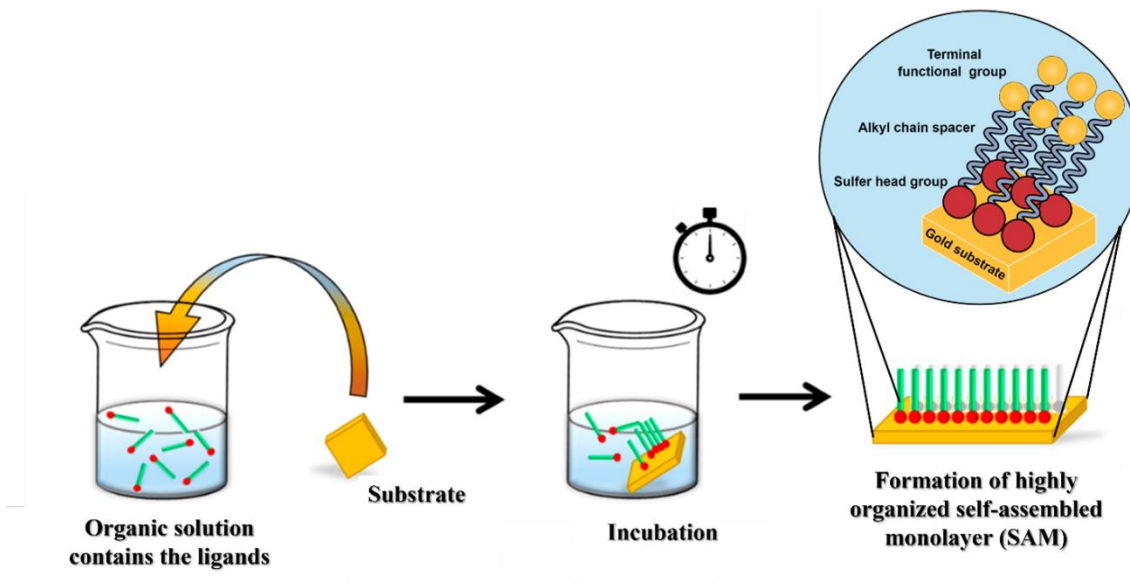


**Figure 6.2.** Schematic illustrates the process for the preparation of a self-assembled monolayer on a flat substrate. First, a clean surface is incubated in a solution containing the ligands with Sulfur head group for a certain time. Second, the substrate is withdrawn and thoroughly rinsed to remove the physisorbed material (the molecules that are not specifically bound).(adopted and modified from (Herrer et al., 2020)).

Studies of nanostructures functionalized with thin organic films arose from the earlier work of Nuzzo, Allara, and Whitesides on SAMs derived from the adsorption of organosulfur compounds on metallic surfaces (Bain et al., 1989; Bain & Whitesides, 1988; Zeira et al., 2011). Since their introduction in the 1980s, SAM technology has expanded to different types of colloid-based materials owing to their broad range of applicability (Irving & Brenner, 2006; Li et al., 2013; Wolf et al., 2005; Xiang & Li, 2009). Among those applications, the attachment of biomolecules to the surface of NPs is considered a crucial step for the development of functional sensing platforms and drug carriers. However, the direct contact between biomolecules and metal surfaces can lead to structural deformation and inactivation of the biomolecule (Sano & Shiba, 2003). For example,

when antimicrobial peptides (AMPs) are physically linked to a metallic surface, they lose their bactericidal capabilities (Gabriel et al., 2006). However, by incorporating a SAM with a spacer of 2–6 methylene units between the AMPs and the metal surface, the AMPs preserve their antibacterial action against bacteria adsorbed on the particle's surface (Haynie et al., 1995). Moreover, Salvati *et al.* demonstrated that the targeting capability of protein-coated NPs can be inhibited by the non-specific interaction between the protein and the surface of the NPs. However, employing OEG spacers to separate the protein targeting sites from the solid surface preserves the functionality of the therapeutic proteins (Salvati et al., 2013). Thus, the spacer group of a SAM prevents biomolecules from interacting directly with the surface of the NPs.

Separately, the functional tailgroup of a monolayer should also be compatible with biomolecules. Chemical functionality on the film terminus serves as a platform on which specific biomolecules, such as antibodies, oligonucleotides and proteins, can bind. While the biomolecules might be attached to the SAM via covalent or non-covalent interactions, robust interactions between the two entities limit the loss of biomolecules and boost the efficiency of biosensing and drug delivery processes.

Maleimide is frequently used as a binding platform for biomolecules. Maleimide-terminated SAMs offers a specific binding site for thiolate-containing biomolecules, which covalently bind via a thiol-Michael addition "*click*" reaction. A facile approach involves tethering a biomolecule at its cysteine residue. Cysteine, an amino acid with a thiol group, can be easily incorporated into, proteins, peptides, and enzymes. Cysteine reacts rapidly with maleimide, enabling the attachment of cysteine-containing biomolecules on the surface. If engineered at one of the protein's termini, Cysteine can provide a useful way to bind the protein to a surface with control of the directionality. A considerable attention has then been given to this type of click reaction due to its efficiency and workability in mild conditions (Nair et al., 2014).

Another strategy to load bio-functional molecules on NPs is to use non-covalent interactions. Electrostatic interactions between cationic-terminated SAMs and anionic oligonucleotides, for instance, can be exploited to load DNA or RNA molecules on the particles. McIntosh *et al.* revealed that AuNPs passivated with mixed monolayers of tetraalkylammonium ( $R_4N^+$ ) and n-alkanethiol, where  $R_4N^+$  groups can bind electrostatically with the phosphate backbone of DNA (McIntosh et al., 2001). Such interactions assemble DNA onto the surface of AuNPs, which was then exploited to inhibit transcription by T7 RNA polymerase in vitro.

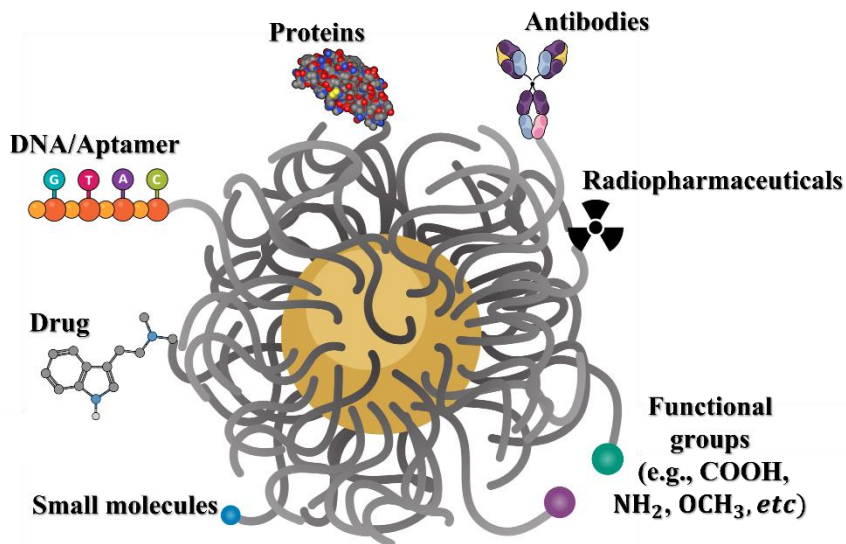


**Figure 7.2.** Surface functionalities of SAM coated AuNPs for various biomedical applications. Such flexibility in surface chemistry enables tailoring optical and chemical properties of the metallic nanostructures.

## 2.5 Optical Properties of Metal Nanoparticles

### 2.5.1 Optical properties of metals

The response of a material to an applied electromagnetic field is described by the complex dielectric function  $\varepsilon(\omega)$ . The dielectric function of metals, characterized by partially filled electronic bands, can be represented with a simple, free-electron gas model. In this approximation, known as the Drude model or plasma model, the free electrons (plasma) are moving within a lattice of fixed, positively charged ion cores. The associated dielectric function is given by:

$$\varepsilon(\omega) = 1 - \frac{\omega_p^2}{\omega^2 - i\gamma\omega} \quad (1.2)$$

where  $\omega$  is the angular frequency of incident light, and  $\omega_p$  is the plasma frequency, which is defined as the natural frequency of undamped oscillations of the free electron plasma. If the electron damping factor  $\gamma$  is neglected, the dielectric function can be further simplified to:

$$\varepsilon(\omega) = 1 - \frac{\omega_p^2}{\omega^2} \quad (2.2)$$

The plasma oscillation can be calculated using the equation:



$$\omega_p = \sqrt{\frac{ne^2}{m_e \epsilon_0}} \quad (3.2)$$

where  $n$  is the number density of free electrons,  $e$  is the charge of an electron,  $m_e$  is the effective mass of the electron and  $\epsilon_0$  is the permittivity of free space. In real conditions, electron collisions cause a damping of the free electron plasma oscillations. The collision frequency  $\gamma$  is related to  $\tau$ , the relaxation time, through:

$$\gamma = \frac{1}{\tau} \quad (4.2)$$

Typical values of  $\tau$  are around  $10^{-14}$  s. Approximating the metal as a driven, damped oscillator, the dielectric function can be described as a combination of phase lag between the driving frequency and natural frequency of the free electrons and the loss of energy through damping. Taken into consideration these factors, the dielectric function can be rewritten as complex number with real and imaginary parts as given in equations **5.2** and **6.2** and respectively.

$$\text{Re}[\epsilon(\omega)] = 1 - \frac{\omega_p^2}{\omega^2 + \gamma^2} \quad (5.2)$$

$$\text{Im}[\epsilon(\omega)] = \frac{\gamma \omega_p^2}{\omega(\omega^2 + \gamma^2)} \quad (6.2)$$

The real part relates to the phase lag caused by the slowing down of an incident electromagnetic wave through the metal, dependent on the metal's permittivity to the light. At angular frequencies less than the plasma frequency, the real dielectric function of metals will be negative. The imaginary part is caused by damping of the wave within the metal, which occurs as a result of losses of the incoming light. The complex dielectric function can be expressed in terms of its real and imaginary counterparts as shown in equation:

$$\epsilon(\omega) = \epsilon_1 + i\epsilon_2 = \left(1 - \frac{\omega_p^2}{\omega^2 + \gamma^2}\right) + i \left(\frac{\gamma \omega_p^2}{\omega(\omega^2 + \gamma^2)}\right) \quad (7.2)$$

The equation above illustrates that the real component of dielectric function varies as the optical frequency decreases. It becomes smaller through the ultraviolet regime, before turning negative in the visible region and is largely negative in the infrared spectrum. This optical property of the real part of dielectric function gives rise to the diverse optical behavior of metals, including the presence of plasmons. Plasmons are the oscillations of the free electrons within the plasma. Plasmons can exist in bulk or at a metal-dielectric boundary, where they are known as a surface

plasmon. To support plasmons, the real dielectric function of the metal must be negative in the specified wavelength range and the imaginary part, which determines absorption, must be small to prevent lossy waves.

### 2.5.2 Surface Plasmons Resonance

Plasmons are longitudinal collective oscillations of the entire volume of a free electron gas formed when a metal interacts with radiation such as light generating a surface-bound electromagnetic wave called a surface plasmon (SP) (Enoch & Bonod, 2012; Raether, 1988a). This SP wave propagates at metal-dielectric interface, which is schematically depicted in **Figure 8.2A**. The associated electric field of the propagating SP wave decays exponentially both in the direction of propagation, due to energy losses to the metal, and perpendicular to the interface into both the metal and the dielectric medium. The decay length is determined by the metal's dielectric characteristics and the surrounding media. The plasmon frequency for an SP wave can be shown to be:

$$\omega_{SP} = \frac{\omega_P}{\sqrt{2}} \quad (8.2)$$

A propagating SP wave carries momentum, and an expression for an SP's dispersion relation can be derived by solving Maxwell's equations with specific boundary conditions.

$$k_{SP} = \frac{\omega}{c} \sqrt{\frac{\epsilon_d \epsilon_m}{\epsilon_d + \epsilon_m}} \quad (9.2)$$

$k_{SP}$  is the wave vector for the SP and  $\epsilon_d$  and  $\epsilon_m$  are the dielectric functions of the metal and the dielectric of the surrounding medium, respectively. In order to excite an SP, both the frequency (energy) and the wave vector (momentum) must be conserved, which cannot be accomplished by merely illuminating a metal surface with light traveling through air. **Figure 8.2B** depicts the dispersion relation between an SP and photons in vacuum. Since the curves do not overlap, the excitation conditions cannot be met. However, Kretschmann and Raether demonstrated in 1968 that SPs can be excited in flat metal films using conventional light by directing the incident light through a coupling medium, such as a quartz prism (Kretschmann & Raether, 1968). If the metal film is thin enough, photons can pass through it and excite an SP wave on the other side of the film at the metal-dielectric interface; the excitation of SPs is dependent on the metal film thickness (Raether, 1988b). SPs can be created at a thick metal film, however, by adding a spacing layer between the metal and the prism, with the Refractive index (RI) of the spacing material lower than

that of the prism. The electromagnetic field of the incident light can couple with the metal via the spacer and excite an SP at the metal interface. This is referred to as the Otto configuration (Otto, 1968). Alternatively, grating coupling is a technique for exciting SPs with electromagnetic waves employing a roughened metal surface instead of a smooth one, allowing for direct excitation without the necessity of a prism (Teng & Stern, 1967). If the RI of the dielectric medium ( $\epsilon_d$ ) at the metal interface is altered, the resonance condition for exciting the SP changes, as seen from Equation (9.2). This is the underlying idea of SPR-based biosensing, which will be discussed shortly in more detail.

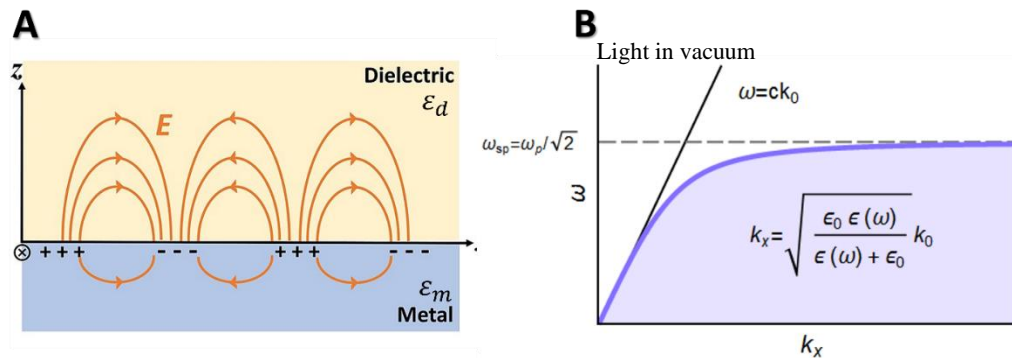


**Figure 8.2.** (A) Schematic depiction of a surface plasmon propagating along the x-axis at the metal dielectric interface with electric field lines (B) Dispersion relation for a surface plasmon and for photons in vacuum.

### 2.5.3 Localized Surface Plasmons

Because there is no place for electrons to propagate in discrete metallic nanostructures, propagating SPs cannot occur. Instead, free electrons in metal nanostructures can be excited and cause a collective oscillation that is limited by the nanostructure's geometrical bounds. These oscillations are known as localized surface plasmons and can be excited by an external electromagnetic field. Since localized SPs do not carry any momentum, only the energy needs to be matched in order to excite the electrons, implying that free photons can be used for excitation and no momentum matching is required. As a result, localized SPs can be explored using relatively simple and inexpensive optical equipment.

Gustav Mie was the first to describe the interaction of light with metal nanoparticles over a century ago (Mie, 1908). He solved Maxwell's equations analytically and came up with an expression for metal nanoparticles in a homogeneous medium interacting with an electromagnetic field. For

spherical metal nanoparticles much smaller than the wavelength of light ( $2r \ll \lambda$ ) the optical extinction cross section can be expressed with the following relationship:

$$\sigma_{ext}(\lambda) = \frac{24\pi^2 r^3 \varepsilon_d^2 N}{\lambda \ln(10)} \frac{\varepsilon_i(\lambda)}{(\varepsilon_r(\lambda) + 2\varepsilon_d)^2 + \varepsilon_i(\lambda)^2} \quad (10.2)$$

Where  $r$  is the nanoparticle's radius,  $\varepsilon_d$  is the dielectric constant of the surrounding medium,  $N$  is the electron density, and  $\varepsilon_r$  and  $\varepsilon_i$  are the real and imaginary part of the complex dielectric function of the bulk metal, respectively. In this quasi-static approximation, it is assumed that the small nanoparticles are in a uniform static electric field. This means that they can be thought of as electrical dipoles. The polarizability ( $\alpha$ ) for such a dipole can be written as:

$$\alpha(\lambda) = 4\pi r^3 \frac{\varepsilon(\lambda) - \varepsilon_d(\lambda)}{\varepsilon(\lambda) + 2\varepsilon_d(\lambda)} \quad (11.2)$$

From Equation (11.2), one can see that maximal polarizability occurs when the term in the denominator approaches zero, hence when  $\varepsilon(\lambda) \approx 2\varepsilon_d(\lambda)$ . The dielectric permittivity of the surrounding medium ( $\varepsilon_d$ ) can be considered a constant and real parameter, which indicates that the metal nanoparticle's dielectric function must have a negative value in order for strong polarization to occur if the imaginary portion is minimal (low losses). As shown in equation (10.2), it is clear that maximum extinction occurs when this condition is met, and plasmon resonance arises. The resonance frequency for a dipolar localized surface plasmon is obtained by using the Drude dielectric function (Dmitriev, 2012b).

$$\omega_{LSP} = \frac{2\omega_p}{\sqrt{1+2\varepsilon_d}} \quad (12.2)$$

for gold and silver nanostructures, this frequency falls within the visible area of the electromagnetic spectrum. Consequently, these nanoparticles exhibit vivid colors in both transmitted and reflected light. When plasmon resonance arises, the conduction band electrons are displaced relative to the nuclei, causing them to move away from their equilibrium position. The coulombic attraction between the relocated electrons and the atomic cores acts as a restoring force on the liberated electrons, causing them to oscillate at a certain frequency. This oscillation normally decays in a matter of femtoseconds (Sönnichsen et al., 2002). However, when an alternating electric field is introduced, a continuous coherent plasmon oscillation can be maintained (**Figure 9.2A**). The plasmon excitation generates a greatly enhanced electric field in the close vicinity of the nanoparticles, which is exploited in a variety of field-enhanced plasmonic applications (**Figure 9.2B**) (Dmitriev, 2012a; Enoch & Bonod, 2012).

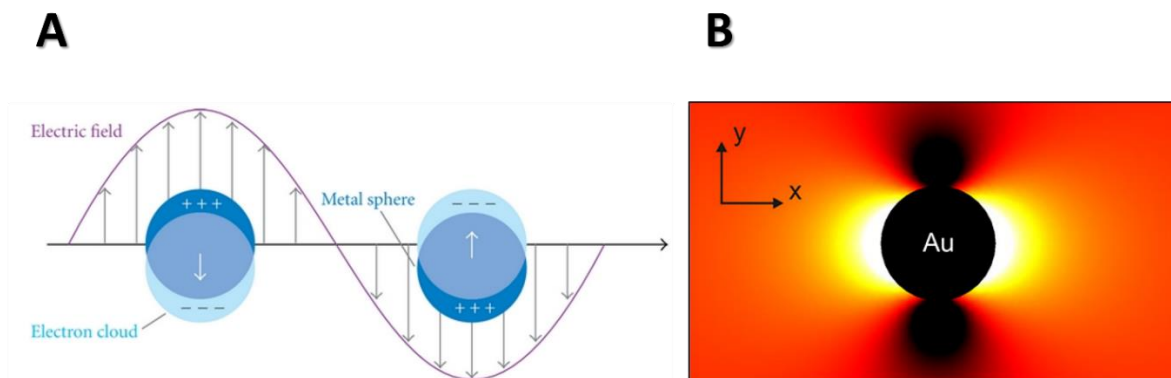


**Figure 9.2.** (A) A schematic illustration of localized surface plasmons, resulting from collective oscillations of relocated electrons as a response to an external electrical field. Notice how electronic clouds are oscillating opposite from the direction of electric field (Hong et al., 2012). (B) The theoretical map depicts the electric field distribution surrounding a gold nanoparticle, demonstrating the highly localized enhancement in the close vicinity of the particle surface (Maier, 2007).

Changes in the dielectric medium close to the nanoparticles, e.g., by biomolecular adsorption on the metal surface, the condition of resonance changes. An increase in the dielectric function of the surroundings causes an increase in the screening of surface charges, which decreases the electrons' restoring force. As a result, less energy is required to excite the electrons, causing the plasmon resonance frequency to redshift (longer wavelength). This is also can be deduced from equation (12.2). As  $\epsilon_d$  increases, the plasmon frequency decreases, resulting in a larger resonance wavelength. This makes metal nanoparticles sensitive sensors for detecting local RI changes, where the sensitivity is determined by the polarizability and strength of the restoring force, both of which are determined by the material and shape of the nanoparticles.

#### 2.5.4 Plasmonic coupling

So far, individual nanoparticles have been considered. However, Due to Coulomb interactions, electromagnetic interactions between adjacent nanoparticles cause an additional spectral shift of the plasmon resonance band. This process is called "plasmonic coupling," and it leads to new hybridized plasmon modes (Prodan et al., 2003). Depending on the polarization of nanoparticles' surface charges, the interaction can generate a "bonding" (lower energy) or an "anti-bonding" (higher energy) plasmon modes. The simplest model can be pictured using two closely spaced spherical metal nanoparticles separated with a distance ( $d$ ), the spectral position of the plasmonic coupling mode is strongly dependent on this interparticle distance (as seen in **Figure 10.2A**), and

red-shifts dramatically as the distance between the particles decreases. Plasmonic coupling between closely spaced nanosized metals results in substantial near-field enhancements in the gap between the particles, which are commonly referred to as "hot spots." When compared to the surrounding electric field, the induced local electrical field can be multiplied by a factor of  $10^2$ . These hotspots are particularly intriguing for SERS, as the enormous field strengths can be utilized to boost the Raman signal from specific molecules positioned within the enhanced nearfield (Camden et al., 2008; Li et al., 2009). **Figure 10.2B** depicts how two interacting metallic spheres or cylinders, sometimes referred to as dimers, generate field amplification levels well above what a single sphere can provide. When the spacing between the particles is large (approximately 10 nm or larger for 10 nm diameter spheres), the particles interact weakly and the field patterns are similar to what would be expected for single particles. While there is some slight field amplification between the spheres, the effect is minor. However, when the particles are brought close together, the fields become quite massive and confined, as shown in the field plots for particles with spacing less than 3 nm. Despite the fact that the color map is scaled for each image, field localization is visible for the strongly connected spheres, with localization volumes less than 1 nm in dimension. The substantial resonance shift caused by the proximity of metal nanoparticles is exploited in a colorimetric sensing biosensing approach. Mirkin *et al.* (Mirkin et al., 1996) pioneered this technology by using DNA to enhance the aggregation of AuNPs. Later, several more sensing techniques based on metal nanoparticle aggregation were developed, capable of detecting a wide range of molecular species (Aili et al., 2009; Chen et al., 2013).

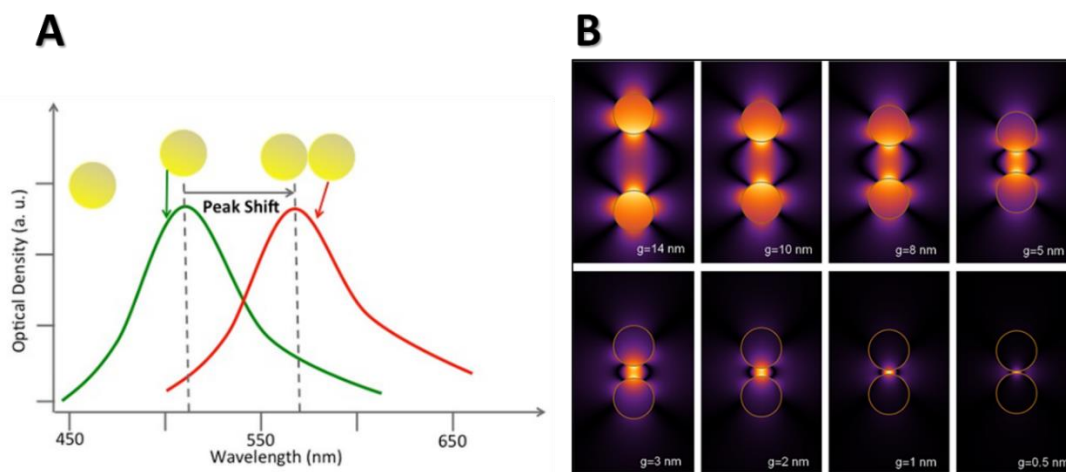


**Figure 10.2.** (A) monodispersed (**green**) and plasmonic-coupled (**red**) AuNPs absorbance spectra. (B) Bringing two metallic nanoparticles close together causes the surface plasmon resonances to pair and alter their resonance frequencies, resulting in a change in the field's properties.

## 2.6 Sensors and Biosensors

A sensor is a device that detects a physical entity and converts the detection into a signal that can be read out. It is often made up of three (3) parts: a detector, a transducer, and a reader. The detector's role is to interact with the physical entity of interest (e.g., an analyte), while the transducer turns the response into a signal that can be evaluated and saved (typically to an electric signal). The reader's function is to capture and make accessible the transformed signal for storage, processing, and visualization. Thus, a sensor is basically an analytical tool. A biosensor is a sensor that combines a biological detector element with a classical physicochemical detector (or, in some disciplines, a sensor that measures biological entities). The biosensor element can be a natural, an engineered biomolecule, or a biomimetic that can interact with the analyte of interest (**Figure 11.2**). The analyte is often a bioactive substance, or a biomarker for illness for diagnostic or prognostic purposes. Indeed, sensors lacking a biological detector element are also referred to as biosensors if they are measuring biological processes. Typical biological detector elements are molecules that can bind with the analyte chemically or non-covalently. Oligonucleotides (Reynolds et al., 2000), immunoglobulins (IgGs) (Jiang et al., 2015), enzymes (Karube & Nomura, 2000), and other affinity reagents, are frequently utilized as detector elements in biosensors. They all have one thing in common: they are all selective detector elements. Detector elements based on organelles, cells, or tissues are also available, but they are less commonly used (Banerjee et al., 2013). The transducer works on the basis of physicochemical detection. The typical transducers in biosensors are a) optical, b) electrochemical, c) electronic, d) piezoelectric, e) gravimetric and f) pyroelectric, of which the optical and electrochemical transducers are the most abundantly used. The optical transducer often involves some form of labelling of the analyte for measurement. For an electrochemical transducer, it depends on good referencing, since the signal is generated by electrochemical reactions that must be linked to the concentration of the analyte being measured. The reader device is usually composed of electronic signal processors, such as computers or handheld devices. The device properties are often determined by how quickly the data can be processed or the intended usage of the biosensor.

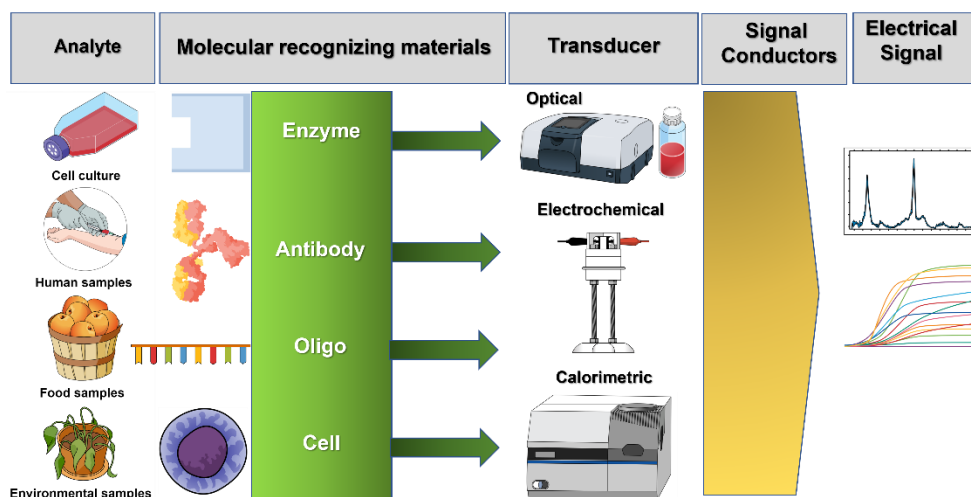


**Figure 11.2.** Schematic illustration of typical components in biosensors.

### 2.6.1 Surface plasmon resonance-based biosensors

SPR-based sensing is a widely used biosensing technology for monitoring and characterizing biomolecular interactions in real time without the need for labeling. Liedberg *et al.* demonstrated SPR-based biosensing for the first time in 1983 by studying the interaction between an antigen and an antibody on a silver surface (Liedberg *et al.*, 1983). Pharmacia Biosensor AB, which was later renamed Biacore, introduced the first commercial SPR-based biosensor equipment. Since then, multiple manufacturers currently produce SPR instruments, rendering the SPR-based biosensor one of the predominant optical biosensing techniques.

The SPR phenomenon arises on the metallic substrate (or other conducting materials) at the interface of two media (e.g., glass and liquid) when polarized light is shone at a certain angle. This produces surface plasmons, which reduce the intensity of reflected light at a certain angle known as the resonance angle. This effect is proportional to the surface mass. A sensorgram can be obtained by measuring the shift of reflectivity, angle or wavelengths as a function of time. The SPR phenomenon allows for straightforward, label-free, and real-time changes in refractive index at the sensor surface that are directly proportional to the concentration of biomolecules. To quantify a ligand–analyte interaction, one of the interacting molecules must be immobilized on the surface of the sensor. A typical SPR apparatus integrates an optical detector component, which typically measures intensity shift, a sensor chip with a gold substrate, a layer enabling ligand immobilization, and a fluidics system allowing flow-through operation. On the basis of the



Kretschmann configuration, a typical setup for conducting SPR biosensing experiment is presented in **Figure 12.2** SPR is widely regarded as a surface sensitive technique since the activation of SPs generates an evanescent field that extends into the sample medium. The penetration depth is defined as the distance traveled when the intensity of the electric field has diminished to approximately 1/e of its value at the immediate surface. Any change in the RI in this region will affect the conditions for SP excitation. In most SPR setups, the penetration depth, which ranges between 150 and 300 nm, is determined by the optical characteristics of the metal, excitation wavelength, and the ambient medium. This results in a surface chemistry consisting of a polymer 3D matrix, which enables a higher ligand surface concentration and exploitation of the entire sensing volume.

The performance of an SPR-based biosensor is determined by numerous variables such as sensitivity, resolution, dynamic range, and detection limit. The sensitivity is defined as the change in sensor response ( $\delta Y$ ) (angle, intensity, or wavelength) resulting from a change in the refractive index ( $\delta n$ ) which can be stated as:

$$\eta = \frac{\delta Y}{\delta n} \quad (13.2)$$

$\eta$  denotes the RI sensitivity, which is dependent on wavelength and incidence angle but is unaffected by the interrogation mode (the mode in which the SPR phase shift can be measured by detecting the phase difference between the signal beam and reference beam). The RI sensitivity can be separated into two expressions: bulk and surface RI sensitivity. The bulk RI sensitivity ( $\eta_{Bulk}$ ) refers to any RI variations in the entire sensing region. However, as SPR is regularly used to explore molecular interactions at surfaces where only a portion of the evanescent field is utilized, it is noteworthy to highlight here a term for surface sensitivity ( $\eta_{surface}$ ). This term refers to the sensitivity for detecting a RI change ( $\delta\eta_d$ ) induced by thickness adsorption on a thin film ( $d$ ). When comparing SPR and LSPR-based sensors, the surface sensitivity term is extremely important.

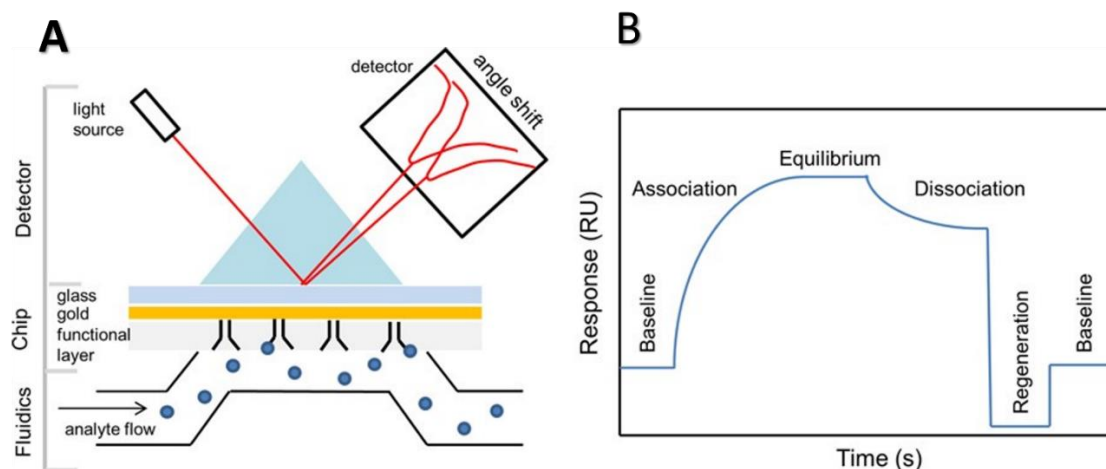


**Figure 12.2.** (A) The SPR working principle, (B) a typical SPR sensorgram depicting the steps of an analytical cycle (Damborský et al., 2016).

Concentration analysis based on the SPR system has been exploited in multiple fields, including clinical diagnostics, environmental analysis, food, etc. For instance, an SPR biosensor assay was utilized to diagnose different stages of Epstein–Barr virus infection in clinical serum samples by detecting antibodies against three distinct antigens found on the virus (Riedel et al., 2014). Also, an SPR chip with an immobilized ligand was used to identify a soluble vascular endothelial growth factor receptor, with a detection limit of 25  $\mu\text{g/L}$  (Pimková et al., 2012). Rapid screening routes that use SPR portable biosensors have a lot of potential in food monitoring. Utilizing a portable six-channel SPR biosensor, milk samples were subjected to sensitive on-site antibiotic screening (Fernández et al., 2010). It was also reported that mycotoxin patulin was detected using an immunochemical SPR biosensor with a 100 pM detection limit (Pennacchio et al., 2014).

### 2.6.2 Localized surface plasmon-based biosensors

Similar to conventional SPR-based sensing, nanostructures supporting an LSPR excitation can be utilized to generate a biosensing event based on LSPR spectrum shifts, which is also referred to as refractive index sensing (RIS) (Rindzevicius et al., 2007). As mentioned before, the dielectric properties of the surrounding medium dictate the condition for creating LSPR on metal nanostructures. This allows for the spectroscopic identification of molecular interactions in the local vicinity of the metal nanostructures. When the energy of the incident light matches the excitation energy of the electrons in the metal, the optical absorbance spectrum shows a distinct peak known as the plasmon peak (**Figure 13.2A**). The resonance condition will be altered by

introducing molecules that cause a change in the RI in the surrounding environment, resulting in a shift of the plasmon peak (**Figure 13.2B**). By monitoring the plasmon peak shift, the amount of material introduced around the metal nanostructures can be quantified.

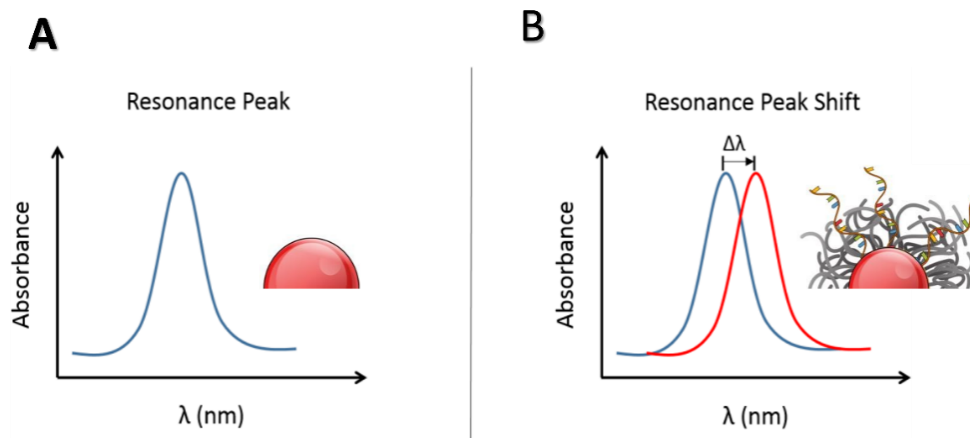


**Figure 13.2.** A schematic illustrates the basic principle of the nanoplasmonic detection based on RIS. (A) The typical surface plasmon band obtained for plasmonic AuNPs. (B) A spectral shift of the plasmon band is observed when an analyte interacts directly or indirectly with the surface of a metal nanoparticle (e.g., AuNPs).

After the first biosensing experiment using propagating surface plasmons in 1983, it took another 15 years to experimentally demonstrate that fixed AuNPs may be used to identify protein interactions by measuring localized surface plasmons (Englebienne, 1998). Since then, a wide range of biomolecular interactions, including biotin-streptavidin (Ferreira et al., 2009; Nath & Chilkoti, 2004), DNA-DNA (Olofsson et al., 2003; Otte et al., 2011), and antibody-antigen (Englebienne, 1998; Haes et al., 2005; Haes et al., 2004) have been detected using LSPR sensing systems. LSPR-based sensing presents a greater promise for miniaturized sensing. Along this line, substantial research has been done on single nanoparticle detection, particularly by the Van Duyne group (McFarland & Van Duyne, 2003; Sherry et al., 2006). In addition, single nanoparticle spectroscopy enables the possibility to investigate the optical properties of a single nanostructure and how this is impacted by morphology, which is a plus. Also, it offers multiplexed sensing strategies, and a substantial reduction of the absolute detection limit, which is essential for obtaining the ultimate sensitivity aim, (i.e., single molecule resolution). However, despite the fact that plasmonic nanostructures have huge extinction cross sections, the signal created by a single nanoparticle is typically quite weak, resulting in a low signal-to-noise ratio. Consequently, spectroscopic studies on a collection of nanoparticles result in an enhanced overall sensing

performance. RIS employing localized surface plasmons focuses primarily on gold or silver plasmonic nanostructures. Other materials, such as aluminum, copper, platinum, and palladium, also exhibit plasmonic characteristics that can be utilized in sensing applications (Chan et al., 2008; Lu et al., 2009; Zoric et al., 2011). Interestingly, plasmonic characteristics have been demonstrated in non-metallic materials such as semiconductor nanocrystals by adding charge carriers via doping (Faucheaux et al., 2014).

### 2.6.3 Refractive index sensitivity









Over a narrow range of RI changes, the bulk RI sensitivity ( $\eta_{Bulk}$ ) can be approximated as a linear function relating the RI change ( $\Delta\eta$ ) and the LSPR peak shift ( $\Delta\lambda_{max}$ ):

$$\Delta\lambda_{max} = \eta_{Bulk}\Delta\eta \quad (14.2)$$

Therefore, to maximize the sensing response, i.e., the peak shift caused by a specific change in the surrounding RI, the  $\eta_{Bulk}$  should be as high as possible. Miller and Lazarides have demonstrated through theoretical calculations that the  $\eta_{Bulk}$  of AuNPs having a plasmon resonance below 800 nm depends only on the position of the plasmon peak (Miller & Lazarides, 2005). This implies that  $\eta_{Bulk}$  is not directly reliant on particle geometry even though the plasmon resonance depends on the shape and size of the nanoparticles. Hence, two nanoparticles with dissimilar shapes but the same plasmon frequency will display similar  $\eta_{Bulk}$ . Numerous studies have been conducted to identify nanoparticles with high  $\eta_{Bulk}$  (Charles et al., 2010; Chen et al., 2008). But this has only been an effort to synthesize nanoparticles with plasmon resonance bands at longer wavelengths. Nonetheless, a longer resonance wavelength does not necessarily result in improved sensing performance. Several experimental groups have demonstrated the association between plasmon peak position and bulk RI sensitivity (Sannomiya et al., 2009; Tesler et al., 2011). Martinsson *et al* showed in their work a linear relationship between the plasmon resonance peak location and the bulk RI sensitivity for a wide range of AuNPs with varying plasmon frequencies (Martinsson et al., 2016). However, it is important to note that this relationship only holds for nanoparticles dispersed in solution. Immobilized nanoparticles on a 2D substrate or a surface functionalization will drastically alter the  $\eta_{Bulk}$ . Besides, when comparing nanoparticles made of various materials, the relationship between plasmon frequency and  $\eta_{Bulk}$  is also invalid. Silver nanoparticles (AgNPs), for example, have plasmon bands that are shorter in wavelength than AuNPs, but they have larger  $\eta_{Bulk}$  (Jakab et al., 2011). This can be attributed to the difference in dielectric

properties of the two materials. Despite their high RI sensitivity, AgNPs are chemically unstable in both air and water, which limits their practical application. **Table 2.2** summarizes some of the experimentally obtained properties of metallic nanoparticle structures.

**Table 2.2.** Summary of physical properties for some of Au and Ag nanostructures

Name	Shape	Size (nm)	$\lambda_{LSPR}$ (nm)	$\eta_{Bulk}$	Name	shape	Size (nm)	$\lambda_{LSPR}$ (nm)	$\eta_{Bulk}$
nanospheres		25	525	60	<b>Nanocube</b>		40	535	91
		50	532	80	<b>nanoprism</b>		50 - 60	775	415
		100	578	180	<b>nanorods</b>		65×20	740	385
Ag		35	398	144	<b>Concave nanocube</b>		50	615	266
Nanosphere									

## 2.7 Thermal lens spectroscopy: beyond a technique on the horizon

### 2.7.1 Historical background

Over the past three decades, the optical detection of nanoparticles and single molecules has had a significant impact on studies of biological and condensed-matter systems. Despite the fact that the first method for detecting a single molecule was based on its absorption, fluorescence-based detection is vastly more prevalent due to its simpler implementation and extremely low background (Moerner & Kador, 1989). However, fluorescence-based detection approaches have several drawbacks; including the photobleaching and photoblinking of fluorophores, and their limitation to a restricted class of probes with high fluorescence quantum yields. Over the past 20 years, several demonstrations of nano-sized object detection using nonfluorescent methods have been made. Notable examples include spatial modulation spectroscopy (Muskens et al., 2008), optical microresonators (Heylman et al., 2014), photothermal microscopy (Berciaud et al., 2006), nanomechanical photothermal sensing (Chien & Schmid, 2020), and photothermal-induced resonance (PTIR) spectroscopy, also known as AFM-IR (Centrone, 2015), and thermal lens spectroscopy (TLS)(Brusnichkin et al., 2007).

Among them, TLS is one of a family of photothermal techniques that can be used for physical and chemical analysis, and well-suited for the characterization of transparent materials (Cabrera et al.,

2006). The limits of optical absorption detection have been improved by three orders of magnitude or more over those obtained by conventional absorbance spectrophotometric techniques. This makes it ideal for ultra-trace determination and absorption spectrum measurements (Swofford et al., 1976). TLS has also been used to measure thermal properties of solid and liquid samples, such as thermal diffusivity (Jiménez Pérez et al., 2008). TLS photothermal measurements are based on the absorption of a heating beam by a small sample, typically a metal nanoparticle. Heat absorbed by the particle and released into its surroundings creates a temperature gradient and thus a refractive index gradient, resulting in a lens-like optical element surrounding the heated nano-object. For different materials, the coefficient of refractive index with temperature ( $\frac{dn}{dT}$ ) varies, and the lens formed can be converging or diverging. However, for gases and almost all liquids, the variation of coefficient of refractive index with temperature is normally negative. The thermal lens effect is shown schematically in **Figure 14.2**.

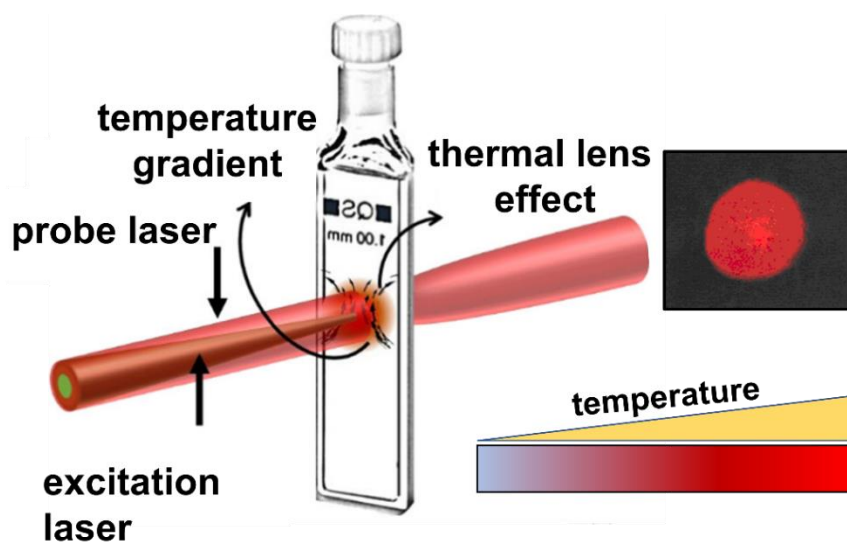


**Figure 14.2.** Schematic representation of the thermal lens effect formation in a fluidic sample.

Gordon and colleagues discovered the thermal lens effect by accident in 1964 while studying laser Raman scattering of pure liquids. The investigation that followed predicted that the most important application would be for measuring small absorbances. Leiti *et al.* were the first to use the intracavity setup to calculate pure liquid absorption coefficients from the focal length of the induced thermal lens (Leite et al., 1964). Solimni measured the absorption coefficients of several pure organic liquids using the same technique used by Leiti *et al.* and later published a comprehensive report on the accuracy and sensitivity of this intracavity method (Solimini, 1966). Callen *et al.*

(1967) discovered a pattern of concentric rings, which is now known as thermal lens spherical aberration (Callen et al., 1967). Dabby *et al.* reported similar findings (Dabby & Paek, 1971). Carman and Kelly investigated the time evolution of the thermal lens formed in iodine CCl<sub>4</sub> solutions (Carman & Kelley, 1968). The authors used a movie camera to record the growth of the thermal lens and measure the size of the beam image. The reproducibility of the results was the most difficult aspect of the intra-cavity experiments. This was because controlling the parameters of such an experimental setup was rather challenging. The first extra cavity thermal lens was made by Rieckhoff, who describes the self-induced divergence of a CW He-Ne laser beam (Rieckhoff, 1966). Hu and Whinnery made the most significant advancement in thermal lens technique in 1973. These authors recognized that the largest fractional change in the radius of curvature of a laser beam wave front (and thus in the divergence of the beam) can be achieved by positioning the lens at the point where the radius of curvature of the beam is minimum, i.e., one confocal length from the laser's minimum beam waist  $\omega_0$  (Hu & Whinnery, 1973). The confocal length, also known as the Rayleigh length, is the distance that the beam expands from its minimum size to a radius of  $\sqrt{2} \omega_0$ . As can be seen from the analysis made by Gordon *et al* who assumes a sample length that is a fraction of the incident beam's confocal length. Most importantly, Hu and Whinnery demonstrated that for samples placed outside the laser cavity, a sensitive detection of thermal lens formation can be achieved by using an auxiliary lens to form a beam waist one confocal length before the sample cell. In 1980, Harris and Dovichi discussed the quantitative behavior of the TL effect (Dovichi & Harris, 1981; Dovichi & Harris, 1980). They found that the general features of the TL behavior can be described by a few straightforward equations, which are helpful for designing instruments and predicting feasibility. They concluded that, as opposed to being an absolute technique, the TL method is a calibrated absorption method. Dovichi and Harris (1981) recognized the improvement in measurement speed that can be attained by capturing the signal's time-dependent buildup rather than just its initial and final amplitudes. Recording the time dependence of the signal avoids the need to wait until the equilibrium thermal lens is established.

### **2.7.2 Sensitivity of TLS technique**

The sensitivity of the thermal lens signal can be understood by comparing TL spectroscopy with UV/Vis spectrophotometry. Consider the basic equation that describes Beer's Law's analytical signal response.

$$I = I_0 e^{-\varepsilon cl} = I_0 e^{-A} \quad (15.2)$$

where  $I_0$  denotes the initial intensity of the optical radiation transmitted through the absorbing medium,  $I$  is the transmitted intensity, and  $A$  is the absorbance, where  $\varepsilon$  is the molar absorption coefficient,  $c$  is the solution concentration, and  $l$  is the absorbing cell's path length. The relative change in the signal for a weakly absorbing solution can be written as:

$$S_A = \frac{\Delta I}{I} = A \quad (16.2)$$

in TLS, the thermal gradient formed after optical absorption and thermal relaxation of the sample causes a change in intensity at the beam center due to induced beam divergence. The thermal lens signal is defined as the relative change in signal as given by:

$$S_{TLS} = \frac{I_0 - I}{I} = \frac{P \left( \frac{dn}{dT} \right) A}{\lambda_p k} \quad (17.2)$$

where  $I_0$  and  $I$  are the transmitted power before and after the formation of the thermal lens, respectively.  $A$  is the absorbance,  $P$  is the power of the excitation laser (in W),  $\frac{dn}{dT}$  is the temperature coefficient of refractive index,  $\lambda_p$  is the wavelength of the probe laser (or excitation laser in a single beam system) and  $k$  is the thermal conductivity of the solvent. Equation (18.2) can be written as:

$$S_{TLS} = \frac{\Delta I}{I} = EA \quad (18.2)$$

where

$$E = \frac{P \left( \frac{dn}{dT} \right)}{\lambda_p k} \quad (19.2)$$

When equations (16.2) and (18.2) for the same absorbance are compared, the thermal lens signal is increased by a factor  $E$ , referred to as the enhancement factor. The enhancement factor is determined by the thermodynamic and optical properties of the medium, and the power used to excite the sample. Using solvents with a high refractive index gradient and low thermal conductivity for a given power increases the sensitivity of the photothermal method.

### 2.7.3 TLS Configurations

A single laser beam is used to create and probe the TL in a single beam configuration. Dovichi and Harris reported the first analytical application of single beam thermal lens spectroscopy (Dovichi & Harris, 1979). The laser beam in a single beam TL spectrometer is focused by a lens and modulated by a chopper or a shutter. After passing through the sample, the far field intensity of



the beam is typically measured with a photodiode placed behind the pinhole. The photodetector output is fed into a storage oscilloscope, which displays the transient change in the intensity of the beam center. A limitation of the single beam measurement is that the spectral response of the optical elements and detectors must be improved when using samples with varying absorption wavelengths. With the advent of dual-beam thermal lens configuration, this limitation can be circumvented. In dual beam configuration, separate lasers are used for thermal lens creation and probing. A pump laser is used to form a thermal lens, while a second, low-power, intensity-stabilized laser is utilized to probe it. The dual beam configuration enables the use of signal processing devices, such as lock-in amplifiers, to improve the signal-to-noise ratio and TL measurement sensitivity. Since the dual beam TL technique is more sensitive than the single beam technique, it is suitable for measuring highly transparent substances. Moreover, detection optics and detectors can be optimized for a single probe laser wavelength, which is a practical option for producing continuous scanning TL spectra. In addition, no correction is required for the spectral response of optical elements and detectors when utilizing different absorption wavelengths. **Figure 15.2** shows the TLS configurations for both systems.

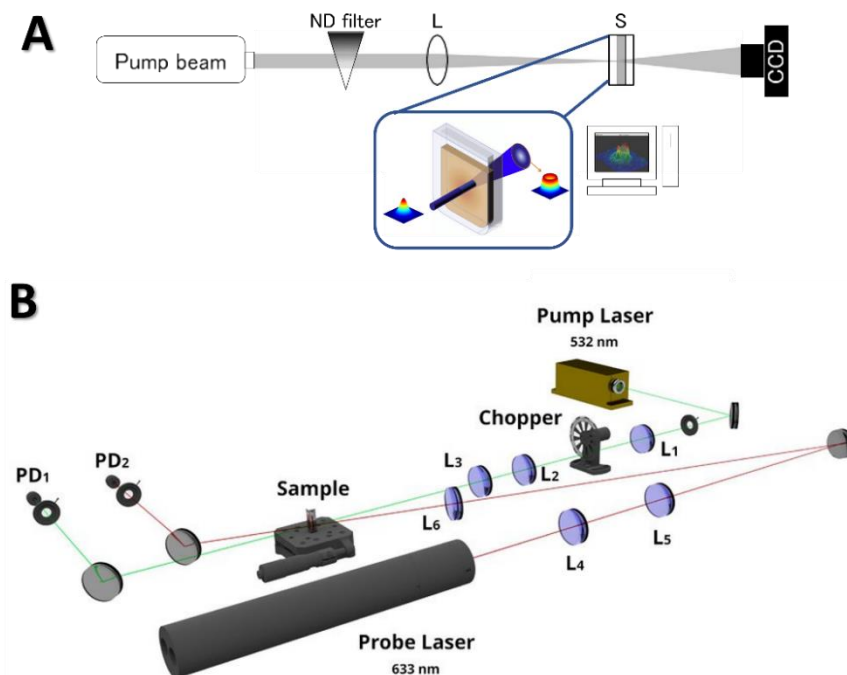


**Figure 15.2.** Schematics illustrate the thermal lens configurations in single beam and dual beam systems in **A**, and **B**, respectively.

#### 2.7.4 Applications of TLS: chemical and biomedical analysis

TLS is often used to detect analytes when the detection sensitivity or time-resolved TLS signal is of concern. TLS was employed to characterize new (heterogeneous) materials including fullerenes and nanodiamond dispersions, which are promising materials for the production of composites and catalysts for biomedicine and biotechnology. However, their applications are limited due to the fact that their dispersions are not fully characterized and, consequently, difficult to regulate. Proskurnin *et al.* recently used TLS for characterization of their optical and colloidal properties to obtain information about the concentration of fullerenes and nanodiamonds in solutions as well as the size of individual colloidal particles, aggregates, and clusters (Mikheev et al., 2015; Volkov et al., 2012). They demonstrated the difference between aqueous fullerene dispersions (AFDs) and organic fullerene solutions due to the formation of large clusters. They measured the kinetics of AFD coagulation at various concentration levels using strong acids and increasing ionic strength. Furthermore, the time-resolved curves were used to measure the thermophysical parameters (thermal diffusivity, thermal conductivity, and thermal effusivity) of AFDs. When compared to conventional spectrophotometry, the LODs for C<sub>60</sub> and C<sub>70</sub> fullerenes are approximately 100 ng·mL<sup>-1</sup>. TLS estimates the size of AFDs in good agreement with data from dynamic light scattering and small-angle neutron scattering. Unfortunately, the theory that connects the size and nature of dispersed particles to the behavior of the transient curve is still in its early stages, and only an estimate of the particle/aggregate/cluster size range can be made. More work should be done to improve theoretical models and their application in characterizing dispersions.

TLS is usually coupled with separation techniques such as chromatographic, and bioanalytical techniques to improve selectivity (immunoassay or enzymatic reaction-based analysis). High performance liquid chromatography coupled with TLS (HPLC-TLS) was used to analyze free bilirubin in human and animal blood serum samples (Martelanc et al., 2014). This hyphenated method allowed for the isocratic separation of all three structural isomers of bilirubin (XIII- $\alpha$ , IX- $\alpha$ , and III- $\alpha$ ) and their respective degradation products in less than seven minutes. The method excels in ultra-high sensitivity, with a limit of detection (LOD) and limit of quantitation (LOQ) of 90 pM and 250 pM, respectively, that are 20 times lower than those obtained with HPLC coupled with diode array detector (HPLC-DAD). Because of the high sensitivity, sample preparation was simplified to just one serum ultrafiltration step, allowing for the first-time qualitative evaluation of sample preparation. Furthermore, free bilirubin was discovered for the first time in human

vascular endothelial cells, and its intracellular antioxidant activity was measured in the nM range. Despite its great potential, TLS has not been extensively used in combination with gel electrophoresis (GE) and only fewer works described that (Briggs & Long, 1996; Liu & Franko, 2014; Mazza et al., 2017). Notably, most of the reported findings were obtained by scanning gels post electrophoresis. B. Abbasgholi N. Asbaghi *et al.* proposed a miniaturized separation system based on miniaturized GE chip (MGEC), coupled with a highly sensitive online TLS detection, using synthesized Fe<sub>3</sub>O<sub>4</sub>-Au core/shell magnetic-plasmonic NPs (MPNPs) as an example of an efficient separation (Asbaghi et al., 2021). This class of hybrid nanomaterials was selected as a model system as it represents a highly potential platform in various applications, especially in theragnostic as an imaging contrast agent, drug transporters, and photothermal therapy agents (Abed et al., 2019). However, it is reported that the preparation of high-quality MPNPs remains a challenging task for researchers (Kwizera et al., 2017). The proposed design was based on coupling the MGEC with online TLM detection system achieved through a homemade chip with reduced buffer and gel volumes of 80 µL and 100 µL, respectively. Additionally, an open-source Arduino enabled digital acquisition and processing of data delivery from a photodiode without performing previous lock-in amplification. This was possible because the gel significantly improves the enhancement factor of the technique giving the possibility of highly sensitive measurements (Briggs & Long, 1996). The findings show that, in less than eleven minutes, the successful separation of the two different nanostructures made by a synthesis intended to prepare the MPNPs was achieved. This study represents the first reported strategy of TLS with counter propagating collimated probe beam as an electrophoresis detector (Cabrera et al., 2015). In this configuration, unlike conventional TLS, it is possible to reach maximum sensitivity and easier alignment without fulfilling the condition for optimum position ( $3^{1/2}$  Rayleigh distance) between probe and excitation beams waists positions. In fact, the probe beam diameter is larger than the excitation beam, testing slightly larger temperature profile, thus higher sensitivity can be achieved.

## **2.8 Biomarkers, diseases, and therapeutic agents**

### **2.8.1 Cancer biomarkers**

A biomarker is a biological molecule that can be objectively detected and assessed in blood, body fluids, or tissues to indicate normal biological processes, pathogenic processes, or pharmacological responses to a therapeutic intervention (Christofi et al., 2019). Cancer biomarkers are biological

entities produced by tumor cells or human tissues as a result of the progression of cancer. These biological molecules are made from several biochemical classes, including proteins, DNA, RNA, microRNA, peptides, hormones, oncofetal antigens, cytokeratins, and carbohydrates. The circulatory system (blood, serum, or plasma), secretions (stool, urine, sputum, or nipple discharge), and other human bodily fluids are all potential sites for cancer biomarker identification. Depends on the ability to accurately measure cancer biomarkers in patient samples, physicians and oncologists can predict cancer risk, screen for early detection, and provide a prognosis for systemic therapy. As a result of recent developments in high-throughput proteomics and genomic technologies, there are numerous cancer biomarker candidates under investigation in preclinical and clinical settings. The U.S. FDA has currently approved 19 protein cancer biomarkers where only 11 of which are detectable in the blood (Chinen et al., 2015). Unfortunately, when used alone, FDA-approved cancer biomarkers do not meet the sensitivity and specificity requirements for clinical usage, and only a few biomarkers essays have been approved for routine clinical use in oncology patients. For example, alpha-fetoprotein (AFP, -fetoprotein) is utilized in the staging and monitoring of non-seminomatous testicular cancer and hepatocellular carcinoma, despite its modest sensitivity (50%) and specificity (70%). However, several other biomarkers are used in clinical applications, including cancer antigen-125 (CA-125) and human epididymis protein 4 (HE4) for ovarian cancer monitoring, PSA for screening and monitoring prostate cancer, thyroglobulin (Tg) for thyroid cancer monitoring, carcinoembryonic antigen (CEA) for pancreatic cancer monitoring, and CA15-3/CA27-29 and human epidermal growth factor receptor 2 (HER2/neu) for breast cancer monitoring (Al-Hussain et al., 2014; Imaoka et al., 2016; Iqbal & Iqbal, 2014; Lilja et al., 2008; Lin, 2008; Sekiguchi et al., 2017; Trudel et al., 2012). In addition to proteins, researchers are investigating for other biological molecules that play a role in carcinogenesis and are detectable in tissues and biological fluids, such as DNA, RNA, microRNA (miRNA), exosomes, and circulating tumor cells (Kinoshita et al., 2017; Schlange & Pantel, 2016; Westphal & Lamszus, 2015; Zhang et al., 2015).

### **2.8.2 Breast cancer and its subtypes**

Cancer is the second leading cause of mortality worldwide, following cardiovascular diseases. Lung, breast, colorectal, prostate, and stomach are the most common sites of tumor growth and spread (Ferlay et al., 2015). Breast cancer is the most frequent type of cancer afflicting women

worldwide, with a greater mortality rate among females, and it is the second most common recurring type of cancer (Siegel et al., 2011). According to biomarker and gene expression profiles, breast cancer is divided into subtypes:

- (1) **Luminal A & B:** luminal breast cancers are linked with the expression of genes encoding for typical luminal epithelial proteins as (estrogen receptor) (ER) and/or progesterone receptor (PR). The luminal A affects around 50–60% of all breast cancer patients. The expression of PR could be positive or negative, and a low level of Ki67 protein with no expression of HER2. Luminal A subtypes commonly metastasize in bone. On the other hand, luminal B is less prevalent (roughly 15-20%) and is defined as ER-positive, HER2-negative and Ki67 high. It can then be distinguished from luminal A using the immunochemical expression of Ki67. It is associated with more aggressive phenotype and worse prognosis.
- (2) **Basal-like breast cancers:** also known as triple-negative because they do not express ER, PR and HER2 but has a high expression of proliferation genes. Among all of subtypes, this has the worst prognosis and commonly metastasizes to lung and nervous system tissues (Barnato & Gradishar, 2015; Yersal & Barutca, 2014).
- (3) **HER2-positive:** Approximately 25-30% of cancer cases fall into this category. Patients with HER2 amplification have chromosome 17(17q12) proliferation, causing a greater production of the proto-oncogene leading to an overexpression of HER2 receptors on the cell surface. HER2 is also a tyrosine kinase receptor (ErbB2). Hence, more epidermal growth factor (EGF) binds to the cells, resulting in increased proliferation. In addition, 40% of patients with HER2 cancer also had a P53 mutation. HER2 tumors have local recurrence and typically metastasis to the brain, liver, and lungs. They had a poor prognosis and survival rate in the past; however, after the development of a targeted HER2 medicine (trastuzumab), survival rates for early-stage diagnosis have improved (Stopeck et al., 2012; Tai et al., 2010).

### **2.8.3 HER receptors: structure and function**

HER2, the human epidermal growth factor receptor 2, is a member of the family of epidermal growth factor receptors (EGFR). The EGFR family consists of the four HER receptors HER1, HER2, HER3, and HER4 (**Figure 16.2**) (Varga et al., 2013). HER family members are

transmembrane receptor tyrosine kinases. Tyrosine kinases are enzymes that carry out tyrosine phosphorylation, namely the transfer of the  $\gamma$  phosphate of adenosine triphosphate (ATP) to tyrosine residues on protein substrate (Bhargava et al., 2005). HER2 is a 1255 amino acid transmembrane glycoprotein (p185<sup>HER2</sup>) of 185 kDa, encoded by a gene localized on chromosome 17q21. Normally, it has a low expression in the healthy adult human body, when overexpression or amplification occurs, it contributes to tumor invasiveness, greater metastasis, higher growth rate associated to worse clinical outcome.

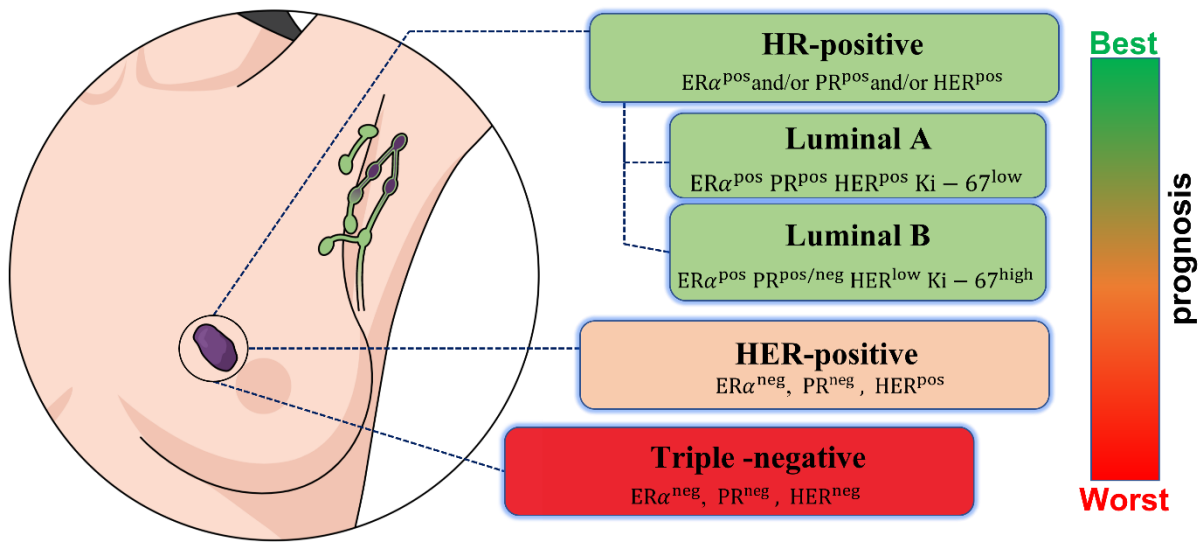


**Figure 16.2.** Breast cancer is classified into three subtypes based on the histological expression of four markers (ER, PR, HER2, and Ki-67): hormone receptor (HR)-positive, HER2-positive, and triple-negative.

HER receptors are structurally similar. They are composed of an extracellular domain (ECD), a transmembrane segment and an intracellular region (Bartlett et al., 2001). The ECD domain is divided into four parts: domains I and III, which are involved in ligand binding, and domains II and IV, which contain numerous cysteine residues that are important for disulfide bond formation (Paik et al., 2002). The transmembrane segment has 19-25 amino acid residues. The intracellular region is composed of a juxtamembrane segment, a functional protein kinase domain (with the exception of HER3, which lacks tyrosine kinase activity and must partner with another family member to be activated (Hicks & Kulkarni, 2008; Persons et al., 1997)), and a C-terminal tail containing multiple phosphorylation sites required for propagation of downstream signaling. The catalytic domain contains the ATP binding pocket, a conserved region for ATP binding. HER receptors are activated by both homo- and heterodimerization, generally triggered by ligand

binding. Crystallographic investigations have recently shown the structural basis for receptor dimerization (Hanna & Kwok, 2006; Lal et al., 2003). Dimerization is mediated by the dimerization arm, a portion of the extracellular region of HER receptors. While in its inactivated state the dimerization arm of EGFR, HER3 and HER4 is hidden, ligand binding induces a receptor conformational change leading to exposure of the dimerization arm (Hanna & Kwok, 2006). In contrast to the other three HER receptors, the dimerization arm of the HER2 receptor is permanently partially exposed, allowing dimerization even if the HER2 receptor lacks ligand binding activity (Lal et al., 2003).

Interaction between the dimerization arms of two HER receptors facilitate the formation of a stable receptor dimer in which the kinase regions of both receptors are closed enough to permit transphosphorylation of tyrosine residues, i.e., the transfer of a phosphate group by a protein kinase to a tyrosine residue in a different kinase molecule (Dal Lago et al., 2006; McCormick et al., 2002). The first dimer member mediates the phosphorylation of the second dimer member, while the second dimer member mediates the phosphorylation of the first dimer member (Paik et al., 2002). After HER receptor activation, the phosphorylation of specific tyrosine residues, followed by the recruitment and activation of downstream signaling proteins, leads to an activation of downstream signaling pathways, which in turn, promote cell proliferation, survival, migration, adhesion, angiogenesis, and differentiation (Vranic et al., 2011). The Phosphatidylinositol 3'-kinase (PI3-K)-Akt pathway and the Ras/Raf/MEK/ERK pathway (also known as extracellular signal regulated kinase/mitogen-activated protein kinase (ERK/MAPK) pathway) are the two most important and most extensively studied downstream signaling pathways triggered by the HER receptors (Ridolfi et al., 2000)(see **Figure 17.2**). These downstream signaling cascades regulate cell cycle, proliferation and survival, apoptosis, metabolism and angiogenesis (Pedersen & Rasmussen, 2009; van de Vijver et al., 2007). Signaling from HER receptors is then terminated through the internalization of the activated receptors from the cell surface by endocytosis. Internalized receptors are then either recycled back to the plasma membrane (HER2, HER3, HER4) or degraded in lysosomes (HER1) (Bilous et al., 2012; Dowsett et al., 2007).

#### **2.8.4 HER2-ECD: a predictive protein breast cancer biomarker**

The HER2-ECD is an essential binding site for two of the most commonly used antibodies in the treatment of HER2-positive breast tumors. When ECD is proteolytically cleaved by several zinc-containing metalloproteases, such as matrix metalloproteinases (MMPs) and ADAM (a disintegrin

and metalloproteinase), a soluble fragment of approximately 105-110 kDa is released in the extracellular environment and ultimately into the blood circulation (Perrier et al., 2018) (**Figure 18.2B**). For this reason, serum HER2-ECD could be neutralized and subsequently reduce their potency via binding with monoclonal antibodies. Furthermore, ECD shedding has another effect; the proteolytic cleavage significantly boosts tyrosine kinase activity and allows the production of a truncated form of HER2 known as p95<sup>HER2</sup> that remains in the cancer cell membrane. This version form of HER2 is 10-100-fold more oncogenic than the entire protein and it is constitutively active, promoting downstream pathways and resulting in rapid growth of tumor, higher aggressiveness and low survival of patients (Tsé et al., 2012).

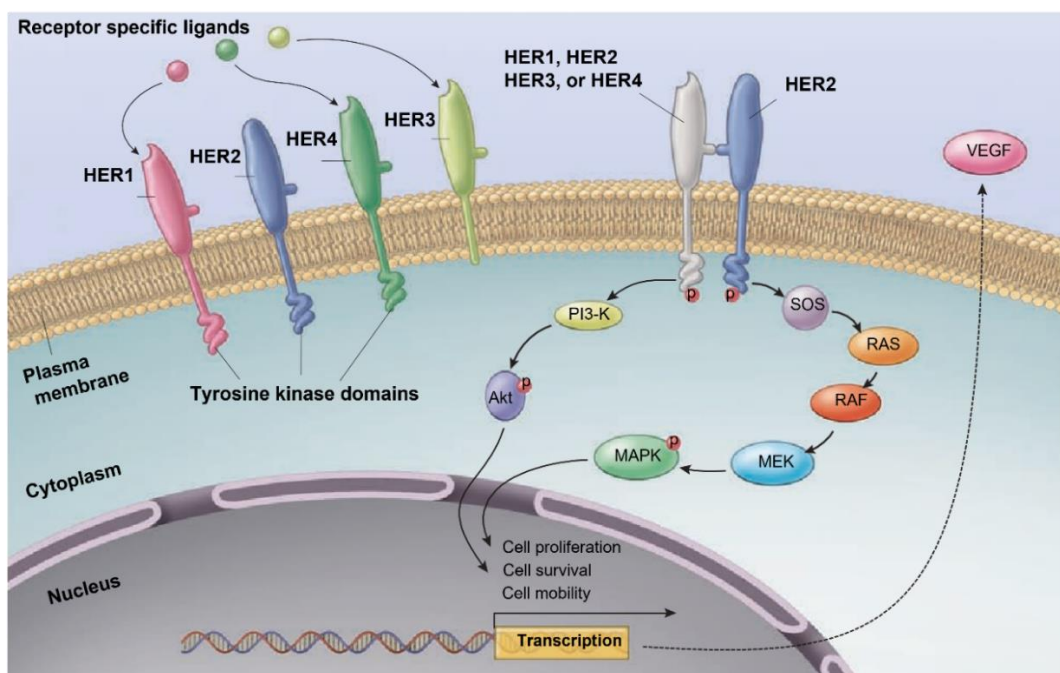


**Figure 17.2.** HER receptors consist of four members: HER1, HER2, HER3, and HER4. HER1, HER3, and HER4 interact with a variety of growth factor ligands. Both homodimerization and heterodimerization of the tyrosine kinase domain enhance cell growth and survival signaling. Phosphorylated tyrosine residues on the intracellular domain of HER2 activate PI3-K/Akt, resulting in cell survival. Furthermore, HER2 activation leads to activation of the RAS/RAF/mitogen-activated protein kinase (MAPK) pathway. (The figure adopted and modified from (Hudis, 2007)).

The biological and clinical relevance of shed HER2-ECD (sHER2-ECD) is still unclear. It has been firstly proposed as a cancer biomarker to correlate serum levels of sHER2-ECD with tissue HER2 (tHER2) but several conflicting works doubted this correlation. So, sHER2-ECD can rather be a useful biomarker for the early detection of breast cancer and to provide information about cancer recurrence, metastasis and response to treatment (Perrier et al., 2018). High levels of



sHER2-ECD are recorded primarily in individuals with metastatic breast cancer, but not in healthy controls. According to Food and Drug Administration (FDA) guidelines, sHER2-ECD levels should be less than 15 ng mL<sup>-1</sup>. HER2-ECD levels in healthy individuals range from 2 to 15 ng mL<sup>-1</sup>, while HER2-ECD levels in breast cancer patients range from 15 to 75 ng mL<sup>-1</sup> (Shi et al., 2017). Moderate levels (up to 50 ng mL<sup>-1</sup>) have been observed in patients with liver disease. This disparity could be attributed to the fact that patients with metastatic breast cancer have liver metastases. According to the American Society of Clinical Oncology (ASCO) and FDA, HER2-ECD can also be used to identify individuals who may benefit from anti-HER2 therapy and to predict Trastuzumab response (Salgado et al., 2015). Despite what has been claimed, serum sHER2-ECD determination cannot replace conventional techniques such as immunohistochemistry (IHC) or fluorescence in situ hybridization (FISH), rather only be employed as a complementary test. However, different splice variants of HER2 may coexist and indeed such heterogeneity seems to play a role in breast cancer development. It might be then extremely meaningful to detect and discriminate the various HER2 splice variants, also in view of the development of personalized therapies (Jackson et al., 2013).

### **2.8.5 Treatment of HER2-positive breast cancer patients**

Current breast cancer treatment strategies depend on histological type and grade, tumor size, lymph node status, cancer stage (early or metastatic), menopausal state, patient age, ER status, and HER2 status. Standard care for HER2-positive breast cancer patients includes segmental or total mastectomy, radiation (when required), systemic chemotherapy, adjuvant hormone therapy (for ER-positive patients), and anti-HER2 agents.

### **2.8.6 Anti-HER2 therapeutic agent: Trastuzumab**

Anti-HER2 agents that have been licensed by the FDA and are currently being used in clinical settings in combination with chemotherapy can be subdivided into two classes (Dietel et al., 2007): (i) recombinant humanized monoclonal antibodies that bind the extracellular regions of HER2. Trastuzumab and pertuzumab are two examples of this class of agents. (ii) small molecule tyrosine kinase inhibitors (TKIs), like lapatinib. They inhibit enzyme function of the intracellular catalytic domain of HER. Trastuzumab (Herceptin<sup>®</sup>) is an IgG1 humanized monoclonal Ab authorized for the treatment of HER2 breast cancer as well as other HER2 cancers such as gastric cancer (**Figure 18.2A**). Trastuzumab has an average molecular weight of 150 kDa and is administered by

intravenous infusion. For HER2 breast cancer patients, the efficacy of trastuzumab as a monotherapy has been shown to be around 30%. As a result, the conventional treatment for metastatic gastric cancer is a combination of trastuzumab and additional chemotherapy medicines such as capecitabine, 5-fluorouracil, and cisplatin (Bang et al., 2010). In addition, most studies recommend combining trastuzumab with paclitaxel, docetaxel, or aromatase inhibitors for postmenopausal women with HER2 breast cancer (Boekhout et al., 2011). Trastuzumab plus chemotherapeutic drugs (mainly Taxanes) has shown disease-free and overall survival advantage in patients with HER2 breast cancer in the early stages. Due to the favorable outcome, Genentech received FDA permission in April 2013 to utilize a combination of trastuzumab and Taxane as an adjuvant therapy for patients with HER2 cancer. Although the combination reduces dysfunction of left ventricular ejection velocity, which is the primary toxicity for trastuzumab, in most cases this ventricular dysfunction is found to be reversible. Trastuzumab (Fab region) functions via binding to the C-terminus of the HER2-ECD, and the mechanism of action is not entirely understood. However, trastuzumab Ab blocks HER2 dimerization which deactivates the intracellular signaling pathways (MAPK/ERK and PI3-K) (**Figure 18.2B**) (Spector & Blackwell, 2009). Trastuzumab also stimulates the immune system by causing antibody-dependent cellular cytotoxicity (ADCC) against HER2 tumor cells, which causes the cells to breakdown (**Figure 18.2C**). Cell death, in this case, will occur as a result of an increase in p27 levels caused by the suppression of the G1 phase of the cell cycle (Scheuer et al., 2009).

### **2.8.7 Novel antibody formats: Nanobodies**

Although trastuzumab, when paired with chemotherapeutic drugs, significantly improves disease-free and overall survival in breast cancer patients, the developed drug resistance, and hence disease recurrence, is common in people treated with such antibody (Korkaya et al., 2012; Pusztai & Esteva, 2006). Furthermore, cardiotoxicity was one of the negative effects associated with trastuzumab usage (Piccart-Gebhart et al., 2005). As a result, the discovery of new binders, either to be used alone or in combination, would provide the desired alternative possibilities. As revealed for the first time in 1993, Heavy chain only antibodies, lacking light chains are naturally occurring in blood of Camelidae. Heavy chain alone antibodies identify their corresponding antigen via the sole variable domain of the heavy chain, as opposed to the antigen binding fragment of normal monoclonal antibodies.

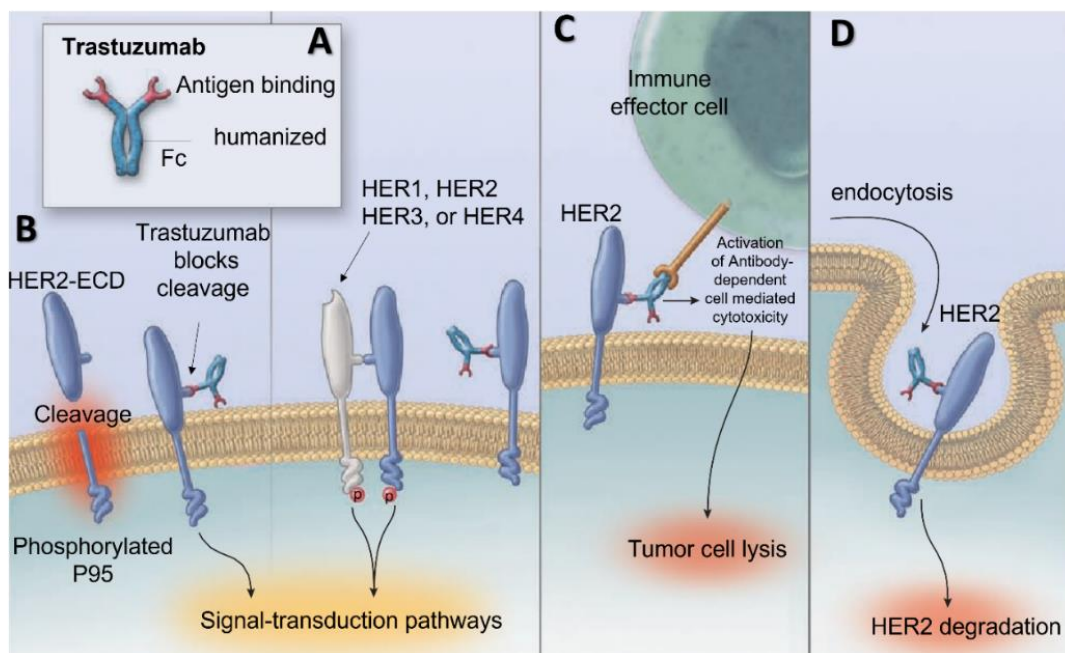


**Figure 18.2.** (A) Trastuzumab is composed of the antigen-binding fragment (Fab) of the murine monoclonal antibody 4D5, directed against the ECD of HER2. (B) Trastuzumab inhibits the release of HER2-ECD, hence inhibiting the development of P95, a membrane-bound fragment with constitutive tyrosine kinase activity. (C) Trastuzumab suppresses HER2 signaling; via recruits Fc-competent immune effector cells, which promotes tumor cell killing. (D) Trastuzumab promotes receptor downregulation by stimulating HER2 endocytosis. (The figure adopted and modified from (Hudis, 2007)).

VHH (Variable domain of the heavy chain of a heavy chain-only antibody) or Nanobody are other names for this variable domain. Major advantages of Nanobodies lies on their high solubility, intrinsic stability, ease of cloning, modular nature, binding to cavities and difficult-to-access antigens, and ease of synthesis in bacteria or yeast. However, despite the appeal of the small size of a Nanobody (~15 kDa), it can be considered as a drawback as such size is below the renal threshold, causing rapid excretion via the kidneys. To elongate the half-life of a Nanobody an albumin-specific Nanobody unit can be fused to the existing Nanobody (Tijink et al., 2008). Nanobodies are suitable for prokaryotic and eukaryotic expression systems, and they are widely used in the development of therapeutic antibody drugs, diagnostic reagents, affinity purification matrices, and scientific research, becoming an emerging force in a new generation of therapeutic biomedical and clinical diagnostic reagents.

Along this context, several works have reported on nanobodies targeting HER2 receptors. For example, it was demonstrated that combining nanobodies targeting HER2 with photochemical internalization (PCI) on polymerized nanoparticles that carry saponin achieved the selectivity of NPs (Martínez-Jothar et al., 2019). Also, a combination of liposome and HER2-nanobody enhanced the magnetic resonance imaging localization of breast cancer cells (MRI) (Khaleghi et al., 2017). HER2-nanobody radiolabeled with  $^{131}\text{I}$ ,  $^{18}\text{F}$ , or  $^{117}\text{Lu}$  was employed used to determine the expression and localization of HER2 protein (D'huyvetter et al., 2014; Pruszynski et al., 2013; Vaidyanathan et al., 2016). Even a phase I study utilizing  $^{68}\text{Ga}$ -labeled HER2-nanobody for PET/CT to determine HER2 expression in breast cancer has been conducted (Keyaerts et al., 2016).

A more innovative approach to utilize these structures in the framework of cancer therapy was demonstrated via functionalizing branched-AuNPs with Anti-HER2 Nbs. Because of their wide absorption cross-section, branched-AuNPs are photothermally active, and can kill tumor cells when exposed to laser light. Anti-HER2 Nbs conjugated to branched-AuNPs have been demonstrated to accumulate on the surface of HER2-expressing tumors and can be employed as antigen-targeted photothermal anticancer treatments (Van de Broek et al., 2011). Therefore, the small size of nanobodies, combined with their versatility, makes them in principle an appealing binder molecule for immuno-gold labeling.

## Materials and methods

### 3.1 Chemicals

A gold (III) chloride solution, Trisodium citrate tribasic dihydrate, Poly-Ornithine, Cobalt (II) chloride hexahydrate, standard human serum, and Tris(3-hydroxypropyltriazolylmethyl) amine (THPTA), Copper (II) sulfate pentahydrate, and antibody anti-His (HRP Sigma #A7058), Nitric acid, and Hydrochloric acid, (Ethylenedinitrilo)tetraacetic acid (EDTA) were purchased from Sigma-Aldrich Chemical Co. (St. Louis, MO, USA). 1-mercaptoundec-11-yl)tri(hexa(ethylene glycol) (HS-(CH<sub>2</sub>)<sub>11</sub>-EG<sub>3/6</sub>OH) and (1-mercaptohexadec-16-yl)tri(ethylene glycol) NTA-terminated, 10-undecyn-1-thiol (for brevity, TOEG3, TOEG6, NTA, and Alkyne respectively) were purchased from Prochimia Surfaces (Gdynia, Poland). The human HER2/ErbB2 protein, His-tagged, was purchased from Acro Biosystems (Newark, DE, USA). The monoclonal antibody Trastuzumab was purchased from MedChemExpress (MCE<sup>®</sup>, Monmouth Junction, NJ, USA). Ni-NTA agarose matrix purchased from QIAGEN (Hilden, Germany). The HEPES buffer was made of 100-mM HEPES buffer containing 0.025% Tween 20, pH 7.4 prepared in ultrapure water (Milli-Q water). Severe acute respiratory syndrome-2019 novel coronavirus (SARS-COV-2(2019-Ncov)) spike neutralizing antibody, Anti- RBD Rabbit mAb, was purchased from Sino Biological (Beijing, P.R. China). DNA sequences were purchased from Biomers (GmbH, Germany). Avidin and Phosphate-buffered saline (PBS) were purchased from (Thermo Fisher Scientific, USA). The chemicals used in the TBE buffer and Ethanol (99.8% pure) were purchased from Merck (Germany). AF594-azide was obtained from (Jena Bioscience). THPTA (tris-hydroxypropyltriazolylmethylamine, and Sodium L-Ascorbate were obtained from Tokyo Chemical Industry (TCI). 1,2-dioleoyl-sn-glycero-3-phosphocholine (DOPC) and powder cholesterol were purchased from (Avanti Polar Lipids, USA). All solutions were prepared using an Ultrapure Milli-Q water for all experiments.

### 3.2 Synthesis of gold nanoparticles (AuNPs)

The preparation of AuNPs stabilized by sodium citrate is the main synthetic platform for the studies described in this thesis. AuNPs were synthesized by sodium citrate reduction of  $\text{HAuCl}_4$  as described by Turkevich *et al* (Turkevich *et al.*, 1951). To avoid unwanted nucleation and aggregation during AuNPs synthesis, all glassware used in this preparation was carefully cleaned with freshly prepared aqua regia ( $\text{HCl}:\text{HNO}_3$ , 3:1<sub>v:v</sub>), rinsed multiple times with Milli-Q water, and oven-dried at 100 °C before to the synthesis. As demonstrated in **Figure 19.3**, in a 250 mL round bottom flask, 1.1 mL of 17.3 mM  $\text{HAuCl}_4$  was added to 43.6 mL of Milli-Q water and brought to a boil with vigorous stirring on a magnetic stirrer hotplate. Then, 300  $\mu\text{L}$  of 72 mg/mL of trisodium citrate dihydrate was added rapidly. The solution underwent a color change from yellow to colorless, then dark blue, and, finally, deep red within a few minutes. The reaction was maintained at the boiling point for 30 mins to assure the complete reduction of the gold salt; after which, the solution was cooled down to room temperature. The resulting gold colloids were protected from light and stored at 4 °C until required.

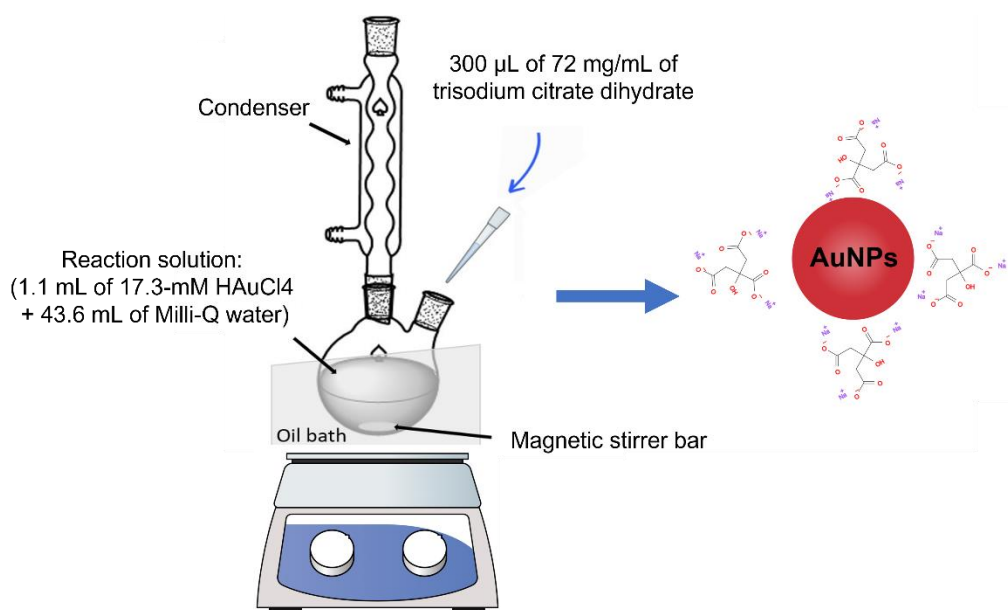


**Figure 19.3.** Experimental set-up used in the synthesis of citrate capped of AuNPs.

### **3.3 Functionalization of AuNPs: NTA-based strategy**

#### **3.3.1 NTA and TOEG3 mixed-SAM**

The functionalization of AuNPs with NTA and TOEG3 mixed-SAM was obtained via a place exchange approach. After determining the minimum concentration of TOEG3 that fully covers the AuNPs, the citrate ligands covering the AuNPs were replaced by NTA and TOEG3 ligands gently mixed at a 50:50 ratio, forming a fully mixed monolayer on the AuNPs by self-assembling overnight at room temperature. Following the protocol described in Reference (Swartz et al., 2011), the particles were purified via centrifugation (twice,  $7200 \times g$  for 45 mins). The final pellet was redispersed in 500  $\mu\text{L}$  of the buffer (100-mM HEPES containing 0.025% Tween 20, pH 7.4). Successful surface functionalization was confirmed by monitoring the change of the hydrodynamic diameter of particles using DLS, gel electrophoresis, and the characteristic surface plasmon band (SPB) peak before and after the passivation using UV/Vis spectroscopy.

#### **3.3.2 $\text{Co}^{2+}$ chelation and attachment of Histidine-Tagged HER2 Protein**

As seen in **Figure 20.3**, functionalized AuNPs (450  $\mu\text{L}$ , 2 nM) were incubated with  $\text{CoCl}_2$  (50  $\mu\text{L}$ , 100 mM) for 1 h at room temperature. After charging with  $\text{Co}^{2+}$ , the particles were centrifuged (twice,  $7200 \times g$  for 30 mins) and washed twice with the buffer. Ultimately, the particles were suspended in the same buffer and filtered through a 0.1- $\mu\text{m}$  syringe filter. For the protein immobilization onto the particles, 2  $\mu\text{L}$ , 6.3  $\mu\text{M}$  of His-tagged HER2 protein (His-tagged HER2, 0.1% BSA in PBS) was introduced to the mixture and left to react at room temperature under mild shaking for 1 h. Following that, the particles were centrifuged (twice,  $5000 \times g$  for 20 mins) and, finally, redispersed in 500  $\mu\text{L}$  of the buffer. Subsequently, the particles were characterized using UV/Vis spectroscopy and DLS.

#### **3.3.3 Assessment of HER2-Trastuzumab recognition via indirect ELISA**

As described in **Figure 21.3**, Indirect ELISA was performed to confirm HER2-trastuzumab binding. Firstly, the wells (96-well plate) were coated with 1 and 5  $\text{ng}/\mu\text{L}$  of trastuzumab (100 mM sodium carbonate/bicarbonate, pH 9.6) and incubated overnight at  $4^\circ\text{C}$ . The following day, the wells were washed 3x, with PBST (PBS +Tween 0.05%), and incubated for an hour with a blocking solution (PBST+1% BSA) followed by 4x of washings. Next, His-HER2 (5, 25, and 50 ng) protein was added to the wells and left to react for 3 hours. The plates were washed 4x, 5 mins

each. 100  $\mu\text{L}$  of the antibody anti-His was diluted 1:2000 in PBST+1%BSA and was added to the wells, incubated for 90 min, and followed by 4x washings for 5min each. Finally, 100  $\mu\text{L}$  TMB was added to each well and incubated for 15 min. The reaction was stopped with the addition of 1.0 M HCl. The absorption of each well was determined at 450 nm by a plate reader (Tecan, Infinite F200 Pro). The experiment was carried out in duplicate.

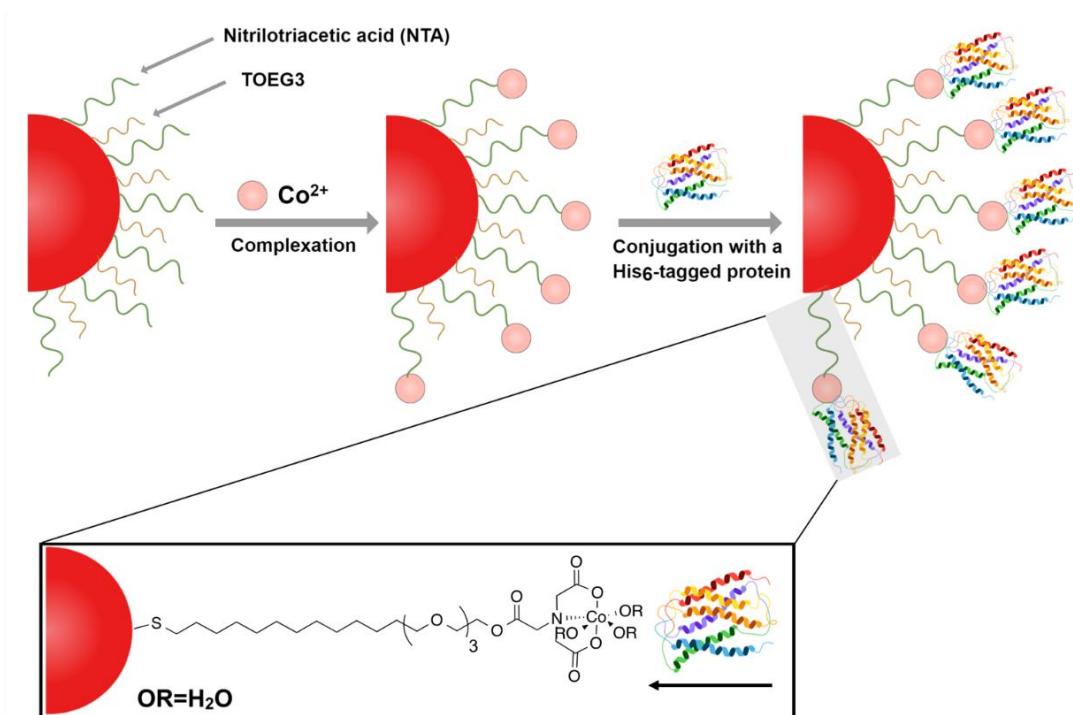


**Figure 20.3.** representation illustrates the attachment strategy of the His-tagged protein onto the surface of the Co(II)NTA/TOEG3 AuNPs.

### 3.3.4 LSPR-Based Detection of Trastuzumab using HER2 Decorated AuNPs

Trastuzumab antibody at various concentrations ranging from 0.1 to 40  $\mu\text{g}/\text{mL}$  was added to His-tagged HER2/AuNP bioconjugates in a final volume of 500  $\mu\text{L}$ , well-redispersed, and left to react for 5 min before conducting the spectroscopic scan. The corresponding absorption spectra were recorded in the wavelength range from 400 to 750 nm. The degree of aggregation was assessed by computing the ratio of the absorption recorded at two selected wavelengths ( $A_{600}/A_{520}$ ) and normalizing this ratio to the corresponding values before addition of the antibody.



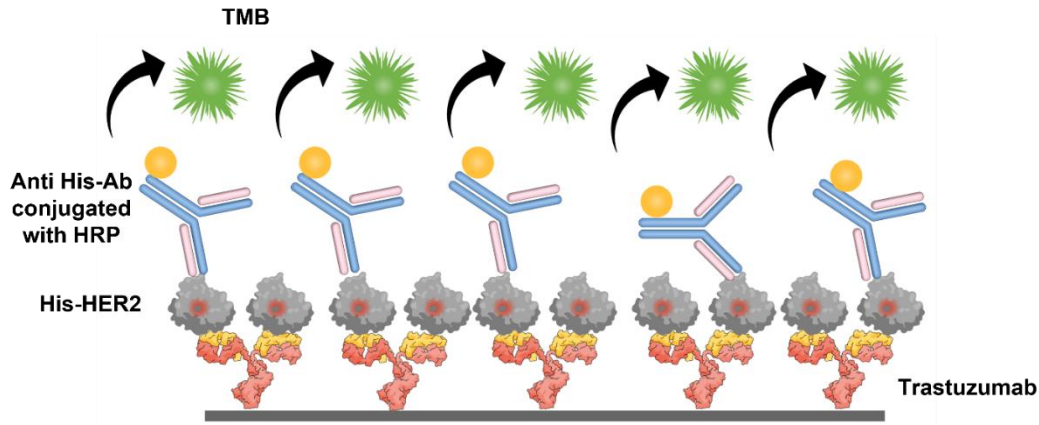


**Figure 21.3.** Indirect ELISA performed for trastuzumab antibody and His-HER2 antigen.

### 3.3.5 Filtering a human serum with Ni-NTA agarose matrix

Ni-NTA agarose matrix was used to remove proteins containing Histidine-repeats (from 3-10 amino acids). Briefly, 100  $\mu\text{L}$  of the resin was incubated with 900  $\mu\text{L}$ , 5% diluted serum for 30 min. Then, the supernatant was collected after each centrifugation ( $500\times g$ , 3 min). After the third wash, the matrix was eluted (2M imidazole, pH 8.0). All the samples obtained from each step were run in SDS-PAGE gel (gradient gel).

## 3.4 Functionalization of AuNPs: DNA-based strategy

### 3.4.1 Single-stranded DNA sequences

F9-SH: 5'-CTTCACGATTGCCACTTCCAC-3' with 5'-thiol C6 modification (22 bases); F9-maleimide: 5'-GTGGAAAGTGGCAATCGTGAA-3' with 5'-maleimide modification (22 bases). cF9 and F9 are complementary sequences. All lyophilized DNA sequences were dissolved in TE buffer (Tris 10 mM, EDTA 1 mM) pH 8.0 at a concentration of 100  $\mu\text{M}$ , aliquoted, and stored up in  $-20\text{ }^{\circ}\text{C}$  freezer. Aliquots are crucial to avoid detrimental freezing and thawing of DNA sequences.

### 3.4.2 Nanobodies optimization and production

Nanobodies (single-domain antibodies or VHHs) referred to as C8 were produced in Dr. Sara Fortuna's laboratory at the Department of Chemical and Pharmaceutical Sciences (University of Trieste, Italy). Nanobodies sequences were first optimized through in silico computational

strategies, cloned in DNA expression vector, produced in *E. coli* bacteria, and purified using the 6xHis-tag present at the C-terminal of all nanobodies. To allow the following conjugation with ssDNA, in sequences of nanobodies at the C-end was also inserted a terminal cysteine (Cys), before the 6xHis-tag. All nanobodies were aliquoted to avoid detrimental freezing and thawing of proteins and stored up in -20 °C freezer.

### **3.4.3 C8-DNA Conjugate production**

The conjugation of nanobodies with single-stranded DNA sequence F9-maleimide was conducted by means of a maleimide reaction as presented in the **Figure 22.3**. The nanobodies contain a C-terminal cysteine with -SH group (thiol group) that is involved in the reaction. Nanobodies were first diluted to a concentration of 100  $\mu\text{M}$  in HEPES 10 mM pH 7.4 buffer and kept reduced by the addition of TCEP (reducing agent) in 10-fold molar 30 excess for 20 minutes at room temperature. Then F9-maleimide, diluted in TE buffer (Tris 10 mM, EDTA 1 mM, pH 8.0) was added to the nanobodies with a molar ratio of 10:1<sub>ssDNA: protein</sub> (e.g., 100  $\mu\text{M}$ :10  $\mu\text{M}$ ). The reaction has to be conducted in HEPES 10 mM pH 7.0 buffer to avoid cross-reaction between amines and free thiol group of cysteines. After 2 hours incubation at room temperature, the conjugates were purified from reaction biomolecules using a G-25 Illustra Microspin Columns (GE Healthcare Life Sciences). Conjugates were then aliquoted to avoid detrimental freezing and thawing and store up in -20 °C freezer.

### **3.4.4 Preparation of ssDNA and ssDNA/TOEG6 customized SAM on AuNPs**

A low pH assisted method was used to modify citrate capped AuNPs according to a published protocol with slight adjustments (Deka et al., 2015). As presented in **Figure 23.3**, cF9-SH (5.9  $\mu\text{L}$  of 100  $\mu\text{M}$  stock) was added to the AuNPs (750  $\mu\text{L}$  of 2.6 nM stock) then mixed by vortexing and left to react at room temperature for 10 min. Next, HCl-citrate buffer (1.5 mL of 10 mM stock, pH 4.3) was added to neutralize the negative charges of the DNA backbone. The solution was then incubated for 30 mins allowing the thiols at the termina of the DNA strands to form bonds with the AuNP surface. Nanoparticles were then purified by centrifugation (twice, 14462  $\times$  g, 15 mins each in Milli-Q water). The final pellet was redispersed in either 1.0 mL of 10 mM phosphate buffer (pH 7.0) or 500  $\mu\text{L}$  of 10 mM Saline phosphate buffer (100 mM NaCl, pH 7.0) as a hybridization buffer.

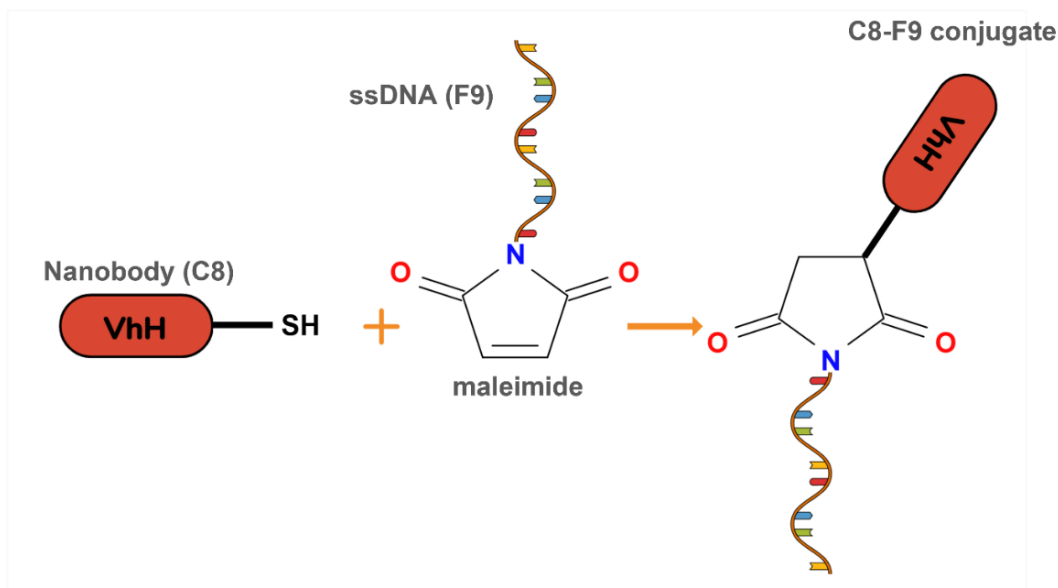


**Figure 22.3.** Reaction of an SH-modified VHH with a maleimide-modified oligo leads to the formation of a stable nanobody-oligonucleotide conjugate.

For thermal lens spectroscopy characterization part, five ssDNA-AuNPs samples with different AuNPs: DNA ratios including 1:100, 200, 300, 400 and 500 were prepared and named: 100DNA, 200DNA, 300DNA, 400DNA, and 500DNA, respectively. For ssDNA/TOEG6 mixed-SAM coated AuNPs, identical steps were followed. After the incubation with HCl-Citrate for 30 mins, TOEG6 (17  $\mu$ L of 300  $\mu$ M stock) was added to the mixture, vortexed and left to react for 10 min to passivate the remaining surface. Nanoparticles were then purified by centrifugation (twice,  $14462 \times g$ , 15 mins each in Milli-Q water). The final pellet was redispersed in either 1.0 mL of 10 mM phosphate buffer (pH 7.0) or 500  $\mu$ L of 10 mM Saline phosphate buffer (100 mM NaCl, pH 7.0) as a hybridization buffer. Functionalized particles were characterized with UV/Vis and gel GE (1x TAE, 10% glycerol, 80 V, 45 min).

### 3.4.5 Assessing the conformation of DNA strands on AuNP surface

The possible configurations of ssDNA on the AuNP surface were assessed using a Zetasizer Nano ZS dynamic light scattering technique (DLS, Malvern-Instrument, UK). Particles were prepared as described previously and dispersed in 10 mM phosphate buffer (pH 7.0). For preparing DNA/TOEG6@AuNPs, ssDNA/TOEG6@AuNPs were dispersed in the hybridization buffer. Then the complementary sequence was added to the particles in 10x excess, gently mixed, and kept at room temperature for one hour. Unbound DNA strands were then removed by

centrifugation (twice,  $14462 \times g$ , 15 mins) and the resulting samples were finally dispersed in the same buffer; 500  $\mu\text{L}$  of each of the samples was used for DLS analysis.

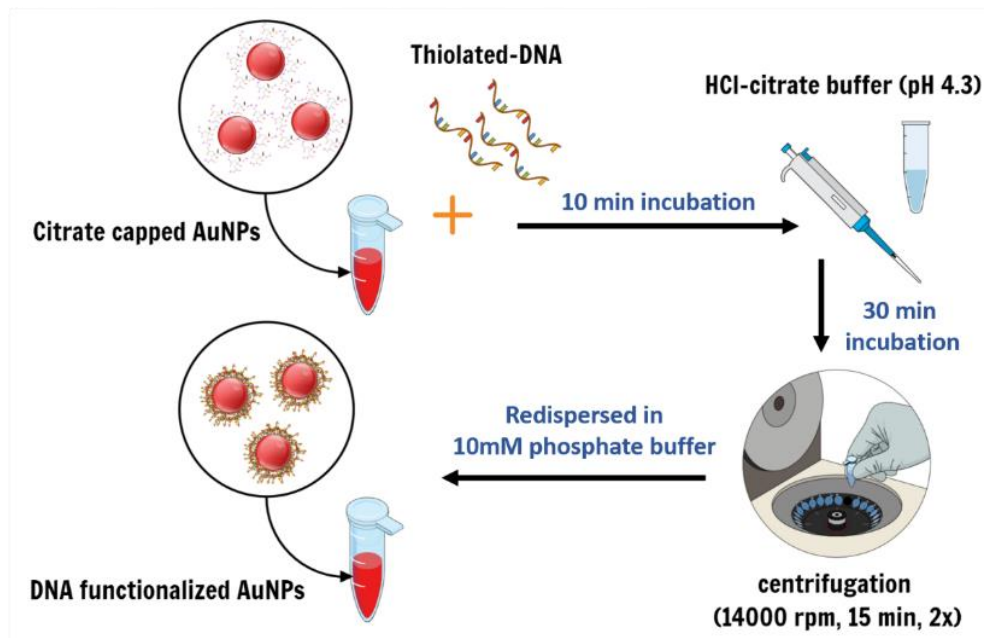


**Figure 23.3.** A cartoon illustrates of the ssDNA@AuNPs sample preparation steps using low pH assisted method.

### 3.4.6 Stability of ssDNA/TOEG6@AuNPs in a biological environment

AuNPs, and DNA/TOEG6@AuNPs were prepared and redispersed in a final volume of 500  $\mu\text{L}$  of diluted serum (1:1<sub>v.v</sub>) in Milli-Q water. Samples were incubated for 0.5, 4, and 24 h at room temperature and then analyzed spectrophotometrically in a range from 400 to 800 nm. A baseline correction using diluted serum with identical concentration was used.

### 3.4.7 Avidin interaction with Biotinylated AuNPs

An ssDNA/TOEG6@AuNPs sample was prepared as described previously and redispersed in the hybridization buffer. A complementary sequence of DNA labeled with biotin referred to as cF9-Biotin was introduced with 10x molar excess to the concentration of the DNA strands bound on AuNPs after dilution from the 100  $\mu\text{M}$  stock. The mixture was left to react for an hour at 25 °C under shaking. The supernatant was discarded after 15 minutes of centrifugation at 15,000 $\times g$ . The particles were washed with Milli-Q water, then redispersed in 400  $\mu\text{L}$  of the hybridization buffer.

Next, in a final volume of 500  $\mu\text{L}$ , various concentrations (2 to 100  $\mu\text{g}/\text{mL}$  of Avidin were added, followed by incubation for 40 min at 25  $^{\circ}\text{C}$ . Finally, the corresponding UV/Vis absorption spectrum was recorded.

### **3.4.8 Biofunctionalization of AuNPs with C8 nanobodies**

Target DNA strands conjugated with C8 nanobody referred to as C8-F9 were introduced to ssDNA/TOEG6@AuNPs nanosystem with a concentration of 100 nM to ssDNA attached to the AuNPs to guarantee the interaction with the C8. After an hour of incubation at room temperature with moderate shaking, the resulting NPs were characterized with UV/Vis spectroscopy, DLS as well as gel electrophoresis.

### **3.4.9 Dot blot immunological assay for detection of HER2 antigen**

Dot blotting is an excellent technique for measuring the amounts of a target antigen in several samples at once. It is also a popular method for mapping epitopes and screening antibodies for target specificity. In this work, dot blot was employed to test the binding between the anti-HER2 nanobody and the HER2-ECD antigen (**Figure 24.3**). To accomplish this, 3  $\mu\text{L}$  of C8-labelled AuNPs were slowly spotted on the center of a grid drawn on nitrocellulose membranes ( $3 \times 3 \text{ cm}^2$ ), stored for drying, and blocked with 5% bovine serum albumin (BSA) in PBST (1X PBS buffer + 0.01% tween) at room temperature for 60 mins to saturate aspecific binding sites on the membranes. Next, the saturated membranes were incubated at room temperature for 60 mins with 1:1000 diluted His-tagged HER2 ( $C_{\text{initial}} = 0.44 \text{ mg}/\text{mL}$ ) in PBS. The membranes were then washed with PBST buffer (3 times, 5 mins each) and incubated with 1:2500 diluted anti-His antibody conjugated with HRP ( $C_{\text{initial}} = 50 \text{ U}/\text{mL}$ ) for 60 mins at room temperature, washed thrice with PBST buffer (once for 15 mins, 2 times for 5 min each), followed by incubation with ECL western blotting reagent for 2 mins. Finally, the membranes were developed with chemiluminescence and analyzed using an ImageQuant<sup>TM</sup> LAS 4000 digital imaging system and the corresponding software. Membranes spotted with control samples, and C8-AuNP conjugates were prepared following the same protocol.

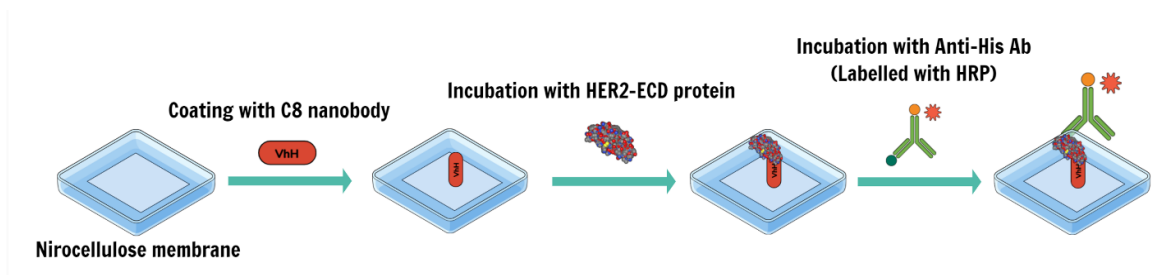


**Figure 24.3.** A schematic briefly illustrates the dot blot immunological assay used to qualitatively confirm the binding between C8 nanobodies and HER2-ECD antigen.

### 3.4.10 Detection of HER2 using Online TLS coupled with MGEC

As seen in **Figure 25.3A**, the MGEC electrophoretic channel ( $3 \times 50 \text{ mm}^2$ ) was fabricated using three PMMA Poly(methylmethacrylate) plates ( $25 \times 80 \text{ mm}^2$ ) by our collaborator Dr. Behnaz Asbaghi (Optics Lab at Abdus Salam International Centre for Theoretical Physics, Trieste, Italy). Briefly, with thickness of 3, 0.8, and 3 mm, bottom, middle, and cover plates respectively. They were cut using a CO<sub>2</sub> laser system (LVTC390/100W, Laser Veronese) and after that were attached using chloroform. The depth of the channel is 0.8 mm, whereas its length is 40 mm. One inlet hole for injecting the sample is located in the negative buffer reservoir named sample reservoir (SR) and the outlet hole is in the positive buffer reservoir named waste reservoir (WR). Before each analysis, the channel was filled with agarose gel (100  $\mu\text{L}$ ). To prepare the gel, a solution of 0.5% agarose in  $0.5 \times \text{TBE}$  (Tris-borate-EDTA) buffer was boiled in a microwave for 20 seconds. One minute after boiling, a 100  $\mu\text{L}$  of gel was injected in the channel using a micropipette. The polymerization process lasted 5 minutes. This handling procedure is schematically presented in **Figure 25.3B**. For the quantitative detection of the different amounts of HER2-ECD in solution, HER2-ECD (from 1 nM to 50 nM) was incubated with C8-decorated AuNPs for 60 mins at room temperature before being subjected to analysis. Then the buffer and the samples (75  $\mu\text{L}$  each) were carefully loaded into the WR and SR using a micropipette. For 5 mins, 150V is applied to the solution through Platinum electrodes connected to the power supply (BV140U, Eutro). After each run, the gel was removed from the channel using hot water bath.

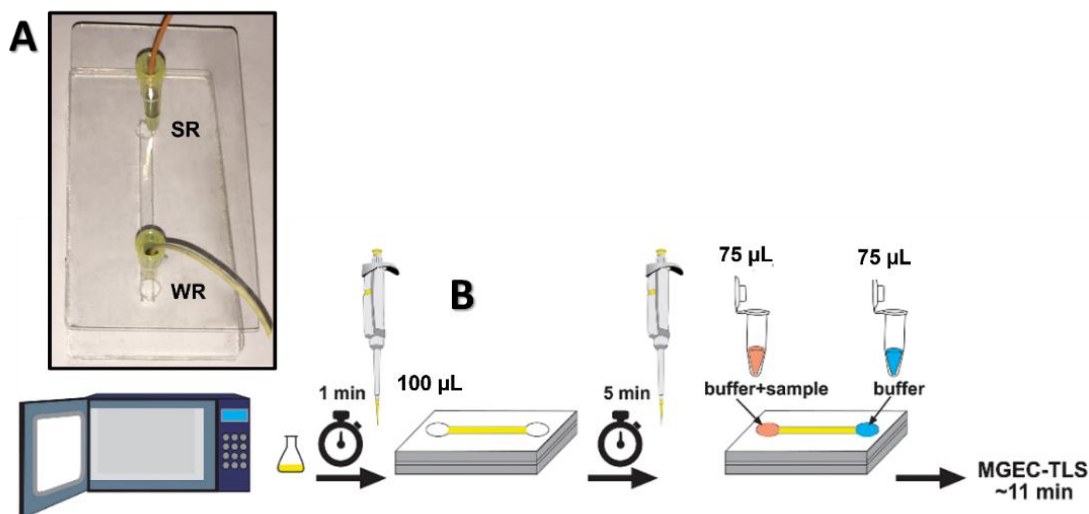


**Figure 25.3.** (A) digital Photograph of the MGEC. (B) scheme of handling procedure for loading the sample.

### 3.4.11 Investigating the interaction between ssDNA/TOEG6 coated AuNPs and lipid membranes

Liposomes alone and liposomes-encapsulated AuNPs were prepared following a protocol proposed by Thakur *et al* (Thakur *et al.*, 2018). Briefly, and as shown in **Figure26 .3**, 10 mg of DOPC and 0.5 mg of cholesterol were dissolved in 1 mL of chloroform and diluted up to 4 mL with diethyl ether. Then, 1 mL of AuNPs solution in 10 mM PBS (phosphate buffered saline) containing 20 µL of tween 80, was added to lipids solution and sonication at room temperature for 20 minutes was used to produce a water-in-oil emulsion. Afterward, using R-210 rotary evaporator system, organic solvents were evaporated in a vacuum environment at 38 °C until the gel phase disappeared. Finally, the water-dispersed liposomes were filtered through a 0.45 µm filter. The same protocol was also used to encapsulate ssDNA/TOEG6@AuNPs inside liposomes, in the absence of Tween 80.

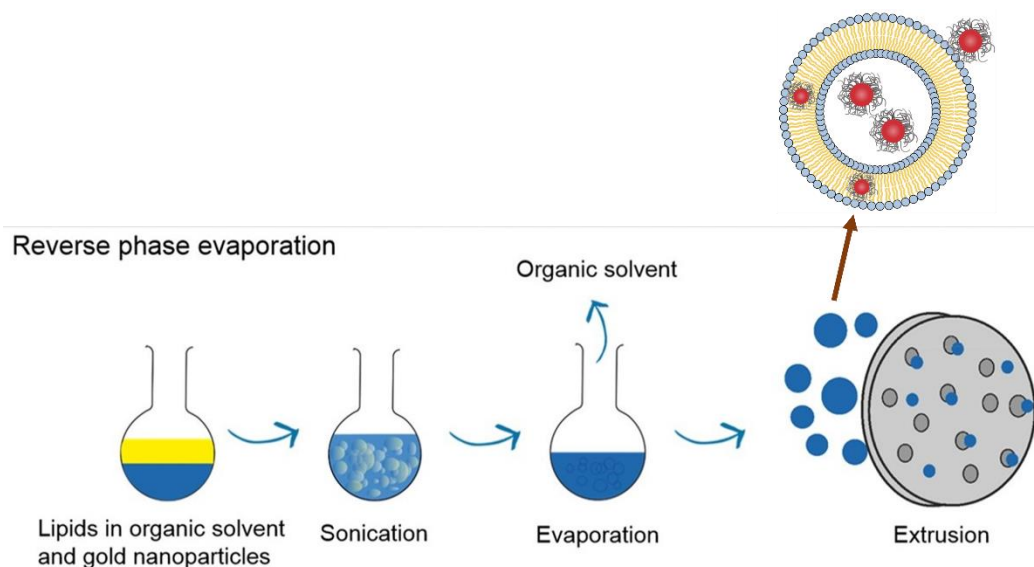


**Figure 26 .3.** Schematic of AuNPs–Liposome preparation using reverse phase evaporation method.

### 3.5 Functionalization of AuNPs: Click chemistry-based strategy

#### 3.5.1 Preparation of water-soluble alkyne-functionalized AuNPs

Functionalized AuNPs (alkyne/TOEG6@ AuNPs) were prepared as follows. the formation of SAM was performed at room temperature for 24 h by mixing a certain volume of as-prepared gold colloids ( $C_{\text{final}} = 2 \text{ nM}$ ) with an ethanol/water solution containing a 1:1 v/v ratio of excess of terminal alkyne- thiol and TOEG6 ligands. The mixture was then centrifuged to remove excess reagents and washed twice. The red precipitate was redispersed in 500  $\mu\text{L}$  of ethanol/water solution.

#### 3.5.2 Linking of azide modified molecules to the prepared particles

Copper-catalyzed azide–alkyne click cycloaddition (CuAAC) was carried out with the non-purified Alkyne-terminated AuNPs dispersion. As model compounds, the azide-modified dye (AF594-Azide) was clicked to the particles (see **Figure 27.3**): in a final volume of 1 mL, 2  $\mu\text{L}$  of AF594-Azide was added to 150  $\mu\text{L}$  of Alkyne modified NPs. Subsequently, a mixture of 2  $\mu\text{L}$  of 2 mM copper (II) sulfate and 1.77  $\mu\text{L}$  of 11.3 mM THPTA in Milli-Q water with a molar ratio of 1:5 was added. Finally, the addition of 1  $\mu\text{L}$  of 1 mM sodium ascorbate generated the Cu(I) complex in situ. The solution was vortexed and left to react overnight at room temperature. The Sample was then subjected to fluorescence analysis.



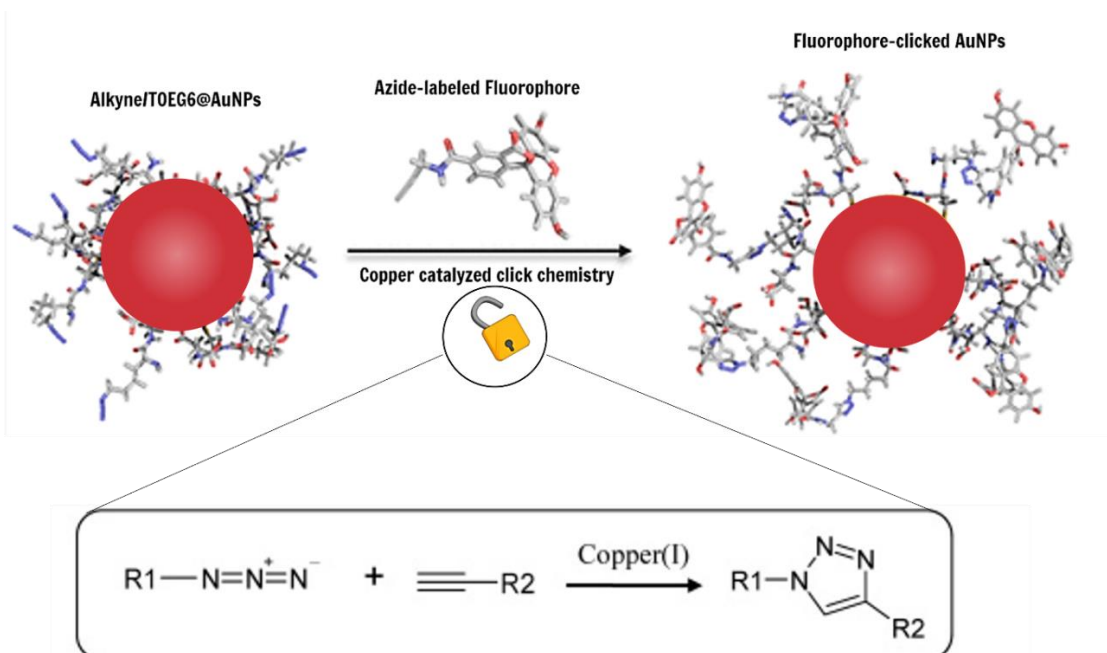


**Figure 27.3.** Coating of AuNPs with Alkyne/TOEG6 mixed-SAM, and linking of dye-modified azide to these nanoparticles using click chemistry. The figure is adopted and modified from (van der Meer et al., 2019).

### 3.5.3 TLS analysis of the clicked dye-AuNPs

A stock solution of azide-fluorescent dye (AF594), (5.8  $\mu\text{M}$ ) was prepared in MeOH solution. For detecting the effect of the dye on the thermal lens of AuNPs, various concentrations of AF594 (0-100 nM) were added to the functionalized particles along with the other components required for the click reaction in a final volume of 1 mL, the mixture was left to react overnight prior the measurement of the thermal lens at room temperature. The TLS, and MGEC-TLS system was aligned and optimized as will be described in section 3.6.7.

## 3.6 Characterization techniques

The formulation of nanoparticles is a procedure, which is always followed by their characterization. The parameters that need to be defined are the shape, size, distribution, surface modification, formulation of aggregates etc. Different techniques were used to characterize the as prepared AuNPs colloids, the functionalized AuNPs. These techniques are described in the following sections.

### 3.6.1 Ultraviolet/Visible (UV/Vis) spectrophotometry

Ultraviolet/visible (UV/Vis) spectrophotometry is used to measure how much a molecule absorbs at certain wavelengths when electrons are excited by electromagnetic radiation (Schmid, 2001). AuNPs have a sharp absorption band in the visible region, between 510 and 550 nm (Cai et al., 2008). The absorption of a molecule in a solution is determined by three main parameters which are molar extinction coefficient ( $\epsilon$ ), the concentration of the sample ( $c$ ) and the path length ( $l$ ), directed by Beer-Lambert's law as shown in the following equation:

$$A = \epsilon cl \quad (20.3)$$

The colloidal solutions were redispersed in the solvent of interest and then analyzed spectrophotometrically (Lambda 25 UV/vis spectrometer, PerkinElmer). The solutions were scanned between 400 and 800 nm. Before each scan the instrument was set to autozero by performing the baseline correction with a corresponding solvent (blank). Separate plastic cuvettes (1 mL, 10 mm path length) were used in all studies were used for each measurement.

### 3.6.2 Dynamic light scattering (DLS)

Dynamic Light Scattering is also known as Photon Correlation Spectroscopy. This is one of the most often used techniques for determining particle size. When a monochromatic light beam, such as a laser, is shone onto a solution containing spherical particles moving in Brownian motion, the light undergoes a Doppler shift, changing the wavelength of the incoming light. This variation is proportional to the particle's size. By measuring the particle's diffusion coefficient and utilizing the autocorrelation function, it is possible to compute the sphere size distribution and provide a description of the particle's mobility in the medium. This method has numerous advantages: first, the experiment is fast, and it is almost entirely automated, thus no prior experience is required for routine measurements. Furthermore, the development costs for this technology are relatively low. The majority of commercial "particle sizing" systems employ red light (675 nm), and operate at only one angle (90°). The influence on concentration is usually ignored in these systems. For all experiments in this thesis, DLS was performed on a Zetasizer Nano ZS (Malvern Panalytical, UK) (Figure 28.3) in backscatter mode. Measures were carried out on nanoparticle solutions in triplicate using 15 accumulating scans in disposable microcuvettes at room temperature.



**Figure 28.3.** Zetasizer Nano ZS used for DLS readouts.

### **3.6.3 Transmission Electron Microscopy (TEM)**

The transmission electron microscope (TEM) works on the same principles as a light microscope, except instead of light, it employs electrons. The wavelength of light limits the information obtained in a light microscope. TEMs use electrons as their "light source," and their significantly shorter wavelength allows for a thousand times higher resolution than a light microscope. A "electron source" located at the top of the microscope emits the electrons that flow through vacuum in the column of the microscope. In contrast to the light microscope, TEM uses electromagnetic lenses to focus electrons into a very narrow beam. The electron beam then passes through the specimen subjected to analysis. Depending on the density of the existing material, some of the electrons are scattered and vanish from the beam. At the bottom of the microscope the unscattered electrons hit a fluorescent screen, which gives rise to a "shadow image" of the specimen with its different parts displayed in varied darkness according to their density. The image can be examined directly by the operator or photographed with a camera (**Figure 29.3**). TEM measurements were performed on a Philips EM208 electron microscope operating at 100kV. Samples were prepared by casting 5 microliters of solution on 200 mesh carbon coated copper grids.

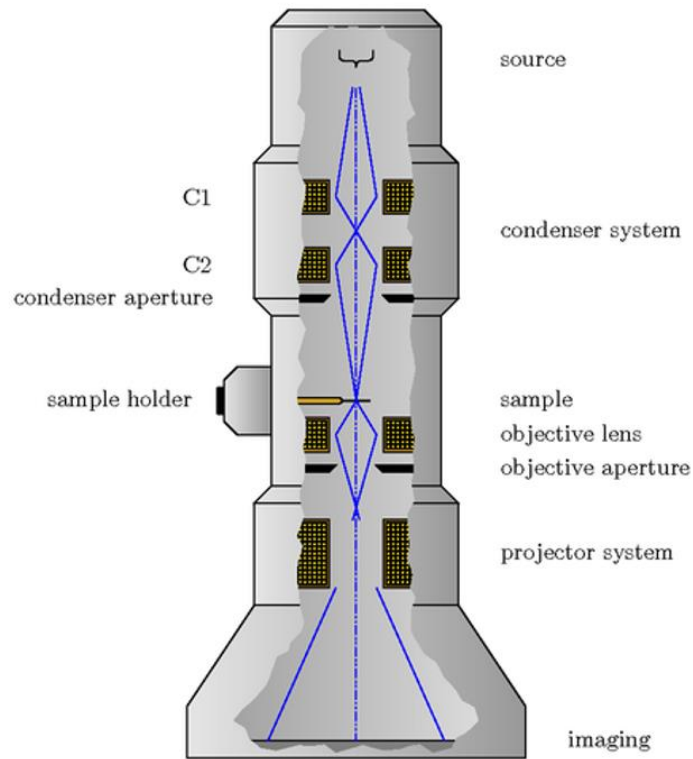


**Figure 29.3.** The schematic outline of a TEM.

### 3.6.4 Scanning Electron Microscopy (SEM)

The scanning electron microscope (SEM) generates a variety of signals at the surface of solid specimens using a focused beam of high-energy electrons. The signals generated by electron-sample interactions provide information on the sample's external morphology (texture), chemical composition, and crystalline structure and orientation of the materials that make up the sample. In most applications, data are collected over a selected area of the surface of the sample, and a 2-dimensional image is generated that displays spatial variations in these properties. Areas ranging from approximately 1 cm to 5 microns in width can be imaged in a scanning mode using conventional SEM techniques (magnification ranging from 20X to approximately 30,000X, spatial resolution of 50 to 100 nm). In a SEM, accelerated electrons carry a lot of kinetic energy, which is dissipated as a variety of signals caused by electron-sample interactions when the incident electrons decelerate in the solid sample (**Figure 30.3**). These signals include secondary electrons (that produce SEM images), backscattered electrons, diffracted backscattered electrons (that are used to determine crystal structures and orientations of minerals, photons that are used for

elemental analysis and continuum X-rays), visible light and heat. Secondary electrons and backscattered electrons are both often employed to image samples: secondary electrons are most valuable for displaying morphology and topography on samples, while backscattered electrons are superior for highlighting compositional contrasts in multiphase samples (i.e., for rapid phase discrimination). Inelastic collisions of incoming electrons with electrons in discrete orbitals (shells) of atoms in the sample produce X-rays. When excited electrons return to lower energy states, they emit X-rays with a specific wavelength (that is related to the difference in energy levels of electrons in different shells for a given element). As a result, each element in a mineral that is "excited" by the electron beam produces distinct X-rays. SEM images were acquired with a ZEISS FEG-SEM Supra 40. Imaging was performed at 5-10 keV of acceleration voltage by detecting electrons with an Everhart Thornley Secondary Electron Detector and a High efficiency In-lens Detector. For the preparation of the SEM samples, 0.5-1 cm pre-cut pieces of Si (111) wafer were cleaned by sonication in acetone and isopropanol. Then, a drop of Poly-Ornithine was added, to facilitate the capture of nanoparticles via electrostatic charges. After removing the excess of poly-ornithine by a thorough washing step with Milli-Q water, we deposit 15  $\mu\text{L}$  of nanoparticles and incubated for 15 minutes. The sample was then washed with Milli-Q water, dried with a gentle nitrogen stream and promptly inserted in the SEM chamber for measurements.

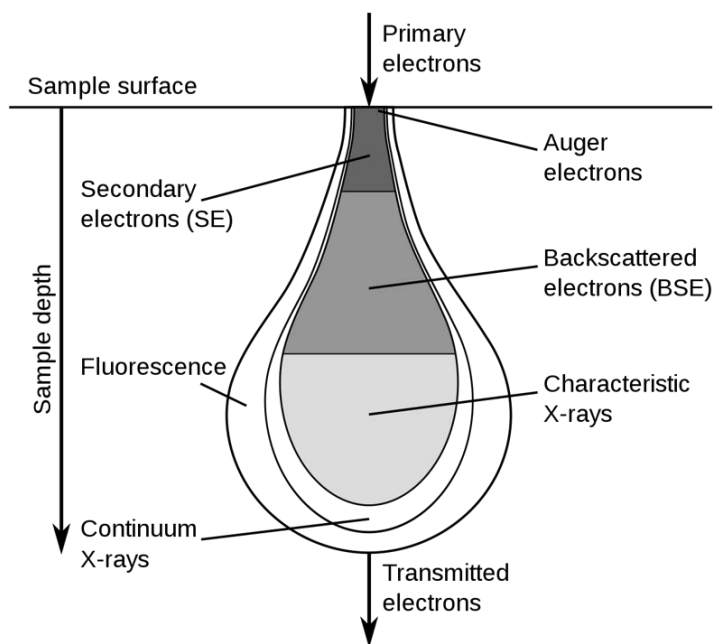


**Figure 30.3.** SEM electron-sample interactions.

### 3.6.5 Atomic Force Microscopy (AFM)

AFM provides images with nearly atomic resolution by measuring the sample's surface contour. By quantifying the forces between the probe (an ultra-small probe tip at the end of a cantilever) and the sample, AFM can produce incredibly high-resolution images. A typical AFM instrument is comprised of four components: a nanoscope controller, a computer with control and display, a multimode, and two monitors. The multimode is the AFM's most important component. It is equipped with an optical head, a removable scanner, and a multimode base. The probe, the laser and photodiode array, and the adjustment knobs used to align the system are all housed in the head. Generally, the sample is placed on top of the scanner containing the piezotube which controls the movement of the sample. The base has controls for raising and lowering the probe, a mode selector switch and a digital display (**Figure 31.3A**).

The main difference between AFM and light microscope is that the former employs a cantilever, composed of silicon or silicon nitride with a very low spring constant to image a sample, instead of visible light. At one end of the cantilever, a very sharp tip is fabricated using semiconductor processing techniques. The cantilever scans over the surface of the sample by progressively moving backward and forward across the surface. A piezoelectric crystal raises or lowers the cantilever to maintain a constant bending of the cantilever. The force exerted on the tip varies depending on the difference in surface height, causing the cantilever to bend. A laser beam is constantly reflected from the top of the cantilever towards a position-sensitive photodetector made up of four photodiodes arranged side by side. This laser beam detects the bend in the cantilever and calculates the cantilever's real position. Thus, AFM records a three-dimensional image of the surface topography of the sample under a constant applied force, which provides a maximum resolution image without causing any damage to the sample surface (non-contact mode). As the tip scans the surface of the sample, the force between the tip and the sample varies. This change in force is detected by the tip attached to the flexible cantilever. The amount of force between the probe and the sample is dependent on the spring constant of the cantilever and the distance between the probe and the sample surface.

Nanoparticle-AFM based image requires the particle to be rigidly anchored to AFM substrate which is virtually known to be mica. As presented in **Figure 31.3B**, the deposition of AuNPs on AFM substrate was done as following; The mica substrate was freshly cleaved and directly coated with 10  $\mu$ L of poly-L-ornithine solution. After 3 min of incubation, the surface of the mica was

rinsed with 400  $\mu\text{L}$  of Milli-Q and dried under the flow of nitrogen. 25  $\mu\text{L}$  of sample suspension (diluted 1:50) was spotted on the mica modified surface, allowed to react for approximately 5 min, rinsed off with Milli-Q followed by nitrogen for complete dry. Imaging was recorded with Asylum research MFP-3D AFM operating in non-contact mode. The n-type silicon tip with 8 nm radius and cantilever with  $110 \pm 5 \mu\text{m}$  length,  $32.5 \pm 3 \mu\text{m}$  width,  $1 \pm 0.5 \mu\text{m}$  thickness, force constant of 1 N/m and resonance frequency of approximately 90 kHz was used.

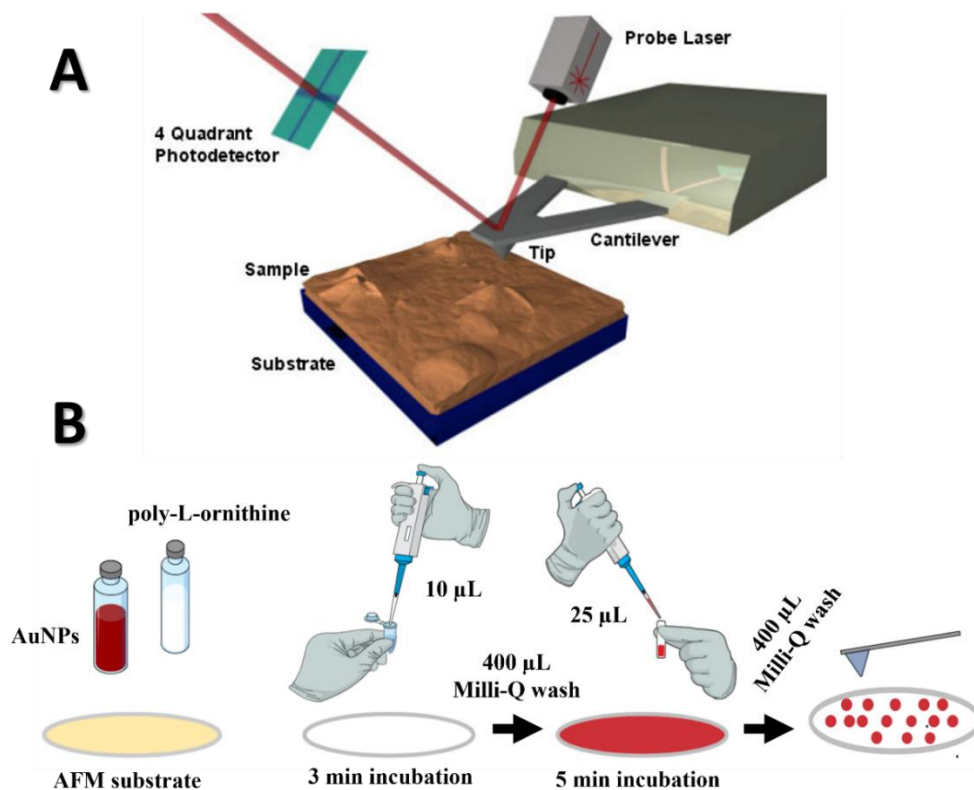


**Figure 31.3.** (A) and schematic diagram of an AFM. (B) Sample preparation used for Nanoparticle-AFM imaging.

### 3.6.7 Thermal Lens Microscopy (TLS)

As described in *Chapter 2*, TL sensitivity is much higher than that of the conventional transmission or reflection measurements. The reason of the remarkable sensitivity is due to the so-called enhancement factor ( $E = [P(\partial n/\partial T)/\lambda k]$ ) (Dovich & Harris, 1979). The unique features of TLS have been exploited either to further increase its sensitivity or to use it for sensitive and accurate determination of thermal physical properties of a variety of substances including solids, liquids,

and gases. In our context, upon light excitation at the SPR resonance, AuNPs experiences a localized energy-to-heat conversion **Figure 32.3A**). Due to the temperature gradient generated around the AuNPs, there are subtle variations in the refractive index of the surrounding medium and ultrasensitive technique such as Thermal Lens Spectrometry (TLS) can be particularly useful in detecting them (Miti et al., 2020). Considering all these facts and the high extinction coefficient of AuNPs, TLS represents a particularly viable route for the sensitive detection of DNA functionalized on AuNPs embedded in a gel microchannel. This was the motivation for constructing a more sophisticated detection platform that provides the desired sensitivity to discern the small difference of electrophoretic mobility as well as photothermal properties of bio-nano conjugates.

We used MGEC in the experimental setup to build up MGEC-TLS systems as shown in **Figure 33.3**. Basically, in this system a 532 nm diode-pumped solid-state laser (DPSS) (MGL-III- 532 nm-100, Ultra-Lasers) of maximum power 100 mW is used as an excitation source (EL). A signal generator (SG) (Rigol DG 2041A, Batronix) modulates the EL at a frequency of 118 Hz. A neutral density filter (NF) (NDC 50S-3, Thorlabs) is placed after the EL to adjust its power to 15 mW. The excitation beam coming from the EL is first collimated by the lens L1 (LB1027-A,  $f = 40$  mm, Thorlabs) and L2 (LB1676-A,  $f = 100$  mm, Thorlabs). After that, the beam is focused onto the MC or MGEC channel using a 0.25NA focusing objective (OL) (LMH-10X-532, Thorlabs) or the lens (LB1811-A-ML,  $f = 35$  mm, Thorlabs), respectively. The radii of the excitation beam (2.6  $\mu\text{m}$ , 10  $\mu\text{m}$ ) were measured using a commercial dual scanning slit beam profiler (BP209-VISM, Thorlabs). The variable iris (I) enabled to match the size of the excitation beam with the aperture of the microscope objective (MO). The probe laser (PL), a He-Ne laser (05-UR-111, 2 mW, Melles Griot), is collimated by a set of lenses L3 (LB1027-A,  $f = 40$  mm, Thorlabs) and L4 (LB1676-A,  $f = 100$  mm, Thorlabs) and directed to the sample using the mirrors M3 and M4. Then the beam is directed to a Silicon detector (PD) (PDA 36A-EC, Thorlabs) across a 0.5 mm pinhole (P) and an interference filter (F2) (632.8 nm, MELLES GRIOT). The 532 nm filter (F1) was used for removing any residual emission of the fundamental wavelength 1064 nm. The analog signal from the photodiode is filtered and amplified using a lock-in amplifier (SR5 10, Stanford Research System) and further digitalized at 1 k samples/s sampling rate. The data acquisition system mainly consists of a microcontroller-based digitization Arduino board (Mega 2560) and a graphical user interface (GUI) running on a PC. The GUI was build using the LabVIEW graphical programming



software to visualize the incoming data, capture the TLS signal (peaks) and online recording of data. Additionally, a CMOS color camera (C) (acA2440-20gc, Basler) is used for visualizing and adjusting the channel position at the working distance of the objective lens. The image of the microfluidic channel is projected on the CMOS camera by the tube lens (TL) using the probe light as illumination. A power supply (EPS) (BV140U, Eutro) is used to supply the desired voltage for electrophoretic nanoanalysis of NPs in the MGEC.

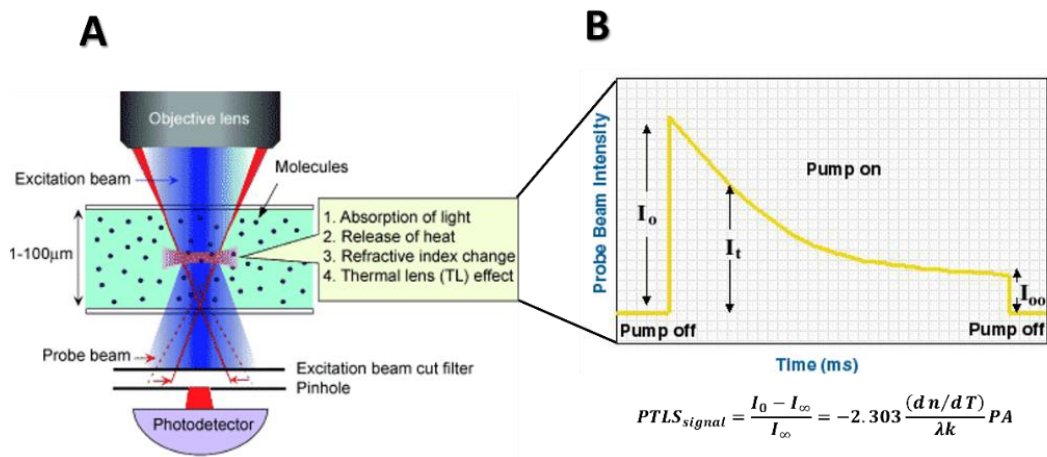


**Figure 32.3.** (A) A schematic illustration of the mechanism of TL effect. (B) Typical TL signal thermal lens signal generation.

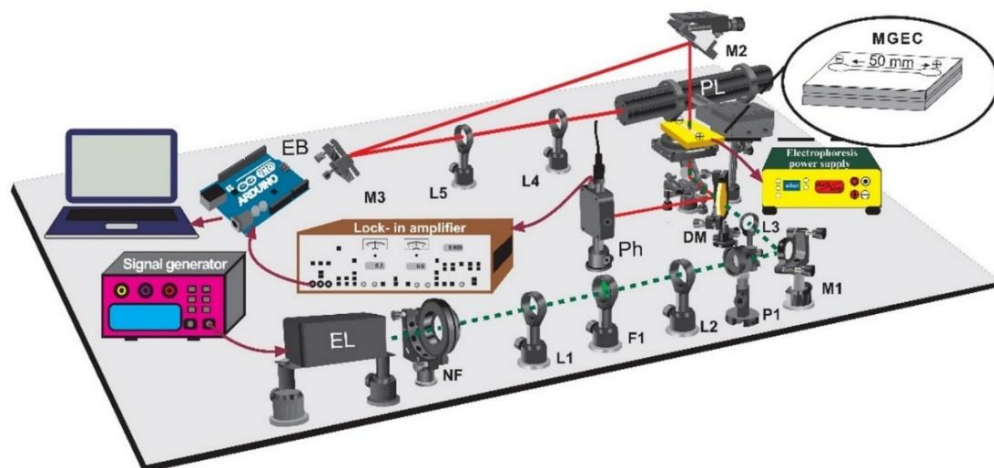


**Figure 33.3.** Schematic illustration of the pump-probe photothermal lens setup. EL: excitation laser, PL: probe laser, C: CMOS camera, PD: photodiode, NF: neutral density filter, L1 to L4: lenses, M1 to M4: mirrors, DM: dichroic mirror, OL: focusing objective, P: pinhole, F1: 532 nm filter, F2: 632.8 nm filter, I: iris, BS: beam splitter, TL: tube lens, SG: signal generator, LA: lock-in amplifier, EPS: electrophoresis power supply.

### 3.6.8 Gel electrophoresis

Gel electrophoresis is a popular technique for separating macromolecules like DNA, RNA, and proteins in life science labs. Molecules are separated using this method based on their size and electric charge. The sample to be separated is loaded on to a porous gel placed in an ionic buffer medium. Upon application of electric charge, each molecule having different size and charge will move through the gel at different speeds. This approach uses a porous gel to act as a molecular sieve, separating larger molecules from smaller ones. Smaller molecules move through the gel faster, whereas larger molecules are left behind. The particular electric charge of the particles also influences their movement. On the basis of their charge, two oppositely charged electrodes in the system pull molecules towards them. In many cases, the gel used in gel electrophoresis is formed of agarose, a gelatinous substance produced from seaweed. This porous gel has the potential to separate macromolecules of various sizes. In an electrophoresis chamber, the gel is submerged in a salt buffer solution. The running buffer is usually tris-borate-EDTA (TBE) or tris-acetate-EDTA (TAE). Its main purpose is to keep the system's pH in control. At each end of the chamber are two electrodes, one positive and the other negative. With the use of a pipette, samples that need to be analyzed are loaded into tiny wells in the gel. After the loading is complete, a 50–150 V electrical current is applied (**Figure 34.3**). At this point, charged molecules in the sample begin to migrate through the gel towards the electrodes. Positively charged molecules migrate to the negative electrode, while negatively charged molecules migrate to the positive electrode. The gel is stained with a dye to reveal the separation bands once the separation is complete. Ethidium bromide is regularly used fluorescent dye in gel electrophoresis. To see the separation bands, the gel is soaked in a diluted ethidium bromide solution and then placed on a UV transilluminator. The bands are promptly photographed for future reference, as they will diffuse into the gel over time. The dye can also be loaded into the gel well in advance to track the migration of the molecules as it happens. Samples prepared for the electrophoretic mobility investigations were centrifuged as indicated, washed, then pellets were collected, mixed with 10% glycerol in a final volume of 50  $\mu\text{L}$ , and loaded onto a 1% agarose gel, run at 80 V for 30 mins in 1x TAE buffer. Since the AuNPs are colored and their movement could be traced in the gel, there was no need to mix a tracking-dye with them.

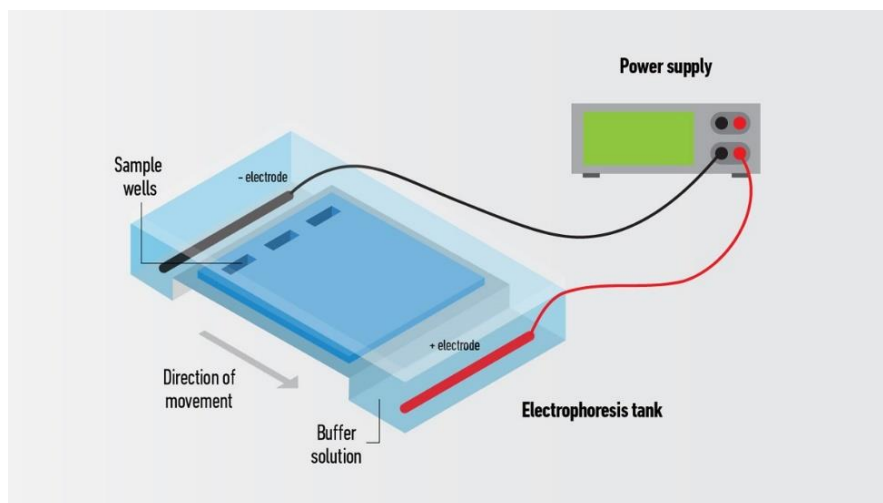


**Figure 34.3.** Diagram of an agarose gel electrophoresis apparatus.

### 3.6.9 Fluorescence intensity measurements

Fluorescence is the phenomena that occurs after fluorophores absorb light. After absorbing light, the electron of the fluorophore molecule is excited to a higher energy state. This is followed by vibrational relaxation to the excited state's lowest level. Finally, the electron returns to its ground state by emitting fluorescence energy (**Figure 35.3A**). Sir G. G. Stokes demonstrated for the first time that the energy of light released by a fluorophore is always less than the energy of absorption (i.e., longer wavelength) due to energy loss at the vibrational state. The Stokes shift is the name given to this phenomenon. Then, the conjugation of azide-modified dyes (red-fluorescent Alexa Fluor® 594 azide), as model compounds, to gold nanoparticles was performed. To assess the fluorescence intensity and the possible quenching due to the click reaction, a 96-well plate was used in the experiments. The overall volume in each well was 50  $\mu\text{L}$  containing a solution of clicked AuNPs. The plate was incubated at room temperature for 30 min before measurements with microplate reader (Tecan, Infinite F200 Pro) A filter excites at 535 nm and emits at 590 nm was used **Figure 35.3B**.

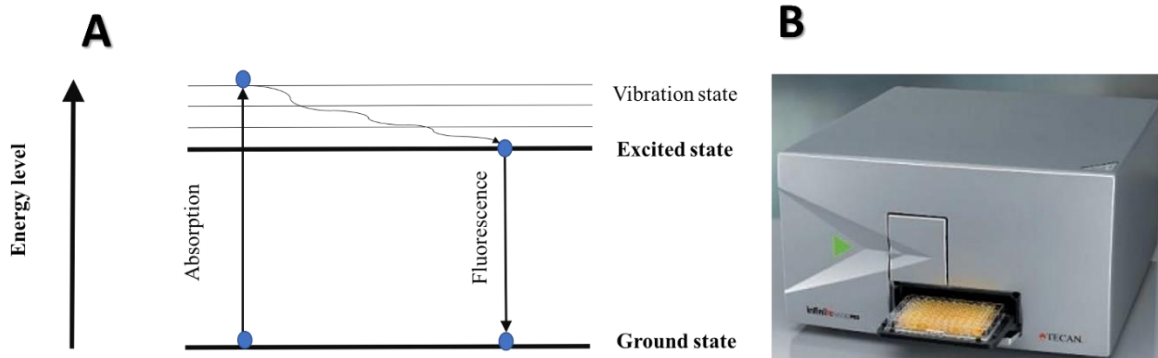
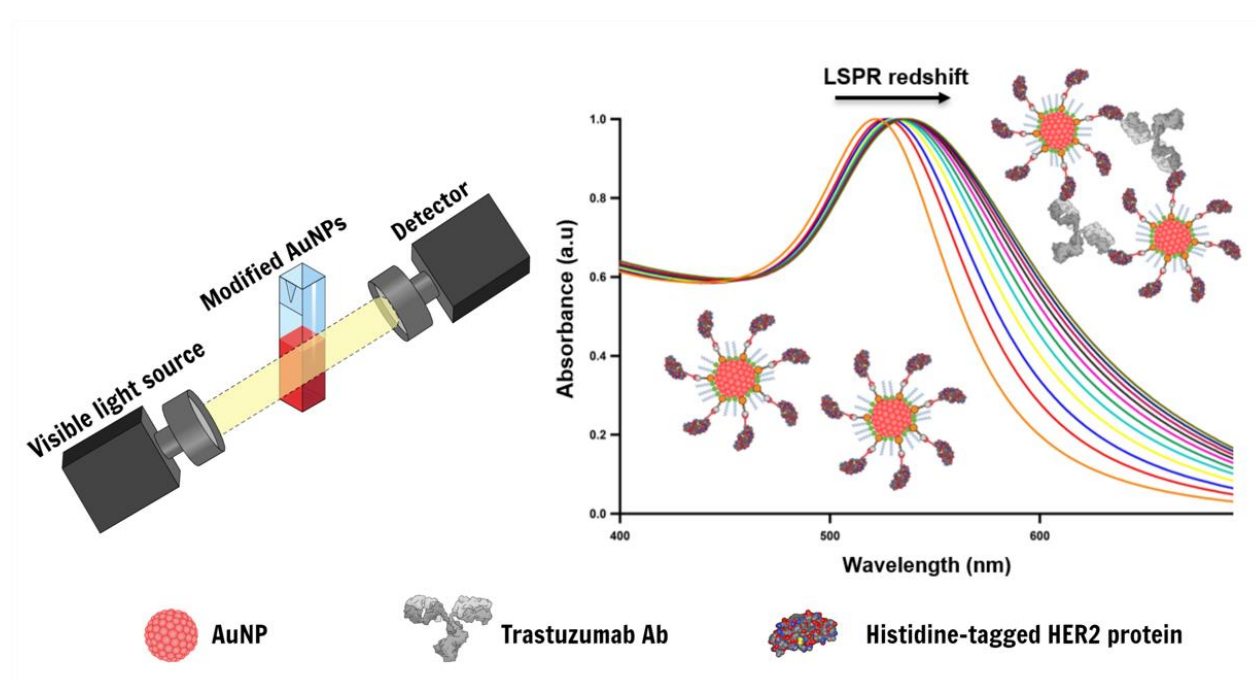


**Figure 35.3.** (A) A schematic depicts the fluorescence phenomena in a simplified Jablonski diagram. (B) The Infinite F200 PRO multimode microplate reader.

## Results and Discussion

### Development of plasmonic based-assay for trastuzumab Quantification

**Disclosure:** This chapter is a slightly modified version of the publication: Label-free, Rapid, and Facile Gold-Nanoparticles-Based Assay as a Potential Spectroscopic Tool for Trastuzumab Quantification. Alsadig, Ahmed, et al. *Nanomaterials* 11.12 (2021): 3181(Alsadig et al., 2021). The preparation and characterizations were carried out following the protocols described in section 3.2.



#### 4.1 Motivation

Trastuzumab is one of the most used monoclonal antibodies in HER2 positive gastric and breast cancer therapy, and more recently in several metastatic cancers. It has been shown that controlling the effective concentration of trastuzumab during therapy is crucial to optimize clinical benefits and to decrease other risks associated to the therapy itself, as for instance cardiac failure. The development of a simple, cost-effective, and sensitive biosensor to monitor the functionality and the concentration of trastuzumab is therefore highly desirable.

## 4.2 Introduction

In 1998, the Food and Drug Administration (FDA) approved the use of trastuzumab in immunotherapy due to its potential inhibitory function to increase the overall survival in HER2-overexpressed metastatic cancers such as gastric and breast cancers (Hudis, 2007; Nahta et al., 2004; Orlova et al., 2009). Although trastuzumab has improved the clinical outcomes, several studies have reported an increased risk of cardiac failure in patients who received trastuzumab in combination with chemotherapeutic agents (Ewer et al., 1999; Jerusalem et al., 2019). Recent studies have shown that the concentration of trastuzumab delivered to patients at the beginning of the course of a treatment has a direct impact on the overall survival (González García et al., 2020). It was demonstrated that trastuzumab did not show the desired clinical benefit in HER2-positive gastric cancer patients when the effective concentration of trastuzumab was less than 20  $\mu\text{g}/\text{mL}$  in the blood plasma after the first administered dose (Cosson et al., 2014). At the same time, the pharmacokinetics of trastuzumab is complicated, since the overexpression of HER2 can vary, and the antibody can also bind to the HER2-ECD that is shed from HER2 into the bloodstream.

Up to now, the quantification of trastuzumab has remained restricted due to the limited capabilities of the available analytical techniques, which are either laborious or not accessible to all laboratories. For instance, B. Cardinali *et al.* reported the development of a sandwich ELISA protocol to quantify the trastuzumab concentration in serum using a peptide that mimics the HER2 epitope (Cardinali et al., 2014). The study demonstrated the ability to detect antibody concentrations from 10 to 180  $\mu\text{g}/\text{mL}$  in serum. However, despite the appeal, a commercial production of this peptide does not seem within reach. As an alternative to ELISA, high-performance liquid chromatography (HPLC) coupled to tandem mass spectrometry (MS/MS) was described by C.W.N. Damen *et al.* The presented assay quantified trastuzumab from 5 to 40  $\mu\text{g}/\text{mL}$  in human serum with accuracies  $<20\%$ , which is complex and requires a particular extraction procedure from human serum (Damen et al., 2009). Based on that, the development of a simple, cost-effective, and sensitive biosensor to monitor the functionality and the concentration of trastuzumab is highly needed.

Biosensors that harness the plasmonic properties of noble metal nano-constructs have fascinated researchers and received considerable attention as alternatives to conventional signal transduction modalities (Cetin et al., 2014; Kailasa et al., 2018; Tseng et al., 2017). Among them, localized surface plasmon resonance (LSPR) sensors, which employ metal nanoparticles (e.g., gold or

silver), are increasingly used due to the presence of highly localized electromagnetic fields at the nanoparticle surfaces, which renders them hypersensitive to external environments (Anker et al., 2010). Lately, gold nanoparticle (AuNP)-based nanosensor mechanisms are considered a rising hope for fabricating smart sensors (Jin et al., 2003; Swartz et al., 2011; Ventura et al., 2020). Since these nanoparticles possess a high surface-to-volume ratio, any tiny perturbation caused within the surroundings can be verified by a spectral shift of their surface plasmonic band. Another advantage of AuNPs is their robust reactivity with thiolated ligands. This allows for surface functionalization that can be specifically geared to detect targets of interest.

The immobilization of biomolecules, including proteins, on 2D or 3D substrates has become a crucial process to develop biosensors (Mohamad et al., 2015; Rusmini et al., 2007). While maintaining the functionality of proteins, directed immobilization can be achieved by using affinity-based techniques between a tag and a biocompatible surface. Nitrilotriacetic acid (NTA)-modified materials is a widely adopted technology for the purification and isolation of histidine (His)-tagged recombinant proteins in the presence of  $\text{Ni}^{2+}$ ,  $\text{Cu}^{2+}$ , and  $\text{Co}^{2+}$  ions as chelating agents (Mori, Shinohata, et al., 2003; Mori, Takahashi, et al., 2003; Terpe, 2003). The high affinity of His-tagged protein–NTA interactions and the facile disruption of the complex make NTA highly useful for various applications, including protein purification, labeling, specific immobilization, and the construction of advanced functional materials (Chao et al., 2017; Crowe et al., 1995; Khan et al., 2006).

In this work, we aim to explore the use of AuNPs coated with a self-assembled mixed monolayer (mixed-SAM) of NTA-modified and oligoethylene glycol (OEG)-modified alkylthios. The novelty of the present work lies in the particle functionalization strategy that offers: (1) excellent dispersion stability and proper biorecognition endowed by the mixed SAM containing smaller molecules in comparison with bulky PEGylated ligands, (2) the possibility of finely tuning AuNP surface loading to meet the expectation of various bio-applications, and (3) a much faster sample-to-answer LSPR-based plasmonic platform than the lengthy incubation protocols used in ELISA assays. In our design, antibody recognition results in forming a nanoparticle network thanks to the capability of antibodies to link one protein at each arm, leading to plasmonic coupling of the particles that can readily be detected by optical spectroscopy (Arcas et al., 2021; El Alami et al., 2020). Thus, such an optical readout system could be implemented in affordable point-of-care devices to aid personalized therapies or more sophisticated high-throughput clinical analysis

settings. As a proof of principle, in this study, we selected the His-tagged HER2 antigen for the selective detection of trastuzumab.

## 4.3 Results and discussion

### 4.3.1 Characterization of Synthesized AuNPs

Most commonly, AuNPs are synthesized using the reduction of the soluble gold salt ( $\text{HAuCl}_4$ ) in the presence of capping agent such as sodium citrate, a compound able to attach to the nanoparticle surface, preventing its growth beyond the desired size and conferring stability of the colloid in the solvent used. The particle shape and dimensions can be controlled by tuning the experimental parameters, such as the reaction time, temperature, and most importantly, the ratio between the reducing agent used and gold precursor. The UV/Vis spectrum, as shown in **Figure 36.4**, of AuNPs synthesized using the citrate reduction method and the corresponding TEM of citrate-capped AuNPs exhibited a maximum absorption at 518 nm, consistent with the typical SPR band of AuNPs. This renders a colloidal solution of spherical AuNPs, which is visibly red in color. The TEM in **Figure 36.4** revealed a size distribution of the resulting nanoparticles of  $13 \pm 1$  nm, while the DLS measurements showed that the particles have an average diameter of  $15 \pm 6$  nm (see **Appendix 1**), which is compatible with the AuNP size considering the hydration shell. The selected diameter size (13 nm) was based on finding a compromise between having a significant loading of biorecognition sites while maintaining the advantages of the small size.

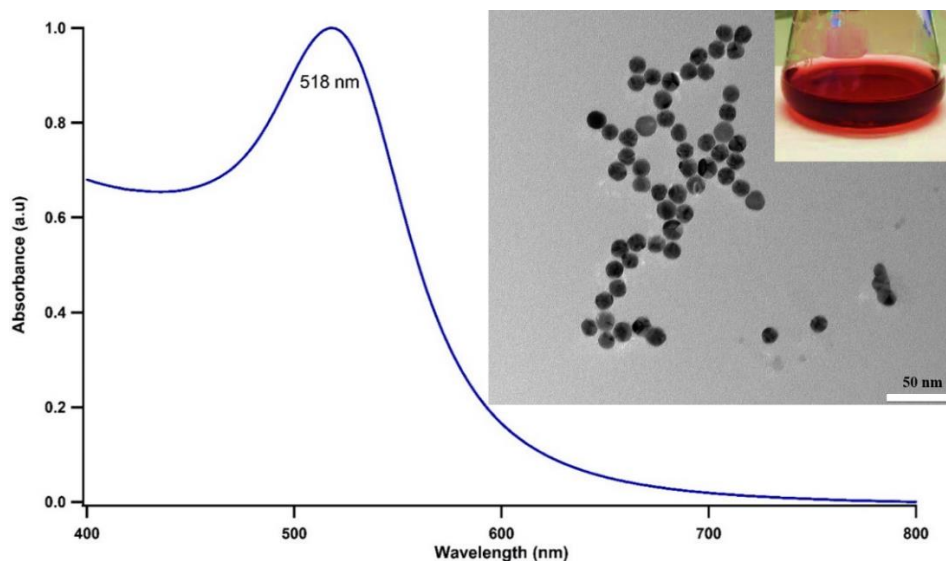


**Figure 36.4.** UV/Vis spectrum of AuNPs synthesized using citrate reduction method and the corresponding TEM micrograph. Red color of the solution confirmed the production of AuNPs.



### 4.3.2 Passivation of AuNPs with NTA/TOEG3 SAM

The variety of applications of NTA-based technology in the purification, immobilization, and separation of His-tagged macromolecules is unparalleled. The incorporation of the NTA moiety on nanosized particles was reported by Xu *et al.*, demonstrating the ability of these nanoparticles to chelate to bidentate Ni<sup>2+</sup> or Co<sup>2+</sup> cations (Xu *et al.*, 2004). Later, Chen *et al* further employed this strategy by incorporating Ni-NTA onto superparamagnetic particles to enrich His-tagged proteins and other phosphorylated peptides (Li *et al.*, 2007). Sosibo *et al* reported the synthesis of stable, hydrophilic monolayer-protected clusters of gold (Au-MPCs) functionalized with PEG-NTA and co-stabilized with PEG--OH as probes for targeting histidine-tagged proteins (Sosibo *et al.*, 2007). It was demonstrated that it is crucial to incorporate a spacing ligand, forming a mixed monolayer onto the particle surface to enhance the long-term stability of NTA-functionalized nanoparticles. However, long PEGylated alkylthiol might hinder the plasmonic effect we would like to exploit for high sensitivity biorecognition (see **Appendix 1**). In the present study, in a single-step reaction, the shorter NTA/TOEG3 were made self-assembling onto AuNPs via the ligand place exchange approach of the loosely bound citrates capping the colloidal surface. TOEG3 was chosen as the spacing ligand due to its high hydrophilicity that promotes favorable interactions with the gold colloids. Besides, TOEG3 acts as a protein-repellent thiol, reducing the risk of the nonspecific adsorption of biomolecules onto AuNP surfaces, as already demonstrated in our group on flat Au surfaces (Sanavio *et al.*, 2010). In previous studies on AuNPs, however, it was reported that short-chain OEG thiols with  $\leq 4$  EG units can stabilize only a suspension of small AuNPs (10 nm), OEG thiols  $<6$  EG units were found to be insufficient to stabilize the colloids (Schollbach *et al.*, 2014). Contrastingly, from our UV/Vis absorption measurements reported in **Figure 37.4**, we found that, starting from the concentration of 5  $\mu\text{M}$ , TOEG3 successfully prevented a 2 nM solution of 13 nm diameter AuNPs from aggregation. In this condition, we assumed a fully covered SAM was formed on the nanoparticle. As a starting point for the formation of mixed, functional SAM, we then used a 50:50 concentration of NTA and TOEG3-terminated alkylthiols and 2.5  $\mu\text{M}$  of NTA plus 2.5  $\mu\text{M}$  of TOEG3 to form a homogenous and stable mixed SAM onto the AuNP surface. The successful ligands attachment was confirmed by the 3 nm redshift in the UV/Vis spectrum, as shown in **Figure 38.4**. Gel electrophoresis revealed a slower mobility of NTA/TOEG3 than only NTA (see **Figure 38.4** for the discrepancy)-coated particles, indicating surface modification of the particles towards the formation of a mixed

monolayer of the dissimilar ligands that are covalently bonded to AuNP surfaces. This finding also demonstrates the potential of agarose gel electrophoresis to confirm the SAM formation of charged SAMs on the surfaces of the AuNPs.

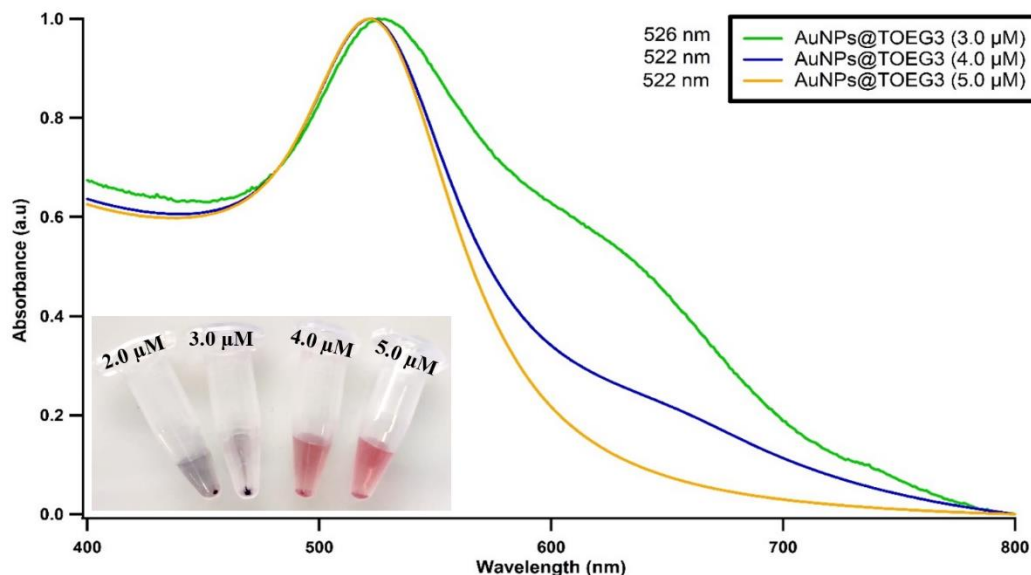


**Figure 37.4.** UV/Vis absorption spectra of AuNPs coupled with different concentrations of TOEG3. The blue color indicated that the TOEG3 was insufficient to cover the surface of particles. Once a sufficient amount is used, the colloidal solution does not form agglomerates and the red color is maintained.

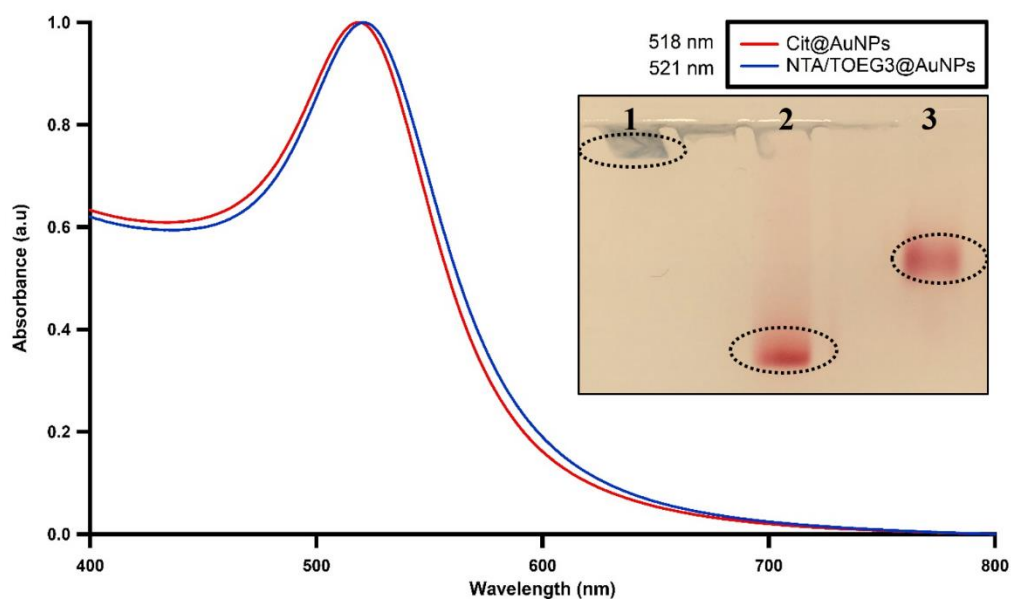


**Figure 38.4.** UV/Vis spectra of citrate- and protected AuNPs to monitor surface modification. Inset: Gel electrophoresis bands for (1) citrate capped AuNPs, (2) NTA@AuNPs, (3) NTA/TOEG3@AuNPs.

### 4.3.3 Incorporation of Co<sup>2+</sup> and Immobilization of the His-Tagged HER2

To detect trastuzumab, the His-tagged HER2 protein was first anchored on the AuNPs surface based on the Co(II)–NTA complexation strategy depicted in **Figure 20.3**. The quadridentate NTA ligand occupies four coordination positions on the hexadentate central cobalt cation, allowing for the availability of the two vacant binding sites for the His-tagged biomolecules to attach. Following the reaction of the modified AuNPs with excess CoCl<sub>2</sub>, there was no observable change in the optical properties of the particles, as verified by UV/Vis spectroscopy.

It is noteworthy that controlling the reaction time and the concentration of CoCl<sub>2</sub> is crucial to prevent any agglomeration of the particles. When the Co<sup>2+</sup> concentration is high, particles form visible aggregation during the purification process, likely because of the formation of polynuclear Co–NTA complexes instead of well-defined mononuclear ones that may trigger NP aggregation, while, if the Co<sup>2+</sup> concentration is too low, there are not enough ions on the particles to conjugate enough proteins on the particle surface. However, in our study, incubating with 10 mM of CoCl<sub>2</sub> for 1 h was ideal to charge the particles without causing any agglomeration.

Upon the introduction of the His-tagged HER2 protein, the resultant bioconjugates were readily soluble in the solvent buffer and showed the typical red color of the gold colloids. While the UV/Vis absorption spectra remained identical to that of the NTA/TOEG3-modified particles spectrum, the DLS readouts confirmed the successful functionalization upon each step of preparation (**Figure 39.4**). This is not surprising, given the different principles of both techniques. Whereas UV/Vis spectrophotometry relies on detecting changes in the optical properties reflected in LSPR, DLS can reveal differences in the particle hydrodynamic diameter size upon functionalization that do not necessarily cause observable variations in the overall optical properties.

### 4.3.4 Detection of trastuzumab by LSPR in Buffer

After demonstrating that trastuzumab binds to the His-tagged HER2 protein receptor using indirect ELISA (**Figure 40.4**), the sensing capability of our platform was then tested by monitoring the LSPR shifts induced by the immunoconjugate recognition across a wide range of trastuzumab concentrations (0.1–40 µg/mL), physiologically relevant in anti-HER2 cancer treatment, in 100-mM HEPES buffer containing 0.025% Tween 20 (pH 7.4). The range tested here covers the therapeutic relevant range of 5–40 µg/mL, i.e., the range of concentrations of circulating

trastuzumab in the blood used to dose the therapy in a personalized manner (Baselga et al., 2005). The LSPR peak of AuNP depends on the geometry, surface chemistry, and the refractive index of the surrounding environment (Chen et al., 2008). Nanomaterials that exhibit high refractive index sensitivities are strongly desired for fabricating plasmonic nanosensors. Herein, it was expected that shifts in LSPR would be dependent on the amount of antibody bound to antigen-decorated particles.

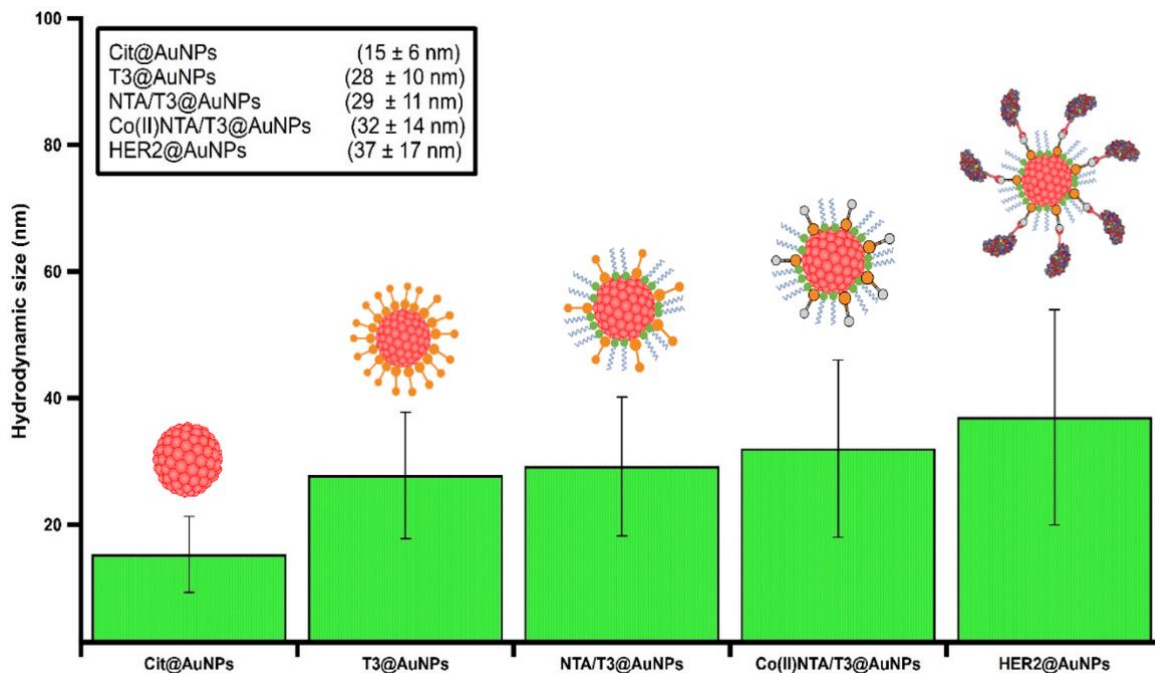


**Figure 39.4.** Volume-weighted distributions of hydrodynamic diameters of nanoparticles as determined by dynamic light scattering after different functionalization steps. The measurements were triplicated, and the error bars in the plot represent the measurement standard deviation.

As clearly observable from **Figure 41.4**, the LSPR undergoes a redshift upon the addition of a concentration of at least  $1.3 \mu\text{g/mL}$  of trastuzumab. Increasing concentrations of the antibody led to a more substantial redshift of the LSPR band due to the binding of the immunoconjugate. A similar trend was also observed in previous studies (Cao & Sim, 2007; Han et al., 2020; Yoshimura et al., 2020). Generally, the LSPR spectral shifts are attributed to the combination of local refractive index changes induced by analyte adsorbed onto the particle surface and the coupling of surface plasmons of adjacent particles. The latter heavily depends on multiple interactions between the ligands and target receptors. In the present case, the significant redshift presumably corresponds to the interparticle coupling of surface plasmons due to the presence of trastuzumab.

It shall be mentioned that the absorbance measurements were taken 5 min after completing the titration process for the respective amount of the antibody. The timeframe required in this step of biorecognition, especially in comparison to the lengthy incubation protocols used in ELISA assays, highlights the utility of this platform for the development of a rapid LSPR-based plasmonic nanosensor.

The shift in LSPR as a function of trastuzumab concentration was quantified as shown in **Figure 42.4 (blue dots)**. Additionally, the normalized ratio of the absorbance at 600 nm ( $A_{600}$ ) and at 520 nm ( $A_{520}$ ) with respect to the antibody concentration was determined. This relation reveals the arrangement of the particles in the assay suspension. Whereas the former is related to the wavelength at which aggregation is observed, the latter corresponds to the LSPR absorption peak of unperturbed AuNPs. Normalization to the absorbance value displayed by the nanoparticles decorated with His-tagged HER2 enables us to quantify NP clusterization: the higher the ratio, the greater the degree of aggregation. The normalized ratio of the aggregation was plotted as a function of the target antibody concentration. **Figure 42.4 (red dots)** shows a near-sigmoidal titration curve for the various concentrations used in this study. When a small amount of antibody was added (300 ng/mL), the aggregation induced resulted in a small rise in the aggregation ratio ( $>1$ ), presumably due to the onset formation of antibody-mediated dimers. The presence of an increasing quantity of the antibody promotes the aggregation with a monotonic increase of the signal observed between 4  $\mu\text{g/mL}$  and 20  $\mu\text{g/mL}$  before reaching a plateau at a concentration of 40  $\mu\text{g/mL}$  of the target analyte. First, we can conclude that the limit of trastuzumab detection (LOD) of our assay is as low as 300 ng/mL by examining the formation assemblies through the aggregation ratio relationship, which gives a more sensitive and a better quantitative description of the particle status with increasing concentrations of the target analyte. Moreover, the saturation is reached at 40  $\mu\text{g/mL}$ , which is the limit of the clinically relevant concentrations of antibody freely circulating in the blood in trastuzumab-based therapy. To further validate this result, SEM and TEM micrographs were acquired, shown in **Figure 43.4** and **Figure 44.4**, displaying the morphology of the His-tagged HER2-decorated particles before and after the addition of trastuzumab (2, 10, and 20  $\mu\text{g/mL}$ ). The findings demonstrate that the capture of antibodies leads to a decrease in the interparticle distance and, subsequently, leads to cluster formation, enabling us to develop a rapid sensing platform using a simple UV/Vis spectrophotometer. The DLS readouts further confirmed our observations by detecting the clusterization of AuNPs induced by the trastuzumab in the assay

solution. As shown in **Figure 44.4e**, the average hydrodynamic diameter of His-tagged HER2-decorated AuNPs was greatly increased from 37 nm to 265, 528, 747, 837, and 923 nm upon binding to trastuzumab with concentrations ranging from 2 to 10  $\mu\text{g/mL}$ , respectively, indicating that the modified AuNPs were agglutinated together into aggregates.

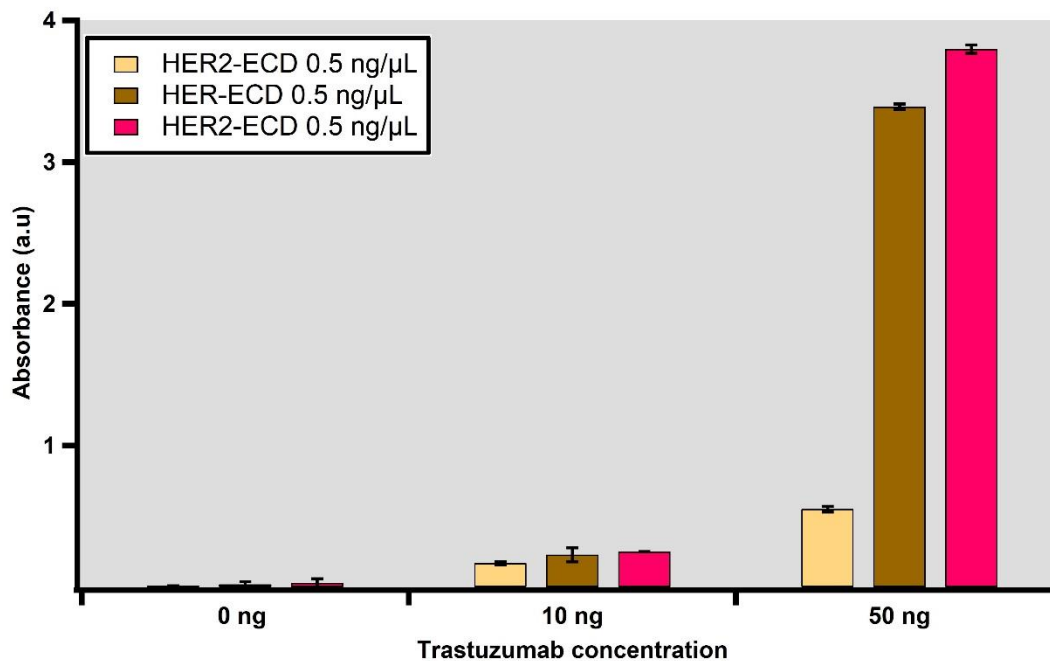


**Figure 40.4.** Indirect ELISA analysis performed for trastuzumab antibody with various concentrations of His-HER2 antigen. Each measurement was conducted in duplicate.

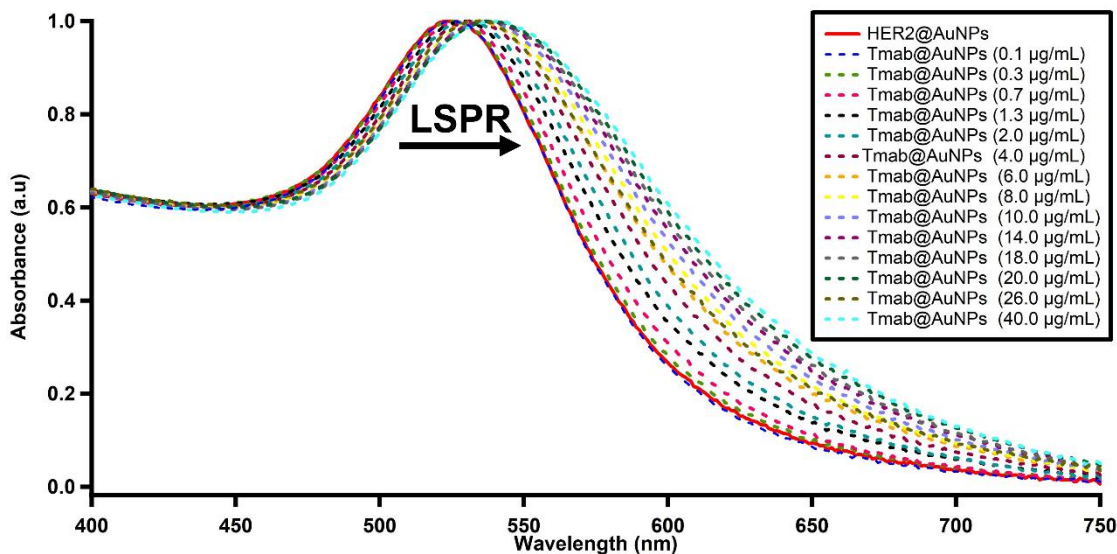


**Figure 41.4.** UV/Vis absorption spectra for His-HER2 decorated AuNPs before and after the incubation with trastuzumab. LSPR peaks redshifted upon varying the concentration of the antibody.

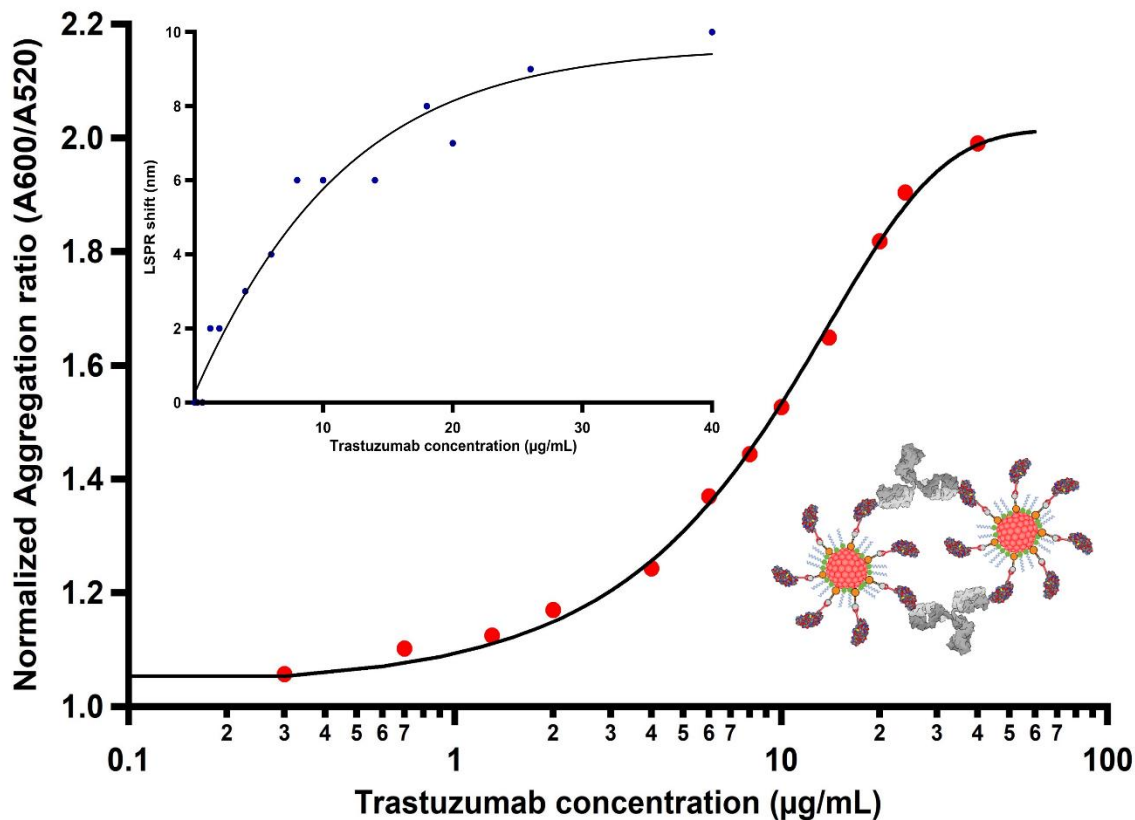


**Figure 42.4.** Quantification of the LSPR shift (**blue dots**) and normalized aggregation ratio (**red dots**) of immunoconjugates with various concentrations of trastuzumab. Dose-response presented in each plot was fitted with the four-parameter logistic sigmoidal curve. The coefficient values  $\pm$  one standard deviation used in the fitting equation as follows: Base =  $-0.42318 \pm 0.987$ , Max =  $2.4566 \pm 1.01$ ,  $X_{\text{half}} = -3.9633 \pm 7.3$ , and Rate =  $10.289 \pm 1.96$ . The analysis was performed with Igor Pro 6.02A software.

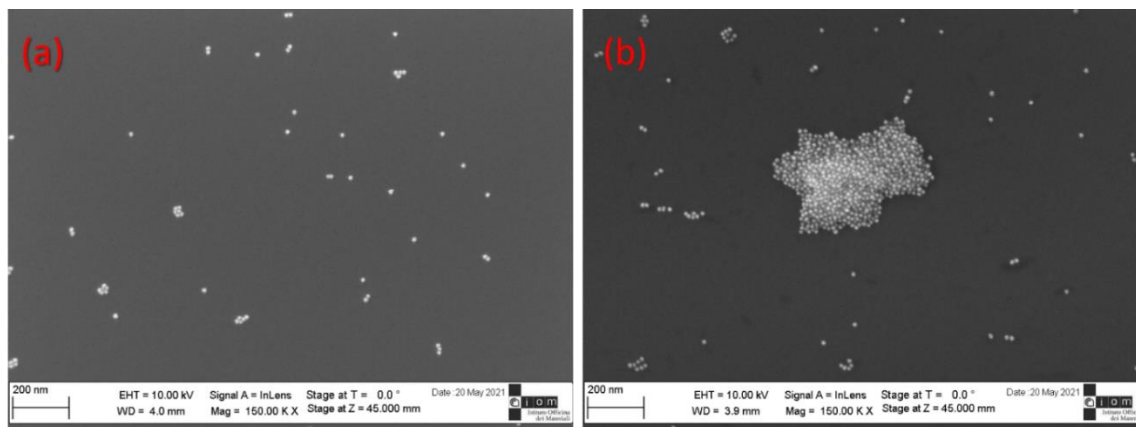


**Figure 43.4.** SEM micrographs of (a) NTA/TOEG3 coated AuNPs, (b) HER2-decorated AuNPs treated with 10 µg/mL of trastuzumab. Note the crosslinking of the nanoparticles caused by the presence of the target antibody.



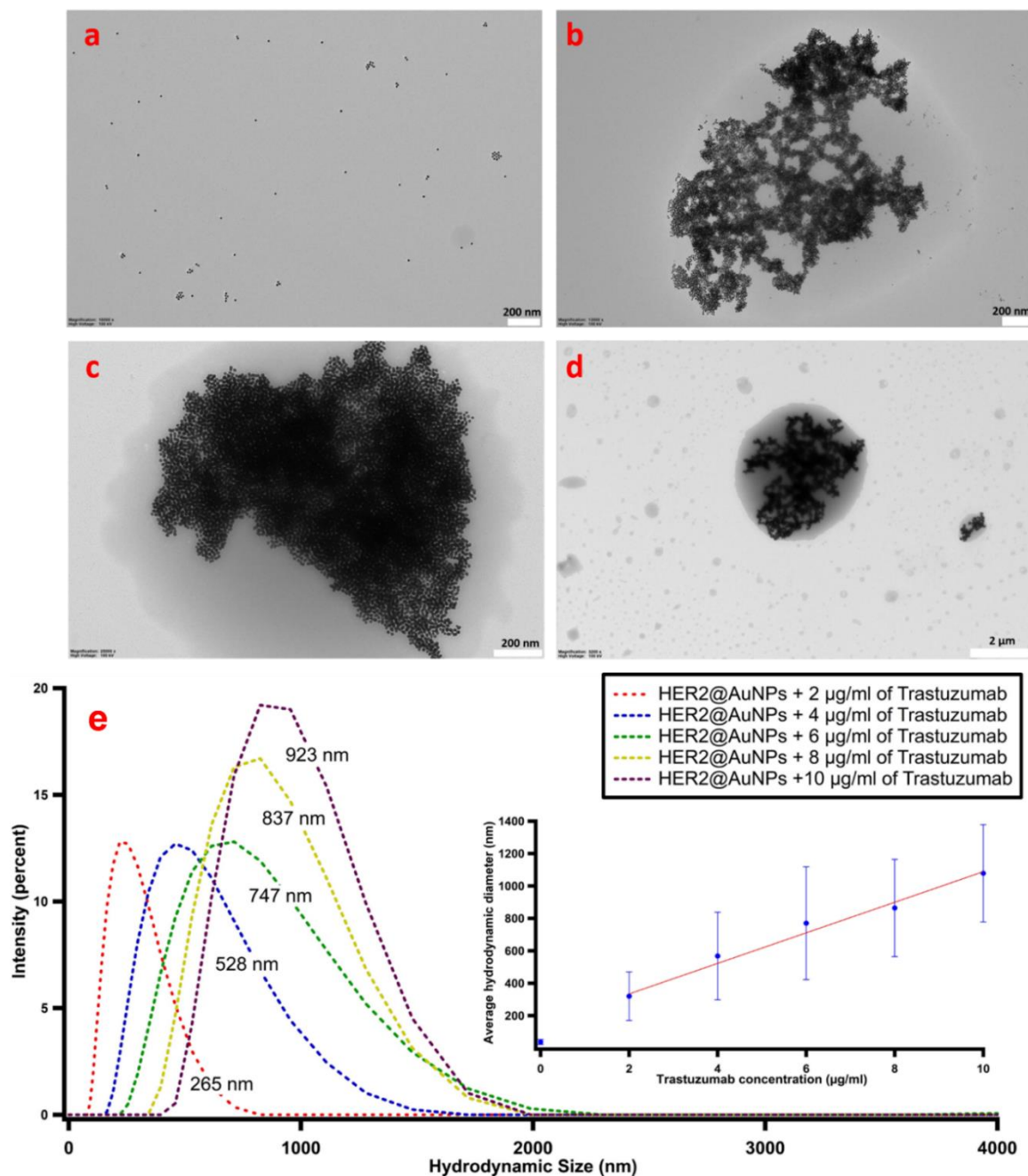


**Figure 44.4.** (a–d) Representative TEM images of (a) HER2-decorated AuNPs (b–d) incubated with 2, 10, and 20 µg/mL of trastuzumab, respectively. The formation of a 3D network indicates the successful coupling of AuNPs through trastuzumab linking. (e) DLS readouts for AuNPs probes treated with various concentrations of trastuzumab (up to 10 µg/mL). Upon mixing the HER2-decorated AuNP probes with trastuzumab, the particles are clustered together, leading to an average particle size increase of the assay solution. The DLS measurements were conducted in triplicate.



### 4.3.5 Evaluating the Specificity of the Platform

Having tested the concentration-dependent LSPR shifts of His-tagged HER2-decorated particles over a wide range of trastuzumab concentrations, the next step was to evaluate the specificity of the platform. In this case, we used a non-HER2-specific antibody, Anti-RBD, to interact with the particles instead of trastuzumab, using the same method to observe if any assembly would form. As expected, upon incubation with various concentrations of off-target antibodies, no change in the UV/Vis absorption spectra was observed (**Figure 45.4**), indicating that the particles sensed no or negligible interactions. These findings demonstrate the high specificity of our platform for detecting trastuzumab.

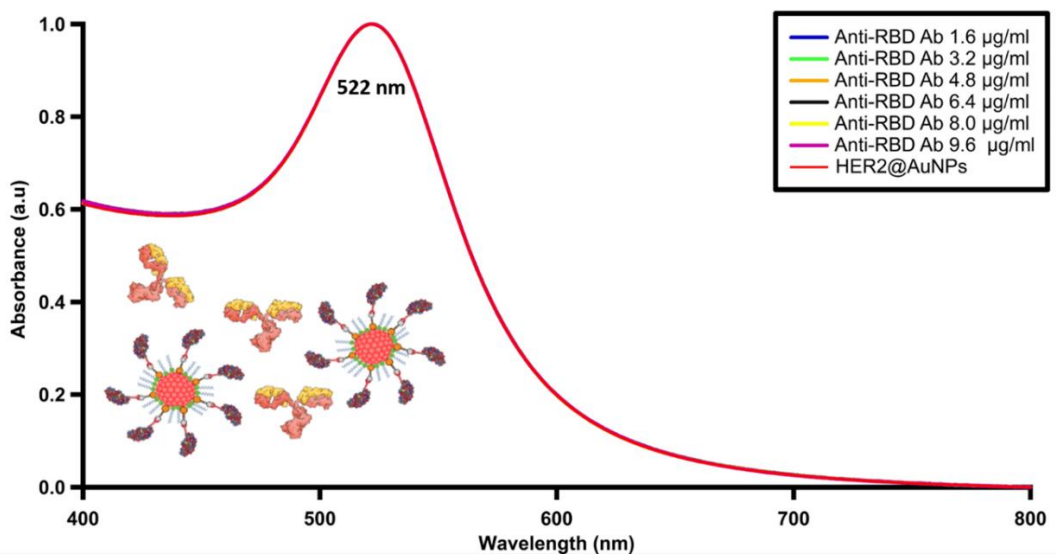


**Figure 45.4.** UV/Vis absorption spectra for His-HER2 incubated with various concentrations of non-HER2 recognizing antibody. The spectroscopic signal was similar to HER2 capped AuNPs.

### 4.3.6 Elucidating the Impact of Free His-Tagged HER2 on LSPR Response

To acquire a deeper understanding about the role played by the free His-tagged HER2 proteins in the LSPR response, we devised an experiment in which a dispersion of the bioconjugates was treated with increasing amounts of free His-tagged HER2 prior to the addition of a fixed concentration of trastuzumab (10 µg/mL). As can clearly be seen in Error! Reference source not found., an increasing amount of the proteins caused a dramatic drop in the normalized ratio ( $A_{600}/A_{520}$ ), indicating a marginal aggregation of the nanoparticles. Interestingly, nearly 5 nM of

free HER2 protein in the colloidal suspension was sufficient to cause a drastic drop in the normalized ratio ( $A_{600}/A_{520}$ ). This implies that all antigen-binding recognition sites of the antibody were saturated and no longer accessible for bridging His-tagged HER2 immobilized on decorated AuNPs. Thus, our analysis indicates the importance of removing unbound proteins after the conjugation process with Co(II) NTA.

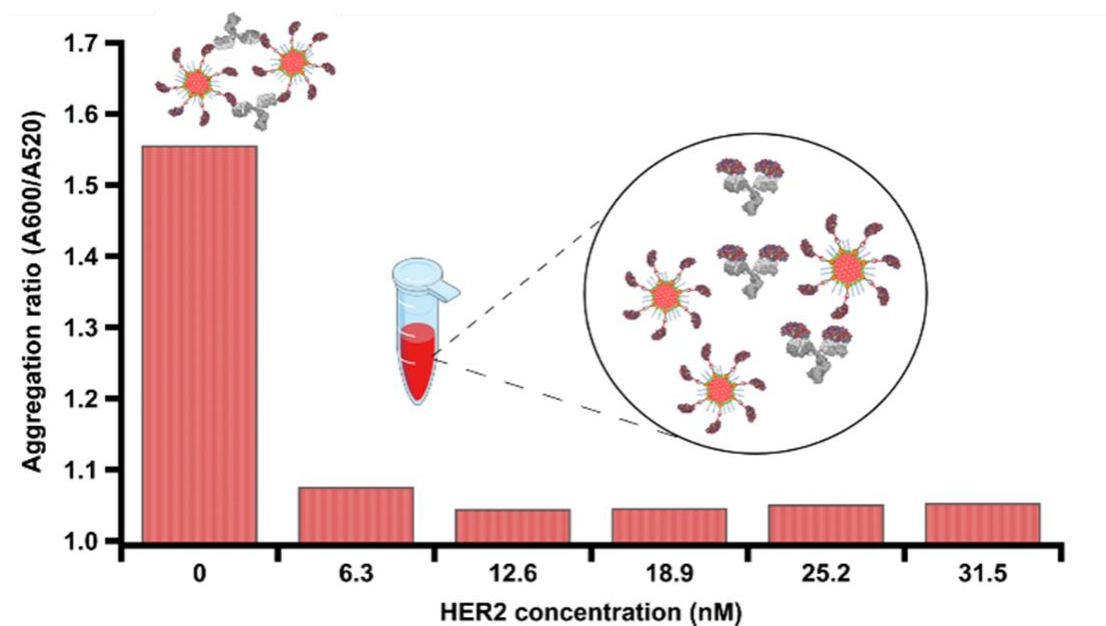


**Figure 46.4.** Spectrophotometric titration ranging from 6-32 nM free His-tagged HER2 concentrations.

#### 4.3.7 LSPR Response upon Tuning the Density of the Surface Grafted SAM

To investigate the possibility of optimizing the density of the His-tagged HER2 protein immobilized onto the particle surface, we varied the molar ratio of the NTA anchor and the TOEG3 spacer ligands up to the saturation density. The coating densities were adjusted by using the 20:80, 50:50, and 80:20 ratios between NTA and TOEG3, respectively. At first glance, **Figure 47.4** shows that the aggregation ratio measured with UV/Vis gradually increases for the various AuNP–trastuzumab immunocomplexes when the amount of NTA–ligand increases. AuNPs passivated with increasing NTA-coating density also revealed a gradual increase in the hydrodynamic size, indicating a higher protein loading capacity. However, we observed that, with an 80:20 coverage density, the chance of having aggregates after protein loading is relatively high (see **Figure 48.4**), likely because there are still  $\text{Co}^{2+}$  ions bound to the NP surface. Thus, the chance for electrostatic

interactions with other NTA-terminated AuNPs is increased. Therefore, we maintained a 50:50 ratio for the rest of the study.

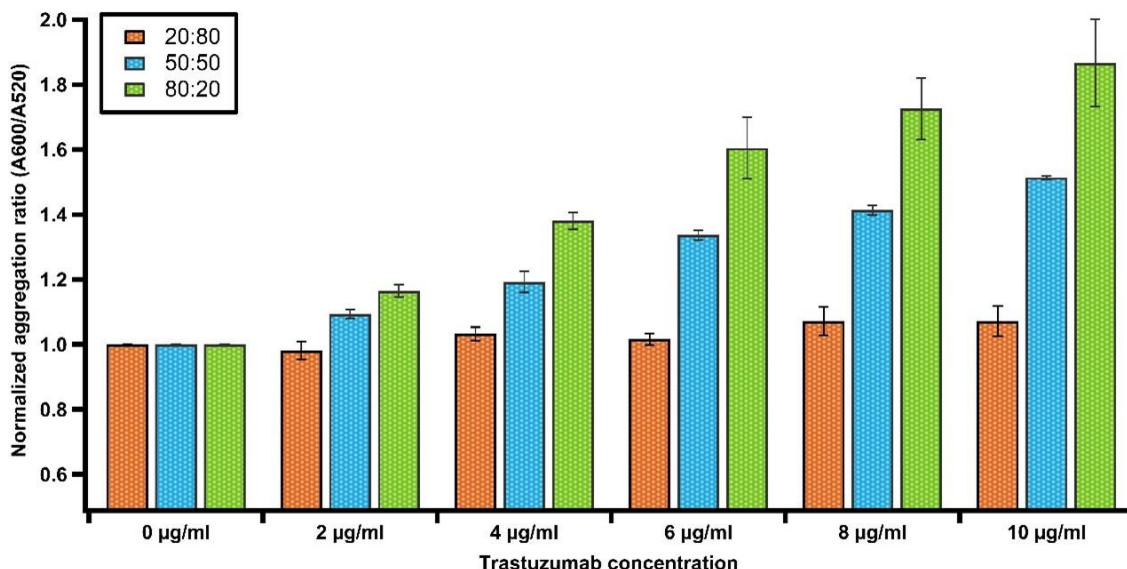


**Figure 47.4.** Comparison of the LSPR response for various concentrations of trastuzumab upon adjusting the SAM density on the surfaces of AuNPs. Note that, with a 20:80 ratio, no plasmonic response was observed across all doses of the antibody.

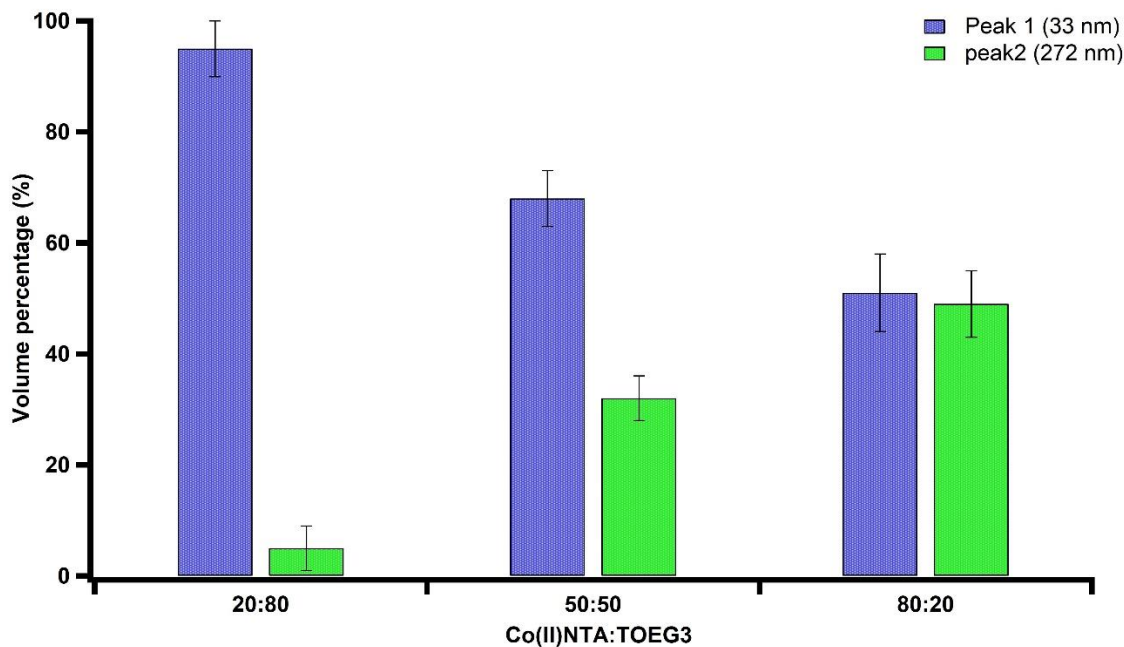


**Figure 48.4.** DLS volume-weighted size distributions comparing AuNPs coated with NTA and TOEG3 SAM with molar ratios of 20:80, 50:50, and 80:20, respectively. The 50:50 molar ratio was chosen to reach to a compromise the number of His-HER2 proteins and the instability issue due to the electrostatic attractive forces which lead to nanoparticle plasmonic coupling prior the assay.

#### 4.3.8 Evaluating Trastuzumab detection by LSPR in Human serum

At this stage, we investigated the biosensor performance in detecting trastuzumab in a complex matrix, such as human serum. Solutions containing His-tagged HER2-decorated particles were incubated with a range of diluted human serum (100, 75, 50, 25, and 10×) containing trastuzumab (2, 10, and 20 µg/mL) to show the results of direct detection in diluted human serum. As seen in **Figure 49.4**, it is highly challenging to detect trastuzumab in a colloidal suspension containing tenfold diluted serum. This is not surprising, as, in extremely complex biological mixtures, several proteins, including transferrin (TF) or histidine-rich glycoprotein (HRG), are present in high concentrations and can act as interferents (Swartz et al., 2011). It was reported that the latter highly interacts with several ligands, including metal ions (Terpe, 2003).

To verify this possibility, we incubated the bioconjugates in 10% serum to allow the possible displacement of the His-tagged HER2 protein from the surface. Then, the bioconjugates were separated from the serum and evaluated in an assay with various concentrations of trastuzumab (in buffer). As shown in **Figure 50.4**, no LSPR response was observed across all the doses of the antibody, demonstrating a loss of sensitivity due to less effective conjugates. The presence of histidine-rich proteins that may highly interfere with the conjugation of the immunocomplex was investigated by employing Ni-NTA agarose beads (**Figure 51.4**). Contrastingly, upon the purification trial conducted to remove proteins containing histidine repeats in 1% and 5% diluted serums (**Figure 52.4**), the shifts in LSPR became more pronounced with the addition of 2 µg/mL of the target antibody, as seen in **Figure 52.4**. Additionally, as reported in the same figure, the gel electrophoresis showed a slower mobility for the immunocomplex dispersed in the post-treated 5% diluted serum, indicating a higher chance for trastuzumab to recognize His-tagged HER2-decorated particles compared to nontreated serum. These findings are in agreement with the findings of a recent report that demonstrated that 100 times the dilution of the human serum was the optimum for detection using NPs (Duan et al., 2020). However, further optimization and the investigation of other possible routes to filter the biological media in order to enhance the sensitivity of the proposed platform are part of ongoing research.

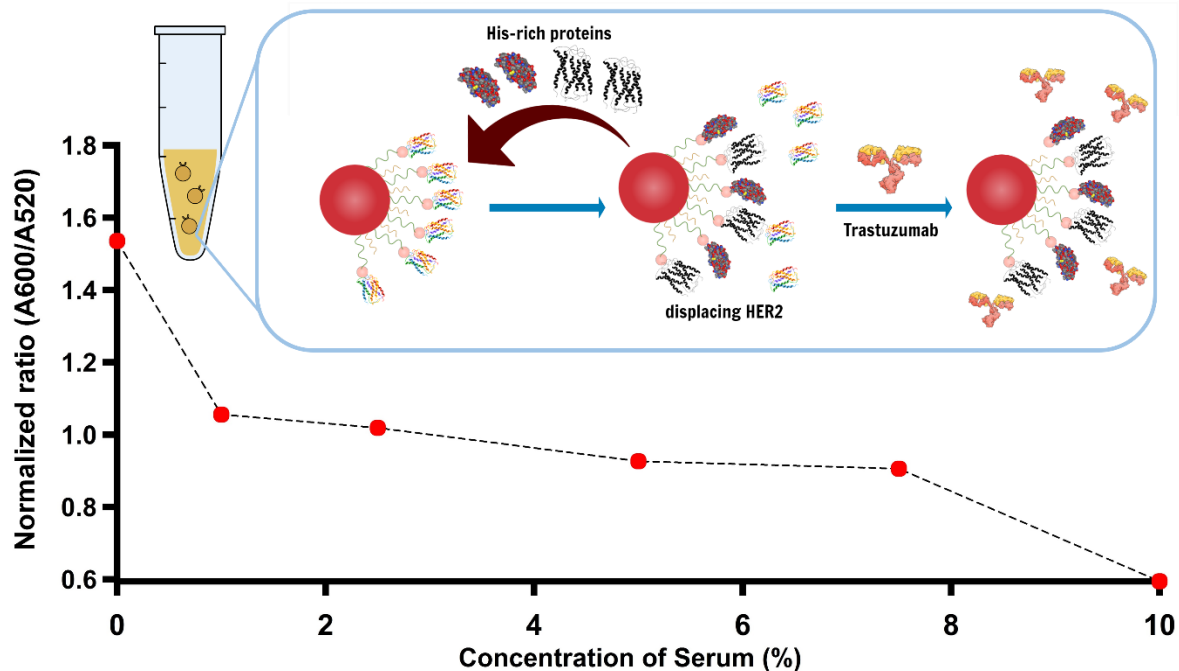


**Figure 49.4.** Plasmonic response for His-tagged HER2-decorated particles incubated with various dilutions of human serum-containing trastuzumab. It is clearly seen the challenge in obtaining a plasmonic response when the assay was conducted in a diluted serum (> 5%).

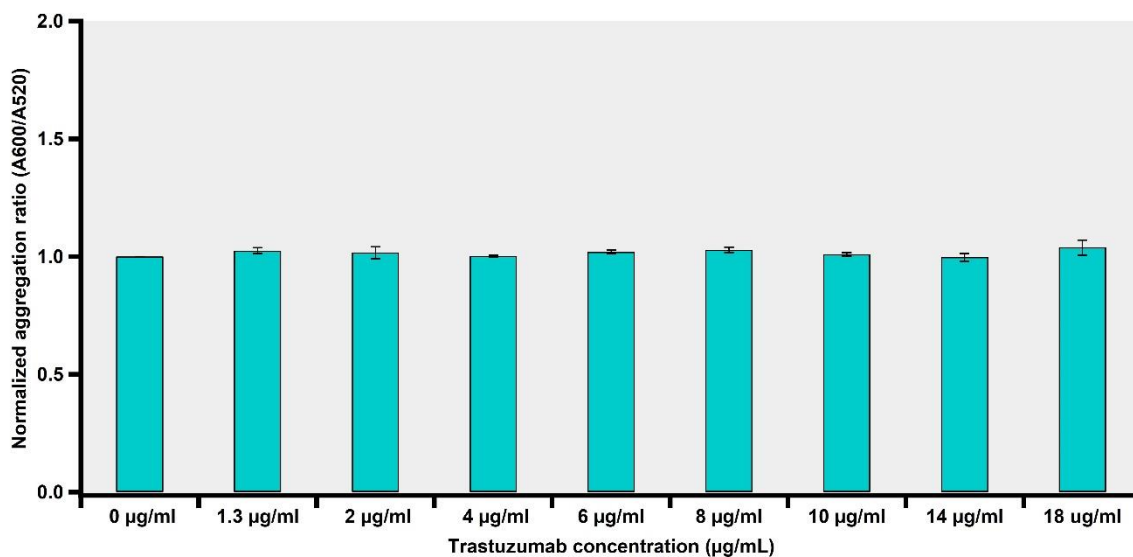


**Figure 50.4.** The presence of competing Histidine rich proteins that may have interfered and disrupted the bioconjugate leading to the less sensitive complex formation toward the target antibody.

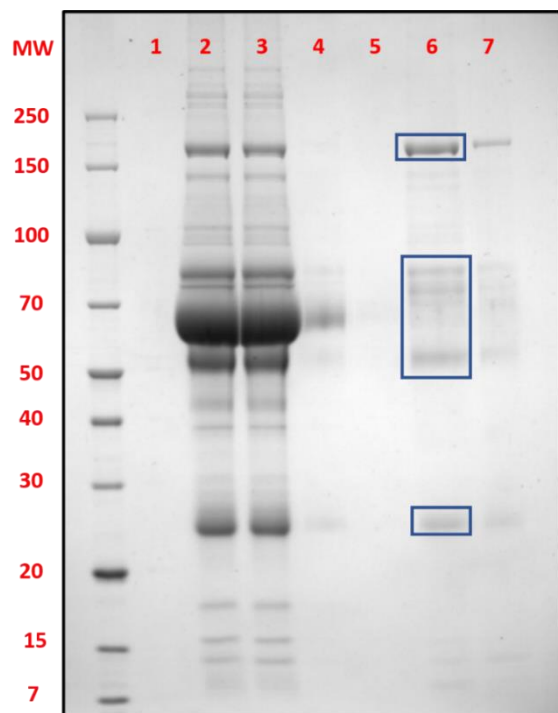


**Figure 51.4.** SDS-PAGE image of (1) empty lane, (2) 5% diluted serum, (3) flow through of the serum after incubation with the matrix, (4,5) first and second wash of the matrix, (6) after eluting the Ni-NTA matrix with imidazole, (7) the Ni-NTA matrix. Note that proteins containing Histidine-repeats were released after the elution step.

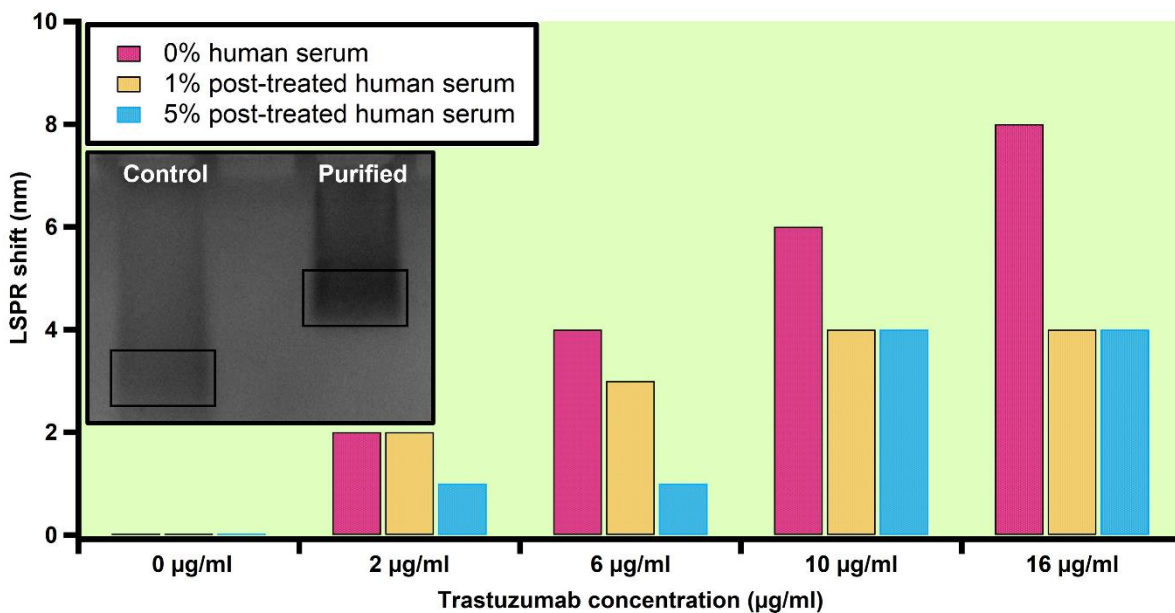


**Figure 52.4.** LSPR shifts for the particles treated with various concentration of the target antibody dispersed in 1% and 5% filtered serum. **Inset:** the gel electrophoresis photograph revealed a slower mobility for the immunocomplex in the filtered diluted serum.

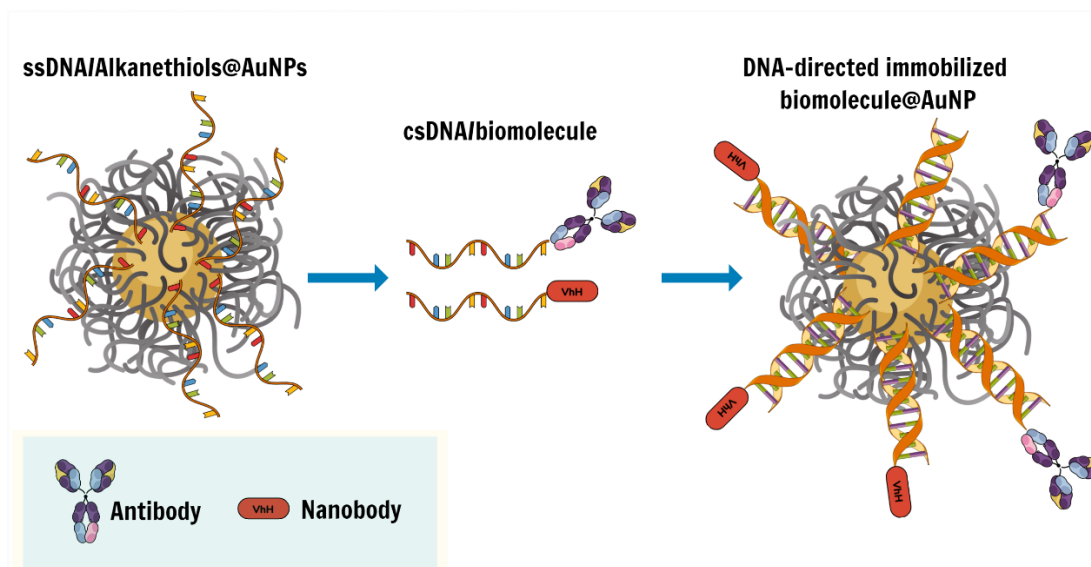
## 4.4 Conclusions

Optical, label-free biosensors represent precious means for real-time, direct analyses of biomolecular interactions that can be exploited to boost the development of precise and individualized therapies for severe diseases like cancer. In this work, we described the development of a facile, rapid, and specific AuNP-based platform for the detection and quantification of trastuzumab. To accomplish this, the His-tagged HER2 protein was anchored on AuNP surfaces by employing the coordination chemistry of metal complexes attached to a mixed self-assembled monolayer (mixed-SAM) onto the nanoparticle surface. We characterized and optimized the Co(II)NTA AuNP platform incorporated with TOEG3 as a spacing ligand for passivating the particle surface to achieve both excellent dispersibility and high reliability in protein immobilization. The successful tethering of the His-tagged HER2 protein was demonstrated, confirming the fully functional attachment of the protein to the Co(II)NTA/TOEG3@AuNP platform. This methodology is readily applicable to other histidine-rich biomolecules. In line with the expectations for this type of assay, the biorecognition of antibodies and antigen-decorated AuNP conjugates results in a substantial LSPR shift due to the formation of particle assemblies, enabling the detection of the antibody in clinically relevant concentrations. Although our sensing platform showed a different sensitivity when comparing the buffer and the human serum matrix, with further optimizations and improvements, we anticipate our platform will pave the way for fabricating lab-free and ready-to-use nanoprobes, which may have application potentials in point-of-care medical diagnoses. In parallel, and with the aim of fabricating a facile yet robust diagnostic platform, another appealing strategy, known as the DNA-directed immobilization (DDI) technique, will be explored in the next chapter.

## Results and Discussion

### DNA-coated gold nanoparticle: a versatile platform for biosensing applications

**Disclosure:** This chapter is slightly modified from two separate manuscripts.; One has been published: “An electrophoresis approach with online thermal lens detection to monitoring DNA surface coatings on gold nanoparticles. Asbaghi, Behnaz Abbasgholi N., Alsadig, A., et al. *Microchemical Journal* 173 (2022): 106961106961(Asbaghi et al., 2022)”. The other one is ready for publication: DNA-Directed Protein Anchoring on Oligo/Alkanethiol Coated Gold Nanoparticles: “A Versatile Platform for Biosensing Applications by Ahmed Alsadig et al.” The preparation and characterizations were carried out following the protocols described in section 3.4.



#### 5.1 Motivation

The immobilization of proteins on 2-D or 3-D substrates has shown great potential to revolutionize protein diagnostics. Still, the major challenge tasks of the direct anchoring of proteins on a solid substrate lie in the risk of altering the protein structure, function, and homogeneity due to the



attachment. This motivates us to explore the utility of a DNA-directed immobilization (DDI) methodology as an easy-to-use strategy that enables the decoration of AuNPs surface with a broad class of biofunctional molecules, and a potential diagnostic assay for a targeted detection benefiting from the self-assembly capabilities of ssDNA. Finally, we also shed the light on the interaction between the proposed nanosystem with synthetic membranes which has relevant indications of the NP uses in nanomedicine and biosensing applications.

## **5.2 Introduction**

The way a biomolecule is anchored on a nano-construct has a direct influence on the performance of the nanosystem (Spicer et al., 2018). Recent advancements in nanobiotechnology have allowed for the development of advanced linking strategies for biological molecules such as peptides, proteins, aptamers, and nucleic acids to 2-D and 3-D surfaces, allowing for the fabrication of functional platforms for therapeutic and diagnostic purposes (Medintz, 2016; Rana et al., 2010; Sapsford et al., 2013). Several immobilization strategies have been reported, many of which rely on direct linking of proteins to a surface, even for the multiplexing detection of different biomarkers as in protein microarrays (Sun et al., 2013). This emerging class of proteomic technology has received widespread attention and has become an essential tool in molecular biology (Chen & Zhu, 2006). Several technical drawbacks of direct covalent immobilization of macromolecules have been reported which restrict their usability: the steric hindrance of the recognition sites and the structural alterations of the proteins during the immobilization are the most important. The latter will undoubtedly influence the overall protein functionality (Schwenk et al., 2007). As an alternative, DNA-directed immobilization (DDI) provides a promising versatile approach that combines the advantages of the self-assembling of short single stranded DNA oligos on surfaces with facile conjugation of proteins with short, complementary DNA strands, and the facile sequence-specific hybridization of DNA strands: by conjugating different proteins with a different oligo sequences, their respective immobilization on a DNA microarray of complementary strands is straightforward, allowing the easy transformation of a DNA microarray into a protein microarray by Watson-Crick hybridization (Arrabito et al., 2013; Bano et al., 2009; Du et al., 2015; Fruk et al., 2007; Yang et al., 2015).

In contrast to the covalent attachment, biomolecules tethered through DDI have shown full retention of the functionality as they are anchored onto the substrate via DNA spacers. Moreover,

utilizing DNA strands as spacers between the substrate and the biomolecule of interest reduces the steric hindrance and enhances the chances for biomolecular recognition. However, while DDI + DNA grafting is a well-known technique on 2D substrates, it has not been exploited in association with 3D gold nanostructures, essentially because of the low sensitivity of plasmonic detection when the AuNPs are decorated with nm-size molecules.

DNA-Au nano-conjugates have become one of the most versatile nanomaterials due to the potentialities of combined effect, including the DNA addressability with large surface area and facile conjugation with AuNPs (Dam et al., 2015). In the framework of biosensing, several groups have elegantly demonstrated the utility of the DDI approach. For example, N. Tort *et al.*, reported a strategy employing bio-functional plasmonic nanostructured chips manufactured on a DNA microarray to detect Anabolic-androgenic steroids (AAS) based on localized surface plasmon resonance (LSPR)(Tort et al., 2017). Deka *et al.* developed a colorimetric assay for monitoring helicase activity using DNA conjugated to AuNPs and promoting the formation DNA-AuNPs aggregates through the addition of DNA linkers (Deka et al., 2017). The desegregation of particle assemblies promoted by the helicase activity caused a change of their optical properties, as monitored through adsorbance measurements. Changes in the disassembling kinetics were related to the enzymatic activity, and can be used to screen specific inhibitor of the enzyme. Here, we propose to load protein-conjugates through DDI on ssDNA-AuNPs. Clearly, this would offer a great opportunity to construct a multifunctional platform that can be geared to a wide range of applications ranging from bioimaging to biosensing, gene regulations, and drug delivery. However, we should be able to demonstrate that the system used is sensitive enough to quantify the number of proteins loaded on the particle and then to habilitate biorecognition detection.

Along this line, we set out to implement the DDI approach utilizing a mixed self-assembled monolayer of thiolated ssDNA moieties and a bio-repellent thioalkylated oligo-ethylene glycol (OEG) molecules, following the protocol developed by *Deka et al.*(Deka et al., 2015). The right number of ssDNA molecules was needed to guarantee the active loading of DNA-protein conjugates while the OEG terminated molecules avoid the aspecific binding of proteins/small molecules on the particle surface. To guarantee an improved sensitivity of the assay, we reported a novel approach based on a miniaturized gel electrophoresis chip (MGEC) integrated with online thermal lens detection for monitoring the DNA loaded on the surface AuNPs and then the protein conjugates through DDI. This implementation offers a rapid, sensitive, straightforward

measurements of the surface coverage, and can be considered as an independent verification tool of other nanoparticle-based nanosystems that utilize oligonucleotide probes. As a proof of concept, we demonstrated the functionality of our design in two cases: to detect avidin in solution via hybridizing the oligomers anchored on the particles with the biotinylated complementary DNA; in the framework of cancer-associated antigen detection, to qualitatively detect the HER2-ECD antigen by means of ssDNA-conjugated nanobody fragments, referred to as C8.

## **5.3 Results and discussion**

### **5.3.1 Characterization of synthesized AuNPs**

A characteristic surface plasmon resonance band (SPR) of as prepared AuNPs exhibits a maximum absorption at 520 nm (**Appendix 2**), indicating slightly larger particles compared to the ones previously prepared and used in *chapter 4*. This was further confirmed with DLS, and TEM micrographs. DLS shows a hydrodynamic size of AuNPs with an average particle diameter of  $23 \pm 5$  nm, while TEM reveals an average diameter of a typical particle of  $17.3 \pm 1.4$  nm (**Figure 53.5A** and **Figure 53.5B**). The concentration of the gold colloids was found to be 2.6 nM. In addition to DLS and TEM analyses, we also used AFM for characterizing the particles; sample preparation for AFM is faster and the analysis can be performed in air or in liquid instead of high vacuum. Few works in the literature reported the attachment of AuNPs to a flat surface for AFM imaging. Therefore, we established a procedure to immobilize AuNPs on AFM substrate (mica) to avoid the displacement of the particles during AFM scanning. This procedure involved poly-L-Ornithine (PLO) coated mica, a polymer containing amine groups, which bind electrostatically the negatively charged, naked AuNPs. The same polymer is used to bind DNA through the phosphate backbone, and is used in the literature both for DNA imaging in dried and in liquid conditions (Podesta et al., 2004). By optimizing the concentration of PLO and AuNPs, the proposed methodology has proven to be a simple, fast, and reliable method to create a substrate that firmly secures the attachment of AuNPs for AFM imaging. AFM measurements yielded a value of  $17.5 \pm 2.4$  nm which is in agreement with reported TEM analysis mentioned above (**Figure 53.5C** and **Figure 53.5D**).

### **5.3.2 Detection of AuNPs functionalized with different DNA density**

The loading of thiolated DNA on AuNPs was based on the pH-assisted method (Deka et al., 2015). This approach offers higher loading efficiency, and a single-step process that takes less than an

hour compared to 4–24 h and multiple steps needed for salt aging. Next, we characterized the particle surface coating via UV/Vis spectroscopy, gel electrophoresis and TLS coupled with microchip (MC) channel. The absorption profile shows that the bound DNA caused a slight redshift in the characteristic SPR peak position (as seen in **Figure 54.5**). It is well-known that the evanescent field of SPR is highly sensitive towards the refractive-index change of the surrounding medium due to surface modifications, and the SPR peak generally redshifts as the refractive index of the surrounding environment is altered (Li & Rothberg, 2004; Zeng et al., 2014).

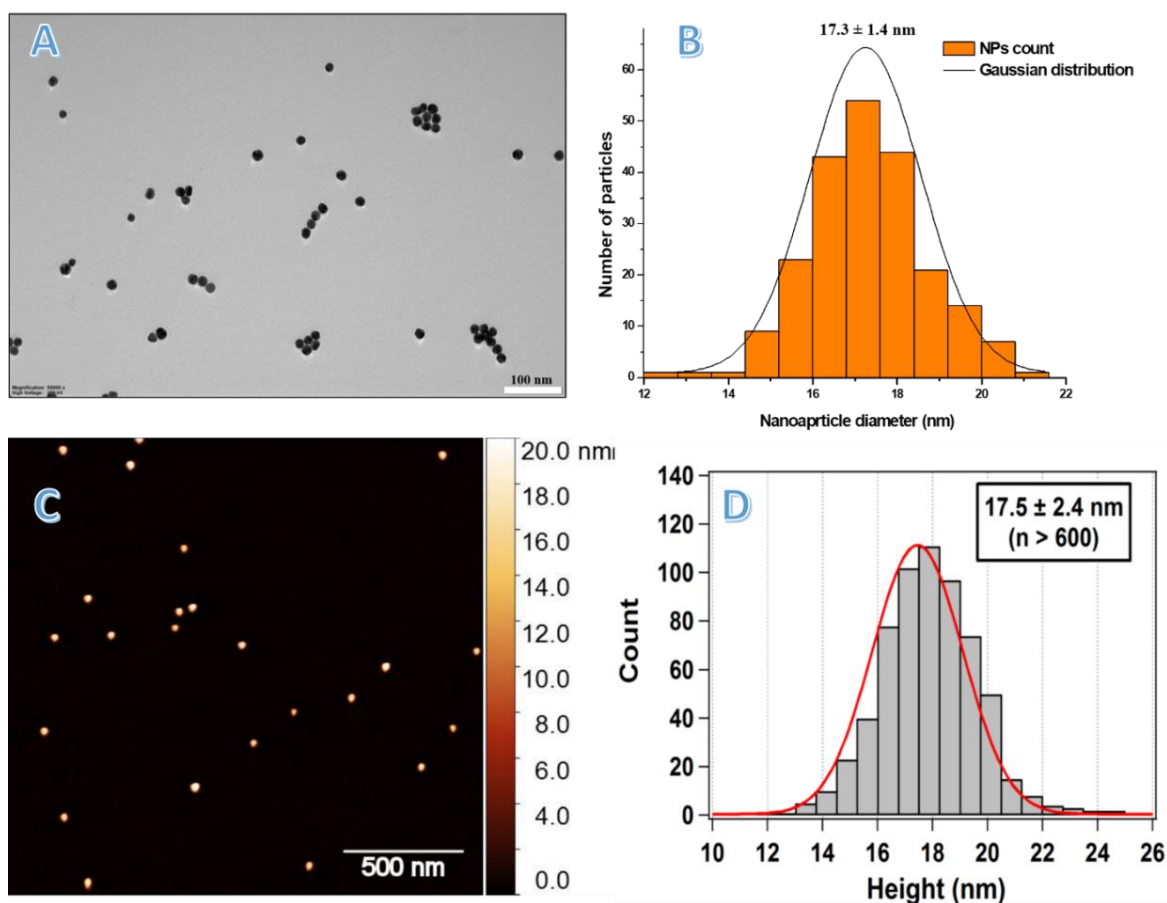


**Figure 53.5.** (A-B) TEM micrograph of synthesized AuNPs with a scale bar of 100 nm, and the statistical analysis indicating nanoparticles size distribution evaluated for over 250 nanoparticles. (C-D)  $2 \times 2 \mu\text{m}^2$  AFM non-contact mode image of AuNPs deposited on poly-L-ornithine coated mica, and its corresponding statistical analysis.

Notably, modification of AuNP surface with variable DNA densities causes subtle changes in the refractive index that can hardly be detected via UV/Vis spectroscopy due to the low resolution of

the UV/Vis system ( $\pm 0.005$ ) (**Figure 54.5**). To discern these small variations, TLS can be highly effective tool to measure subtle refractive index changes ( $\sim 10^{-5}$  RIU) and low absorbance (down to  $10^{-7}$ ) in the medium (Li & Rothberg, 2004; Liu & Franko, 2014). Because of these advantages, it is predicted an increase of the TLS signal with the increase in DNA amount loaded to the AuNPs surface. **Figure 55.5** shows that the TLS signal is linearly proportional to the ssDNA concentration over the range 5–220 nM with a LOD of 3 nM. The inset shows that the TLS signal increases with the loaded DNA amount up to 300DNA, reaching a saturation around 400DNA. These findings indicate that the optimum surface coverage is between 300DNA and 400DNA.

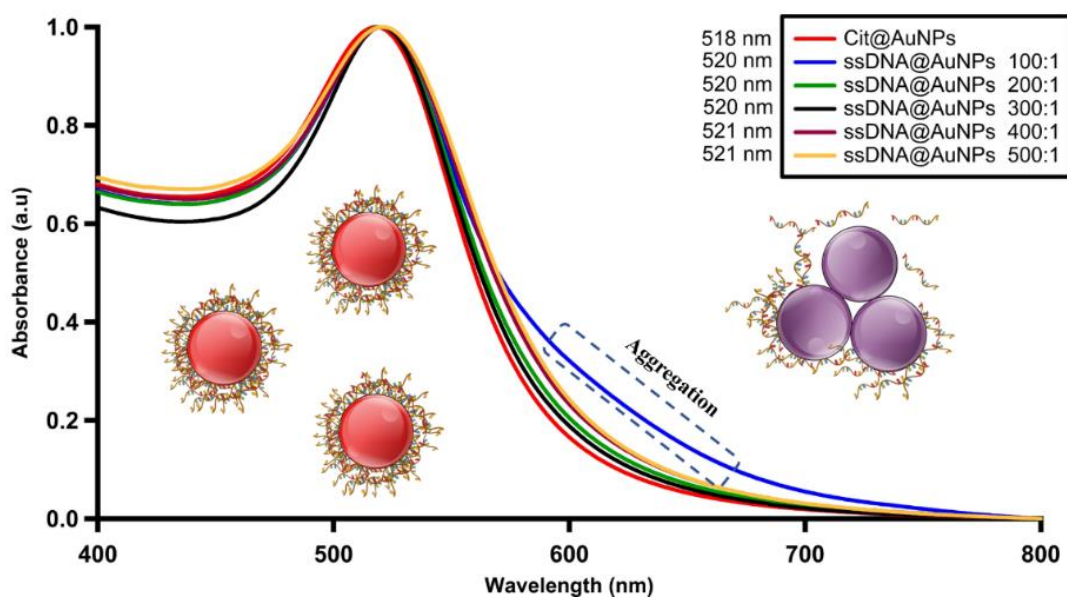


**Figure 54.5.** UV/Vis spectra of ssDNA-AuNPs with different DNA: AuNPs density. The onset of aggregation reflected on the broadening in the spectrum of 100DNA indicates insufficient covering of the AuNPs surface. Notice the indiscernible differences in the surface plasmon resonance bands between all coated AuNPs.

However, this hypothesis can be verified by an electrophoretic analysis determining the migration time for each sample. Therefore, samples were initially evaluated using conventional slab GE. A relatively high concentration of agarose gel (2%) was used to reduce the size of the porous enabling high selectivity. As seen in **Figure 56.5**, it is very challenging to distinguish between the bands representing the conjugates with various DNA densities. Therefore, we considered evaluating the possibility of correlating the DNA/AuNP density with the migration time using MGEC-TLS. The sensitivity of TLS detection can be improved by using agarose gel electrophoresis. By controlling

the conductivity of electrophoresis and that of the sample, an enhancement factor and stacking of particles would happen in a narrow band of the miniaturized channel. **Figure 57.5A** shows the electropherograms of the AuNPs tuned with different DNA surface charge densities, the inset shows migration times. As predicted, due to stacking of particles, high enhancement of gel as well as high spatial resolution, higher TLS signals were obtained. The mobility of such conjugates in the gel electrophoresis relies on the size and the overall surface charge: Relatively large conjugate size results in slower migration times, while higher surface charge will speed up migration in the gel. The results were consistent with our expectations: if the increase in charge is the dominant effect over the increase in size, then the effect of electrophoretic mobility of the AuNPs under the influence of the electric field would be the dominant parameter. It was also apparent that the DNA strands covering AuNPs in a 100:1 ratio had the slowest mobility among all DNA functionalized samples. It is highly probable that the DNA strands were insufficient to fully protect the surface of AuNPs; consequently, the particles had the tendency to aggregate in the running buffer, which contains salts that cause a charge screening and eventually agglutination of the particles via attractive Van der Waals forces. The onset of aggregation was further confirmed by the UV/Vis spectrum, where a shoulder was observed around 600 nm (see **Figure 54.5**). On the other hand, the 300:1 M ratio modified particles showed the fastest mobility with a sharp peak (**Figure 57.5A**), indicating that DNA density was high enough to support increased charge providing particle stability while still small enough to avoid the too-thick capping layer of ssDNA that could cause a retardation in the band. We found that a 300:1 DNA ratio is optimized, as both the 200:1 and 400:1 ratio led to slower migration, due to effects of smaller charge or larger size. At a molar ratio 500:1 the retardation of the band of the conjugates further increases, which indicated that the AuNP surface was fully saturated. It is noteworthy that the 300:1 DNA/AuNPs ratio represents an equilibrium point with the fastest migration with no sign of aggregation observed optically via UV/Vis spectrum. Interestingly, the area under the peak increased linearly with the amount of DNA loaded on the NPs surface as shown in **Figure 57.5B**. The obtained narrow band related to 300:1 DNA/AuNPs is illustrated in **Figure 57.5C**. Furthermore, the tight focusing of the excitation beam resulted in much higher power density as well as better spatial and temporal resolution, while at the same time enabled high sensitivity detection and determination of small differences in migration time. It is important to highlight the potentiality of our approach, which allows us to resolve in a short time the particle surface modification with different DNA densities that are

otherwise indiscernible especially for low densities of the strands using a UV/Vis spectrophotometer. In addition, a comparison with the performance of slab-gel electrophoresis indicates that the proposed system has considerable advantages such as the capability of online detection, short running time, and significantly low volume consumption of reagents.

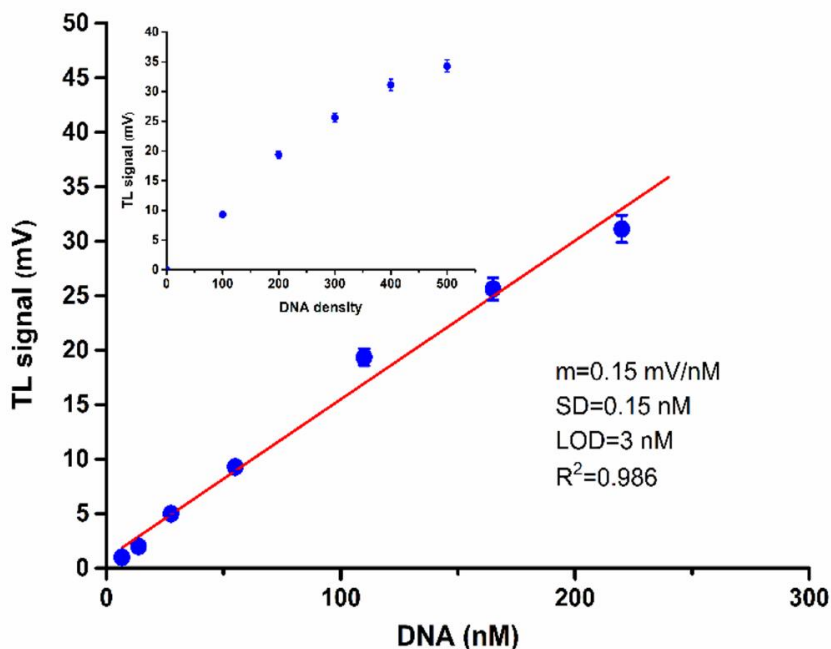


**Figure 55.5.** TLS signal as a function DNA/AuNPs ratios. The calibration curve was obtained to determine the LOD of the system based on the equation:  $LOD = 3(SD/m)$ . **Inset:** Notice the significant difference in the sensitivity in comparison with the conventional UV/Vis spectroscopy for low DNA densities used in the study to coat the AuNPs.

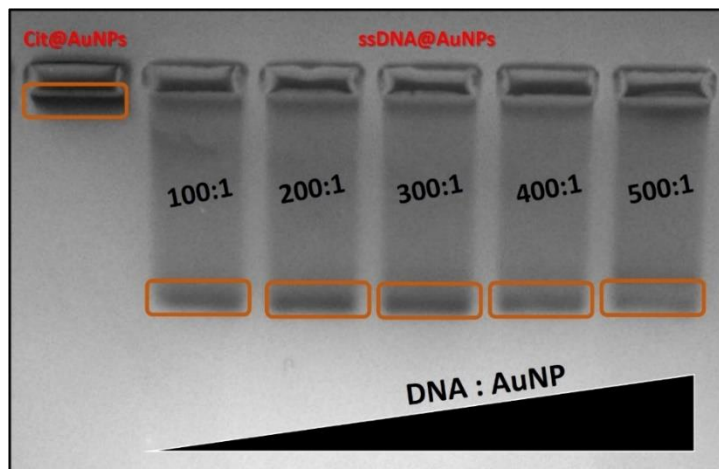


**Figure 56.5.** The slab gel electrophoresis image of ssDNA-AuNPs with different loaded DNA densities. The image was converted to gray scale format.

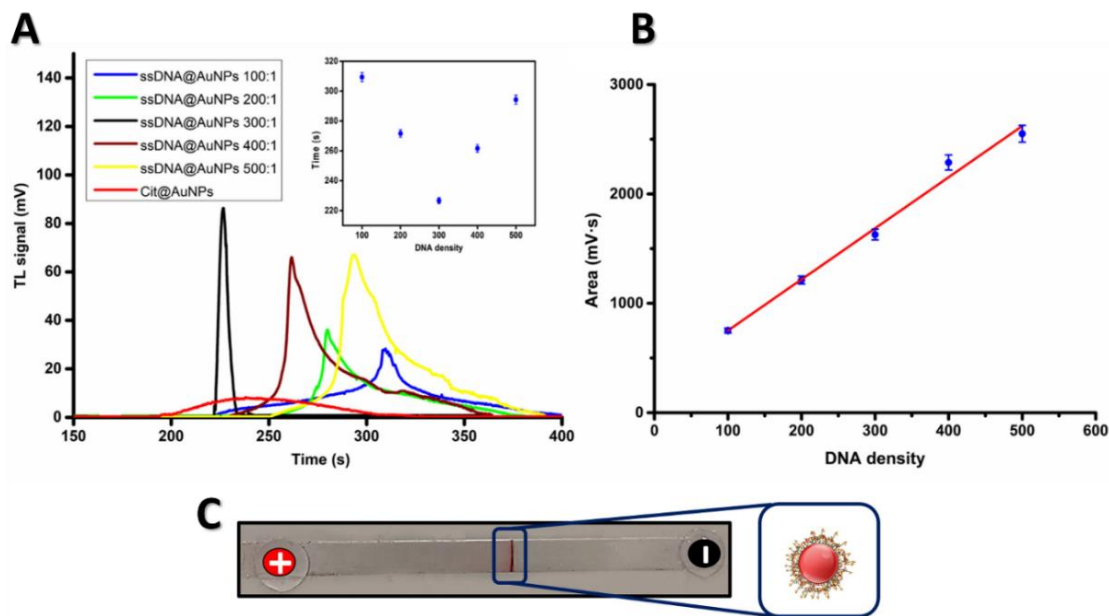


**Figure 57.5.** (A) Electropherogram of ssDNA-AuNPs with different loaded DNA densities, the **inset** shows migration times (B) area under the peak versus various DNA densities coated AuNPs, (C) the inset shows a photograph of 300 DNA separation in the channel.

### 5.3.5 ssDNA/TOEG6 customized SAM formation on AuNP surface

Then, we modified the DNA-AuNPs nanosystem by mediating a top-terminated oligo ethylene glycol alkanethiol, referred to as TOEG6, as the spacing ligand. This choice of molecule was based on several factors: (i) a thiol group at its terminus to anchor onto AuNP surface; (ii) a hydrophobic spacing alkyl chain that provides to the structure the possibility to self-assembled into closely packed layer; and (iii) an oligo-ethylene oxide sequence to enhance the colloidal stability in aqueous solution including a physiological and biological media. DNA/TOEG6 SAM presents a protein-resistant background and allows for rational control over the DNA probe surface density (Deka et al., 2015). The fabrication of a highly stable DNA-AuNPs with controlled surface density will pave the way to construct more sophisticated functional architectures for various applications including a biosensing (Zhang et al., 2011). The conjugates were characterized by UV/Vis spectroscopy, TEM and GE (**Figure 58.5**). The findings revealed the formation of highly stable functionalized particles with the ligands. The successful binding was further confirmed by simple slab agarose gel and MGEC-TLS, in which the modified AuNPs were able to migrate on the gel with the conjugated DNA indicating a retardation of ssDNA/TOEG6@AuNPs band compared to



DNA@AuNPs. The delay was attributed to a combination of the size increment and the reduced number of DNA strands replaced by the neutral TOEG6 molecules (**Figure 58.5C**). The number of DNA strands per AuNP was computed for (300:1) ratio by a DTT-induced detachment of FAM-labeled ssDNA from AuNP surface as described in the literature (Lee et al., 2006). The coverage of 42 strands per AuNP ( $8 \times 10^{12}$  strands/cm<sup>2</sup>) was quantified (see the details in **the Appendix 3**).

### 5.3.6 Conformational and electrophoretic analysis of the mixed-SAM

After demonstrating the successful functionalization of AuNPs with ssDNA and ssDNA/TOEG6 SAM, the online analysis capability of MGEC-TLS platform was then tested by monitoring the electrophoretic mobility of these conjugates. As is well known, ssDNA has a persistent length of about 1 nm. At low density, the 22 base-pair long thiolated strands self-assemble to form a film in which they adopt a mushroom-like conformation resulting in a compact structure around the particle. Also, under these conditions, there might be some nonspecific adsorption of DNA strands wrapped around the AuNPs. When the TOEG6 molecule is introduced, the size of AuNPs increases compared to ssDNA@NPs. This result is compatible with the substitution of some of the DNA strands by TOEG6 and the TOEG SAM domains' local formation. Since it is well packed on the surface, it is reasonable to think that TOEG6 SAM domains will force the residual DNA strands in a more elongated, rod-like conformation.

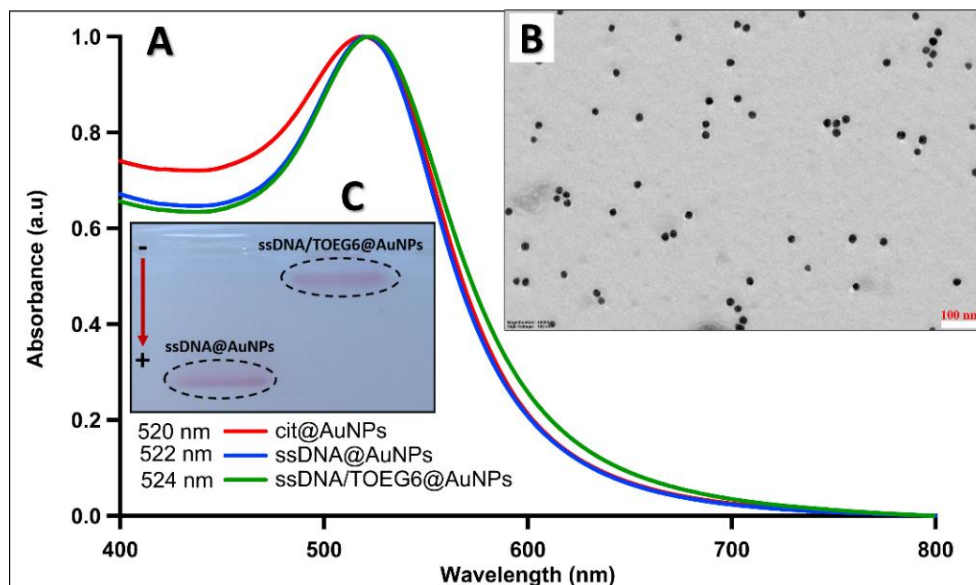


**Figure 58.5.** (A) UV/Vis absorption spectra of functionalized AuNPs at each step of mixed SAM formation, (B) TEM image of ssDNA/TOEG6@AuNPs, (C) Gel electrophoresis digital photograph of AuNPs passivated with ssDNA and the mixed SAM.

This explains the increase in size resulting in slower mobility and broadening in the peak as observed in **Figure 59.5A**. Additionally, we found that the area under the peak was 2.67 times larger than its counterpart for ssDNA@AuNPs. We note that any redshift facilitates the absorption peak to be closer to the excitation laser wavelength (532 nm) thus producing an increase TLS signal (**Figure 59.5A**). The possible configuration of adsorbed DNA strands on AuNP was derived from DLS readouts of the evolution of the hydrodynamic size ( $D_H$ ) as displayed in **Figure 59.5B**. The replacement of citrate ions adsorbed on the AuNP surface by thiolated DNA strands and TOEG6 molecules showed a significant increment in the hydrodynamic diameter ( $\sim 6$  nm) which is in consistent with the above-mentioned findings. It was reported that the upright conformation of DNA strands anchored on AuNP enhances the efficiency of the hybridization event. To confirm the functionality of our platform, we hybridized the system using a target DNA that is complementary to the ssDNA probe on the particle. Upon hybridization, the  $D_H$  of the particles further increased in agreement with the increased rigidity of dsDNA when compared to ssDNA demonstrating the preserved functionality of ssDNA coated AuNPs.

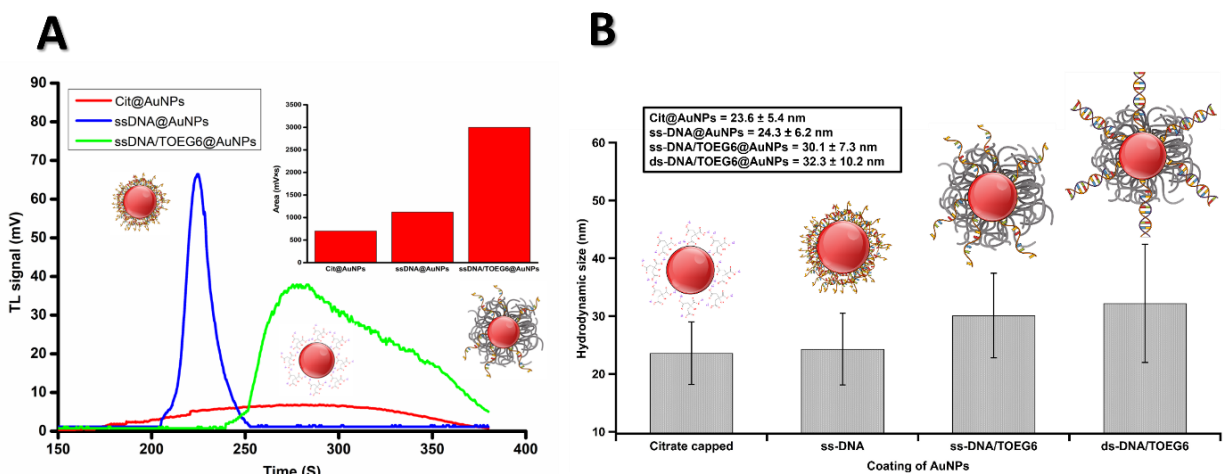


**Figure 59.5.** (A) Electropherogram of loaded samples; citrate capped AuNPs (**red**) and the conjugates with DNA only (**blue**) or with DNA and TOEG6 (**green**). **The inset** shows the area under the curve for each sample. (B) Summary of volume weighted DLS measurements After each step of functionalization and the cartoon illustrates possible configurations of adsorbed oligos on AuNP surface.

### 5.3.7 The stability of ssDNA/TOEG6@AuNPs in a physiological environment

Next, we aimed to look at the stability of the ssDNA/TOEG6@AuNPs and possible alterations in its optical properties. Several In vitro studies demonstrated that DNA-coated nanomaterials are prone to degradation in biological and physiological media (Alexander et al., 2012; Seferos et al., 2009; Song et al., 2015). Therefore, we performed our stability test by incubating AuNPs and AuNPs grafted with ssDNA/TOEG6 with 50% diluted human serum for 0.5, 4, and 24 h. As expected, the incubation of citrate-capped AuNPs with the serum resulted in a dramatic LSPR shift accompanied by a marked broadening of the spectrum due to nonspecific protein adsorption on the surface of AuNP (**Figure 60.5**). At variance, in the case of ssDNA/TOEG6@AuNPs, no broadening in the spectrum was observed, indicating that AuNPs remained highly monodispersed in the serum even after 24 h of incubation. It turns out that the presence of TOEG6 was able to effectively hinder the interaction between AuNP surface and proteins in the serum preventing aggregation in agreement with previously reported findings of the excellent stability of such nanosystem in a high salt concentration environment (Deka et al., 2015). These results are complementary to the stability profile of TOEG6 mediated ssDNA functionalized AuNPs.

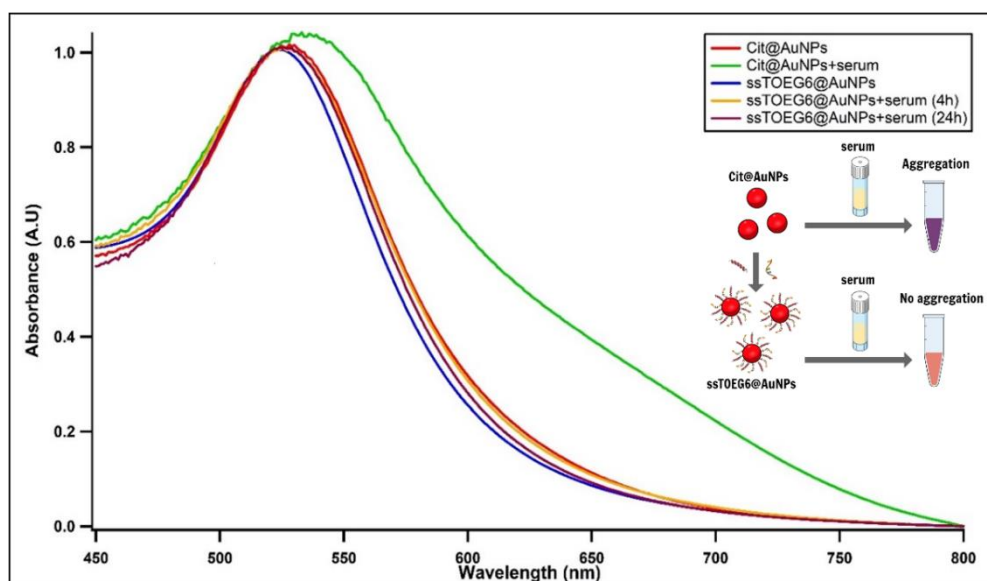


**Figure 60.5.** Normalized optical spectra for AuNPs incubated with 1:1 diluted human serum at various incubation time. The aggregation seen in the optical profile (**green**) displays the aggregation behavior of the bare particles in the serum. Once coated with the mixed-SAM, a remarkable stability in the other optical spectra up to 24 hours was observed.

### 5.3.8 The interaction between mixed-SAM coated AuNPs and the liposomes

Understanding the interaction between AuNPs and liposomes is crucial due to the numerous nano- and biotechnology applications of their combination. They can also be regarded as a model in research of nanomaterial interactions with lipid bilayers in cells and tissues. Experiments with liposome-nanoparticle composites have ranged from the development of potential drug delivery systems over better optical substrates to liposome stability using AuNPs (Allen & Cullis, 2013; Lum et al., 2017; Michel et al., 2013; Savarala et al., 2011). The interactions between vesicles and nanoparticles are influenced by a number of factors. These include, but are not limited to, the surface charge, the size of both the particles and the liposomes (Fošnarič et al., 2009; Savarala et al., 2011), the lipid composition of the membranes, as well as the surface chemistry of the particles (Alipour et al., 2017). Depending on the specific AuNPs, membrane and dispersant properties, various interaction outcomes have been observed. For instance, cationic or hydrophobically functionalized AuNPs (less than 5 nm) have been shown to be capable of being successfully internalized within the membrane bilayer (Rasch et al., 2010; Tatur et al., 2013). Anionic AuNP of the same size, on the other hand, only interact with the membrane's outer surface (Tatur et al., 2013). Furthermore, recent study has shown that citrate-stabilized AuNPs (15 nm) interact strongly with zwitterionic phosphocholine (PC) lipids, and that the development of AuNPs aggregates on liposome surfaces is dependent on lipid membrane fluidization and the presence of protein corona (Montis et al., 2014; Sugikawa et al., 2016; F. Wang et al., 2015; Wang & Liu, 2015). Herein, the aim was to obtain an insight into the fate of mixed-SAM coated AuNPs when interacting with lipid model membranes. We employed ssDNA/TOEG6@AuNPs with the same particle size and the formulation of unilamellar liposome: DOPC (1,2-dioleoyl-sn-glycero-3-phosphocholine). Assemblies of liposomes and coated AuNPs were obtained using reverse phase evaporation method, and the mixture (in Milli-Q water solvent) was analyzed with transmission electron microscopy (TEM). As clearly visible in all panels in **Figure 61.5**, the interaction between the two entities resulted in the formation of an inhomogeneous decoration of the lipid vesicles. Our observations are in agreement with previous studies where the aggregation of AuNPs (~15 nm) on the outer surface of PC membranes has been reported (Liu et al., 2018; F. Wang et al., 2015; Wang & Liu, 2015). The micrographs reveal different outcomes: absorption events of single particles, partial wrapping, and a linear cooperative absorption on the outer surface of the membrane (**Figure 61.5A-C**). Interestingly, very minor encapsulation events of the coated particles were spotted.

These scenarios reflect the interplay between adhesion and the elastic response of the liposome when the particles adsorb on the liposome's membrane surface.

As mentioned, earlier works looked into the interaction of 15 nm citrate-stabilized AuNPs with PC membranes (Sugikawa et al., 2016; F. Wang et al., 2015; Wang & Liu, 2015). These studies were carried out in the presence of salt. However, to explore the impact of salt on the hybrid system, we used a PBS solution instead of water to prepare the mixture. In TEM images in **Figure 62.5**, we mainly observed the presence of salt crystals with few stable liposomes. This instability could be attributed to salt, as it can weaken the electrostatic interactions between the individual particles, making disruption or particles-attached membranes challenging to accomplish. These findings highlight that the difference in ionic strength can drastically influence the interaction of lipids with the particles, which in turn, impact the stability of the entire hybrid system.

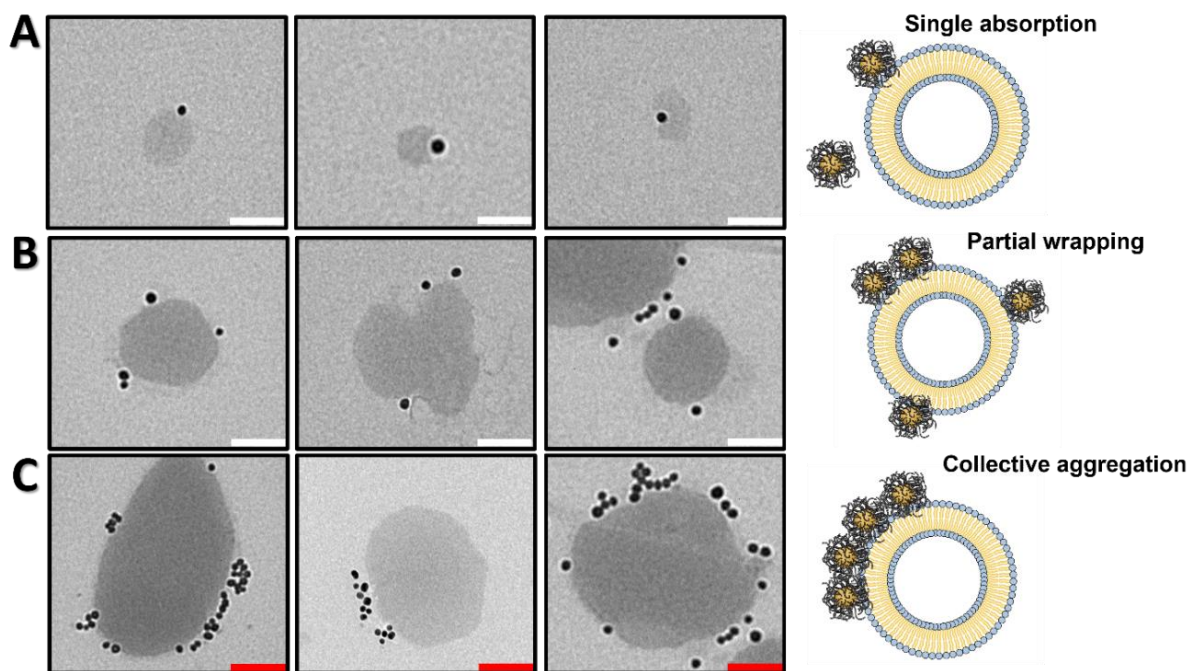


**Figure 61.5.** TEM micrographs of mixed-SAM coated AuNPs interacting with lipid model membranes. Scale bars: 150 nm (**white**), and 200 nm (**red**). Note the difference in the decoration density of the particles on the surface of the liposomes.

### 5.3.9 Elucidating the functionality of the mixed-SAM coated AuNPs

To elucidate our platform's functionality in immobilizing biomolecule of interest on AuNP surface through DDI, we used the Avidin-biotin complex as a proof-of-concept due to its extremely high affinity and fast kinetics (**Figure 63.5A**). Biotinylated-DNA conjugates were hybridized into DNA

probes on the AuNPs surface. Upon hybridization, no spectroscopic change was observed in the characteristic SPR absorption band for the DNA duplex-carrying particles compared to the non-hybridized counterparts, while the physical size evaluated through DLS revealed a 2 nm increment of the  $h D_H$  (**Figure 63.5B**). In contrast, upon the addition of Avidin to biotinylated-gold colloid, the  $D_H$  increase substantially up to 1.4  $\mu\text{m}$ , indicating the formation of AuNP aggregates due to the interparticle plasmonic coupling. To confirm that, a Remarkable SPR band shift was also observed (from 524 nm to around 569 nm with increasing concentrations of the Avidin (from 2  $\mu\text{g/mL}$  to 100  $\mu\text{g/mL}$ ) (**Figure 63.5C**). In fact, avidin is a tetrameric molecule that can sterically bind at least two biotinylated nanoparticles, promoting in this way the formation of a 3D network of particles. This finding was supported by a TEM micrograph that revealed large particle complexes induced by the presence of Avidin in the assay solution as shown in **Figure 63.5D**.

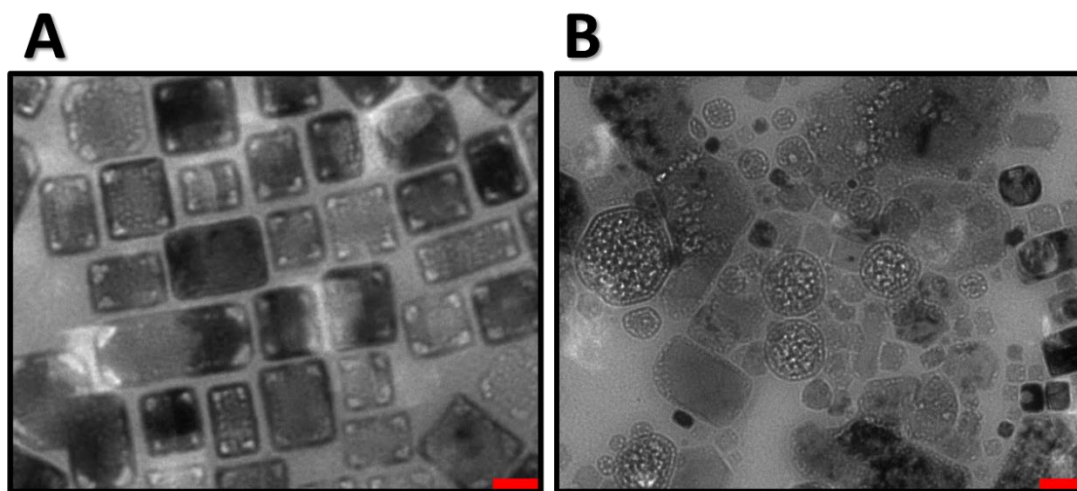


**Figure 62.5.** (A and B) TEM micrographs for the AuNPs-Liposomes mixture prepared in PBS. The presence of salt in PBS modulated the electrostatic interactions between the hybrid components rendering perturbation in the whole nano-Liposomes. Scale bar: 100 nm.

Having demonstrated that the system was binding avidin in the assay solution, we sought to explore it in the frame of cancer associated antigen detection. For such purpose, particles were conjugated with C8 nanobodies. Nanobodies (Nbs) are the smallest antibody fragments (~15 kDa) that function as active antigen-binding units derived from the variable domains (VHH) of unique camelid heavy-chain antibodies (HC-Abs) devoid of light chains (Hamers-Casterman et al., 1993). Nbs exhibit striking properties, including the small size, intrinsic stability, high affinity, and specificity which make them an important subject of study in a variety of research areas



(Hassanzadeh-Ghassabeh et al., 2013; Revets et al., 2005; Van de Broek et al., 2011). Nbs exhibit striking properties, including the small size, intrinsic stability, high affinity, and specificity which make them an important subject of study in a variety of research areas (Hassanzadeh-Ghassabeh et al., 2013; Revets et al., 2005; Van de Broek et al., 2011).

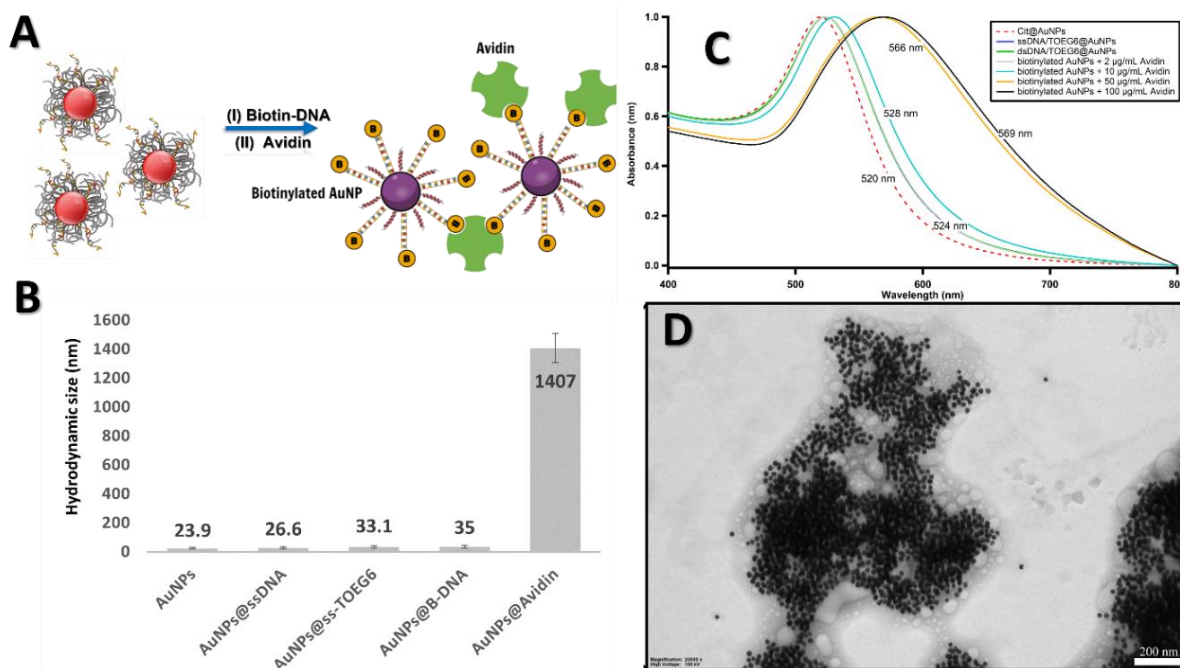


**Figure 63.5.** (A) Cartoon depicts the plasmonic coupling induced by the presence of the avidin in the assay solution. (B) DLS readouts on the functionalization steps. (C) UV/Vis spectra for Biotinylated AuNPs incubated with various concentrations of Avidin. The redshift in the LSPR indicates the interparticle crosslinking. (D) TEM micrograph displayed the NPs Avidin-induced aggregation ( $C_{\text{avidin}} = 35 \mu\text{g/mL}$ ). Scale bar: 200 nm.

In this study, AuNPs were labelled with a nanobody, termed C8, a specific *in silico* “optimized” antibody fragment designated to bind HER2-ECD to an epitope close to the one recognized by trastuzumab (Soler et al., 2021). The same ssDNA density was used as for the detection of the complementary biotinylated DNA. The functionalized AuNPs with the C8-modified conjugates. A concentration of 100 nM was chosen to guarantee the interaction of the antigen with the C8, which has shown a binding affinity of about 9 nM with growth factor receptors (1 and 2)(Monegal et al., 2009; Soler et al., 2021). As can be seen in **Figure 64.5A**, when the particles were hybridized with the C8-labelled DNA target, we observed a slight redshift in the SPR pointing to a successful conjugation of nanobodies to the particles. **Figure 64.5B** shows a gel electrophoresis photograph of particles at different steps of the surface modification. Among all the bands, Nb-terminated

AuNP conjugates (lane 6), had the slowest migration indicating the presence of C8 nanobodies on the AuNPs.

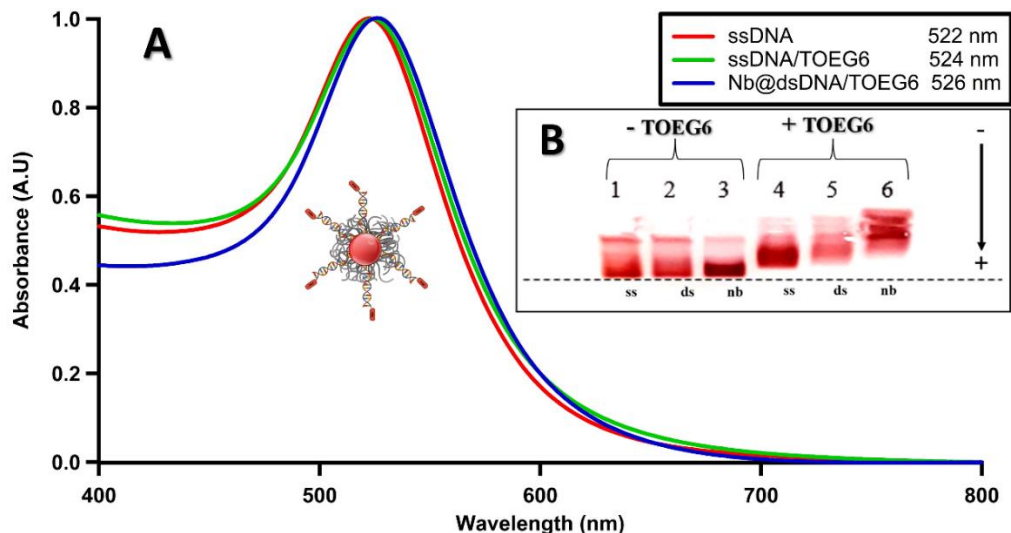


**Figure 64.5.** (A) UV/Vis absorption spectra of Nanobody-terminated DNA/TOEG6@AuNPs. (B) Gel electrophoresis of AuNPs functionalized with: (1) ssDNA, (2) dsDNA (3) (dsDNA + C8 Nbs), (4) ssDNA/TOEG6, (5) dsDNA/TOEG6, (6) (dsDNA/TOEG6 + C8 Nbs). The arrow indicates the direction of the applied electric field, and the direction of migration.

### 5.3.10 Evaluating the binding capability of C8-terminated AuNPs

To assess the efficacy and the biorecognition capability of this nanosystem, we employed the commercially available protein HER2-ECD (MW = 70.2 kDa). The specific recognition and quantification of HER2-ECD represents an important goal in breast cancer treatment and can play a key role for devising new personalized therapeutic strategies. To this end, DLS and dot blot immunoassay measurements were initially performed to obtain insights about the binding affinity. As expected, DLS readouts showed a sequential increase in the average particle size (**Figure 65.5A**). For the immunological assay, C8-conjugated ssDNA was immobilized on a nitrocellulose membrane, then soaked into His-tagged HER2-containing solution. After incubation, an anti-His antibody was employed to detect the formation of the immunocomplex. As shown in (**Figure 65.5B**), C8-conjugated ssDNA were detected upon the interaction with the antigen, indicating successful binding (C8-ssDNA/HER2). In contrast, no signal was observed for the ssDNA without labelling with C8 nanobody (ssDNA/HER2). Next, the capability of forming a complex between gold nanoprobe and the target epitope was also evaluated by exposing, with a similar fashion, C8-



labeled AuNPs to the His-tagged HER2-ECD which also showed a noticeable response, albeit less intense. From these preliminary results, we concluded that the nanobodies linked to C8 decorated NPs were capable to capture the HER2-ECD protein from the solution down to 6.2 nM of the antigen. As further validation, we used MGEC-TLS implementation to quantitatively relate the biorecognition of the immunocomplex to the mobility of the particles. Since mobility is not an illustrative quantity, we measured the time required for the conjugates to reach the measurement point, as depicted in **Figure 66.5A**. In line with our expectation, the time needed for the immunoconjugates to travel the required distance consistently increases with the quantity of HER2-ECD up to 50 nM (**Figure 66.5B**). This resulted in a comprehensive trend which relates the concentration of loaded HER2-ECD to the MGEC-TLS signal acquisition time (the obtained signal when a sample passes the measurement point) (**Figure 66.5C**). It is interesting to note that the newly developed system demonstrated real time signal response and the capability of probing sub- $\mu\text{L}$  volume. More appealing, the device made use of online detection, instead of scanning in the gel and staining post electrophoresis, to offer better reproducibility, short running time and lower standard deviation in measurements.

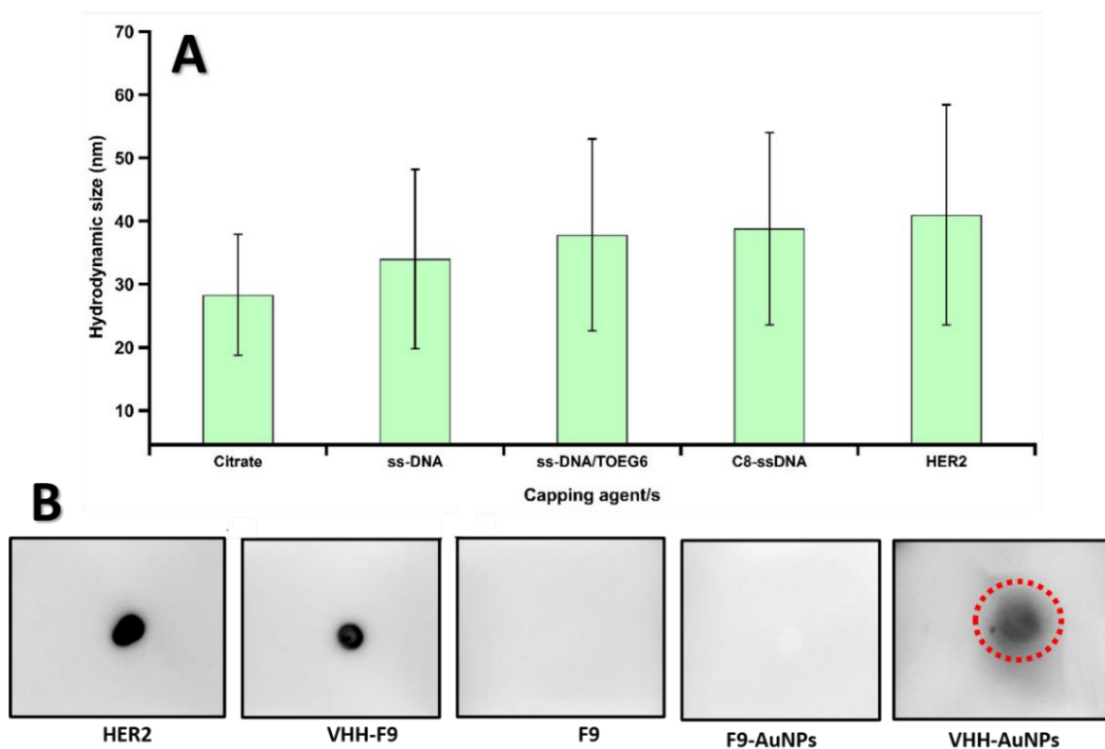


**Figure 65.5.** (A) Volume-weighted DLS analysis showed that the resultant HER2 bioconjugation was achieved by the increment of  $D_H$  size from 38 to 41 nm for C8-terminated AuNPs and HER2@AuNPs respectively can be attributed to the antigen recognition. (B) dot blot immunological assay optical readouts.

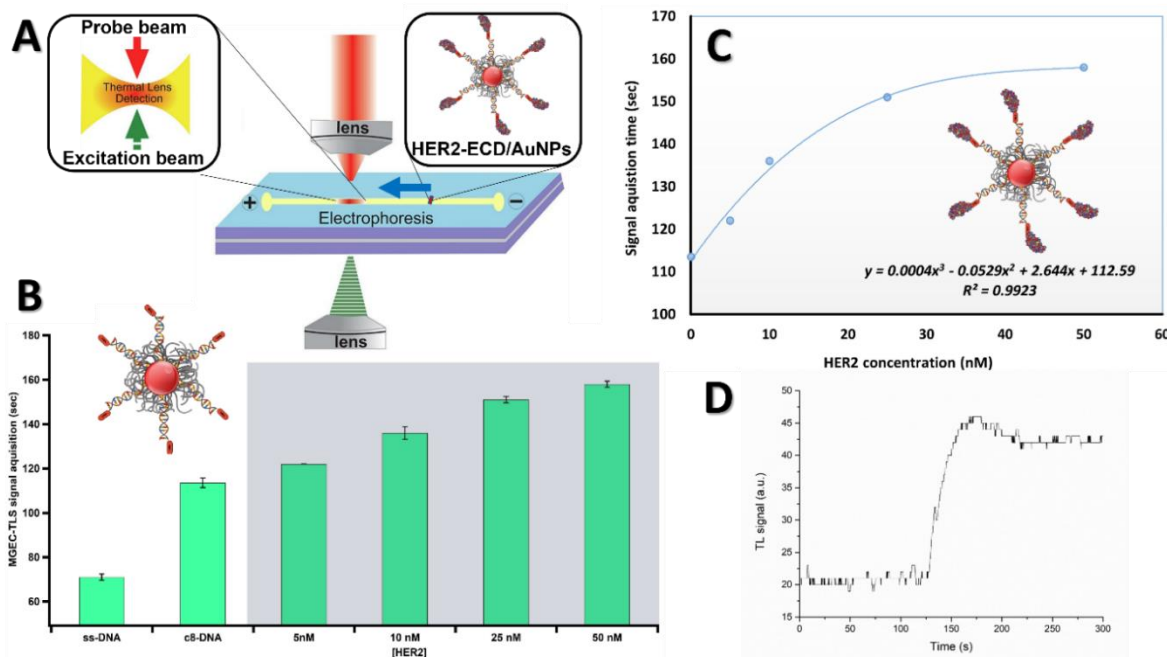


**Figure 66.5.** (A) A schematic illustrates of the MGEC-TLS design employed for investigating HER2-ECD binding to C8 decorated AuNPs. The resulted immunoconjugates migrate toward the positive anode crossing the measurement point. Note that the design does not need to use bulky cost devices and long running time as well as scanning of the gel post electrophoresis. (B) MGEC-TLS signal acquisition time as a function of different steps of surface coating of AuNPs. The concentration of the antigen was varied from 5-50 nM. (C) Calibration curve of HER2-ECD measured with MGEC-TLS. The signal acquisition time is plotted versus HER2-ECD concentration; experimental data was fitted with polynomial of third degree. (D) An example of a typical signal acquired during the measurements.

## 5.4 Conclusions

Nanoparticles decorated with biomolecules hold promise for various potential applications in biotechnology and biosensing. In this study, we further exploited the easiness of AuNPs surface functionalization by attaching thiolated ssDNA molecules (22 bases long) and an oligo (ethylene glycol) (TOEG6) terminated thiols forming a mixed self-assembled monolayer (mix-SAM). The bio-functionality of particles was ensured by conjugated DNA, and its remarkable stability in physiological environment was attained by TOEG6, which is capable of forming well packed films through Van der Waals interactions, passivation. We also demonstrated a rapid yet sensitive approach for online monitoring the surface coverage of ssDNA loaded on AuNPs using MGEC coupled with TLS. The design presented does not require long signal acquisition times, or tedious post-treatment steps including chemical modifications. With our implementation, we showed an excellent electrophoretic analysis of DNA strands attached to AuNPs and a rapid nanoparticle

separation in gel. Comparing with traditional GE techniques, we showed that our system could acquire results in remarkably shorter running times (<6 min) and consuming significantly fewer chemicals. Specifically, we showed that for smaller size AuNPs (~20 nm) and short DNA strands (<30 bases), 300 DNA/AuNPs density can fully coat the particles, which represent a conjugate with high stability. Online TLS-based MGEC offers a rapid and simple approach to discerning the surface coverage of oligonucleotides bound onto gold nanoparticles, which is crucial to develop a AuNPs-based biosensors.

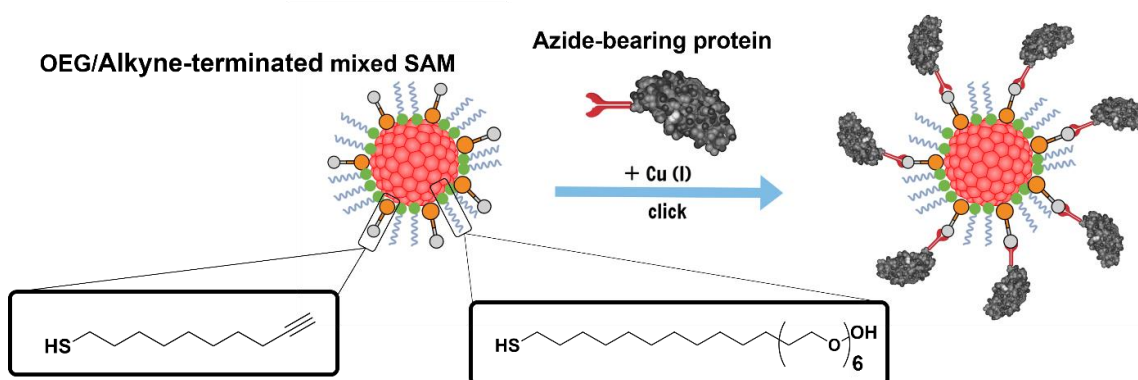
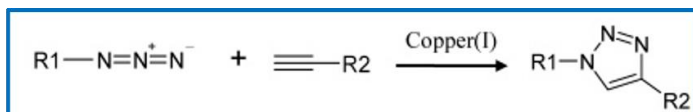
In addition, we employed lipid vesicles as a model membrane to investigate the mixed-SAM coated AuNP–membrane interaction. This model system has been chosen to mimic the interaction between nanosized particles and the surface of biological membranes. We found that AuNPs interacting with the vesicle undergo single absorption, partial wrapping, and linear cooperative absorption events on the membrane's outer surface. These findings should help understand better the critical initiating events in the development of nanotoxicity and the design of nanoparticle vectors for drug delivery.

Then, exploiting the DNA-directed immobilization (DDI) approach, we converted DNA/TOEG6 SAM surface into a biosensor surface; thanks to the Watson-Crick bio-affinity interaction, any binder chemically linked to an ssDNA target with a sequence complementary to the surface-bound ssDNA probes can be immobilized on the particle surface. As a proof of concept, we applied this platform to the detection of avidin, using localized surface plasmon resonance (LSPR), starting from hybridizing the mixed-SAM coated AuNPs with the biotinylated complementary DNA strands. Having demonstrated that the system was binding avidin in the assay solution, we sought to explore the design in the frame of cancer-associated antigen detection. For such purpose, particles were labelled with a nanobody (Nb), called C8, an antibody fragment designated to bind HER2-ECD to an epitope close to the one recognized by trastuzumab. Nb-AuNPs conjugates showed a noticeable change in LSPR band, hydrodynamic size, and the mobility in gel electrophoresis indicating successful immobilization of the biomolecule on the particle surface. Next, A simple, and rapid AuNPs-based dot-blot immunoassay was used for detecting HER2-ECD antigen down to a concentration of 440 ng/mL. The binding capability was further verified by using MGEC-TLS where the retardation of the immunocomplex as a function of the loaded HER2-ECD protein was quantified. Though further verification needed to ensure the platform recognition capability in a clinical sample, this study provides a methodology template that can contribute to

the development of a multifunctional platform based on the conjugation of DNA, protein, or protein fragments to AuNPs. The synergy of directed protein immobilization through DNA hybridization on plasmonic scaffolds introduces a new biosensing strategy with a faster detection time and label-free procedure (Asbaghi et al., 2021).

## Results and Discussion

### Application of click chemistry in nanoparticle surface modification



### 6.1 Motivation

To circumvent the limitation encountered when working in complex, non-purified biological fluids, the well-established copper-catalyzed azide-alkyne cycloaddition (CuAAC) was selected as an efficient, versatile, and convenient attachment strategy that can be widely applied for all kinds of molecules that carry an azide/alkyne group. Click chemistry integrated with functional nanoparticles have drawn increasing attention in biochemical assays due to its potentials in developing biosensors with effective signal transformation/amplification and facile signal readout for clinical diagnostic assays. However, there are few studies and restricted information available, particularly on the structural properties and stability of OEG/Alkyne mixed SAMs functionalized AuNPs, which are critical for developing better control over its surface properties. Our final goal is to conjugate the azide-tagged spike protein S1 of the SARS-COV2 receptor binding domain (SARS-COV-2 RBD) to the alkyne-modified nanoparticle scaffold, using the above-mentioned strategy in order to obtain a platform to recognize target antibodies. This platform holds great

potential to serve as a cost-effective and highly specific alternative to classical immunoassays and commercially rapid tests that lack quantitative readouts of the targeting analyte.

## 6.2 Introduction

Click chemistry is an excellent platform for biomedical applications, particularly for effective signal translation, surface modification, and nanomaterial bioconjugation (Chen et al., 2015; Haun et al., 2010; J. Wang et al., 2015; Yang et al., 2012). In 2001, the concept of "click chemistry" was introduced for the first time (Kolb et al., 2001). This new form of organic reaction is selective, orthogonal to most known reactions, and efficient at ambient temperature in aqueous solvents with no side products (Maiyun & Chen, 2015; Speers et al., 2003; Wu et al., 2004). High selectivity and yields are the most significant benefits of "click chemistry" when compared to conventional reactions, which enable control and flexibility for manipulating biological systems with high selectivity and speed in bio-reaction. Furthermore, because the reaction ligands of click chemistry are tiny molecules, biomacromolecules (antibodies, enzymes) or nanoparticles (NPs) can easily conjugate to them, making them appropriate for a wide range of labeling applications (Hoffmann et al., 2015; Walper et al., 2015). More notably, given the small size of the ligands in click chemistry, the bioconjugation process does not impair the activity of the biomolecules (Blizzard et al., 2015; Neef et al., 2015).

Four types of click chemistry reactions are commonly used in biochemical assays and biomedical applications: cycloaddition reaction (Cu (I)-catalyzed 1,3-dipolar cycloaddition of azides and alkynes and copper-free cycloadditions), nucleophilic ring-opening reaction, non-aldol carbonylation reaction, and carbon-carbon multiple bonds addition reaction. Cu(I)-catalyzed 1,3-dipolar cycloaddition of azides and alkynes (CuAAC) is the most popular and widely utilized reaction among all others. In the past decade, CuAAC has been broadly adopted as the signal transformation mechanism in nanosensors for detecting several types of targets, thereby establishing a new platform for biochemical investigation.

Surface coating of 2-D and 3-D substrates with self-assembled monolayers (SAMs) benefits significantly from click chemistry because it provides a more general and robust method of surface modification, allowing for the immobilization of a wide range of functionalities on the surfaces for applications in biochips, biosensors, antifouling interfaces, nanostructures, organic electronics and electroactive surfaces (Casalini et al., 2017; Collman et al., 2004; Lee, 2008; Shakiba et al.,

2015; Zheng et al., 2015). Similar to the applications of SAM used in SPR/Biacore sensors, which are powerful analytical methods for detecting and evaluating interactions of molecules on surfaces through the monitoring of the refractive index of the surrounding media (Holzer et al., 2017; Sajfutdinow et al., 2017; Schasfoort, 2017; Wang et al., 2017). Previously, azide-terminated alkanethiol SAMs were investigated for surface modification via the CuAAC reaction with alkyne-containing species (Collman et al., 2004; Yan et al., 2016). Previous studies have demonstrated CuAAC reactions for functionalizing azide-terminated-SAMs with peptides, ferrocene, polymers, and biotins (Dubacheva et al., 2010; Dugger & Webb, 2015; Gallardo & Webb, 2012; Hudalla & Murphy, 2009; Raigoza et al., 2017; Shakiba et al., 2015). Also, SAMs having both a N<sub>3</sub>-terminal group and an OEG unit have been described in previous studies. For instance, azide-terminated OEG structures were used in mixed SAMs on AuNPs and then cross-coupled with peptides to make biomimetic materials (Lebitania et al., 2021). Similarly, luciferase was conjugated to AuNPs via click chemistry and an intein-mediated ligation, followed by the measurement of protease activity using the AuNP-quenched BL (Y.-P. Kim et al., 2010). In another study, acetylene-functionalized thermomyces lanuginosus lipase has been attached to azide-functionalized water-soluble AuNPs under retention of enzymatic activity (Brennan et al., 2006). In addition, Zheng *et al.* described azide-terminated SAMs functionalized with tetra(ethylene glycol)-substituted phenyl-capped bithiophene for bio-sensing applications, with the ethylene glycol group inhibiting non-specific protein adsorption (Zheng et al., 2015). However, though OEG/alkyne-terminated mixed-SAM is expected to exhibit both cross-coupling activity and adsorption resistance, there are only a few reports on the properties of alkyne-terminated mixed-SAMs functionalized AuNPs despite their importance.

Herein, we demonstrate a surface modification mixed-ligand alkyne-functionalized AuNPs that react with a large scope of azide to produce highly stable and water-dispersible NPs. with a minimalist coating strategy, we obtained clickable, highly stable, and water-dispersible NPs. To demonstrate the functionality of the modified nanoparticles, azide-modified dyes (AF594-Azide), as model compounds, was covalently linked to the nanoparticle surface by showing that AuNPs efficiently quenched the emission from the upon the clicking reaction. This strategy was used for the purpose of heading toward our goal of creating a highly stable, sensitive, and easy to use platform for biomolecule immobilization, conjugation and biosensing, we envisioned the findings presented here on the plasmonic substrate together with the local cross-coupling activity of the

product provide essential information for surface chemistries, particularly for abovementioned applications.

## 6.3 Results and discussion

### 6.3.1 Characterization of optimization of mixed-SAM AuNPs

As building blocks, 13 nm Citrate-stabilized particles were freshly prepared as previously described. Representative TEM micrograph and DLS measurement are shown in the **Appendix 4**. In the first step, various concentrations of TOEG6 (up 2.5  $\mu\text{M}$ ) were mixed with suspension of colloidal gold to determine the required amount of the bio-repellent molecule to fully passivate the particles and permit stability in an electrolyte solution. As seen in **Figure 67.6A**, a fully covered SAM was formed on the nanoparticle with 2.5 $\mu\text{M}$  of TOEG6, with no perturbation in the particle optical properties, and tolerating salt concentrations up to 150 mM (PBS solution). Interestingly, TOEG6 coated NPs in water solvent were not highly stable when  $\text{CuSO}_4$  was added and revealed a substantial shift in the surface plasmon band indicating the onset of agglomeration (**Figure 67.6B**). At variance, when a mixture of 1:1 diluted ethanol with water was employed as a solvent, the particles were extremely stable and can be centrifuged, and resuspended in same aqueous mixture several times without significant loss of material. therefore, we continued the preparations in this condition. Next, to alter the surface density of self-assembling ligands, colloidal suspensions of AuNPs conjugated with both Alkyne and TOEG6 ligands were prepared by adding either a set amount of Alkyne molecules and various amounts of TOEG6, or vice versa. As clearly displayed from the optical UV/Vis spectra in **Figure 67.6C**, all the modified particles exhibited identical surface plasmon bands (SPBs) with no observable sign of aggregations except for the 1:1<sub>c:c</sub> sample. The products were subjected to analysis by gel electrophoresis (1.0% agarose gel, 80 V, 45 min). **Figure 67.6D** shows a gel comparing the particles treated with the different ratio of the ligands and subsequently conjugated with copper (I) catalyst. The result indicates qualitatively the conjugation of the copper ions to the particles in lanes (3-5) corresponding to TOEG6 concentration of 1.5, 2, and 2.5  $\mu\text{M}$ , respectively. The lower mobility of the reaction products in lanes 3-5 is due to the covalent attachment of positively charged ions to the modified particles. However, we selected the ratio of 5: 2.5  $\mu\text{M}$  as it was observed the most stable and dispersible particles during preparation.



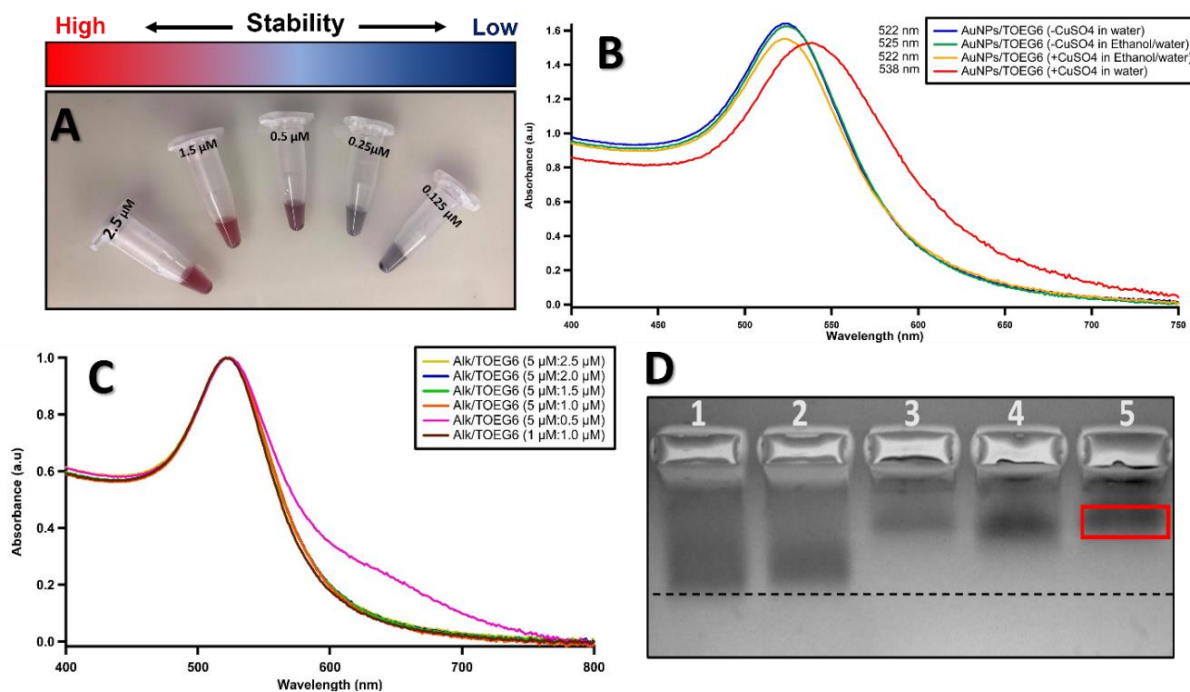


**Figure 67.6.** (A) digital photograph of AuNPs mixed with various concentrations of TOEG6. (B) optical profile of AuNPs capped with TOEG6 in a  $\text{CuSO}_4$  containing solutions with their corresponding references. (C) UV/Vis spectra of AuNPs functionalized with different ratios of TOEG6 and alkyne-terminated ligands. (D) Gel electrophoresis bands for the alkyne/TOEG6 ( $\mu\text{M}$ ) ratios of: (1) 1:1, (2) 5:1, (3) 5: 1.5, (4) 5: 2, and (5) 5: 2.5.

### 6.3.2 Conjugating the NPs with red-fluorescent azide-activated probe

To demonstrate the functionality of the Alkynated AuNPs, we employed a commercial fluorescent dye with an azide functional group, referred to as AF594, which is bright, red-fluorescent azide-activated probe that can be reacted with terminal alkynes on the particles via a copper-catalyzed click reaction (**Figure 68.6A**). The probe absorbs and emits at 590 and 617 nm, respectively. This dye can be attached to a variety of antibodies, peptides, proteins, tracers, and amplification substrates and is commonly used in imaging and flow cytometry to produce a stable signal. A calibration curve for the fluorescence signals was generated (**Appendix 5**). The particles were treated with 5 nM of AF594 fluorescent dye in the presence of THPTA/ $\text{CuSO}_4$ , and ascorbate to couple the AuNPs with azide-bearing fluorophore. The conjugated AuNPs displayed a higher mobility band shift in agarose gel electrophoresis (**lane 3 in Figure 68.6B**) when compared to the negative controls lacking either the AF594 (lane 1), or  $\text{CuSO}_4$  (lane 2). This result indicates that the Cu(I)-mediated click reaction enabled the conjugation of the particles to AF594. We further

confirmed this conjugation using UV/Vis spectroscopy. Because of their surface modification, the AF594 conjugated AuNPs had a slightly redshifted spectrum (525 nm) compared to the unconjugated AuNPs (Alkyne/TOEG6 coated NPs), which had a strong absorption at 521 nm (**Figure 68.6C**). When a fluorophore is placed in the proximity a metal particle with a high plasmon field, within 10 nm, the electrons involved of the fluorophore participating in the excitation/emission interact with the field. The contact alters the fluorescence emission level, either by quenching or enhancing it. This phenomenon was also observed as shown in **Figure 68.6C**. when AF594 was clicked to the gold surface, the fluorescence intensity significantly decreased as compared to the free AF594 in the assay solution. In **Figure 68.6D**, Similar optical response of the dye interacting with mixed-SAM decorated NPs is observed when one of the reaction components was removed (Cu(I)).

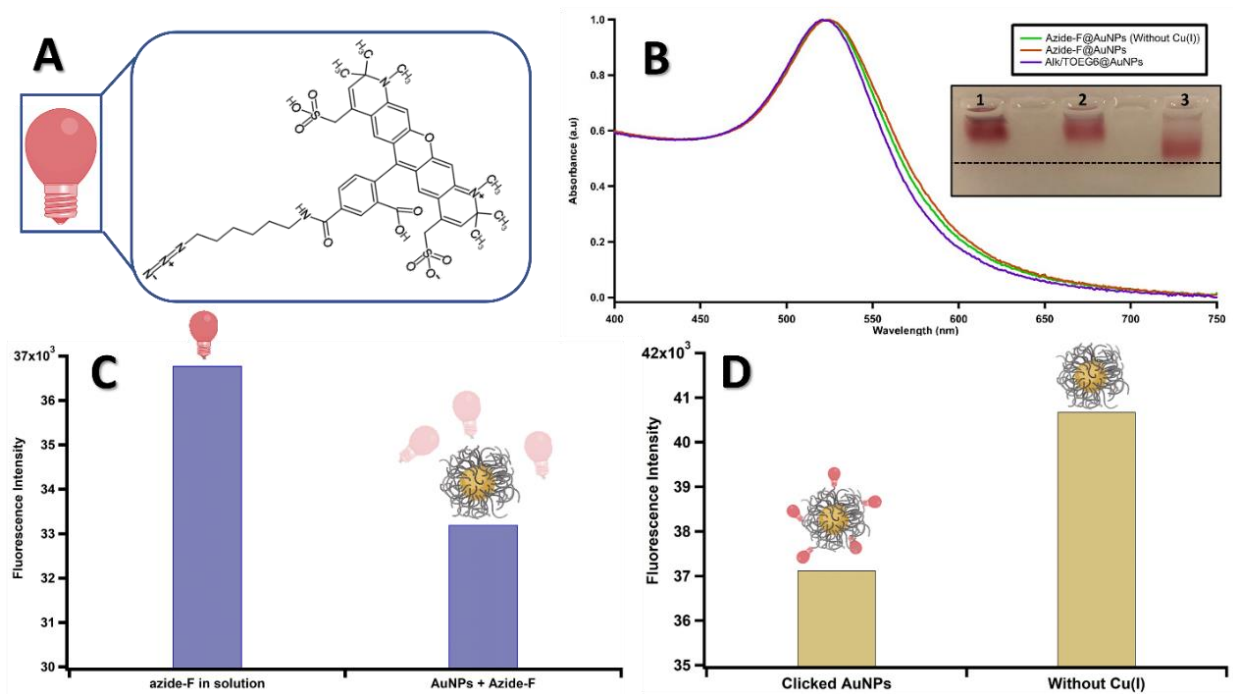


**Figure 68.6.** (A) Structural formula of AF594-Azide. (B) UV/Vis spectroscopy analysis and agarose gel electrophoresis (1%). The loaded samples in the gel analysis represented particles treated to varied conditions in which one of the reaction components was removed: without AF594 (**lane 1**), or without CuSO<sub>4</sub> (**lane 2**). (C) Fluorescence intensity measurements of free AF594 and clicked to NPs. (D) the absence of the Cu(I) indicated in the reaction solution confirms that AF594 was not clicked to the gold surface and remained “freer” in the assay solution, therefore, more fluorescence signals were recorded.

### 6.3.3 Confirmation of the conjugation through fluorescence amplified thermal lens spectroscopy.

To capitalize on the capabilities of thermal lens spectrometry (TLS), we devised an experiment based on fluorescence resonance energy transfer and thermal lens spectrometry (FRET-TLS). We hypothesized that if AF594 molecules bind to the surface of AuNPs via the performed click reaction, the distance between the AF594 and AuNPs must be reduced, and the energy absorbed by AF594 should be transferred to AuNPs and enhance the thermal lens effect, as depicted in **Figure 69.6**. Since such phenomenon requires a specific distance (less than 10 nm) between the acceptor and the donor, interactions such as covalent bonding is required. In our case, once complexes between the plasmonic NPs and AF594 are formed as a result of the click reaction, a FRET process occurs in which energy is transferred from the excited donor to the acceptor, resulting in a decrease in the donor's fluorescence emission. AF594 excites at 590 nm and exhibits an emission at 617 nm. As we demonstrated before, the fluorescence of AF594 reduces in the presence of AuNPs due to FRET. In various experimental conditions, the impact of AuNP on fluorescence behavior was investigated with the TLS technique. It is clearly shown in **Figure 70.6A** that the thermal lens of AF594 alone is very low, not surprisingly, as fluorescence molecules indicate an insignificant thermal lens effect because they emit a significant part of their excited energy in the form of radiation de-excitation (Shokoufi & Vaziri Heshi, 2021; Vaziri Heshi & Shokoufi, 2021). In the absence ascorbate and the  $\text{CuSO}_4$ , the two components required for the click reaction, the figure similarly displayed higher TL signals which can be attributed to the presence of plasmonic AuNPs. In the CuAAC reaction, sodium ascorbate is generally utilized as a reducing agent to reduce Cu(II) to Cu (I). Cu(II) salts such as  $\text{CuSO}_4$  can be used to make active Cu(I) catalyst. However, an enhancement in the TL signal was observed for clicked AF594 to AuNPs. As described before, the thermal lens effect emanates from the absorption of AF594 and the energy transfer to AuNPs using the FRET mechanism in the focal point of the laser beam. The effect of the dye concentration varied from 0 to 100 nM was also investigated. As **Figure 70.6B** shows, the TL signal increases substantially at concentrations below 25 nM; upon increasing the concentrations, the TL signal does not rise considerably, indicating AuNP surface saturation.

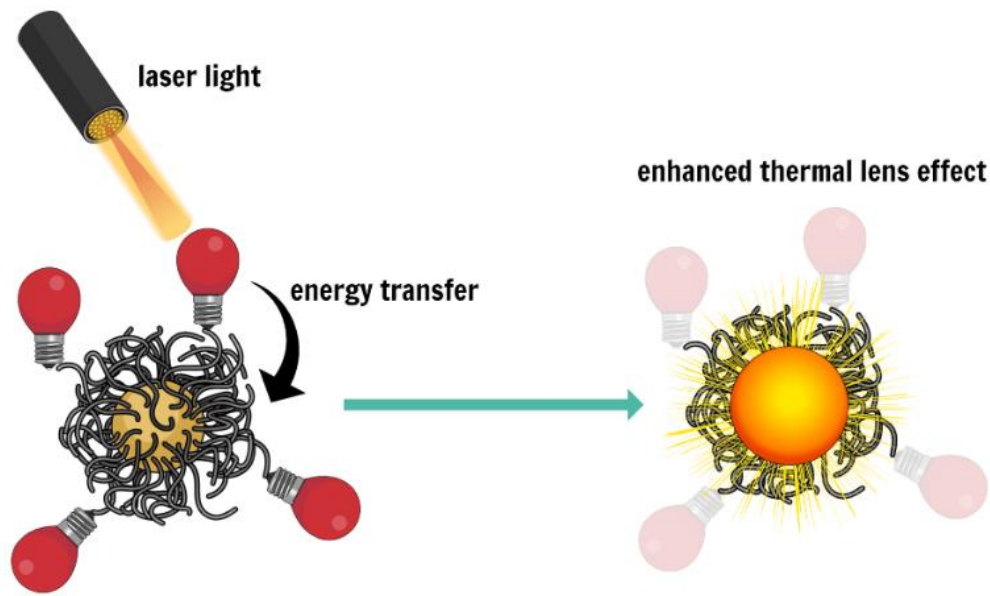


**Figure 69.6.** Schematic illustrates the amplified thermal lens effect induced by fluorescence energy transfer.

### 6.3.4 Attempting the formation of click chemistry mediated assembly of AuNPs

To further demonstrate the practicability of this nanosystem, we thought to implement the CuAAC reaction and functionalized AuNPs for designing a colorimetric-based assay that allows quantitative determination of the azide bearing entities, if a colloidal solution of azide-modified AuNPs is prepared, a tethering reaction between azide- and alkyne-modified AuNPs, may result in aggregation with a color change of the solution (**Appendix 6**). To begin, we screened different ratios of thiolated azide ( $\text{HS-PEG}_3\text{-CH}_2\text{CH}_2\text{N}_3$ ) to determine the design parameter for colloidal stability. As shown in **Figure 71.6A**, the particles do not show any colloidal stability as visually indicated by the blue color of the solutions. This instability of AuNP modified with azide functionality in aqueous media was previously reported, which presumably attributed to the charge neutral and hydrophobic property of azides (Elliott III et al., 2017; Mori & Sakurai, 2021; Sakurai et al., 2018). Therefore, we co-functionalized the particles with a hydrophilic TOEG3 as a spacer to achieve colloidal stability of the azide-presenting AuNPs. Contrary to expectations in the original design, the particle stability remained poor despite adjusting the ratio between the two different ligands (**Appendix 7**). By replacing TOEG3 with TOEG6 spacer, the product displays

clear reddish solution with no apparent agglomeration, which was consistent with the UV/Vis spectrum and DLS measurements (**Figure 71.6B&C**).

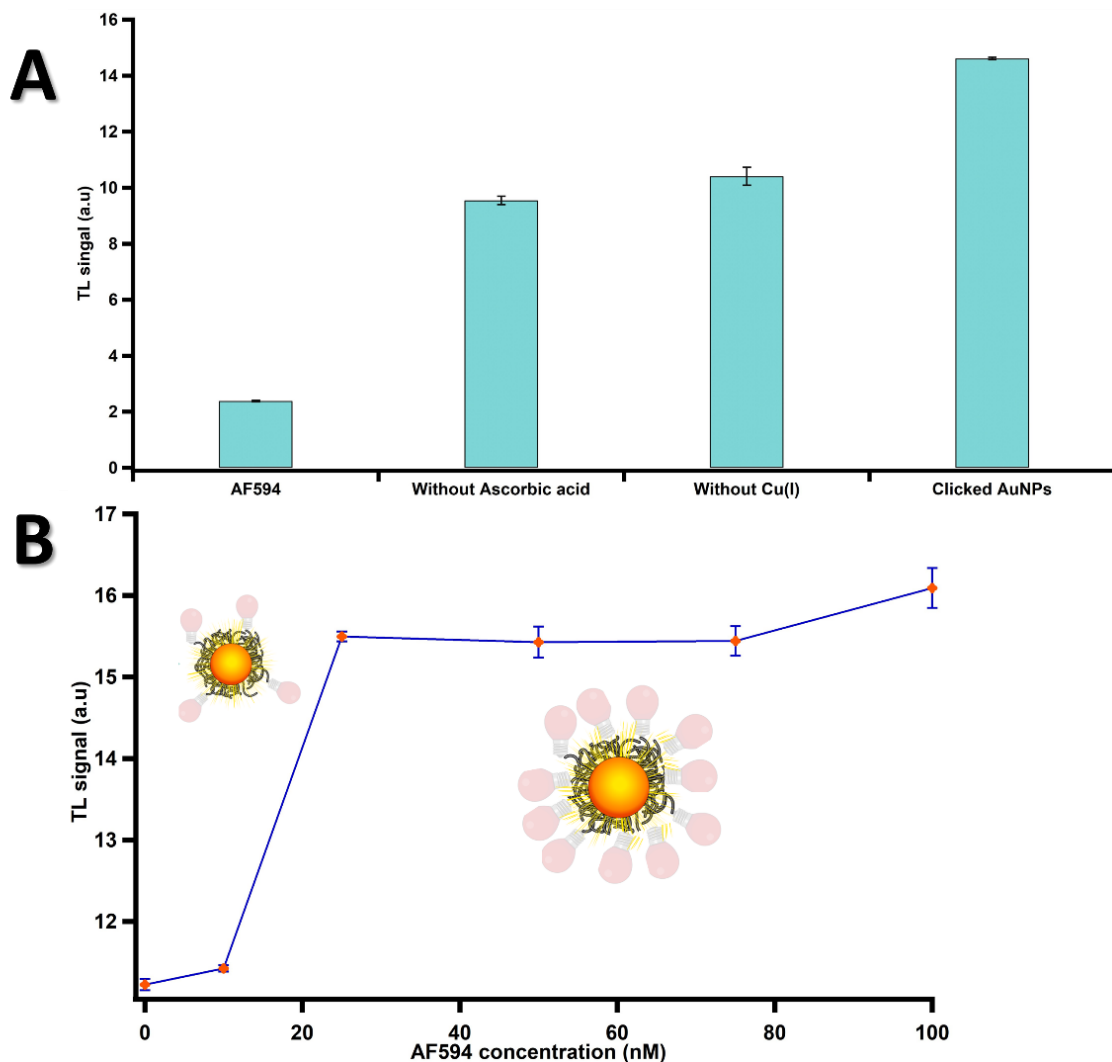


**Figure 70.6.** TL signals obtained: (**A**) for AuNPs and AF594 at various experimental conditions. (**B**) as a function of the dye concentration. The measurements were run in triplicate.

Next, the utility of azide-AuNPs was tested by subjecting them to copper-promoted azide-alkyne cyclization with clicked Alkyne/TOEG6 probes. Digital and TEM Images (**Figure 71.6D**) of the mixtures of the functionalized AuNPs reveal intact particles with no sign of agglomeration. The clusterization of the particles observed in the figure is attributed to the modulation of electrostatic interactions between the functionalized particles. This behavior is indicative of the failure of the coupling reaction between the two batches. The most plausible explanation is related to the

relatively longer TOEG6 spacer (HS-C<sub>11</sub>-EG<sub>6</sub>OH) in comparison with the azide-tagged ligand which sterically hindered the azide-AuNPs to crosslink with the alkyne-terminated AuNPs through CuAAC. This could be partially supported by the identical hydrodynamic size ( $D_H$ ) obtained for TOEG6, and azide-TOEG6 mixed SAM coated AuNPs (**Figure 71.6B**). Thus, we concluded that the incorporation of the thiolated azide during the synthesis of AuNPs would be a solution to circumvent the abovementioned challenge.

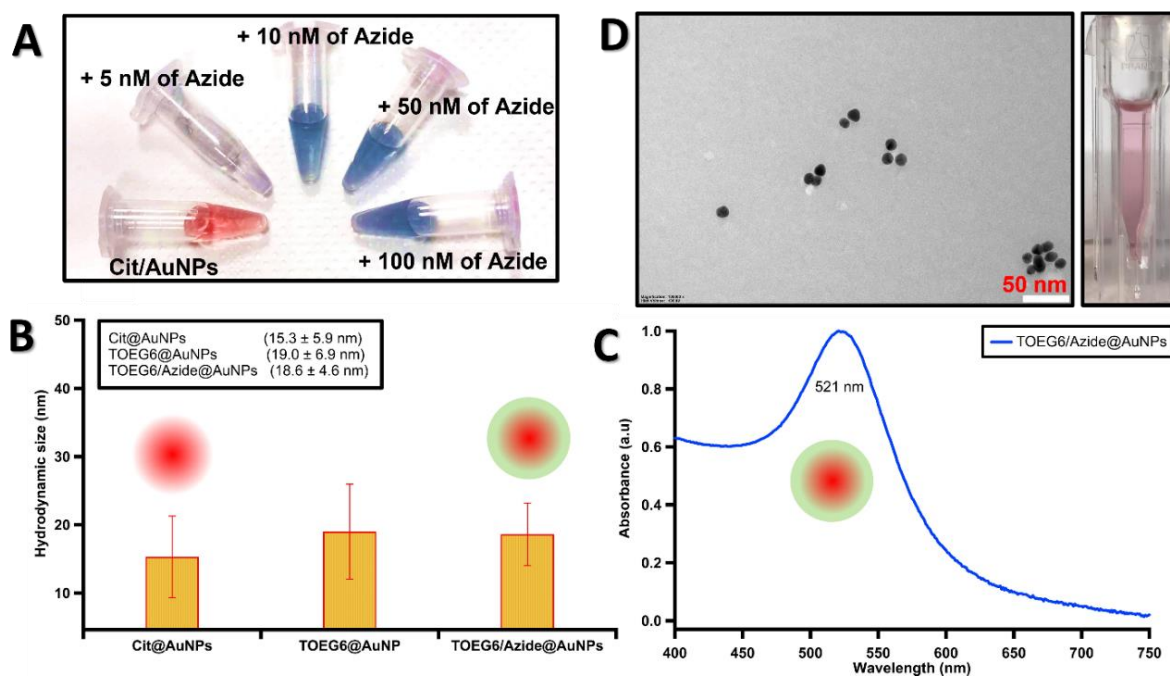


**Figure 71.6.** (A) Intended click-chemistry-mediated colorimetric assay design with two types of AuNPs, each modified with thiols terminated with an azide or alkyne functional group. (B) Digital photographs of AuNPs treated with various concentrations of azide-tagged ligand. (C) DLS measurements showed the slight change in the hydrodynamic size of AuNPs upon functionalization with Azide/TOEG6 ligands. (D) Optical profile of Azide/TOEG6 functionalized AuNPs.

## 6.4 Conclusions

For the preparation of tailored nanohybrid products, nanoparticles with functional groups that can be readily conjugated (e.g., via click chemistry) are vital. Because the azide/alkyne functional groups and their conjugation are selective, essentially inert to water, oxygen, most biological molecules, and are tolerant of a wide range of solvents, temperatures, and pH values, we hypothesized that an assay based on such chemistry could have a multitude of uses. The central

idea of this work was to use AuNPs as plasmonic scaffolds, decorated with Azide-bearing binders mixed with OEG molecules, to tune the surface density of the attached macromolecules and to minimize nonspecific binding events. For this purpose, alkyne coated AuNPs are prepared by grafting Alkyne-end ligand on the surface of citrate-stabilized nanoparticles. To maintain AuNPs stably dispersed, we employed the commercially available TOEG6 alkanethiol. The alkyne/TOEG6 functionalized AuNPs were purified by repeated centrifugation and redispersion in H<sub>2</sub>O/EtOH, to obtain a deep reddish solution. This mixture was characterized using UV/Vis, Gel electrophoresis showed the ligands were successfully grafted onto the AuNP surface rendering such particles compatible with biological buffers. To assess the functionality of the prepared NPs, azide-labeled fluorescent dye, referred to as AF594, was clicked AuNPs by incubating an excess of AF594 and Cu(I) catalyst with the nanoparticle suspensions at room temperature overnight. The product was thoroughly characterized via UV/Vis, gel electrophoresis, Fluorescence intensity measurements. The mixture of the clicked particles exhibits a characteristic plasmon absorption band at 525 nm. Also, the higher mobility of the reaction product is attributed to the covalent attachment of AF594 molecules to the particles. The modulation of surface charge overcompensates here the impact of the increased hydrodynamic size of the particles. The identical mobility of the two different control samples emphasizes this outcome. The fluorescence intensity measurements reveals a lower intensity readouts indicating quenching of fluorescence. Taken together, these results indicate qualitatively the successful formation of Azide-nanoparticle conjugates by click chemistry. Further, a novel and sensitive assay based on TLS has been exploited for the quantitative assessment of AF594 and AuNP conjugation. The thermal lens of AF594, as fluorescence molecules, has been enhanced upon the covalent attachment with AuNPs through the energy transfer mechanism. We also tested the effects of increasing the concentration of AF594 in the solutions up to 100 nM. We deduced from the readout that the minimum concentration of AF594 before causing a signal saturation is about 25 nM. However, before the present nanosystem could be applied for protein detection and quantification assays, we thought of a colorimetric-based approach to determine the practicality of our design. For this purpose, we prepared a new clickable AuNPs terminated with azide groups. We explored the design of probe by varying ratios of azide groups, and spacer moieties on AuNPs to achieve colloidal stability. The reactivity of the product was assessed by incubating the azide-AuNPs with previously prepared alkyne-tagged counterparts. The findings demonstrated that the click reaction between the two batches was not

achieved due to the buried azide in the mixed SAM. Therefore, the incorporation of the azide ligands during the synthesis of AuNPs in which the exposed azide in the AuNP surface can readily undergo click reactions with alkynes. In summary, we demonstrated here that the coupling chemistry used with carefully optimized mixed-SAM is generic and potentially transferable to other active structures of different biomolecular functionalities. For that, efforts in our group are being made to improve and extend current work to application in the desired bioassays.



## Summary and outlooks for future research

### 7.1 Summary

The goal of this doctoral thesis was to explore the use of functionalized AuNPs as a model system to design nanoplasmonic-based assay platforms for small molecules, biomarkers, and antibodies sensing. The broad aim lies in having a design methodology that can be geared to pathogen diagnostic or even cancer treatment applications by controlling the surface chemistry of the assembled structure. In this framework, our strategy was based on careful optimization of the molecular organization on the nanoparticles through self-assembling for the specific biorecognition; going beyond the current sensitivity limitations of LSPR by exploiting novel thermo-optical spectroscopies coupled with the bioanalytical capabilities of gel electrophoresis. We particularly focused on this thesis on the followings:

- i) It is well-known that monoclonal antibody-based immunotherapy is one of the pillars of cancer treatment. However, for an efficient and personalized approach to the therapy, a quantitative evaluation of the right dose for each patient is required. Responding to this need, *in chapter 4*, we developed a simple, label-free, and rapid approach to quantify trastuzumab, a humanized IgG1 monoclonal antibody used against human epidermal growth factor receptor 2 (HER2), overexpressed in breast cancer patients, based on localized surface plasmon resonance (LSPR). The central idea of this work was to use AuNPs as plasmonic scaffolds, decorated with HER2 binders mixed with oligo-ethylene glycol (OEG) molecules, to tune the surface density of the attached macromolecules and to minimize nonspecific binding events. Specifically, we characterized and optimized a self-assembled monolayer of mixed alkylthiols terminated with nitrilotriacetic acid (NTA), and OEG3 as a spacing ligand to achieve both excellent dispersibility and high reliability in protein immobilization. The successful immobilization of histidine-tagged HER2 (His-tagged HER2) on NTA via cobalt (II) chelates was demonstrated, confirming the fully functional attachment of the proteins to the AuNP surface. The proposed design

demonstrates the capability of producing a clear readout that enables the transduction of a trastuzumab/HER2 binding event into optical signals based on the wavelength shifts in LSPR, which allowed for detecting clinically relevant concentrations of trastuzumab down to 300 ng/mL in the buffer and 2  $\mu$ g/mL in the diluted serum. This strategy was found to be fast and highly specific to Trastuzumab. These findings make the present platform an auspicious tool for developing affordable bio-nanosensors.

- ii)** *In chapter 5*, we highlighted the utility of a DNA-directed immobilization (DDI) approach as an efficient strategy for decorating AuNPs surface with a broad class of bifunctional molecules, benefiting from the self-assembly capabilities of bioconjugates of DNA and proteins. The bifunctional AuNP (approximately 20 nm) surface was prepared by site-directed immobilization of biomolecule-DNA conjugates onto a mixed-SAM composed of ssDNA (22 bases long) and TOEG6 terminated thiols. The ssDNA/TOEG6 mixed-SAM is very stable, provides a protein-resistant substrate, and allows for reasonable control over the surface density of the DNA probe. Since such DNA-based strategy is also utilized to construct a biosensor, the bio-repellent TOEG6 spacer is crucial for proper complementary DNA-target conjugate placement. It also reduces the possibility of false detections due to nonspecific adsorption. Besides, we reported a novel approach based on a miniaturized gel electrophoresis chip (MGEC) integrated with online thermal lens detection for monitoring the amount of DNA on the surface of AuNPs. Due to high spatial and temporal resolution of the thermal lens detection system, our approach enables extremely small differences in the electrophoretic mobility of the particles to be resolved. Hence, small differences in the DNA surface density (55–275 nM) on the particles can be easily distinguished in short time (<6 min), not otherwise detectable using conventional UV/Vis spectrophotometers. Also, we looked at how these mixed-SAM coated AuNPs interacted with synthetic liposomes. Our qualitative investigation revealed that in the liposome-based system, these particles do not need to be covalently coupled to the vesicles since the NPs remain in close contact without requiring a direct tether. Furthermore, we demonstrated the feasibility of employing protein-DNA conjugates to convert a DNA/OEG mixed-SAM surface into a biosensor surface and then applied this platform to the detection of HER2-ECD through multiple approaches, including the novel MGEC-TLS technique. This study provides a

methodology template that can contribute to the development of a multifunctional platform based on the conjugation of DNA, protein, or protein fragments to AuNPs.

- iii)** Owing to the multitude of merits of the click chemistry approach, including; (i) being an efficient chemoselective reaction that can be used to functionalize biomolecules and (ii) its workability in an aqueous medium with applications in the complex physiological matrix. *In chapter 6*, we described the use of click-chemistry-based technique to site-specifically conjugate biomolecules to AuNPs for sensing applications. We optimized the conditions for the conjugation of Alkyne functionalized nanoparticles by grafting alkyne-tagged ligands and an OEG moiety as a hydrophilic spacer on the nanoparticle's surface. To test the feasibility of our clickable AuNPs as probe precursors for the cycloaddition reaction, we first chose Alexa Fluor<sup>®</sup> 594-Azide (AF594-Azide), as a model compound. UV/Vis, fluorescence intensity measurements, gel electrophoresis, and TLS were employed to demonstrate the functionality of the ligand-clicked probe in molecular labeling due to the coupling reaction. Besides, the impact of AF594 molecules bound to the surface of AuNPs through the covalent attachment in the thermal lens signal was investigated. The findings show that the energy absorbed by AF594 transferred to AuNPs causes enhancement of the thermal lens effect, which further confirms the successful conjugation. In an attempt to implement a simplified colorimetric assay based on cycloaddition reaction for the demonstration of the functionality of the mixed-SAM coated AuNPs. We aimed to explore a design that relies on minimal synthetic work and basic interface design to induce crosslinking between azide and alkyne-tagged AuNPs yielding a network of the dissimilar batches. Such work requires appropriate functionalization of AuNPs with azide and/or azide terminated groups. For this reason, we prepared clickable AuNPs with azide groups. To achieve colloidal stability, we designed the probe by changing azide and spacer ratios on AuNPs. By incubating azide-AuNPs with alkyne-tagged counterparts, no aggregation was observed as expected, which could be endowed to the buried azide in the mixed SAM prevented crosslinking. We deduced that by incorporating azide ligands during AuNP production allows the azide functionality to be exposed which may boost the chance to interact with alkynes-terminated particles.

## 7.2 Future research

### 7.2.1 NTA-based strategy

The proposed NTA-based strategy limited the quantification of trastuzumab in the buffer since the detection in the biological matrix was challenging. To circumvent this limitation, we propose to apply the same design methodology to magnetic-plasmonic core-shell NPs (MPNPs) as a hybrid scaffold as depicted in **Figure 72.7**. MPNPs of the same size ( $\sim 20$  nm) can be modified with  $\text{Co}^{2+}$  or  $\text{Ni}^{2+}$  so that they have an affinity for His-tagged proteins, as the MPNPs purification protocol itself does not need special equipment except for a magnet. Optimization of the design parameters such as the particle size and the incubation time are crucial for better outcomes. After that, the pre-prepared AuNPs coated with Co(II)-NTA/TOEG3 mixed SAM can be used to detect trastuzumab as a function of the serum concentration. The binding capacity of MPNPs with commercially available elution products can also be investigated.

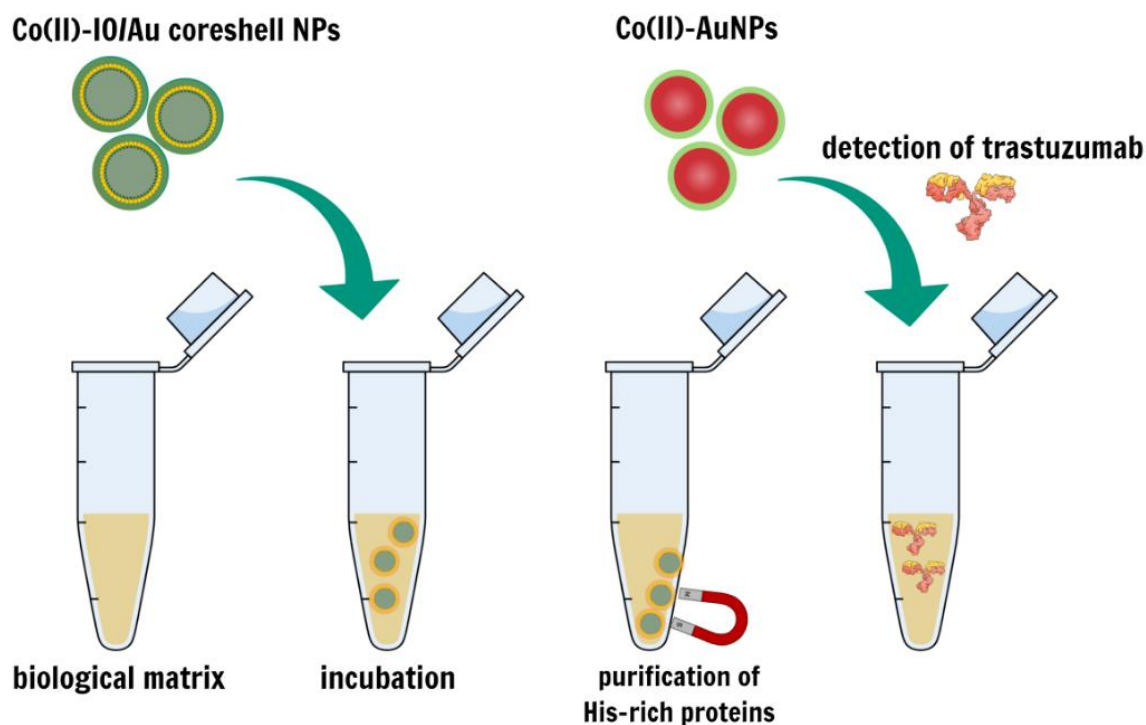


**Figure 72.7.** Schematic diagram of histidine-rich separation using MPNPs. Human serum is incubated with the chelator-charged capturing particles, allowing the proteins to bind. The bound proteins are collected by a magnet. Then, the pre-prepared AuNPs with Co(II)NTA/TOEG3 mixed-SAM are used to detect and quantify trastuzumab using LSPR sensing mechanism.

### 7.2.2 DNA-based strategy

Future perspectives to improve the presented method in sensibility might involve, for example, the exploitation of different sizes and shapes of gold nanoparticles to tune the SPR band. In particular, we could think of moving toward a colorimetric sandwich system based on DNA-mediated AuNPs assembly (**Figure 73.7**). Using two batches of AuNPs with attached two binders (one each) that recognize different epitopes of the same target (in the case of Her2-ECD, for instance, C8 and pertuzumab), it will be possible to create aggregates of nanoparticles mediated by the protein in solution. This system is expected to be more reactive even in the presence of small concentrations of the target protein.

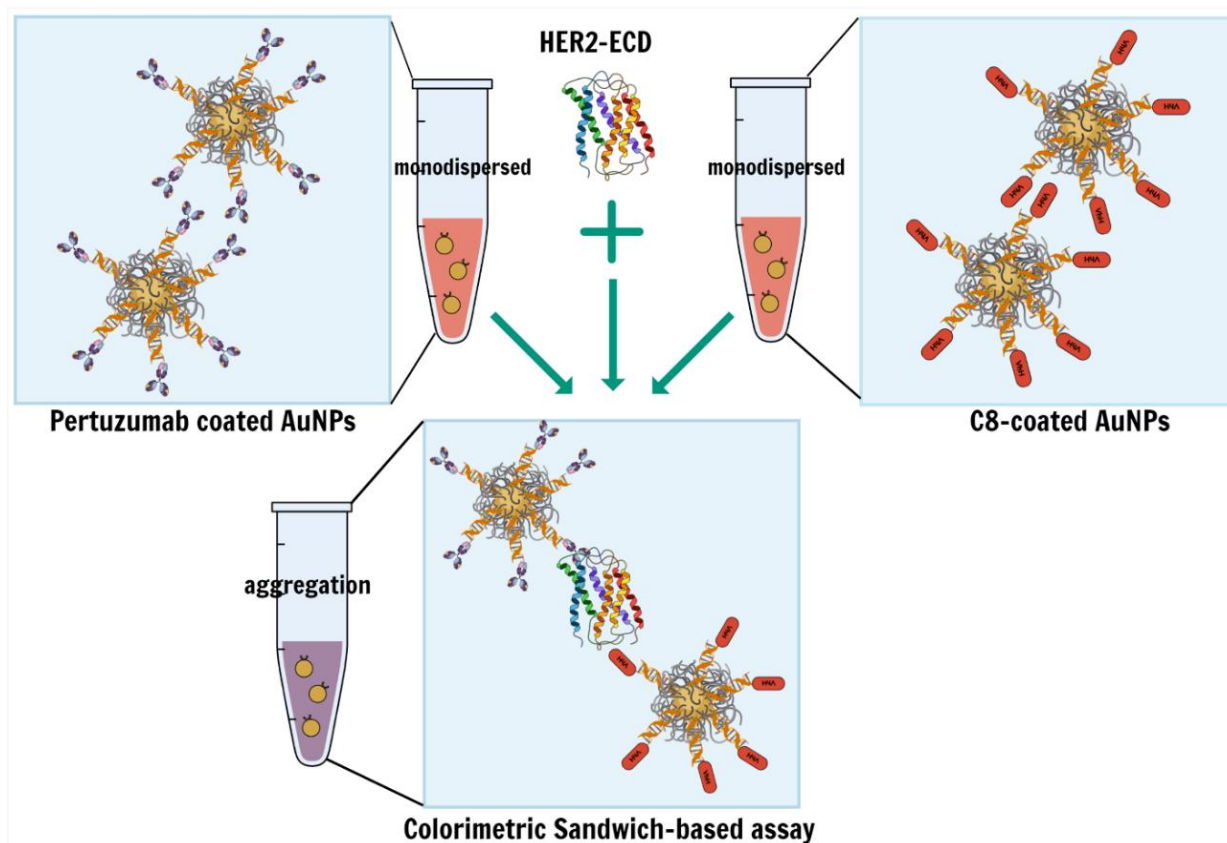


**Figure 73.7.** An illustration of a colorimetric sandwich assay based on DNA-mediated AuNPs assembly.

### 7.2.3 Click chemistry-based strategy

The primary reason for introducing the click chemistry in this thesis was to conjugate the azide-tagged spike protein S1 of the SARS-COV2 receptor-binding domain (SARS-COV-2 RBD) to the

alkyne-modified nanoparticle scaffold to recognize the target antibodies. However, obtaining a decent yield of RBD protein for azide modification was somewhat challenging. Also, the recognition ability of His-tagged RBD produced by our collaborations did not show convincing results to proceed. Therefore, taken together, we decided to continue with the azide-tagged fluorophore and azide-terminated AuNPs. However, Further research should prioritize the simulation of the bioconjugation with a relatively economical commercial azide modified product such as BSA-tagged Azide. This protein is often used as a positive control for click chemistry-based enrichment of azide-tagged proteins. Bovine Serum Albumin (BSA) is chemically modified on a single cysteine residue with Azide-PEG3-Maleimide (MW 369.37). Such an experiment with an anti-BSA antibody which is readily within reach can give a better insight into the capability of the presented design for the desired purpose (**Figure 74.7**).

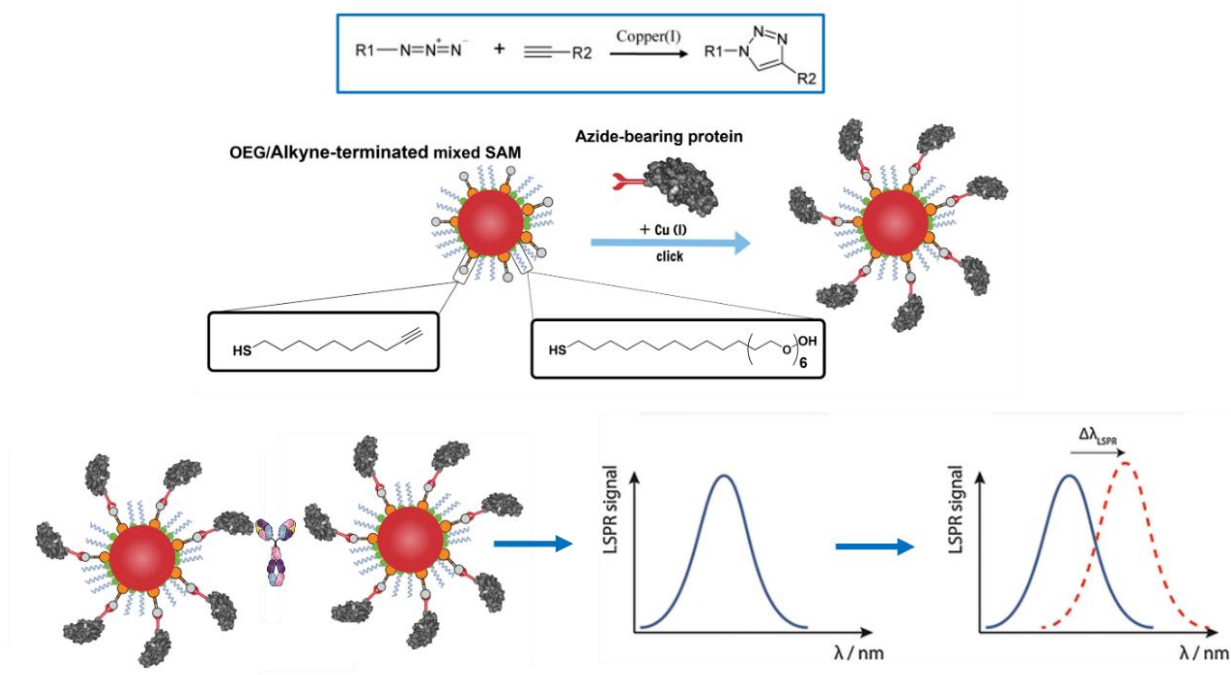
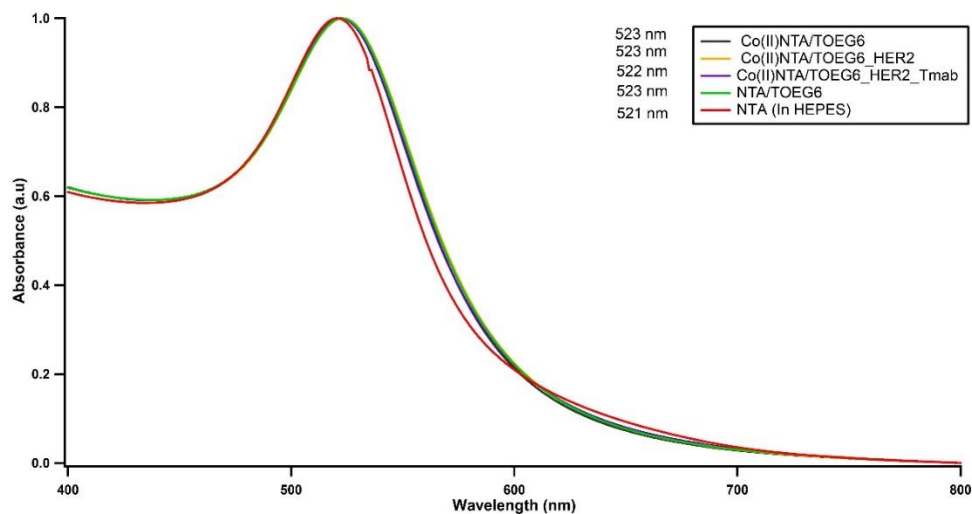
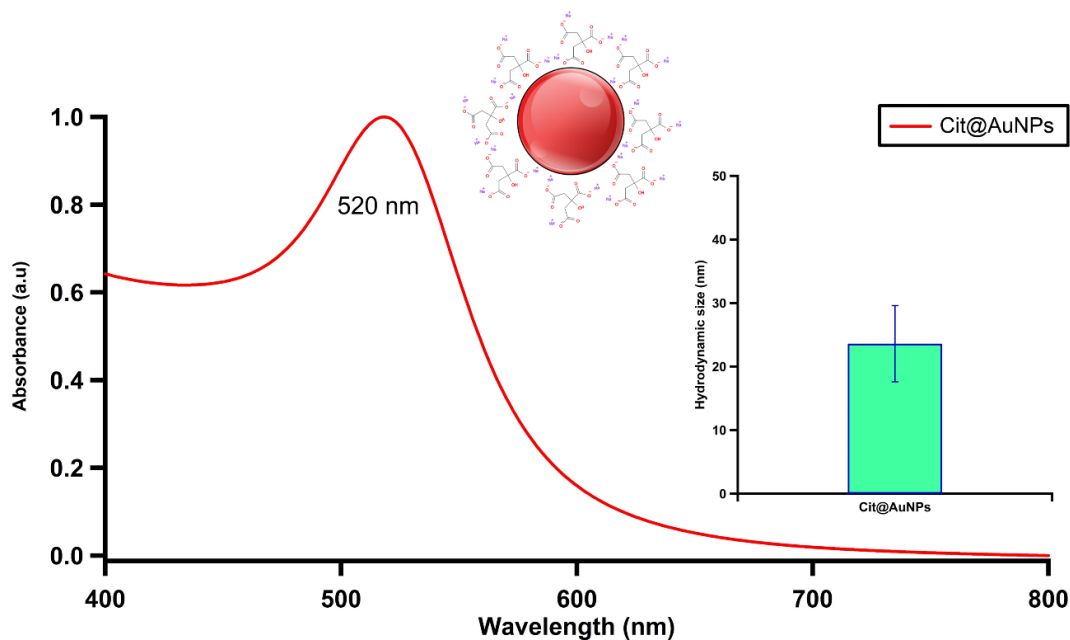


**Figure 74.7.** Cartoon illustrates the induced aggregation on a click-chemistry mediated mixed-SAM functionalized AuNPs.

## Appendix



**Appendix 1.** The ligand-chain length presents a crucial parameter in forming stable yet functional nanoparticles. Although TOEG6 as a spacing ligand offers highly stable conjugates, the desired plasmonic effect upon the introduction of trastuzumab was challenging to be observed. The plausible explanation could be attributed to the steric hindrance induced by the slightly longer OEG chain.

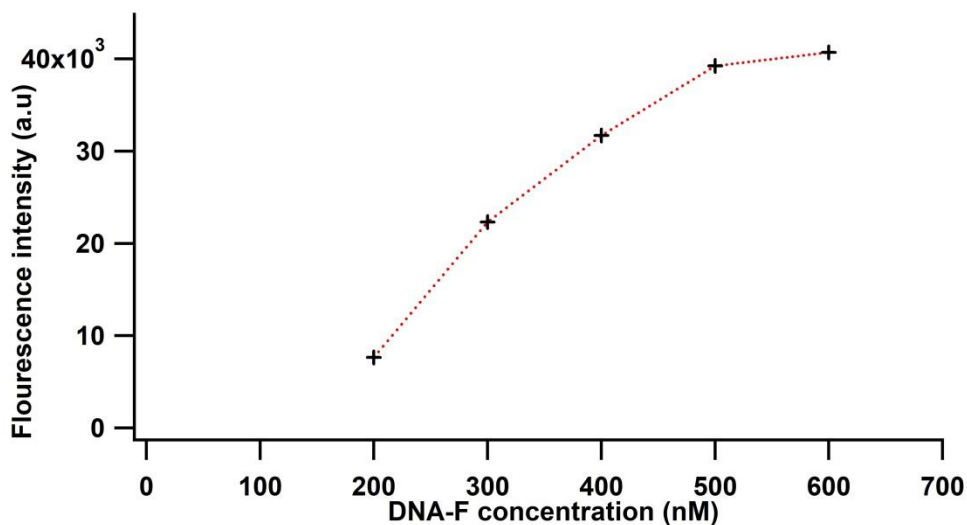


**Appendix 2.** UV/Vis spectrum and intensity-weighted size distribution (**inset**) of synthesized AuNPs.

## Quantification of DNA strands per gold nanoparticles

In order to determine the number of oligonucleotides attached per AuNPs, we attached a fluorescent ssDNA (DNA-F, with the same base sequence as DNA) to AuNPs following the same procedure as for DNA/TOEG6@AuNP. The DNA-F/TOEG6@ AuNP thus prepared was redispersed in 0.2 M phosphate buffer, pH 8.0. The DNA-F was displaced from the DNA-F/TOEG6@AuNP by adding equal volumes of DNA-F/TOEG6@AuNP and 1.0 M DTT in 0.2 M phosphate buffer, pH 8.0. An overnight incubation of the mixture ensures the complete displacement of DNA-F from the AuNPs. The AuNPs were then separated from the solution by centrifugation at 14,000 rpm for 10 min. The supernatant collected was checked for fluorescence using a luminescence spectrometer (Infinite 200Pro, TECAN), exciting at 485 nm and collecting emission at 535 nm. To convert the fluorescence reading from the solution to DNA-F concentration, we generated a calibration curve with known concentrations of DNA-F prepared in the same DTT buffer solution and analyzed in the same well plate.

$$Y = -3E-06x^4 + 0.0051x^3 - 3.0678x^2 + 923.97x - 89945$$



**Appendix 3.** Calibration curve for the quantification of ssDNA attached per AuNP.

- Using UV/Vis spectroscopy, the concentration of AuNPs@TOEG/DNA-F was determined from the equation below:

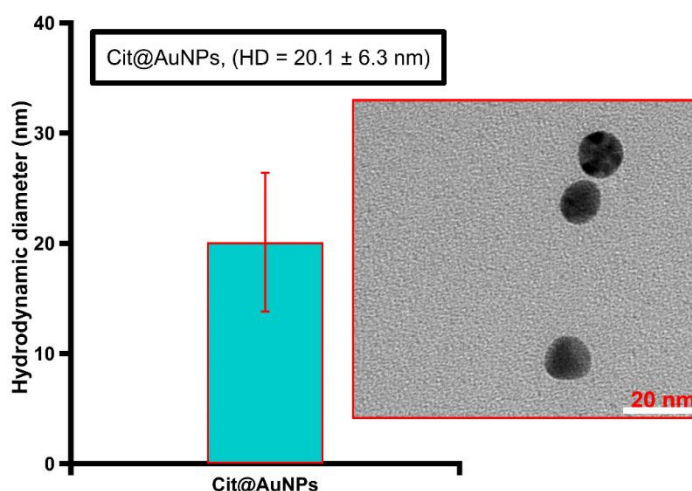
$$\text{absorbance} = 0.4438 (\text{concentration}) - 0.0301$$



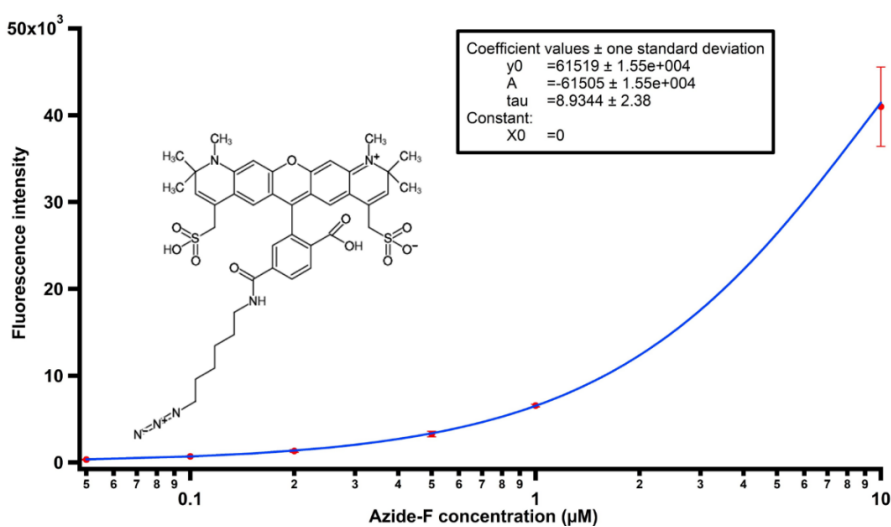
Maximum absorbance at 523 nm was 0.71527.

$$[\text{AuNP}] = \frac{0.71527 + 0.0301}{0.4438} = 1.68 \text{ nM}$$

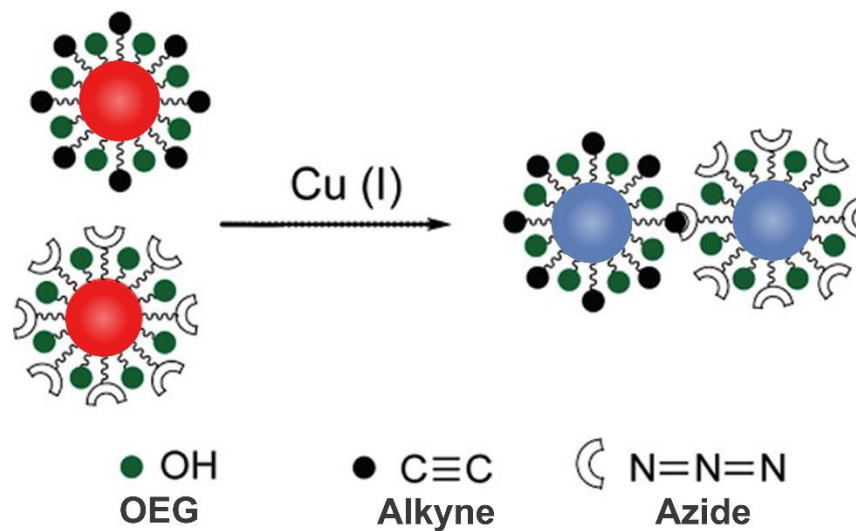
- From the luminescence spectrophotometry analysis which showed that the fluorescence intensity of DNA-F is 2264 a.u which corresponds to 174.79 nM
- Molar ratio =  $\frac{\# \text{ of moles of DNA-F}}{\# \text{ of moles of AuNPs}} = \frac{174.79 \text{ nM} \times 200 \mu\text{l}}{1.68 \text{ nM} \times 500 \mu\text{l}} = 41.62$
- So, there are 42 ssDNA/AuNPs.



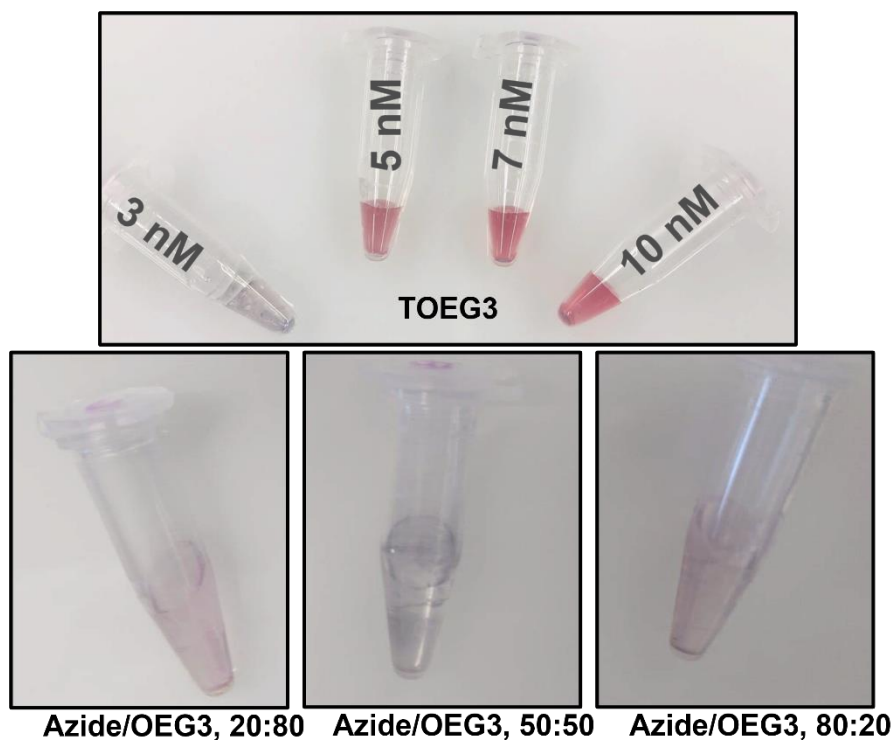
**Appendix 4.** DLS readout of as prepared AuNPs with the corresponding TEM micrograph.



**Appendix 5.** Calibration curve for the azide-bearing dye (AF594).



**Appendix 6.** Intended click-chemistry-mediated colorimetric assay design with two types of AuNPs, each modified with thiols terminated with an azide or alkyne functional group.



**Appendix 7.** digital photographs of the TOEG3 treated AuNPs, and Azide/OEG3 modified AuNPs prepared at different ligand ratios.

## References

- Abed, Z., Beik, J., Laurent, S., Eslahi, N., Khani, T., Davani, E. S., Ghaznavi, H., & Shakeri-Zadeh, A. (2019). Iron oxide–gold core–shell nano-theranostic for magnetically targeted photothermal therapy under magnetic resonance imaging guidance. *Journal of cancer research and clinical oncology*, *145*(5), 1213-1219.
- Aili, D., Selegård, R., Baltzer, L., Enander, K., & Liedberg, B. (2009). Colorimetric protein sensing by controlled assembly of gold nanoparticles functionalized with synthetic receptors. *Small*, *5*(21), 2445-2452.
- Al-Hussain, R. S., Kathaem, E. M., Baker, L. N., Assi, S. H., Abdulbaqi, S. S., & Kalaf, R. K. (2014). Early detection of Breast Cancer by Tumor Marker CA15. 3, CA27. 29 and relationship with P53 and Vitamin D. *Journal of Biotechnology Research Center*, *8*(1), 59-65.
- Alexander, C. M., Dabrowiak, J. C., & Maye, M. M. (2012). Investigation of the drug binding properties and cytotoxicity of DNA-capped nanoparticles designed as delivery vehicles for the anticancer agents doxorubicin and actinomycin D. *Bioconjugate chemistry*, *23*(10), 2061-2070.
- Alipour, E., Halverson, D., McWhirter, S., & Walker, G. C. (2017). Phospholipid bilayers: stability and encapsulation of nanoparticles. *Annual review of physical chemistry*, *68*, 261-283.
- Allen, T. M., & Cullis, P. R. (2013). Liposomal drug delivery systems: from concept to clinical applications. *Advanced drug delivery reviews*, *65*(1), 36-48.
- Alsadig, A., Vondracek, H., Pengo, P., Pasquato, L., Posocco, P., Parris, P., & Casalis, L. (2021). Label-Free, Rapid and Facile Gold-Nanoparticles-Based Assay as a Potential Spectroscopic Tool for Trastuzumab Quantification. *Nanomaterials*, *11*(12), 3181.
- Anker, J. N., Hall, W. P., Lyandres, O., Shah, N. C., Zhao, J., & Van Duyne, R. P. (2010). Biosensing with plasmonic nanosensors. *Nanoscience and Technology: A Collection of Reviews from Nature Journals*, 308-319.
- Arcas, A. S., Jaramillo, L., Costa, N. S., Allil, R. C. S., & Werneck, M. M. (2021). Localized surface plasmon resonance-based biosensor on gold nanoparticles for *Taenia solium* detection. *Applied Optics*, *60*(26), 8137-8144.
- Arrabito, G., Reisewitz, S., Dehmelt, L., Bastiaens, P. I., Pignataro, B., Schroeder, H., & Niemeyer, C. M. (2013). Biochips for Cell Biology by Combined Dip-Pen Nanolithography and DNA-Directed Protein Immobilization. *Small*, *9*(24), 4243-4249.
- Asbaghi, B. A. N., Alsadig, A., & Cabrera, H. (2021). Online electrophoretic nanoanalysis using miniaturized gel electrophoresis and thermal lens microscopy detection. *Journal of Chromatography A*, *1657*, 462596.
- Asbaghi, B. A. N., Alsadig, A., Casalis, L., Parris, P., Niemela, J., Bellucci, S., & Cabrera, H. (2022). An electrophoresis approach with online thermal lens detection to monitoring DNA surface coatings on gold nanoparticles. *Microchemical Journal*, *173*, 106961.
- Bain, C. D., Troughton, E. B., Tao, Y. T., Evall, J., Whitesides, G. M., & Nuzzo, R. G. (1989). Formation of monolayer films by the spontaneous assembly of organic thiols from solution onto gold. *Journal of the American Chemical Society*, *111*(1), 321-335.
- Bain, C. D., & Whitesides, G. M. (1988). Correlations between wettability and structure in monolayers of alkanethiols adsorbed on gold. *Journal of the American Chemical Society*, *110*(11), 3665-3666.

- Banerjee, P., Kintzios, S., & Prabhakarpanidyan, B. (2013). Biotoxin detection using cell-based sensors. *Toxins*, 5(12), 2366-2383.
- Bang, Y.-J., Van Cutsem, E., Feyereislova, A., Chung, H. C., Shen, L., Sawaki, A., Lordick, F., Ohtsu, A., Omuro, Y., & Satoh, T. (2010). Trastuzumab in combination with chemotherapy versus chemotherapy alone for treatment of HER2-positive advanced gastric or gastro-oesophageal junction cancer (ToGA): a phase 3, open-label, randomised controlled trial. *The Lancet*, 376(9742), 687-697.
- Bano, F., Fruk, L., Sanavio, B., Glettenberg, M., Casalis, L., Niemeyer, C. M., & Scoles, G. (2009). Toward multiprotein nanoarrays using nanografting and DNA directed immobilization of proteins. *Nano letters*, 9(7), 2614-2618.
- Barnato, S. E., & Gradishar, W. J. (2015). Biological subtypes of breast cancer. In *Breast Cancer Biology for the Radiation Oncologist* (pp. 1-6). Springer.
- Bartlett, J. M., Going, J. J., Mallon, E. A., Watters, A. D., Reeves, J. R., Stanton, P., Richmond, J., Donald, B., Ferrier, R., & Cooke, T. G. (2001). Evaluating HER2 amplification and overexpression in breast cancer. *The Journal of Pathology: A Journal of the Pathological Society of Great Britain and Ireland*, 195(4), 422-428.
- Baselga, J., Carbonell, X., Castañeda-Soto, N.-J., Clemens, M., Green, M., Harvey, V., Morales, S., Barton, C., & Ghahramani, P. (2005). Phase II study of efficacy, safety, and pharmacokinetics of trastuzumab monotherapy administered on a 3-weekly schedule. *Journal of Clinical Oncology*, 23(10), 2162-2171.
- Berciaud, S., Lasne, D., Blab, G. A., Cognet, L., & Lounis, B. (2006). Photothermal heterodyne imaging of individual metallic nanoparticles: Theory versus experiment. *Physical Review B*, 73(4), 045424.
- Bhargava, R., Lal, P., & Chen, B. (2005). Chromogenic in situ hybridization for the detection of HER-2/neu gene amplification in breast cancer with an emphasis on tumors with borderline and low-level amplification: does it measure up to fluorescence in situ hybridization? *American journal of clinical pathology*, 123(2), 237-243.
- Bilous, M., Morey, A. L., Armes, J. E., Bell, R., Button, P. H., Cummings, M. C., Fox, S. B., Francis, G. D., Waite, B., & McCue, G. (2012). Assessing HER2 amplification in breast cancer: findings from the Australian In Situ Hybridization Program. *Breast cancer research and treatment*, 134(2), 617-624.
- Binnig, G., Quate, C. F., & Gerber, C. (1986). Atomic force microscope. *Physical review letters*, 56(9), 930.
- Binnig, G., & Rohrer, H. (1983). Scanning tunneling microscopy. *Surface science*, 126(1-3), 236-244.
- Blizzard, R. J., Backus, D. R., Brown, W., Bazewicz, C. G., Li, Y., & Mehl, R. A. (2015). Ideal bioorthogonal reactions using a site-specifically encoded tetrazine amino acid. *Journal of the American Chemical Society*, 137(32), 10044-10047.
- Boekhout, A. H., Beijnen, J. H., & Schellens, J. H. (2011). Trastuzumab. *The oncologist*, 16(6), 800-810.
- Brennan, J. L., Hatzakis, N. S., Tshikhudo, T. R., Dirvianskyte, N., Razumas, V., Patkar, S., Vind, J., Svendsen, A., Nolte, R. J., & Rowan, A. E. (2006). Bionanoconjugation via click chemistry: The creation of functional hybrids of lipases and gold nanoparticles. *Bioconjugate chemistry*, 17(6), 1373-1375.
- Briggs, M. W., & Long, G. R. (1996). Thermal lens spectrophotometry in agarose gels. *Applied spectroscopy*, 50(2), 241-244.

- Brusnichkin, A. V., Nedosekin, D. A., Proskurnin, M. A., & Zharov, V. P. (2007). Photothermal lens detection of gold nanoparticles: Theory and experiments. *Applied spectroscopy*, *61*(11), 1191-1201.
- Brust, M., Walker, M., Bethell, D., Schiffrin, D. J., & Whyman, R. (1994). Synthesis of thiol-derivatised gold nanoparticles in a two-phase liquid-liquid system. *Journal of the Chemical Society, Chemical Communications*(7), 801-802.
- Buschow, K. J. (2001). *Encyclopedia of materials: science and technology* (Vol. 1). Elsevier.
- Cabrera, H., Korte, D., & Franko, M. (2015). Mode-mismatched confocal thermal-lens microscope with collimated probe beam. *Review of Scientific Instruments*, *86*(5), 053701.
- Cabrera, H., Marcano, A., & Castellanos, Y. (2006). Absorption coefficient of nearly transparent liquids measured using thermal lens spectrometry. *Condensed Matter Physics*.
- Cai, W., Gao, T., Hong, H., & Sun, J. (2008). Applications of gold nanoparticles in cancer nanotechnology. *Nanotechnology, science and applications*, *1*, 17.
- Callen, W., Huth, B., & Pantell, R. (1967). Optical patterns of thermally self-defocused light. *Applied Physics Letters*, *11*(3), 103-105.
- Camden, J. P., Dieringer, J. A., Wang, Y., Masiello, D. J., Marks, L. D., Schatz, G. C., & Van Duyne, R. P. (2008). Probing the structure of single-molecule surface-enhanced Raman scattering hot spots. *Journal of the American Chemical Society*, *130*(38), 12616-12617.
- Cao, C., Kim, J. P., Kim, B. W., Chae, H., Yoon, H. C., Yang, S. S., & Sim, S. J. (2006). A strategy for sensitivity and specificity enhancements in prostate specific antigen- $\alpha$ 1-antichymotrypsin detection based on surface plasmon resonance. *Biosensors and Bioelectronics*, *21*(11), 2106-2113.
- Cao, C., & Sim, S. J. (2007). Preparation of highly stable oligo (ethylene glycol) derivatives-functionalized gold nanoparticles and their application in LSPR-based detection of PSA/ACT complex. *Journal of Nanoscience and Nanotechnology*, *7*(11), 3754-3757.
- Cardinali, B., Lunardi, G., Millo, E., Armirotti, A., Damonte, G., Profumo, A., Gori, S., Iacono, G., Levaggi, A., & Del Mastro, L. (2014). Trastuzumab quantification in serum: a new, rapid, robust ELISA assay based on a mimetic peptide that specifically recognizes trastuzumab. *Analytical and bioanalytical chemistry*, *406*(18), 4557-4561.
- Carman, R., & Kelley, P. (1968). Time dependence in the thermal blooming of laser beams. *Applied Physics Letters*, *12*(8), 241-243.
- Casalini, S., Bortolotti, C. A., Leonardi, F., & Biscarini, F. (2017). Self-assembled monolayers in organic electronics. *Chemical Society Reviews*, *46*(1), 40-71.
- Castillo-Henríguez, L., Alfaro-Aguilar, K., Ugalde-Álvarez, J., Vega-Fernández, L., Montes de Oca-Vásquez, G., & Vega-Baudrit, J. R. (2020). Green synthesis of gold and silver nanoparticles from plant extracts and their possible applications as antimicrobial agents in the agricultural area. *Nanomaterials*, *10*(9), 1763.
- Centrone, A. (2015). Absorption Spectroscopy and Imaging from the Visible through Mid-IR with 20 nm Resolution Using AFM probes. APS March Meeting Abstracts,
- Cetin, A. E., Coskun, A. F., Galarreta, B. C., Huang, M., Herman, D., Ozcan, A., & Altug, H. (2014). Handheld high-throughput plasmonic biosensor using computational on-chip imaging. *Light: Science & Applications*, *3*(1), e122-e122.
- Chan, G. H., Zhao, J., Schatz, G. C., & Van Duyne, R. P. (2008). Localized surface plasmon resonance spectroscopy of triangular aluminum nanoparticles. *The Journal of Physical Chemistry C*, *112*(36), 13958-13963.

- Chan, W. C., & Nie, S. (1998). Quantum dot bioconjugates for ultrasensitive nonisotopic detection. *Science*, 281(5385), 2016-2018.
- Chao, A., Jiang, N., Yang, Y., Li, H., & Sun, H. (2017). A Ni-NTA-based red fluorescence probe for protein labelling in live cells. *Journal of Materials Chemistry B*, 5(6), 1166-1173.
- Charles, D. E., Aherne, D., Gara, M., Ledwith, D. M., Gun'ko, Y. K., Kelly, J. M., Blau, W. J., & Brennan-Fournet, M. E. (2010). Versatile solution phase triangular silver nanoplates for highly sensitive plasmon resonance sensing. *ACS nano*, 4(1), 55-64.
- Chen, C.-S., & Zhu, H. (2006). Protein microarrays. *Biotechniques*, 40(4), 423-429.
- Chen, H., Kou, X., Yang, Z., Ni, W., & Wang, J. (2008). Shape- and size-dependent refractive index sensitivity of gold nanoparticles. *Langmuir*, 24(10), 5233-5237.
- Chen, P., Selegård, R., Aili, D., & Liedberg, B. (2013). Peptide functionalized gold nanoparticles for colorimetric detection of matrix metalloproteinase-7 (MMP-7) activity. *Nanoscale*, 5(19), 8973-8976.
- Chen, X., Li, F., & Wu, Y.-W. (2015). Chemical labeling of intracellular proteins via affinity conjugation and strain-promoted cycloadditions in live cells. *Chemical Communications*, 51(92), 16537-16540.
- Chien, M.-H., & Schmid, S. (2020). Nanoelectromechanical photothermal polarization microscopy with 3 Å localization precision. *Journal of Applied Physics*, 128(13), 134501.
- Chinen, A. B., Guan, C. M., Ferrer, J. R., Barnaby, S. N., Merkel, T. J., & Mirkin, C. A. (2015). Nanoparticle probes for the detection of cancer biomarkers, cells, and tissues by fluorescence. *Chemical reviews*, 115(19), 10530-10574.
- Christofi, T., Baritaki, S., Falzone, L., Libra, M., & Zaravinos, A. (2019). Current perspectives in cancer immunotherapy. *Cancers*, 11(10), 1472.
- Collman, J. P., Devaraj, N. K., & Chidsey, C. E. (2004). "Clicking" functionality onto electrode surfaces. *Langmuir*, 20(4), 1051-1053.
- Cosson, V. F., Ng, V. W., Lehle, M., & Lum, B. L. (2014). Population pharmacokinetics and exposure-response analyses of trastuzumab in patients with advanced gastric or gastroesophageal junction cancer. *Cancer chemotherapy and pharmacology*, 73(4), 737-747.
- Crowe, J., Masone, B. S., & Ribbe, J. (1995). One-step purification of recombinant proteins with the 6xHis tag and Ni-NTA resin. *Molecular biotechnology*, 4(3), 247-258.
- D'huyvetter, M., Vincke, C., Xavier, C., Aerts, A., Impens, N., Baatout, S., De Raeve, H., Muyldermans, S., Caveliers, V., & Devoogdt, N. (2014). Targeted radionuclide therapy with A 177Lu-labeled anti-HER2 nanobody. *Theranostics*, 4(7), 708.
- Dabby, F., & Paek, U. (1971). cw SELF-INDUCED FREQUENCY MODULATION AND SWITCHING OF A LASER BEAM IN LIQUIDS. *Applied Physics Letters*, 18(10), 430-432.
- Dal Lago, L., Durbecq, V., Desmedt, C., Salgado, R., Verjat, T., Lespagnard, L., Ma, Y., Veys, I., Di Leo, A., & Sotiriou, C. (2006). Correction for chromosome-17 is critical for the determination of true Her-2/neu gene amplification status in breast cancer. *Molecular cancer therapeutics*, 5(10), 2572-2579.
- Dam, D. H. M., Lee, H., Lee, R. C., Kim, K. H., Kelleher, N. L., & Odom, T. W. (2015). Tunable loading of oligonucleotides with secondary structure on gold nanoparticles through a pH-driven method. *Bioconjugate chemistry*, 26(2), 279-285.
- Damborský, P., Švitel, J., & Katrlík, J. (2016). Optical biosensors. *Essays in biochemistry*, 60(1), 91-100.

- Damen, C. W., Derissen, E. J., Schellens, J. H., Rosing, H., & Beijnen, J. H. (2009). The bioanalysis of the monoclonal antibody trastuzumab by high-performance liquid chromatography with fluorescence detection after immuno-affinity purification from human serum. *Journal of pharmaceutical and biomedical analysis*, 50(5), 861-866.
- Deka, J., Mech, R., Ianeselli, L., Amenitsch, H., Cacho-Nerin, F., Parisse, P., & Casalis, L. (2015). Surface passivation improves the synthesis of highly stable and specific DNA-functionalized gold nanoparticles with variable DNA density. *ACS applied materials & interfaces*, 7(12), 7033-7040.
- Deka, J., Mojumdar, A., Parisse, P., Onesti, S., & Casalis, L. (2017). DNA-conjugated gold nanoparticles based colorimetric assay to assess helicase activity: a novel route to screen potential helicase inhibitors. *Scientific reports*, 7(1), 1-9.
- Díaz-González, M., Escosura-Muñiz, A. d. l., Fernandez-Argüelles, M. T., Alonso, F. J. G., & Costa-Fernandez, J. M. (2020). Quantum dot bioconjugates for diagnostic applications. *Surface-modified Nanobiomaterials for Electrochemical and Biomedicine Applications*, 133-176.
- Dietel, M., Ellis, I., Höfler, H., Kreipe, H., Moch, H., Dankof, A., Kölbl, K., & Kristiansen, G. (2007). Comparison of automated silver enhanced in situ hybridisation (SISH) and fluorescence ISH (FISH) for the validation of HER2 gene status in breast carcinoma according to the guidelines of the American Society of Clinical Oncology and the College of American Pathologists. *Virchows Archiv*, 451(1), 19-25.
- Dmitriev, A. (2012a). Future Directions: Nanoplasmonic Sensing Tomorrow. In *Nanoplasmonic Sensors* (pp. 385-387). Springer.
- Dmitriev, A. (2012b). *Nanoplasmonic sensors*. Springer Science & Business Media.
- Dovichi, N., & Harris, J. (1981). Time-resolved thermal lens calorimetry. *Analytical chemistry*, 53(1), 106-109.
- Dovichi, N. J., & Harris, J. (1979). Laser induced thermal lens effect for calorimetric trace analysis. *Analytical chemistry*, 51(6), 728-731.
- Dovichi, N. J., & Harris, J. (1980). Differential thermal lens calorimetry. *Analytical chemistry*, 52(14), 2338-2342.
- Dowsett, M., Hanna, W. M., Kockx, M., Penault-Llorca, F., Rüschoff, J., Gutjahr, T., Habben, K., & van de Vijver, M. J. (2007). Standardization of HER2 testing: results of an international proficiency-testing ring study. *Modern Pathology*, 20(5), 584-591.
- Drexler, K. E. (1986). *Engines of creation*. Anchor books.
- Du, L., Zou, L., Wang, Q., Zhao, L., Huang, L., Wang, P., & Wu, C. (2015). A novel biomimetic olfactory cell-based biosensor with DNA-directed site-specific immobilization of cells on a microelectrode array. *Sensors and Actuators B: Chemical*, 217, 186-192.
- Duan, Y., Wu, W., Zhao, Q., Liu, S., Liu, H., Huang, M., Wang, T., Liang, M., & Wang, Z. (2020). Enzyme-antibody-modified gold nanoparticle probes for the ultrasensitive detection of nucleocapsid protein in SFTSV. *International Journal of Environmental Research and Public Health*, 17(12), 4427.
- Dubacheva, G. V., Van Der Heyden, A., Dumy, P., Kaftan, O., Auzély-Velty, R., Coche-Guerente, L., & Labbé, P. (2010). Electrochemically controlled adsorption of Fc-functionalized polymers on  $\beta$ -CD-modified self-assembled monolayers. *Langmuir*, 26(17), 13976-13986.
- Dugger, J. W., & Webb, L. J. (2015). Fibrillar structures formed by covalently bound, short,  $\beta$ -stranded peptides on self-assembled monolayers. *Langmuir*, 31(11), 3441-3450.

- El Alami, A., Lagarde, F., Huo, Q., Zheng, T., Baitoul, M., & Daniel, P. (2020). Acetylcholine and acetylcholinesterase inhibitors detection using gold nanoparticles coupled with dynamic light scattering. *Sensors International*, 1, 100007.
- Elliott III, E. W., Ginzburg, A. L., Kennedy, Z. C., Feng, Z., & Hutchison, J. E. (2017). Single-step synthesis of small, azide-functionalized gold nanoparticles: versatile, water-dispersible reagents for click chemistry. *Langmuir*, 33(23), 5796-5802.
- Englebienne, P. (1998). Use of colloidal gold surface plasmon resonance peak shift to infer affinity constants from the interactions between protein antigens and antibodies specific for single or multiple epitopes. *Analyst*, 123(7), 1599-1603.
- Enoch, S., & Bonod, N. (2012). *Plasmonics: from basics to advanced topics* (Vol. 167). Springer.
- Ewer, M. S., Gibbs, H. R., Swafford, J., & Benjamin, R. S. (1999). Cardiotoxicity in patients receiving transtuzumab (Herceptin): primary toxicity, synergistic or sequential stress, or surveillance artifact? *Seminars in oncology*.
- Fabris, L. (2015). Gold-based SERS tags for biomedical imaging. *Journal of Optics*, 17(11), 114002.
- Faucheaux, J. A., Stanton, A. L., & Jain, P. K. (2014). Plasmon resonances of semiconductor nanocrystals: physical principles and new opportunities. *The journal of physical chemistry letters*, 5(6), 976-985.
- Ferlay, J., Soerjomataram, I., Dikshit, R., Eser, S., Mathers, C., Rebelo, M., Parkin, D. M., Forman, D., & Bray, F. (2015). Cancer incidence and mortality worldwide: sources, methods and major patterns in GLOBOCAN 2012. *International journal of cancer*, 136(5), E359-E386.
- Fernández-Barahona, I., Muñoz-Hernando, M., Ruiz-Cabello, J., Herranz, F., & Pellico, J. (2020). Iron oxide nanoparticles: An alternative for positive contrast in magnetic resonance imaging. *Inorganics*, 8(4), 28.
- Fernández, F., Hegnerová, K., Piliarik, M., Sanchez-Baeza, F., Homola, J., & Marco, M.-P. (2010). A label-free and portable multichannel surface plasmon resonance immunosensor for on site analysis of antibiotics in milk samples. *Biosensors and Bioelectronics*, 26(4), 1231-1238.
- Ferreira, J., Santos, M. J., Rahman, M. M., Brolo, A. G., Gordon, R., Sinton, D., & Girotto, E. M. (2009). Attomolar protein detection using in-hole surface plasmon resonance. *Journal of the American Chemical Society*, 131(2), 436-437.
- Ferretti, S., Paynter, S., Russell, D. A., Sapsford, K. E., & Richardson, D. J. (2000). Self-assembled monolayers: a versatile tool for the formulation of bio-surfaces. *TrAC Trends in Analytical Chemistry*, 19(9), 530-540.
- Feynman, R. (2013). California Institute of Technology. *Symmetries in Elementary Particle Physics: 1964 International School of Physics Ettore Majorana, a CERN-MPI-NATO Advanced Study Institute*.
- Fošnarič, M., Igljč, A., Kroll, D. M., & May, S. (2009). Monte Carlo simulations of complex formation between a mixed fluid vesicle and a charged colloid. *The Journal of Chemical Physics*, 131(10), 09B610.
- Frens, G. (1973). Controlled nucleation for the regulation of the particle size in monodisperse gold suspensions. *Nature physical science*, 241(105), 20-22.
- Fruk, L., Müller, J., Weber, G., Narváez, A., Domínguez, E., & Niemeyer, C. M. (2007). DNA-Directed Immobilization of Horseradish Peroxidase–DNA Conjugates on Microelectrode Arrays: Towards Electrochemical Screening of Enzyme Libraries. *Chemistry—A European Journal*, 13(18), 5223-5231.



- Gabriel, M., Nazmi, K., Veerman, E. C., Nieuw Amerongen, A. V., & Zentner, A. (2006). Preparation of LL-37-grafted titanium surfaces with bactericidal activity. *Bioconjugate chemistry*, *17*(2), 548-550.
- Gallardo, I. F., & Webb, L. J. (2012). Demonstration of  $\alpha$ -helical structure of peptides tethered to gold surfaces using surface infrared and circular dichroic spectroscopies. *Langmuir*, *28*(7), 3510-3515.
- García, M. A. (2011). Surface plasmons in metallic nanoparticles: fundamentals and applications. *Journal of Physics D: Applied Physics*, *44*(28), 283001.
- Ghosh, D., & Chattopadhyay, N. (2015). Gold and silver nanoparticles based superquenching of fluorescence: A review. *Journal of luminescence*, *160*, 223-232.
- Giljohann, D. A., Seferos, D. S., Daniel, W. L., Massich, M. D., Patel, P. C., & Mirkin, C. A. (2020). Gold nanoparticles for biology and medicine. *Spherical Nucleic Acids*, 55-90.
- González García, J., Gutiérrez Nicolás, F., Ramos Díaz, R., Nazco Casariego, G. J., Viña Romero, M. M., Llabres Martínez, M., Llanos Muñoz, M., Batista Lopez, J. N., Jiménez Sosa, A., & Ceballos Lenza, I. (2020). Pharmacokinetics of trastuzumab after subcutaneous and intravenous administration in obese patients. *Annals of Pharmacotherapy*, *54*(8), 775-779.
- Haes, A. J., Chang, L., Klein, W. L., & Van Duyne, R. P. (2005). Detection of a biomarker for Alzheimer's disease from synthetic and clinical samples using a nanoscale optical biosensor. *Journal of the American Chemical Society*, *127*(7), 2264-2271.
- Haes, A. J., Hall, W. P., Chang, L., Klein, W. L., & Van Duyne, R. P. (2004). A localized surface plasmon resonance biosensor: First steps toward an assay for Alzheimer's disease. *Nano letters*, *4*(6), 1029-1034.
- Hamers-Casterman, C., Atarhouch, T., Muyldermans, S. a., Robinson, G., Hammers, C., Songa, E. B., Bendahman, N., & Hammers, R. (1993). Naturally occurring antibodies devoid of light chains. *Nature*, *363*(6428), 446-448.
- Han, J.-H., Li, F., & Gunawan, R. C. (2020). Development of homogeneous plasmonic potency assay using gold nanoparticle immunocomplexes. *Journal of pharmaceutical and biomedical analysis*, *181*, 113101.
- Hanna, W. M., & Kwok, K. (2006). Chromogenic in-situ hybridization: a viable alternative to fluorescence in-situ hybridization in the HER2 testing algorithm. *Modern Pathology*, *19*(4), 481-487.
- Hassanzadeh-Ghassabeh, G., Devoogdt, N., De Pauw, P., Vincke, C., & Muyldermans, S. (2013). Nanobodies and their potential applications. *Nanomedicine*, *8*(6), 1013-1026.
- Haun, J. B., Devaraj, N. K., Hilderbrand, S. A., Lee, H., & Weissleder, R. (2010). Bioorthogonal chemistry amplifies nanoparticle binding and enhances the sensitivity of cell detection. *Nature nanotechnology*, *5*(9), 660-665.
- Haynie, S. L., Crum, G. A., & Doele, B. A. (1995). Antimicrobial activities of amphiphilic peptides covalently bonded to a water-insoluble resin. *Antimicrobial agents and chemotherapy*, *39*(2), 301-307.
- Herrer, L., Martín, S., & Cea, P. (2020). Nanofabrication techniques in large-area molecular electronic devices. *Applied Sciences*, *10*(17), 6064.
- Heylman, K. D., Knapper, K. A., & Goldsmith, R. H. (2014). Photothermal microscopy of nonluminescent single particles enabled by optical microresonators. *The journal of physical chemistry letters*, *5*(11), 1917-1923.
- Hicks, D. G., & Kulkarni, S. (2008). HER2+ breast cancer: review of biologic relevance and optimal use of diagnostic tools. *American journal of clinical pathology*, *129*(2), 263-273.

- Hoeppener, S., Maoz, R., & Sagiv, J. (2003). Constructive microlithography: electrochemical printing of monolayer template patterns extends constructive nanolithography to the micrometer– millimeter dimension range. *Nano letters*, 3(6), 761-767.
- Hoffmann, J. E., Plass, T., Nikić, I., Aramburu, I. V., Koehler, C., Gillandt, H., Lemke, E. A., & Schultz, C. (2015). Highly Stable trans-Cyclooctene Amino Acids for Live-Cell Labeling. *Chemistry—A European Journal*, 21(35), 12266-12270.
- Holzer, B., Manoli, K., Ditaranto, N., Macchia, E., Tiwari, A., Di Franco, C., Scamarcio, G., Palazzo, G., & Torsi, L. (2017). Characterization of Covalently Bound Anti-Human Immunoglobulins on Self-Assembled Monolayer Modified Gold Electrodes. *Advanced Biosystems*, 1(11), 1700055.
- Hong, Y., Huh, Y.-M., Yoon, D. S., & Yang, J. (2012). Nanobiosensors based on localized surface plasmon resonance for biomarker detection. *Journal of Nanomaterials*, 2012.
- Hu, C., & Whinnery, J. (1973). New thermo-optical measurement method and a comparison with other methods. *Applied Optics*, 12(1), 72-79.
- Huang, C.-J., Chen, Y.-S., & Chang, Y. (2015). Counterion-activated nanoactuator: reversibly switchable killing/releasing bacteria on polycation brushes. *ACS applied materials & interfaces*, 7(4), 2415-2423.
- Hudalla, G. A., & Murphy, W. L. (2009). Using “click” chemistry to prepare SAM substrates to study stem cell adhesion. *Langmuir*, 25(10), 5737-5746.
- Hudis, C. A. (2007). Trastuzumab—mechanism of action and use in clinical practice. *New England journal of medicine*, 357(1), 39-51.
- Huo, L., Du, P., Zhang, K., Liu, P., & Zhou, H. (2019). Self-assembled monolayer of multiply-alkylated cyclopentenes on silicon via thiol-ene “click” reaction and its self-lubricating properties. *Applied Surface Science*, 477, 96-103.
- Hurst, S. J., Lytton-Jean, A. K., & Mirkin, C. A. (2006). Maximizing DNA loading on a range of gold nanoparticle sizes. *Analytical chemistry*, 78(24), 8313-8318.
- Ilyas, S., Ilyas, M., van der Hoorn, R. A., & Mathur, S. (2013). Selective conjugation of proteins by mining active proteomes through click-functionalized magnetic nanoparticles. *ACS nano*, 7(11), 9655-9663.
- Imaoka, H., Mizuno, N., Hara, K., Hijioka, S., Tajika, M., Tanaka, T., Ishihara, M., Hirayama, Y., Hieda, N., & Yoshida, T. (2016). Prognostic impact of carcinoembryonic antigen (CEA) on patients with metastatic pancreatic cancer: a retrospective cohort study. *Pancreatology*, 16(5), 859-864.
- Iqbal, N., & Iqbal, N. (2014). Human epidermal growth factor receptor 2 (HER2) in cancers: overexpression and therapeutic implications. *Molecular biology international*, 2014.
- Irving, D. L., & Brenner, D. W. (2006). Diffusion on a self-assembled monolayer: molecular modeling of a bound+ mobile lubricant. *The Journal of Physical Chemistry B*, 110(31), 15426-15431.
- Jackson, C., Browell, D., Gautrey, H., & Tyson-Capper, A. (2013). Clinical significance of HER-2 splice variants in breast cancer progression and drug resistance. *International journal of cell biology*, 2013.
- Jain, P. K., El-Sayed, I. H., & El-Sayed, M. A. (2007). Au nanoparticles target cancer. *nano today*, 2(1), 18-29.
- Jakab, A., Rosman, C., Khalavka, Y., Becker, J., Trugler, A., Hohenester, U., & Sonnichsen, C. (2011). Highly sensitive plasmonic silver nanorods. *ACS nano*, 5(9), 6880-6885.

- Jerusalem, G., Lancellotti, P., & Kim, S.-B. (2019). HER2+ breast cancer treatment and cardiotoxicity: monitoring and management. *Breast cancer research and treatment*, *177*(2), 237-250.
- Jiang, B., Li, F., Yang, C., Xie, J., Xiang, Y., & Yuan, R. (2015). Aptamer pseudoknot-functionalized electronic sensor for reagentless and single-step detection of immunoglobulin E in human serum. *Analytical chemistry*, *87*(5), 3094-3098.
- Jiménez Pérez, J. L., Gutierrez Fuentes, R., Sanchez Ramirez, J. F., & Cruz-Orea, A. (2008). Study of gold nanoparticles effect on thermal diffusivity of nanofluids based on various solvents by using thermal lens spectroscopy. *The European Physical Journal Special Topics*, *153*(1), 159-161.
- Jin, R., Wu, G., Li, Z., Mirkin, C. A., & Schatz, G. C. (2003). What controls the melting properties of DNA-linked gold nanoparticle assemblies? *Journal of the American Chemical Society*, *125*(6), 1643-1654.
- Kailasa, S. K., Koduru, J. R., Desai, M. L., Park, T. J., Singhal, R. K., & Basu, H. (2018). Recent progress on surface chemistry of plasmonic metal nanoparticles for colorimetric assay of drugs in pharmaceutical and biological samples. *TrAC Trends in Analytical Chemistry*, *105*, 106-120.
- Karube, I., & Nomura, Y. (2000). Enzyme sensors for environmental analysis. *Journal of Molecular Catalysis B: Enzymatic*, *10*(1-3), 177-181.
- Keyaerts, M., Xavier, C., Heemskerk, J., Devoogdt, N., Everaert, H., Ackaert, C., Vanhoeij, M., Duhoux, F. P., Gevaert, T., & Simon, P. (2016). Phase I study of 68Ga-HER2-nanobody for PET/CT assessment of HER2 expression in breast carcinoma. *Journal of Nuclear Medicine*, *57*(1), 27-33.
- Khaleghi, S., Rahbarizadeh, F., Ahmadvand, D., & Hosseini, H. R. M. (2017). Anti-HER2 VHH targeted magnetoliposome for intelligent magnetic resonance imaging of breast cancer cells. *Cellular and Molecular Bioengineering*, *10*(3), 263-272.
- Khan, F., He, M., & Taussig, M. J. (2006). Double-hexahistidine tag with high-affinity binding for protein immobilization, purification, and detection on Ni<sup>2+</sup>-nitrilotriacetic acid surfaces. *Analytical chemistry*, *78*(9), 3072-3079.
- Khantamat, O., Li, C.-H., Yu, F., Jamison, A. C., Shih, W.-C., Cai, C., & Lee, T. R. (2015). Gold nanoshell-decorated silicone surfaces for the near-infrared (NIR) photothermal destruction of the pathogenic bacterium *E. faecalis*. *ACS applied materials & interfaces*, *7*(7), 3981-3993.
- Kim, B., Rutka, J., & Chan, W. (2010). Effect of Coumarate 3-zhydroxylase Down regulation on lignin structure. *Nanomed. N. Engl. J. Med*, *363*, 2434-2443.
- Kim, Y.-P., Daniel, W. L., Xia, Z., Xie, H., Mirkin, C. A., & Rao, J. (2010). Bioluminescent nanosensors for protease detection based upon gold nanoparticle-luciferase conjugates. *Chemical Communications*, *46*(1), 76-78.
- Kinoshita, T., Yip, K. W., Spence, T., & Liu, F.-F. (2017). MicroRNAs in extracellular vesicles: potential cancer biomarkers. *Journal of human genetics*, *62*(1), 67-74.
- Kolb, H. C., Finn, M., & Sharpless, K. B. (2001). Click chemistry: diverse chemical function from a few good reactions. *Angewandte Chemie International Edition*, *40*(11), 2004-2021.
- Korkaya, H., Kim, G.-i., Davis, A., Malik, F., Henry, N. L., Ithimakin, S., Quraishi, A. A., Tawakkol, N., D'Angelo, R., & Paulson, A. K. (2012). Activation of an IL6 inflammatory loop mediates trastuzumab resistance in HER2+ breast cancer by expanding the cancer stem cell population. *Molecular cell*, *47*(4), 570-584.

- Kretschmann, E., & Raether, H. (1968). Radiative decay of non radiative surface plasmons excited by light. *Zeitschrift für Naturforschung A*, 23(12), 2135-2136.
- Kroto, H. W., Heath, J. R., O'Brien, S. C., Curl, R. F., & Smalley, R. E. (1985). C60: Buckminsterfullerene. *Nature*, 318(6042), 162-163.
- Kwizera, E. A., Chaffin, E., Wang, Y., & Huang, X. (2017). Synthesis and properties of magnetic-optical core-shell nanoparticles. *Rsc Advances*, 7(28), 17137-17153.
- Lal, P., Salazar, P. A., Ladanyi, M., & Chen, B. (2003). Impact of polysomy 17 on HER-2/neu immunohistochemistry in breast carcinomas without HER-2/neu gene amplification. *The Journal of molecular diagnostics*, 5(3), 155-159.
- Lebitania, J. A., Inada, N., Morimoto, M., You, J., Shahiduzzaman, M., Taima, T., Hirata, K., Fukuma, T., Ohta, A., & Asakawa, T. (2021). Local Cross-Coupling Activity of Azide-Hexa (ethylene glycol)-Terminated Self-Assembled Monolayers Investigated by Atomic Force Microscopy. *Langmuir*, 37(50), 14688-14696.
- Lee, J.-S., Stoeva, S. I., & Mirkin, C. A. (2006). DNA-induced size-selective separation of mixtures of gold nanoparticles. *Journal of the American Chemical Society*, 128(27), 8899-8903.
- Lee, K. X., Shameli, K., Yew, Y. P., Teow, S.-Y., Jahangirian, H., Rafiee-Moghaddam, R., & Webster, T. J. (2020). Recent developments in the facile bio-synthesis of gold nanoparticles (AuNPs) and their biomedical applications. *International journal of nanomedicine*, 15, 275.
- Lee, Y. S. (2008). *Self-assembly and nanotechnology: a force balance approach*. John Wiley & Sons.
- Leite, R., Moore, R., & Whinnery, J. (1964). Low absorption measurements by means of the thermal lens effect using an He-Ne laser. *Applied Physics Letters*, 5(7), 141-143.
- Li, H., & Rothberg, L. (2004). Colorimetric detection of DNA sequences based on electrostatic interactions with unmodified gold nanoparticles. *Proceedings of the National Academy of Sciences*, 101(39), 14036-14039.
- Li, S., Yang, D., Tu, H., Deng, H., Du, D., & Zhang, A. (2013). Protein adsorption and cell adhesion controlled by the surface chemistry of binary perfluoroalkyl/oligo (ethylene glycol) self-assembled monolayers. *Journal of colloid and interface science*, 402, 284-290.
- Li, W., Camargo, P. H., Lu, X., & Xia, Y. (2009). Dimers of silver nanospheres: facile synthesis and their use as hot spots for surface-enhanced Raman scattering. *Nano letters*, 9(1), 485-490.
- Li, X., Zhang, Y., Liu, G., Zhou, L., Xue, Y., & Liu, M. (2022). Recent progress in the applications of gold-based nanoparticles towards tumor-targeted imaging and therapy. *Rsc Advances*, 12(13), 7635-7651.
- Li, Y.-C., Lin, Y.-S., Tsai, P.-J., Chen, C.-T., Chen, W.-Y., & Chen, Y.-C. (2007). Nitrilotriacetic acid-coated magnetic nanoparticles as affinity probes for enrichment of histidine-tagged proteins and phosphorylated peptides. *Analytical chemistry*, 79(19), 7519-7525.
- Lidén, G. (2011). The European commission tries to define nanomaterials. *Annals of Occupational Hygiene*, 55(1), 1-5.
- Liedberg, B., Nylander, C., & Lunström, I. (1983). Surface plasmon resonance for gas detection and biosensing. *Sensors and actuators*, 4, 299-304.
- Lilja, H., Ulmert, D., & Vickers, A. J. (2008). Prostate-specific antigen and prostate cancer: prediction, detection and monitoring. *Nature Reviews Cancer*, 8(4), 268-278.

- Lin, J.-D. (2008). Thyroglobulin and human thyroid cancer. *Clinica chimica acta*, 388(1-2), 15-21.
- Link, S., & El-Sayed, M. A. (2000). Shape and size dependence of radiative, non-radiative and photothermal properties of gold nanocrystals. *International reviews in physical chemistry*, 19(3), 409-453.
- Liu, M., & Franko, M. (2014). Progress in thermal lens spectrometry and its applications in microscale analytical devices. *Critical Reviews in Analytical Chemistry*, 44(4), 328-353.
- Liu, X., Li, X., Xu, W., Zhang, X., Huang, Z., Wang, F., & Liu, J. (2018). Sub-angstrom gold nanoparticle/liposome interfaces controlled by halides. *Langmuir*, 34(22), 6628-6635.
- Liz-Marzán, L. M. (2013). Gold nanoparticle research before and after the Brust–Schiffrin method. *Chemical Communications*, 49(1), 16-18.
- Love, J. C., Estroff, L. A., Kriebel, J. K., Nuzzo, R. G., & Whitesides, G. M. (2005). Self-assembled monolayers of thiolates on metals as a form of nanotechnology. *Chemical reviews*, 105(4), 1103-1170.
- Lu, X., Rycenga, M., Skrabalak, S. E., Wiley, B., & Xia, Y. (2009). Chemical synthesis of novel plasmonic nanoparticles. *Annual review of physical chemistry*, 60, 167-192.
- Lum, W., Bruzas, I., Gorunmez, Z., Unser, S., Beck, T., & Sagle, L. (2017). Novel liposome-based surface-enhanced raman spectroscopy (SERS) substrate. *The journal of physical chemistry letters*, 8(12), 2639-2646.
- Maier, S. A. (2007). *Plasmonics: fundamentals and applications* (Vol. 1). Springer.
- Maiyun, Y., & Chen, P. R. (2015). Progress in the bioorthogonal labeling reactions. *ACTA CHIMICA SINICA*, 73(8), 783-792.
- Martelanc, M., Žiberna, L., Passamonti, S., & Franko, M. (2014). Direct determination of free bilirubin in serum at sub-nanomolar levels. *Analytica chimica acta*, 809, 174-182.
- Martínez-Jothar, L., Beztsinna, N., van Nostrum, C. F., Hennink, W. E., & Oliveira, S. (2019). Selective cytotoxicity to HER2 positive breast cancer cells by saporin-loaded nanobody-targeted polymeric nanoparticles in combination with photochemical internalization. *Molecular pharmaceutics*, 16(4), 1633-1647.
- Martinsson, E., Shahjamali, M., Large, N., Zaraee, N., Zhou, Y., Schatz, G., Mirkin, C., & Aili, D. (2016). Influence of surfactant bilayers and substrate immobilization on the refractive index sensitivity of anisotropic gold nanoparticles. *Small*, 3, 330-342.
- Mazza, G., Posniecek, T., Wagner, L.-M., Etenauer, J., Zuser, K., Gusenbauer, M., & Brandl, M. (2017). Thermal lens spectrometry applied for a sensitive detection of silver-stained protein bands in polyacrylamide gels. *Sensors and Actuators B: Chemical*, 249, 731-737.
- McCormick, S. R., Lillemoe, T. J., Beneke, J., Schrauth, J., & Reinartz, J. (2002). HER2 assessment by immunohistochemical analysis and fluorescence in situ hybridization: comparison of HercepTest and PathVysion commercial assays. *American journal of clinical pathology*, 117(6), 935-943.
- McFarland, A. D., & Van Duyne, R. P. (2003). Single silver nanoparticles as real-time optical sensors with zeptomole sensitivity. *Nano letters*, 3(8), 1057-1062.
- McIntosh, C. M., Esposito, E. A., Boal, A. K., Simard, J. M., Martin, C. T., & Rotello, V. M. (2001). Inhibition of DNA transcription using cationic mixed monolayer protected gold clusters. *Journal of the American Chemical Society*, 123(31), 7626-7629.
- Medintz, I. L. (2016). Interesting developments at the nanoparticle–protein interface: implications for next generation drug delivery. In (Vol. 7, pp. 513-516): Future Science.

- Michel, R., Plostica, T., Abezgauz, L., Danino, D., & Gradzielski, M. (2013). Control of the stability and structure of liposomes by means of nanoparticles. *Soft Matter*, 9(16), 4167-4177.
- Mie, G. (1908). Beiträge zur Optik trüber Medien, speziell kolloidaler Metallösungen. *Annalen der physik*, 330(3), 377-445.
- Mikheev, I., Volkov, D., Proskurnin, M., & Korobov, M. (2015). Monitoring of aqueous fullerene dispersions by thermal-lens spectrometry. *International Journal of Thermophysics*, 36(5), 956-966.
- Miller, M. M., & Lazarides, A. A. (2005). Sensitivity of metal nanoparticle surface plasmon resonance to the dielectric environment. *The Journal of Physical Chemistry B*, 109(46), 21556-21565.
- Mirkin, C. A., Letsinger, R. L., Mucic, R. C., & Storhoff, J. J. (1996). A DNA-based method for rationally assembling nanoparticles into macroscopic materials. *Nature*, 382(6592), 607-609.
- Miti, A., Thamm, S., Müller, P., Csáki, A., Fritzsche, W., & Zuccheri, G. (2020). A miRNA biosensor based on localized surface plasmon resonance enhanced by surface-bound hybridization chain reaction. *Biosensors and Bioelectronics*, 167, 112465.
- Moerner, W. E., & Kador, L. (1989). Optical detection and spectroscopy of single molecules in a solid. *Physical review letters*, 62(21), 2535.
- Mohamad, N. R., Marzuki, N. H. C., Buang, N. A., Huyop, F., & Wahab, R. A. (2015). An overview of technologies for immobilization of enzymes and surface analysis techniques for immobilized enzymes. *Biotechnology & Biotechnological Equipment*, 29(2), 205-220.
- Monegal, A., Ami, D., Martinelli, C., Huang, H., Aliprandi, M., Capasso, P., Francavilla, C., Ossolengo, G., & de Marco, A. (2009). Immunological applications of single-domain llama recombinant antibodies isolated from a naive library. *Protein Engineering, Design & Selection*, 22(4), 273-280.
- Montis, C., Maiolo, D., Alessandri, I., Bergese, P., & Berti, D. (2014). Interaction of nanoparticles with lipid membranes: a multiscale perspective. *Nanoscale*, 6(12), 6452-6457.
- Mori, K., & Sakurai, K. (2021). Clickable gold-nanoparticles as generic probe precursors for facile photoaffinity labeling application. *Organic & Biomolecular Chemistry*, 19(6), 1268-1273.
- Mori, S., Shinohata, R., Renbutsu, M., Takahashi, H. K., Fang, Y.-I., Yamaoka, K., Okamoto, M., Yamamoto, I., & Nishibori, M. (2003). Histidine-rich glycoprotein plus zinc reverses growth inhibition of vascular smooth muscle cells by heparin. *Cell and tissue research*, 312(3), 353-359.
- Mori, S., Takahashi, H. K., Yamaoka, K., Okamoto, M., & Nishibori, M. (2003). High affinity binding of serum histidine-rich glycoprotein to nickel-nitrilotriacetic acid: the application to microquantification. *Life sciences*, 73(1), 93-102.
- Muskens, O. L., Bachelier, G., Del Fatti, N., Vallee, F., Brioude, A., Jiang, X., & Pileni, M.-P. (2008). Quantitative absorption spectroscopy of a single gold nanorod. *The Journal of Physical Chemistry C*, 112(24), 8917-8921.
- Nahta, R., Takahashi, T., Ueno, N. T., Hung, M.-C., & Esteva, F. J. (2004). P27kip1 down-regulation is associated with trastuzumab resistance in breast cancer cells. *Cancer research*, 64(11), 3981-3986.
- Nair, D. P., Podgorski, M., Chatani, S., Gong, T., Xi, W., Fenoli, C. R., & Bowman, C. N. (2014). The thiol-Michael addition click reaction: a powerful and widely used tool in materials chemistry. *Chemistry of Materials*, 26(1), 724-744.

- Nath, N., & Chilkoti, A. (2004). Label-free biosensing by surface plasmon resonance of nanoparticles on glass: optimization of nanoparticle size. *Analytical chemistry*, 76(18), 5370-5378.
- Neef, A. B., Pernet, L., Schreier, V. N., Scapozza, L., & Luedtke, N. W. (2015). A bioorthogonal chemical reporter of viral infection. *Angewandte Chemie*, 127(27), 8022-8025.
- Nuzzo, R. G., & Allara, D. L. (1983). Adsorption of bifunctional organic disulfides on gold surfaces. *Journal of the American Chemical Society*, 105(13), 4481-4483.
- Olofsson, L., Rindzevicius, T., Pfeiffer, I., Käll, M., & Höök, F. (2003). Surface-based gold-nanoparticle sensor for specific and quantitative DNA hybridization detection. *Langmuir*, 19(24), 10414-10419.
- Orlova, A., Wällberg, H., Stone-Elander, S., & Tolmachev, V. (2009). On the selection of a tracer for PET imaging of HER2-expressing tumors: direct comparison of a 124I-labeled affibody molecule and trastuzumab in a murine xenograft model. *Journal of Nuclear Medicine*, 50(3), 417-425.
- Otte, M. A., Estévez, M.-C., Carrascosa, L. G., González-Guerrero, A. B., Lechuga, L. M., & Sepúlveda, B. (2011). Improved biosensing capability with novel suspended nanodisks. *The Journal of Physical Chemistry C*, 115(13), 5344-5351.
- Otto, A. (1968). Excitation of nonradiative surface plasma waves in silver by the method of frustrated total reflection. *Zeitschrift für Physik A Hadrons and nuclei*, 216(4), 398-410.
- Paik, S., Bryant, J., Tan-Chiu, E., Romond, E., Hiller, W., Park, K., Brown, A., Yothers, G., Anderson, S., & Smith, R. (2002). Real-world performance of HER2 testing—national surgical adjuvant breast and bowel project experience. *Journal of the National Cancer Institute*, 94(11), 852-854.
- Paul, J., Meltzer, C., Braunschweig, B. r., & Peukert, W. (2016). Lubrication of individual microcontacts by a self-assembled alkyl phosphonic acid monolayer on  $\alpha$ -Al<sub>2</sub>O<sub>3</sub> (0001). *Langmuir*, 32(33), 8298-8306.
- Pedersen, M., & Rasmussen, B. B. (2009). The correlation between dual-color chromogenic in situ hybridization and fluorescence in situ hybridization in assessing HER2 gene amplification in breast cancer. *Diagnostic Molecular Pathology*, 18(2), 96-102.
- Pennacchio, A., Ruggiero, G., Staiano, M., Piccialli, G., Oliviero, G., Lewkowicz, A., Synak, A., Bojarski, P., & D'Auria, S. (2014). A surface plasmon resonance based biochip for the detection of patulin toxin. *Optical Materials*, 36(10), 1670-1675.
- Perrier, A., Gligorov, J., Lefèvre, G., & Boissan, M. (2018). The extracellular domain of Her2 in serum as a biomarker of breast cancer. *Laboratory Investigation*, 98(6), 696-707.
- Persons, D., Borelli, K., & Hsu, P. (1997). Quantitation of HER-2/neu and c-myc gene amplification in breast carcinoma using fluorescence in situ hybridization. *Modern pathology: an official journal of the United States and Canadian Academy of Pathology, Inc*, 10(7), 720-727.
- Piccart-Gebhart, M. J., Procter, M., Leyland-Jones, B., Goldhirsch, A., Untch, M., Smith, I., Gianni, L., Baselga, J., Bell, R., & Jackisch, C. (2005). Trastuzumab after adjuvant chemotherapy in HER2-positive breast cancer. *New England journal of medicine*, 353(16), 1659-1672.
- Pimková, K., Bocková, M., Hegnerová, K., Suttar, J., Čermák, J., Homola, J., & Dyr, J. E. (2012). Surface plasmon resonance biosensor for the detection of VEGFR-1—a protein marker of myelodysplastic syndromes. *Analytical and bioanalytical chemistry*, 402(1), 381-387.

- Podesta, A., Imperadori, L., Colnaghi, W., Finzi, L., Milani, P., & Dunlap, D. (2004). Atomic force microscopy study of DNA deposited on poly L-ornithine-coated mica. *Journal of microscopy*, 215(3), 236-240.
- Pons, T., Medintz, I. L., Sapsford, K. E., Higashiya, S., Grimes, A. F., English, D. S., & Mattoussi, H. (2007). On the quenching of semiconductor quantum dot photoluminescence by proximal gold nanoparticles. *Nano letters*, 7(10), 3157-3164.
- Prodan, E., Radloff, C., Halas, N. J., & Nordlander, P. (2003). A hybridization model for the plasmon response of complex nanostructures. *Science*, 302(5644), 419-422.
- Pruszyński, M., Koumariou, E., Vaidyanathan, G., Revets, H., Devoogdt, N., Lahoutte, T., & Zalutsky, M. R. (2013). Targeting breast carcinoma with radioiodinated anti-HER2 Nanobody. *Nuclear medicine and biology*, 40(1), 52-59.
- Pusztai, L., & Esteva, F. J. (2006). Continued use of trastuzumab (herceptin) after progression on prior trastuzumab therapy in HER-2-positive metastatic breast cancer. *Cancer investigation*, 24(2), 187-191.
- Raether, H. (1988a). Surface plasmons on gratings. *Surface plasmons on smooth and rough surfaces and on gratings*, 91-116.
- Raether, H. (1988b). Surface plasmons on smooth surfaces. *Surface plasmons on smooth and rough surfaces and on gratings*, 4-39.
- Raigoza, A. F., Fies, W., Lim, A., Onyirioha, K., & Webb, L. J. (2017). One-pot reaction for the preparation of biofunctionalized self-assembled monolayers on gold surfaces. *Applied Surface Science*, 394, 288-296.
- Rana, S., Yeh, Y.-C., & Rotello, V. M. (2010). Engineering the nanoparticle–protein interface: applications and possibilities. *Current opinion in chemical biology*, 14(6), 828-834.
- Rasch, M. R., Rossinyol, E., Hueso, J. L., Goodfellow, B. W., Arbiol, J., & Korgel, B. A. (2010). Hydrophobic gold nanoparticle self-assembly with phosphatidylcholine lipid: membrane-loaded and janus vesicles. *Nano letters*, 10(9), 3733-3739.
- Reineke, J. (2012). *Nanotoxicity: methods and protocols*. Humana Press.
- Revets, H., De Baetselier, P., & Muyldermans, S. (2005). Nanobodies as novel agents for cancer therapy. *Expert opinion on biological therapy*, 5(1), 111-124.
- Reynolds, R. A., Mirkin, C. A., & Letsinger, R. L. (2000). Homogeneous, nanoparticle-based quantitative colorimetric detection of oligonucleotides. *Journal of the American Chemical Society*, 122(15), 3795-3796.
- Ridolfi, R. L., Jamehdor, M. R., & Arber, J. M. (2000). HER-2/neu testing in breast carcinoma: a combined immunohistochemical and fluorescence in situ hybridization approach. *Modern Pathology*, 13(8), 866-873.
- Rieckhoff, K. E. (1966). SELF-INDUCED DIVERGENCE OF CW LASER BEAMS IN LIQUIDS—A NEW NONLINEAR EFFECT IN THE PROPAGATION OF LIGHT. *Applied Physics Letters*, 9(2), 87-88.
- Riedel, T., Rodriguez-Emmenegger, C., de los Santos Pereira, A., Bědajánková, A., Jinoch, P., Boltovets, P. M., & Brynda, E. (2014). Diagnosis of Epstein–Barr virus infection in clinical serum samples by an SPR biosensor assay. *Biosensors and Bioelectronics*, 55, 278-284.
- Rindzevicius, T., Alaverdyan, Y., Käll, M., Murray, W. A., & Barnes, W. L. (2007). Long-range refractive index sensing using plasmonic nanostructures. *The Journal of Physical Chemistry C*, 111(32), 11806-11810.



- Rossetti, R., Nakahara, S., & Brus, L. E. (1983). Quantum size effects in the redox potentials, resonance Raman spectra, and electronic spectra of CdS crystallites in aqueous solution. *The Journal of Chemical Physics*, 79(2), 1086-1088.
- Rusmini, F., Zhong, Z., & Feijen, J. (2007). Protein immobilization strategies for protein biochips. *Biomacromolecules*, 8(6), 1775-1789.
- Sajfutdinow, M., Uhlig, K., Prager, A., Schneider, C., Abel, B., & Smith, D. (2017). Nanoscale patterning of self-assembled monolayer (SAM)-functionalised substrates with single molecule contact printing. *Nanoscale*, 9(39), 15098-15106.
- Sakura, T., Takahashi, T., Kataoka, K., & Nagasaki, Y. (2005). One-pot preparation of mono-dispersed and physiologically stabilized gold colloid. *Colloid and Polymer Science*, 284(1), 97-101.
- Sakurai, K., Kato, A., & Adachi, K. (2018). Design and synthesis of small molecule-conjugated photoaffinity nanoprobes for a streamlined analysis of binding proteins. *Bioorganic & Medicinal Chemistry Letters*, 28(19), 3227-3230.
- Salgado, R., Denkert, C., Campbell, C., Savas, P., Nuciforo, P., Aura, C., De Azambuja, E., Eidtmann, H., Ellis, C. E., & Baselga, J. (2015). Tumor-infiltrating lymphocytes and associations with pathological complete response and event-free survival in HER2-positive early-stage breast cancer treated with lapatinib and trastuzumab: a secondary analysis of the NeoALTTO trial. *JAMA oncology*, 1(4), 448-455.
- Salvati, A., Pitek, A. S., Monopoli, M. P., Prapainop, K., Bombelli, F. B., Hristov, D. R., Kelly, P. M., Åberg, C., Mahon, E., & Dawson, K. A. (2013). Transferrin-functionalized nanoparticles lose their targeting capabilities when a biomolecule corona adsorbs on the surface. *Nature nanotechnology*, 8(2), 137-143.
- Sanavio, B., Scaini, D., Grunwald, C., Legname, G., Scoles, G., & Casalis, L. (2010). Oriented immobilization of prion protein demonstrated via precise interfacial nanostructure measurements. *ACS nano*, 4(11), 6607-6616.
- Sanchez, F., & Sobolev, K. (2010). Nanotechnology in concrete—a review. *Construction and building materials*, 24(11), 2060-2071.
- Sannomiya, T., Sahoo, P. K., Mahcicek, D. I., Solak, H. H., Hafner, C., Grieshaber, D., & Vörös, J. (2009). Biosensing by densely packed and optically coupled plasmonic particle arrays. *Small*, 5(16), 1889-1896.
- Sano, K.-I., & Shiba, K. (2003). A hexapeptide motif that electrostatically binds to the surface of titanium. *Journal of the American Chemical Society*, 125(47), 14234-14235.
- Sapsford, K. E., Algar, W. R., Berti, L., Gemmill, K. B., Casey, B. J., Oh, E., Stewart, M. H., & Medintz, I. L. (2013). Functionalizing nanoparticles with biological molecules: developing chemistries that facilitate nanotechnology. *Chemical reviews*, 113(3), 1904-2074.
- Savarala, S., Ahmed, S., Ilies, M. A., & Wunder, S. L. (2011). Stabilization of soft lipid colloids: competing effects of nanoparticle decoration and supported lipid bilayer formation. *ACS nano*, 5(4), 2619-2628.
- Schaming, D., & Remita, H. (2015). Nanotechnology: from the ancient time to nowadays. *Foundations of Chemistry*, 17(3), 187-205.
- Schasfoort, R. B. (2017). *Handbook of surface plasmon resonance*. Royal Society of Chemistry.
- Scheuer, W., Friess, T., Burtscher, H., Bossenmaier, B., Endl, J., & Hasmann, M. (2009). Strongly enhanced antitumor activity of trastuzumab and pertuzumab combination treatment on HER2-positive human xenograft tumor models. *Cancer research*, 69(24), 9330-9336.

- Schlange, T., & Pantel, K. (2016). Potential of circulating tumor cells as blood-based biomarkers in cancer liquid biopsy. In (Vol. 17, pp. 183-186): Future Medicine.
- Schmid, F. X. (2001). Biological macromolecules: UV-visible spectrophotometry. *e LS*.
- Schollbach, M., Zhang, F., Roosen-Runge, F., Skoda, M. W., Jacobs, R. M., & Schreiber, F. (2014). Gold nanoparticles decorated with oligo (ethylene glycol) thiols: Surface charges and interactions with proteins in solution. *Journal of colloid and interface science*, *426*, 31-38.
- Schwartz, D. K. (2001). Mechanisms and kinetics of self-assembled monolayer formation. *Annual review of physical chemistry*, *52*(1), 107-137.
- Schwenk, J. M., Lindberg, J., Sundberg, M., Uhlen, M., & Nilsson, P. (2007). Determination of Binding Specificities in Highly Multiplexed Bead-based Assays for Antibody Proteomics\* *S. Molecular & Cellular Proteomics*, *6*(1), 125-132.
- Seferos, D. S., Prigodich, A. E., Giljohann, D. A., Patel, P. C., & Mirkin, C. A. (2009). Polyvalent DNA nanoparticle conjugates stabilize nucleic acids. *Nano letters*, *9*(1), 308-311.
- Sekiguchi, H., Shimamoto, K., Takano, M., Kimura, M., Takahashi, Y., Tatsumi, F., Watanabe, E., Jujo, K., Ishizuka, N., & Kawana, M. (2017). Cancer antigen-125 plasma level as a biomarker of new-onset atrial fibrillation in postmenopausal women. *Heart*, *103*(17), 1368-1373.
- Shah, M., Badwaik, V., Kherde, Y., Waghvani, H. K., Modi, T., Aguilar, Z. P., Rodgers, H., Hamilton, W., Marutharaj, T., & Webb, C. (2014). Gold nanoparticles: various methods of synthesis and antibacterial applications. *Front Biosci*, *19*(8), 1320-1344.
- Shakiba, A., Jamison, A. C., & Lee, T. R. (2015). Poly (L-lysine) interfaces via dual click reactions on surface-bound custom-designed dithiol adsorbates. *Langmuir*, *31*(22), 6154-6163.
- Sherry, L. J., Jin, R., Mirkin, C. A., Schatz, G. C., & Van Duyne, R. P. (2006). Localized surface plasmon resonance spectroscopy of single silver triangular nanoprisms. *Nano letters*, *6*(9), 2060-2065.
- Shi, H.-Z., Wang, Y.-N., Huang, X.-H., Zhang, K.-C., Xi, H.-Q., Cui, J.-X., Liu, G.-X., Liang, W.-T., Wei, B., & Chen, L. (2017). Serum HER2 as a predictive biomarker for tissue HER2 status and prognosis in patients with gastric cancer. *World Journal of Gastroenterology*, *23*(10), 1836.
- Shokoufi, N., & Vaziri Heshi, S. (2021). Enhancement of photo-thermal lens of fluorescence molecules by fluorescence resonance energy transfer mechanism. *Journal of Fluorescence*, *31*(2), 587-593.
- Siegel, R., Ward, E., Brawley, O., & Jemal, A. (2011). Cancer statistics, 2011: the impact of eliminating socioeconomic and racial disparities on premature cancer deaths. *CA: a cancer journal for clinicians*, *61*(4), 212-236.
- Soler, M. A., Medagli, B., Wang, J., Oloketuyi, S., Bajc, G., Huang, H., Fortuna, S., & de Marco, A. (2021). Effect of humanizing mutations on the stability of the llama single-domain variable region. *Biomolecules*, *11*(2), 163.
- Solimini, D. (1966). Loss measurement of organic materials at 6328 Å. *Journal of Applied Physics*, *37*(8), 3314-3315.
- Song, L., Guo, Y., Roebuck, D., Chen, C., Yang, M., Yang, Z., Sreedharan, S., Glover, C., Thomas, J. A., & Liu, D. (2015). Terminal PEGylated DNA-gold nanoparticle conjugates offering high resistance to nuclease degradation and efficient intracellular delivery of DNA binding agents. *ACS applied materials & interfaces*, *7*(33), 18707-18716.

- Sönnichsen, C., Franzl, T., Wilk, T., von Plessen, G., Feldmann, J., Wilson, O., & Mulvaney, P. (2002). Drastic reduction of plasmon damping in gold nanorods. *Physical review letters*, 88(7), 077402.
- Sosibo, N. M., Tshikhudo, R. T., & Revaprasadu, N. (2007). Stable, hydrophilic nitrilotriacetic acid-capped gold monolayer protected clusters. *MRS Online Proceedings Library (OPL)*, 1064.
- Spector, N. L., & Blackwell, K. L. (2009). Understanding the Mechanisms Behind Trastuzumab Therapy for Human Epidermal Growth Factor Receptor 2-Positive Breast Cancer. *Journal of Clinical Oncology*, 27(34), 5838-5847. <https://doi.org/10.1200/jco.2009.22.1507>
- Speers, A. E., Adam, G. C., & Cravatt, B. F. (2003). Activity-based protein profiling in vivo using a copper (i)-catalyzed azide-alkyne [3+ 2] cycloaddition. *Journal of the American Chemical Society*, 125(16), 4686-4687.
- Sperling, R. A., & Parak, W. J. (2010). Surface modification, functionalization and bioconjugation of colloidal inorganic nanoparticles. *Philosophical Transactions of the Royal Society A: Mathematical, Physical and Engineering Sciences*, 368(1915), 1333-1383.
- Spicer, C. D., Jumeaux, C., Gupta, B., & Stevens, M. M. (2018). Peptide and protein nanoparticle conjugates: versatile platforms for biomedical applications. *Chemical Society Reviews*, 47(10), 3574-3620.
- Stopeck, A. T., Brown-Glaberman, U., Wong, H. Y., Park, B. H., Barnato, S. E., Gradishar, W. J., Hudis, C. A., & Rugo, H. S. (2012). The role of targeted therapy and biomarkers in breast cancer treatment. *Clinical & experimental metastasis*, 29(7), 807-819.
- Subara, D., & Jaswir, I. (2018). Gold nanoparticles: Synthesis and application for halal authentication in meat and meat products. *International Journal on Advanced Science, Engineering and Information Technology*, 8(2018), 1633-1641.
- Sugikawa, K., Kadota, T., Yasuhara, K., & Ikeda, A. (2016). Anisotropic Self-Assembly of Citrate-Coated Gold Nanoparticles on Fluidic Liposomes. *Angewandte Chemie International Edition*, 55(12), 4059-4063.
- Sun, H., Chen, G. Y., & Yao, S. Q. (2013). Recent advances in microarray technologies for proteomics. *Chemistry & biology*, 20(5), 685-699.
- Swartz, J. D., Gulka, C. P., Haselton, F. R., & Wright, D. W. (2011). Development of a histidine-targeted spectrophotometric sensor using Ni (II) NTA-functionalized Au and Ag nanoparticles. *Langmuir*, 27(24), 15330-15339.
- Swofford, R. L., Long, M., & Albrecht, A. (1976). C-H vibrational states of benzene, naphthalene, and anthracene in the visible region by thermal lensing spectroscopy and the local mode model. *The Journal of Chemical Physics*, 65(1), 179-190.
- Tai, W., Mahato, R., & Cheng, K. (2010). The role of HER2 in cancer therapy and targeted drug delivery. *Journal of controlled release*, 146(3), 264-275.
- Taniguchi, N. (1974). On the basic concept of nano-technology proceedings of the international conference on production engineering Tokyo part ii japan society of precision engineering. *Pabbati et al.*
- Tatur, S., Maccarini, M., Barker, R., Nelson, A., & Fragneto, G. (2013). Effect of functionalized gold nanoparticles on floating lipid bilayers. *Langmuir*, 29(22), 6606-6614.
- Teng, Y.-Y., & Stern, E. A. (1967). Plasma radiation from metal grating surfaces. *Physical review letters*, 19(9), 511.
- Terpe, K. (2003). Overview of tag protein fusions: from molecular and biochemical fundamentals to commercial systems. *Applied microbiology and biotechnology*, 60(5), 523-533.

- Tesler, A. B., Chuntunov, L., Karakouz, T., Bendikov, T. A., Haran, G., Vaskevich, A., & Rubinstein, I. (2011). Tunable localized plasmon transducers prepared by thermal dewetting of percolated evaporated gold films. *The Journal of Physical Chemistry C*, *115*(50), 24642-24652.
- Testa, C., Zammataro, A., Pappalardo, A., & Sfrazzetto, G. T. (2019). Catalysis with carbon nanoparticles. *Rsc Advances*, *9*(47), 27659-27664.
- Thakur, N. S., Patel, G., Kushwah, V., Jain, S., & Banerjee, U. C. (2018). Self-assembled gold nanoparticle–lipid nanocomposites for on-demand delivery, tumor accumulation, and combined photothermal–photodynamic therapy. *ACS Applied Bio Materials*, *2*(1), 349-361.
- Tijink, B. M., Laeremans, T., Budde, M., Stigter-van Walsum, M., Dreier, T., de Haard, H. J., Leemans, C. R., & van Dongen, G. A. (2008). Improved tumor targeting of anti–epidermal growth factor receptor Nanobodies through albumin binding: taking advantage of modular Nanobody technology. *Molecular cancer therapeutics*, *7*(8), 2288-2297.
- Tort, N., Salvador, J.-P., & Marco, M.-P. (2017). Multimodal plasmonic biosensing nanostructures prepared by DNA-directed immobilization of multifunctional DNA-gold nanoparticles. *Biosensors and Bioelectronics*, *90*, 13-22.
- Trudel, D., Têtu, B., Grégoire, J., Plante, M., Renaud, M.-C., Bachvarov, D., Douville, P., & Bairati, I. (2012). Human epididymis protein 4 (HE4) and ovarian cancer prognosis. *Gynecologic oncology*, *127*(3), 511-515.
- Tsé, C., Gauchez, A.-S., Jacot, W., & Lamy, P.-J. (2012). HER2 shedding and serum HER2 extracellular domain: biology and clinical utility in breast cancer. *Cancer treatment reviews*, *38*(2), 133-142.
- Tseng, S.-Y., Li, S.-Y., Yi, S.-Y., Sun, A. Y., Gao, D.-Y., & Wan, D. (2017). Food quality monitor: paper-based plasmonic sensors prepared through reversal nanoimprinting for rapid detection of biogenic amine odorants. *ACS applied materials & interfaces*, *9*(20), 17306-17316.
- Turkevich, J., Stevenson, P. C., & Hillier, J. (1951). A study of the nucleation and growth processes in the synthesis of colloidal gold. *Discussions of the Faraday Society*, *11*, 55-75.
- Vaidyanathan, G., McDougald, D., Choi, J., Koumariou, E., Weitzel, D., Osada, T., Lyster, H. K., & Zalutsky, M. R. (2016). Preclinical evaluation of 18F-labeled anti-HER2 nanobody conjugates for imaging HER2 receptor expression by immuno-PET. *Journal of Nuclear Medicine*, *57*(6), 967-973.
- Van de Broek, B., Devoogdt, N., D'Hollander, A., Gijs, H.-L., Jans, K., Lagae, L., Muyltermans, S., Maes, G., & Borghs, G. (2011). Specific cell targeting with nanobody conjugated branched gold nanoparticles for photothermal therapy. *ACS nano*, *5*(6), 4319-4328.
- van de Vijver, M., Bilous, M., Hanna, W., Hofmann, M., Kristel, P., Penault-Llorca, F., & Rüschoff, J. (2007). Chromogenic in situ hybridisation for the assessment of HER2 status in breast cancer: an international validation ring study. *Breast Cancer Research*, *9*(5), 1-9.
- van der Meer, S. B., Loza, K., Wey, K., Heggen, M., Beuck, C., Bayer, P., & Epple, M. (2019). Click chemistry on the surface of ultrasmall gold nanoparticles (2 nm) for covalent ligand attachment followed by NMR spectroscopy. *Langmuir*, *35*(22), 7191-7204.
- Varga, Z., Noske, A., Ramach, C., Padberg, B., & Moch, H. (2013). Assessment of HER2 status in breast cancer: overall positivity rate and accuracy by fluorescence in situ hybridization and immunohistochemistry in a single institution over 12 years: a quality control study. *BMC cancer*, *13*(1), 1-9.

- Vaziri Heshi, S., & Shokoufi, N. (2021). Fluorescence resonance energy transfer-thermal lens spectrometry (FRET-TLS) as molecular counting of methamphetamine. *Microchimica Acta*, 188(6), 1-11.
- Ventura, B. D., Cennamo, M., Minopoli, A., Campanile, R., Censi, S. B., Terracciano, D., Portella, G., & Velotta, R. (2020). Colorimetric test for fast detection of SARS-CoV-2 in nasal and throat swabs. *ACS sensors*, 5(10), 3043-3048.
- Volkov, D., Proskurnin, M., Mikheev, I., Vasil'ev, D., Korobov, M., Nedosekin, D., & Zharov, V. (2012). Application of photothermal and photoacoustic spectroscopy for the monitoring of aqueous dispersions of carbon nanomaterials. *ALT Proceedings*, 1.
- Vranic, S., Teruya, B., Repertinger, S., Ulmer, P., Hagenkord, J., & Gatalica, Z. (2011). Assessment of HER2 gene status in breast carcinomas with polysomy of chromosome 17. *Cancer*, 117(1), 48-53.
- Walper, S. A., Turner, K. B., & Medintz, I. L. (2015). Enzymatic bioconjugation of nanoparticles: developing specificity and control. *Current Opinion in Biotechnology*, 34, 232-241.
- Wang, F., Curry, D. E., & Liu, J. (2015). Driving adsorbed gold nanoparticle assembly by merging lipid gel/fluid interfaces. *Langmuir*, 31(49), 13271-13274.
- Wang, F., & Liu, J. (2015). Self-healable and reversible liposome leakage by citrate-capped gold nanoparticles: probing the initial adsorption/desorption induced lipid phase transition. *Nanoscale*, 7(38), 15599-15604.
- Wang, G., Wang, C., Yang, R., Liu, W., & Sun, S. (2017). A sensitive and stable surface plasmon resonance sensor based on monolayer protected silver film. *Sensors*, 17(12), 2777.
- Wang, J., Cheng, B., Li, J., Zhang, Z., Hong, W., Chen, X., & Chen, P. R. (2015). Chemical remodeling of cell-surface sialic acids through a palladium-triggered bioorthogonal elimination reaction. *Angewandte Chemie*, 127(18), 5454-5458.
- Waters, C. A., Mills, A. J., Johnson, K. A., & Schiffrin, D. J. (2003). Purification of dodecanethiol derivatised gold nanoparticles. *Chemical Communications*(4), 540-541.
- Westphal, M., & Lamszus, K. (2015). Circulating biomarkers for gliomas. *Nature Reviews Neurology*, 11(10), 556-566.
- Wich, P. R. (2015). Baukasten der Natur. *Nachrichten aus der Chemie*, 63(2), 128-132.
- Willems, K. A., & Van Duyne, R. P. (2007). Localized surface plasmon resonance spectroscopy and sensing. *Annu. Rev. Phys. Chem.*, 58, 267-297.
- Wolf, L. K., Fullenkamp, D. E., & Georgiadis, R. M. (2005). Quantitative angle-resolved SPR Imaging of DNA– DNA and DNA– drug kinetics. *Journal of the American Chemical Society*, 127(49), 17453-17459.
- Wu, P., Feldman, A. K., Nugent, A. K., Hawker, C. J., Scheel, A., Voit, B., Pyun, J., Fréchet, J. M., Sharpless, K. B., & Fokin, V. V. (2004). Efficiency and fidelity in a click-chemistry route to triazole dendrimers by the copper (I)-catalyzed ligation of azides and alkynes. *Angewandte Chemie*, 116(30), 4018-4022.
- Xiang, H. Y., & Li, W. G. (2009). Electrochemical sensor for trans-resveratrol determination based on indium tin oxide electrode modified with molecularly imprinted self-assembled films. *Electroanalysis: An International Journal Devoted to Fundamental and Practical Aspects of Electroanalysis*, 21(10), 1207-1210.
- Xu, C., Xu, K., Gu, H., Zhong, X., Guo, Z., Zheng, R., Zhang, X., & Xu, B. (2004). Nitrilotriacetic acid-modified magnetic nanoparticles as a general agent to bind histidine-tagged proteins. *Journal of the American Chemical Society*, 126(11), 3392-3393.

- Xue, Y., Li, X., Li, H., & Zhang, W. (2014). Quantifying thiol–gold interactions towards the efficient strength control. *Nature communications*, 5(1), 1-9.
- Yan, R., Le Pleux, L. c., Mayor, M., & Zharnikov, M. (2016). Promoted Exchange Reaction between Alkanethiolate Self-Assembled Monolayers and an Azide-Bearing Substituent. *The Journal of Physical Chemistry C*, 120(45), 25967-25976.
- Yang, K. S., Budin, G., Reiner, T., Vinegoni, C., & Weissleder, R. (2012). Bioorthogonal imaging of aurora kinase A in live cells. *Angewandte Chemie*, 124(27), 6702-6707.
- Yang, Z., Kasprzyk-Hordern, B., Goggins, S., Frost, C. G., & Estrela, P. (2015). A novel immobilization strategy for electrochemical detection of cancer biomarkers: DNA-directed immobilization of aptamer sensors for sensitive detection of prostate specific antigens. *Analyst*, 140(8), 2628-2633.
- Yersal, O., & Barutca, S. (2014). Biological subtypes of breast cancer: Prognostic and therapeutic implications. *World journal of clinical oncology*, 5(3), 412.
- Yoshimura, K., Maeda, M., Kamiya, N., & Zako, T. (2020). Protein-functionalized gold nanoparticles for antibody detection using the darkfield microscopic observation of nanoparticle aggregation. *Analytical Sciences*, 20SCP12.
- Zeira, A., Berson, J., Feldman, I., Maoz, R., & Sagiv, J. (2011). A bipolar electrochemical approach to constructive lithography: metal/monolayer patterns via consecutive site-defined oxidation and reduction. *Langmuir*, 27(13), 8562-8575.
- Zeng, S., Baillargeat, D., Ho, H.-P., & Yong, K.-T. (2014). Nanomaterials enhanced surface plasmon resonance for biological and chemical sensing applications. *Chemical Society Reviews*, 43(10), 3426-3452.
- Zhang, J., Song, Y., Zhang, C., Zhi, X., Fu, H., Ma, Y., Chen, Y., Pan, F., Wang, K., & Ni, J. (2015). Circulating MiR-16-5p and MiR-19b-3p as two novel potential biomarkers to indicate progression of gastric cancer. *Theranostics*, 5(7), 733.
- Zhang, T., Yang, Z., & Liu, D. (2011). DNA discrete modified gold nanoparticles. *Nanoscale*, 3(10), 4015-4021.
- Zhang, X., Servos, M. R., & Liu, J. (2012). Instantaneous and quantitative functionalization of gold nanoparticles with thiolated DNA using a pH-assisted and surfactant-free route. *Journal of the American Chemical Society*, 134(17), 7266-7269.
- Zheng, Y., Cui, J., & Ikeda, T. (2015). Click functionalization of phenyl-capped bithiophene on azide-terminated self-assembled monolayers. *Applied Surface Science*, 355, 213-217.
- Ziegler, C., & Eychmuller, A. (2011). Seeded growth synthesis of uniform gold nanoparticles with diameters of 15– 300 nm. *The Journal of Physical Chemistry C*, 115(11), 4502-4506.
- Zoric, I., Zach, M., Kasemo, B., & Langhammer, C. (2011). Gold, platinum, and aluminum nanodisk plasmons: material independence, subradiance, and damping mechanisms. *ACS nano*, 5(4), 2535-2546.
- Zsigmondy, R. (1909). Colloids and the Ultra Microscope. *Journal of the American Chemical Society*, 31(8), 951-952.
- Екимов, А., & Онущенко, А. (1981). Квантовый размерный эффект в трехмерных микрокристаллах полупроводников. *Письма в ЖЭТФ*, 34(6), 363-366.